FULL-SCALE MECHANISTIC AND PERFORMANCE INVESTIGATION OF A FLEXIBLE PAVEMENT WITH A STABILIZED FOUNDATION

by

Mostafa Nakhaei

A dissertation submitted to the Graduate Faculty of
Auburn University
in partial fulfillment of the
requirements for the Degree of
Doctor of Philosophy

Auburn, Alabama
August 7, 2021

Keywords: Middle-up cracking, cement treated base, bottom-up fatigue cracking, stabilized foundation pavements, pavement modeling, pavement instrumentation

Approved by

David Timm, Chair, Brasfield & Gorrie Professor, Civil and Environmental Engineering
Benjamin Bowers, Assistant Professor, Civil and Environmental Engineering
Nam Tran, Research Professor, National Center for Asphalt Technology
Fabricio Leiva Villacorta, Assistant Research Professor, National Center for Asphalt Technology
Nedret Billor, Professor of Statistics, Mathematics and Statistics

ABSTRACT

The current study aimed to develop a mechanistic understanding of the behavior of flexible pavements with stabilized foundations through full-scale testing, instrumentation, and simulation. In pursuit of this objective, a full-scale pavement section was constructed at the National Center for Asphalt Technology (NCAT) Test Track in 2018 featuring stabilized foundation layers under the asphalt layers. For comparison, three additional full-scale pavement sections were included in this study. The behavior of all sections was observed over time under accelerated truck trafficking using embedded strain and stress sensors. In addition, surface performance was measured routinely with a falling weight deflectometer (FWD) and a condition survey van. The strain measurement at the bottom of asphalt concrete (AC) for the conventional pavement sections showed a familiar trend in which the tensile strain increased exponentially with temperature. However, the tensile strain response for the stabilized foundation section showed a fundamentally different behavior in which the horizontal tensile strain response decreased with the increase in temperature. Further investigation showed the strain response at the bottom of the AC layer switched to predominantly compression for the stabilized foundation section. The compressive strain response at the bottom of AC contradicts the well-established premise that the bottom of AC is in tension. Computational simulations of the stabilized section illustrated the same trend that the bottom of AC should be in compression in summer. However, the analysis predicted that the maximum tensile strain actually occurs near the middle of the AC layer and thus fatigue cracking could initiate at shallower depths leading to middle-up cracking. MASTIC program, originally developed in this research study, was

used for backcalculation since other commercial software programs led to unrealistic results with high variance for the stabilized foundation section. It was found that a four-layer system with the original cross-section and fully bonded condition for the top interface along with a nearly slip conditions for other interfaces was the best-case scenario for having reasonable results and less variability. This study also proposed a new methodology based on Boussinesq elastic half-space equation to remove erroneous deflection basins and thus having less variability. In general, it is suggested that the stabilized foundation sections that behave mechanistically different than conventional flexible pavements be designed and evaluated differently using mechanistic concepts introduced in this study.

DEDICATION

I dedicate this dissertation to my wife, Parisa, for her continued support, patience, and love. This would have never been achieved without you, Parisa, and I am truly thankful for having you in my life. I also dedicate this to my parents, Zohre and Alireza Nakhaei, whom their company I missed during the past four years and whose good examples have taught me to work hard for the things I aspire to achieve.

ACKNOWLEDGMENTS

I would like to thank Dr. David Timm, my major advisor, for his extraordinary supervision and direction in the preparation of this dissertation. Dr. Timm was beyond an extraordinary supervisor for me, he inspired me in many aspects. His commitment to work, his dedication to mentorship, and his love for people and family was inspirational. I would also like to acknowledge the advisory committee members including Dr. Fabricio Leiva Villacorta, Dr. Nam Tran, and Dr. Benjamin Bowers for their time and assistance during this project. Thanks are due to National Center for Asphalt Technology (NCAT) research team and staff. This research would have been impossible without NCAT facilities, staff, and research members. I thank the Test Track sponsors and in particular the Mississippi Department of Transportation for funding of this project and their continued cooperation.

TABLE OF CONTENTS

LIST OF FIGURES

LIST OF TABLES

LIST OF ABBREVIATIONS

AC	Asphalt Concrete
ASG	Asphalt Strain Gauges
CBR	California bearing ratio
CCPR	Cold Central Plant Recycling
CTB	Cement Treated Base
DOT	Departments Of Transportation
EPC	Earth Pressure Cell
ESAL	Single Axle Loads
FWD	Falling Weight Deflectometer
HWTT	Hamburg Wheel Tracking Test
LTS	Lime Treated Soil
MDOT	Mississippi Department of Transportation
M-E	Mechanistic-Empirical
MS soil	Mississippi subgrade soil
NCAT	National Center for Asphalt Technology
NDT	Non-Destructive Test
RMSE	Root Mean Square Error
SMA	Stone-Matrix Asphalt
VDOT	Virginia Department of Transportation

CHAPTER ONE

INTRODUCTION

1.1. Background

Road pavements are traditionally classified into two main categories of flexible and rigid. The semi-flexible pavement, also known as stabilized foundation pavement, is another category that represents an intermediate state between flexible and rigid pavements. Historically, stabilized foundation pavements are structurally designed and considered similar to flexible pavements. They are often composed of asphalt wearing courses and composite base/subbase materials treated or stabilized by cement and/or lime *(Pratelli et al., 2018).* The treated layers usually provide a good working platform for subsequent construction layers as well as adequate structural support for the pavement structure *(Ozyildirim et al., 2017).*

Cement stabilization is different from cement treatment. The two techniques are commonly used to increase bearing capacity of soils and granular materials. Cement/lime stabilization is the process by which the measured amounts of cement/lime are added to the natural subgrade soil to improve its engineering behavior. The hydration of the cement/lime increases soil strength by changing the gradation of soil which binds the fine particles together. Cement treatment, on the other hand, consists primarily of base aggregates mixed with specified percentage of cement and field compacted at moisture contents that are slightly greater than the optimum moisture content to form hard and durable paving materials. In this case, the cement has a full binding effect on

mineral aggregates and produces a bonded base layer *(Isola et al., 2013).* This layer is commonly called a Cement Treated Base (CTB).

CTB pavements are constructed to be stiffer than un-stabilized, granular base flexible pavements, while their flexural strength is lower than that of the concrete pavements. Compared to flexible pavements, they distribute loads over a wider area, and thus reduce the vertical stress on top of subgrade. Because of this load carrying capacity, they have effectively been used in areas with soft subgrade support to minimize the rutting and other structural issues.

The scarcity of natural resources, the increase in heavy traffic, the increase in hauling prices, and often encountered challenging soil conditions are among the reasons for many state Departments Of Transportations (DOTs) to use stabilized foundation pavements. In particular, the Mississippi Department of Transportation (MDOT) has used stabilized foundation pavements for many years to combat their challenging subgrade soil conditions and lack of locally available crushed rock for base layer construction.

The stabilized foundation sections often perform poorly due to variety of reasons such as improper mix design, non-stablished construction practices, and poor structural design. Shrinkage cracking is one of the most common distresses in stabilized pavement sections which can be form due to improper mix design. They generally reflect to the surface and form reflective cracking. The other issue with stabilized sections is top-down cracking, which mostly appears in the form of longitudinal cracking. However, these pavements appear to resist permanent deformation by protecting the subgrade due to higher stiffness of the intermediate layers.

In general, proper consideration should be given to mix design, structural design, and construction procedures of these pavements to achieve a long-lasting pavement. Although there has been extensive research on mix-design, material properties, and construction practices of

stabilized foundation pavements, less attention has been paid to the structural evaluation of these pavements. Even most of the available structural studies are limited to non-destructive tests (NDT) which are often conducted only over short periods of the entire pavement life.

The most widely implemented pavement NDT technology is the falling weight deflectometer (FWD) which provides the data necessary for pavement modulus backcalculation based on measured surface deflections generated from an impact load event. The FWD has been used by many agencies to assess in-situ structural characteristics of pavements for many years and has proven to be very effective on conventional flexible pavements. However, its use on more complex structures such as stabilized foundation pavements has been challenging since the shape of the deflection basin of such pavements is different from conventional flexible pavements. This can prevent searching algorithms to converge to a good solution *(Ozyildirim et al., 2017; Xie et al., 2015).*

The lack of reliable backcalculation solution adds even more to the problem of scarcity of structural studies for such pavements. This fact deters researchers from further investigating the structural behavior of stabilized foundation pavements since the major tool for assessing such pavements is questionable itself. Understanding fundamental differences in the structural response of such pavements helps improve design processes and optimize sections that can lead to better pavement performance.

1.2. **Objective**

The objective of this study was to investigate the performance, structural response, and structural characteristics of a stabilized pavement section over time to obtain fundamental knowledge on how these pavements behave.

1.3. **Scope**

The objective was met by monitoring and investigating the structural integrity and overall health of a full-scale stabilized foundation pavement section. The section was built in 2018 at the National Center for Asphalt Technology (NCAT) Test Track. The section, placed on the south tangent of the track was monitored over time with embedded asphalt strain gauges (ASG), earth pressure cells (EPC), and temperature probes.

This stabilized section was constructed for MDOT to investigate the structural behavior of typical Mississippi highways and consisted of cement and lime treated layers below the multi-lift asphalt concrete (AC) layer. For comparison purposes and to obtain more insight regarding the differences and similarities of stabilized pavements with other pavement types, additional sections built at NCAT Test Track were investigated in this study. To facilitate structural analysis, a new computational program (MASTIC) was developed within this research study and used for developing a backcalculation framework to resolve the backcalculation problem for stabilized pavements. A comparison was made between the new developed MASTIC program and an available commercial software package (EVERCALC). The original multilayer elastic program source code is made available for others to use.

The dissertation is organized into nine chapters including the present introductory chapter. Chapter 2 discusses the literature review of the stabilized foundation sections and the need for structural evaluation of these sections. Chapter three starts with a discussion about the NCAT facility and expands into the full-scale pavement sections included in this study. The construction and instrumentation of the stabilized foundation section are fully discussed along with some quality control data during the construction phase. The laboratory characterization of asphalt mixtures and underlying materials are discussed in chapter 4. Chapter 5 starts with the surface

performance measures of the pavement sections and moves into the structural responses under dynamic load events obtained from the embedded pavement sensors. Chapter 6 provides a mathematical background for the development of MASTIC, a new computer program developed for pavement analysis and backcalculation. The chapter ends by providing the comparison between MASTIC and other commercial programs. Chapter 7 discusses the simulation of the pavement sections using MASTIC and explains the reason for the observed differences in pavement responses of the stabilized foundation section. This chapter introduces a new cracking mechanism and explains how the stabilized foundation sections are prone to middle-up cracking and bottom-up fatigue is less likely to happen. Chapter 8 includes falling weight deflectometer (FWD) test results for all pavement sections and introduce a new methodology for backcalculation of stiff pavement sections. This document ends with chapter 9 in which the summary and conclusions are provided.

CHAPTER 2

LITERATURE REVIEW

2.1. Stabilized Foundation Pavements

Cement treated base layers have been widely used as a base course for flexible and rigid pavements. Since CTB provides a stiffer base than unbound aggregate base, it reduces deflections due to traffic loads, resulting in lower horizontal strains at bottom of asphalt surface and lower vertical stress at top of subgrade. This may delay the onset of surface distress, such as bottom-up fatigue cracking and structural rutting, and extends pavement life *(Halsted et al., 2006)*. Some state DOTs use CTB as a base course to (1) protect the poor subgrade; (2) enhance the pavement structure; (3) use as drainage layer; (4) and to lower overall price *(Ozyildirim et al., 2017)*. Figure 2.1 shows typical sections for stabilized foundation pavements as well as conventional flexible and rigid pavements. Stabilized foundation pavements may include more than one treated layer which may or may not be treated with the same materials.

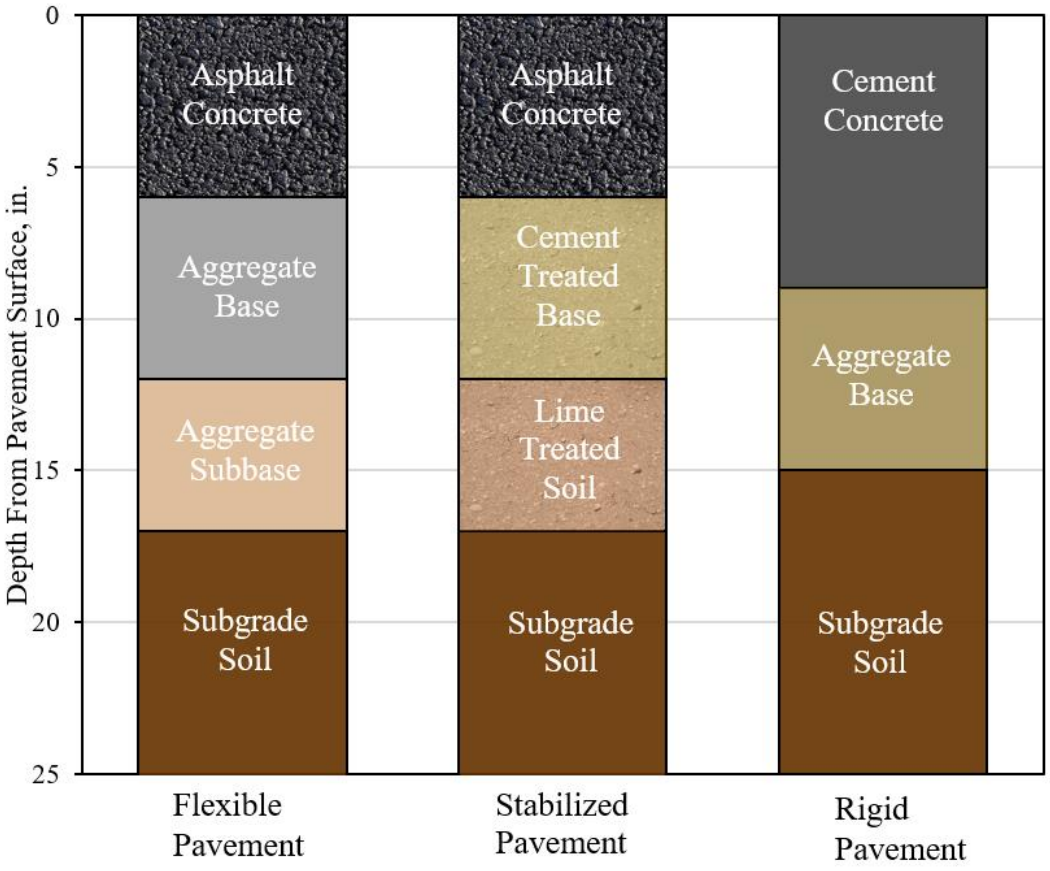

Figure 2.1 Typical Cross Section for Flexible, Rigid, and Stabilized Pavements.

The field performance of stabilized pavements is variable, and poor performance often occurs which can be associated to (a) mix-design related factors such as fine aggregate content, aggregate mineralogy, cement content, and chemical deterioration of the cement matrix, (b) construction related factors, and (c) structural design factors. Thus, in order to achieve high quality pavement, three factors should come together, good mix design, good structural design, and good construction practice. This is particularly important for stabilized pavements and especially for the CTB layer. The mix design for CTB determines the proper proportion of cement and water in the mixture to ensure that the mixture will have the required strength for both load carrying capacity and durability *(George, 1990)*. Additionally, the designed strength should not exceed a certain threshold to minimize the shrinkage cracks that can reflect through the wearing course. The

strength of the CTB layer is sometimes controlled by limiting the cement content. With increased cement contents, cracking became so prevalent that several state DOTs have banned the use of cement stabilization in their roadways *(Guthrie et al., 2002).*

In addition, CTB layers are prone to shrinkage due to moisture loss, cement hydration, and other environmental factors which results in transverse cracking of the treated base, that could then form reflective cracks *(Sebesta, 2005).* CTB shrinkage can be divided into two main categories: (a) autogenous shrinkage that is a shrinkage resulting from the hydration of the cement and (b) drying shrinkage. It is believed that drying shrinkage causes most of the shrinkage problems. There are also other factors that can contribute to shrinkage cracking in CTB pavements. Tensile strength of the base, restraint provided by friction between the base and subgrade, creep characteristics of the base, thermal shrinkage, the content and type of clay in the treated material are all considered as contributors to shrinkage cracking phenomenon *(Sebesta, 2005)*. Figure 2.2 shows a cement treated pavement section with severe shrinkage cracking in Sebesta's study *(Sebesta, 2005).* This test section with drying shrinkage cracks had 4% cement content. Shrinkage cracks can not only adversely affect the performance of the CTB section itself, but also reflect through the asphalt concrete layer and form reflective cracking. Transverse cracking in the surface layer as a result of shrinkage in stabilized base layer has been reported in previous studies *(Wen et al., 2014; Sebesta, 2005).*

Figure 2.2 Cement Treated Pavement Section with Shrinkage Cracks (*Sebesta, 2005).*

According to NCHRP 04-36, block cracking caused by shrinkage of the underlying stabilized base often occurs when the asphalt concrete (AC) layer is thin *(Wen et al., 2014).* Pavements that use stiff bases and thin AC layers also have encountered this *(Wen et al., 2014)*. The shrinkage typically initiates shortly after construction and continues thereafter. This may prohibit the use of thin AC layers on top of stabilized foundation pavements.

Another major issue that has been reported for stabilized pavement sections is the longitudinal cracking along the wheel path. Pavements with high-stiffness base are prone to top down cracking which mostly appears in the form of longitudinal cracking in stabilized pavements *(Wen et al,. 2014).* Figure 2.3 shows the top-down cracking on a stabilized pavement section.

Figure 2.3 A Top-Down Crack on a Stabilized Foundation Pavement *(Wen et al., 2014).*

The Portland Cement Association recommends seven-day unconfined compressive strengths in the range of 300–400 psi to minimize the shrinkage cracks. During construction, it recommends compaction at or slightly lower moisture content *(Adaska and Luhr, 2004)*. The NCHRP project 04-36 study recommends the 28-day compressive strengths to be 392 psi at minimum and 1,296 psi at maximum with typical value of 763 psi to be used in M-E design *(Wen et al., 2014).* In contrast, typical strength for a 28-day cured concrete ranges from 3000 psi to 6000 psi.

The plasticity index is also recommended to be less than six for materials used in CTB. Many state DOTs limit the percent passing the No. 200 sieve *(Ozyildirim, et al., 2017)*. Table 2.1 shows a summary of state agencies specification and common practices for CTB pavements. As shown in the table, most agencies require 7-day unconfined strength as high as 750 psi for CTB layer while some also require an upper limit for strength. The criteria on material properties ensure

durable CTB layer, whereas the criteria on strength ensure sufficient support for subgrade layer while avoid shrinkage cracking.

Table 2.1 Summary of State DOT Specifications and Practices *(Ozyildirim et al., 2017)*.

Agency/DOT	Design 7-Day Compressive Strength, psi		Aggregate Properties			Comments
	Minimum	Maximum	LL	PI	%Passing No. 200 Sieve	
California DOT	750	NA	NA	NA	NA	-
Colorado (City of Thornton)	650	1000	<30	NA	3-15%	Cement > 5%
Federal Aviation Administration	400	NA	<25	<6	NA	28-day strength < 1,000 psi; minimum 98% compaction; sliding pay scale with 98% to 95% compaction; freeze-thaw and wet-dry durability < 14% mass loss as an option
Georgia DOT	300	450	NA	NA	NA	-
Kansas DOT	650	1600	NA	NA	NA	Pay based on percent within limit; reference SD: 260 psi
Maryland DOT	750	NA	NA	<6	0-8%	Cement: 3.25-4.75%
Michigan DOT	750	NA	NA	>6	NA	0-25% passing No. 80 sieve; sliding pay scale with 98% to 95% compaction; freeze-thaw and wet-dry durability < 14% mass loss
Montana DOT	500	1500	<30	<7	4-12%	Minimum 95% compaction; sliding pay scale with 400- 2,000 psi compressive strength
Oklahoma DOT	600	1200	NA	NA	1-15%	Target strength: 800-1,000 psi Cement: 3-5%
South Carolina DOT	600	NA	NA	NA	0-20%	Cement: 2.5-5%
Tennessee DOT	500	NA	NA	NA	NA	-

Since shrinkage cracking is predominant in CTB layers, many state DOTs take precautionary actions to control or mitigate the severity of this distress. Controlling the mix-design factors is not the only technique to prevent shrinkage cracks, another technique includes using a crack relief layer between CTB layer and the surface course. This layer dampens the stress induced by the underlying shrinkage cracks and delays the occurrence of reflective cracks. Another effective method first introduced by the Austria Highway Agency is to create microcracks on the

CTB layer using a vibratory roller on top of the CTB layer after initial curing, usually one or two days after compaction *(Litzka and Haslehner, 1995)*. Sebsta *(2005)* used an FWD to backcalculate the modulus of pavement layer with and without microcracks. Figure 2.4 illustrates the pattern of changes in base modulus with the microcracking procedure *(Sebesta, 2005)*. The modulus increased from day 0 to day 1 as curing proceeded. Then, after two roller passes, the modulus decreased 25% and with one additional pass, the base modulus dropped drastically. The base modulus then recovered in the following days since microcracking took place early in the curing stage of the material. Their study showed microcracking had not resulted in reduced layer moduli compared with the control non-cracked section. Also, the higher cement content in general did not significantly increase in-service modulus.

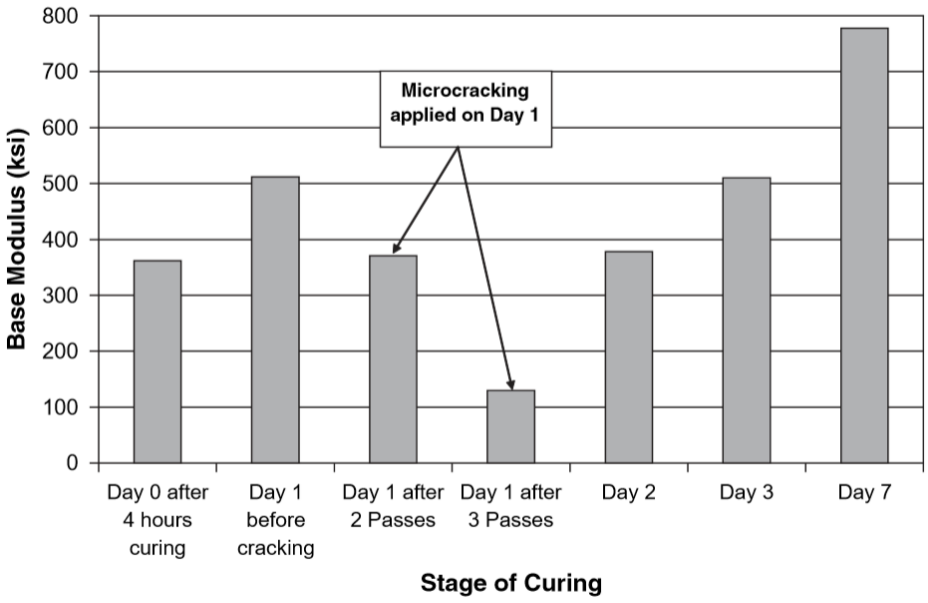

Figure 2.4 Pattern of Base Modulus Changes with Microcracking *(Sebesta, 2005)*.

This portion of the literature review showed studies that investigated the shrinkage cracking in stabilized foundation pavements considered CTB material properties to be the main

reason for having reflective cracking on stabilized foundation pavements, and thus focused on two main objectives, (1) reduction of the stiffness of CTB layer in the mix design such that shrinkage cracks does not occur, or (2) delaying or preventing shrinkage cracks from appearing to the surface using specific methods and techniques such as building crack relief layer on top or introducing micro-cracks. While these methods are demonstrated to prolong the life of stabilized foundation pavements, the source of reflective cracks on stabilized pavements may not necessarily be limited to material properties.

2.2. Backcalculation Methods

While using an FWD is a common tool for evaluating stabilized foundation pavements, presence of a stiff layer at the middle of the pavement section can cause some problems in the backcalculation algorithm. Ozyildirim et al. *(2017)* suggested to use no more than three or four layers with unknown moduli in the backcalculation process of stabilized pavements. In general, to obtain good matches between the calculated and measured deflection basins, root mean square error (RMSE) of 3% or less is considered. However, Ozyildirim et al. *(2017)* suggested that even higher convergence errors do not necessarily reflect high deviation in the backcalculated layer moduli for stabilized pavements.

Lim and Zollinger *(2003)* conducted an experimental study on the strength and the modulus of elasticity of CTB materials. Unconfined uniaxial compression tests and elastic modulus tests were conducted on 189 samples for 16 CTB mixtures at different ages. Test results indicated that there exists a correlation between compressive strength and elastic modulus of CTB material. The relationship could be expressed in a single equation regardless of aggregate type and mixture proportions. Figure 2.5 displays this correlation for different aggregate types (different series

markers). The dotted line is the ACI equation proposed for the estimation of elastic modulus of normal concrete *(Lim and Zollinger, 2003).*

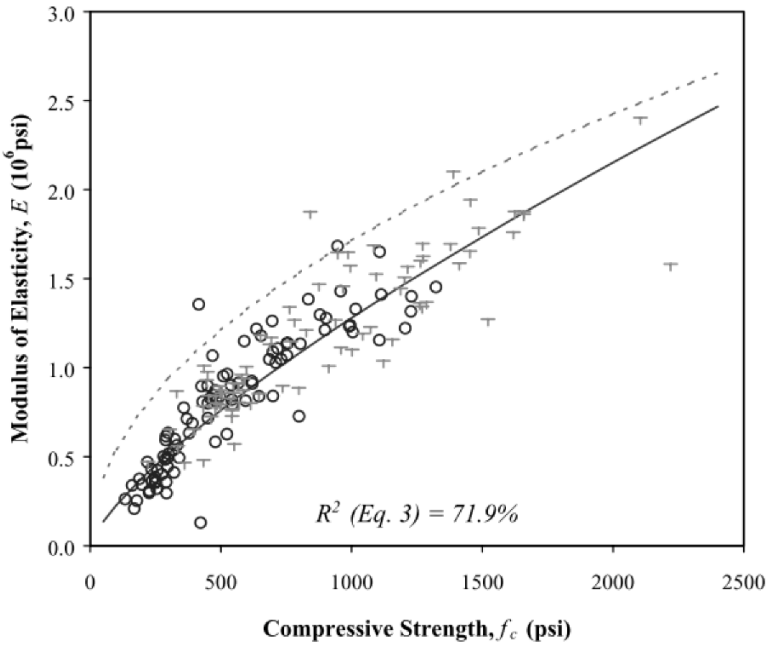

Figure 2.5 The Correlation Between Elastic Modulus and Compressive Strength *(Lim and Zollinger 2003).*

Figure 2.5 reveals the importance of determining the modulus of semi-rigid pavements because modulus is the fundamental properties for stabilized pavements which indeed correlate well to the compressive strength on which the mix design is based.

In another study, to implement Mechanistic-Empirical (M-E) pavement design, the Virginia Department of Transportation (VDOT) had done extensive research on both material and structural properties of CTB layers. The M-E design process presents a major change in pavement design from the 1993 AASHTO Design Guide. It calculates pavement responses through mechanistic analysis and based on inputs such as traffic, climate, and materials properties. It uses the calculated responses to predict the pavement damage for both flexible and rigid pavements. The purpose of the VDOT study was to evaluate the mechanical properties of CTB and recommend

values for use in the AASHTOWare Pavement M-E Design software. Evaluation of in-place CTB was carried out by FWD tests. EVERCALC (developed by the Washington State DOT) was used to analyze the FWD data to estimate the elastic modulus of CTB at three sites. Multiple cores at the FWD location were also taken to measure compressive strength and modulus of elasticity in accordance with ASTM D1633 and ASTM C469, respectively. Information about the layer thickness was obtained from core thickness measurements. Based on laboratory and FWD results, considering the high variability for both coring and FWD testing, they suggested a modulus of elasticity of 1.5 million psi for CTB. However, the lack of reliable FWD results decreased the reliability of their test results *(Ozyildirim et al., 2017)*. In the VDOT study, the average CTB modulus 3 months after the construction was 325,000 psi with coefficient of variation (COV) of 68%. However, backcalculation results after 20 months showed the average CTB moduli increased to 1,520,000 psi with a COV of 42%. This indicates that the CTB layer moduli can increase significantly over longer period of service life. Table 2.2 contains the summary statistics of VDOT project where coefficient of variation was as high as 68%.

Table 2.2 Summary Statistics for CTB backcalculation (*Ozyildirim et al., 2017)*.

Site (year Built)	Pavement structure	Age Tested	Data points	Backcalculated Modulus of elasticity * 10^6 psi				COV, %
				Average	Standard Deviation	Minimum	Maximum	
Middle Ground Boulevard (2013)	10 in. AC 6 in. CTB	3 Months	22	0.326	0.223	0.127	1.075	68
		20 Months	24	1.522	0.640	0.195	2.000	42

Xie et al. *(2015)* used the FWD to evaluate a stabilized pavement structure through the deflection basin and the backcalculated modulus. The FWD test was performed on asphalt pavements with or without cracks. The results indicated that the existence of cracks and having cement-treated base in the asphalt pavement may result in an abnormal deflection basin and make

the backcalculated modulus incorrect. They suggested to prune unusual deflection basins or to decrease the number of structural layers to reduce the unreasonable backcalculation modulus *(Xie et al. 2015)*. They also observed that cracking in the asphalt pavement may result in a significant "bump" in FWD deflection basin and make the shape of deflection basin unusual leading to incorrect moduli. In this condition, the deflection close to cracks increases abruptly making the overall shape unusual and inconsistent compared to non-cracked sections *(Xin et al., 2013)*. Figure 2.6 shows a deflection basin with significant bump based on finite element simulation. In this figure, the legend indicates the location of the crack with respect to the center of the FWD loading plate. For example, RC750 shows a crack that exists 750 mm away from the center of load plate. This indicates that there exists a bump at the location of cracks which can affect the backcalculation process.

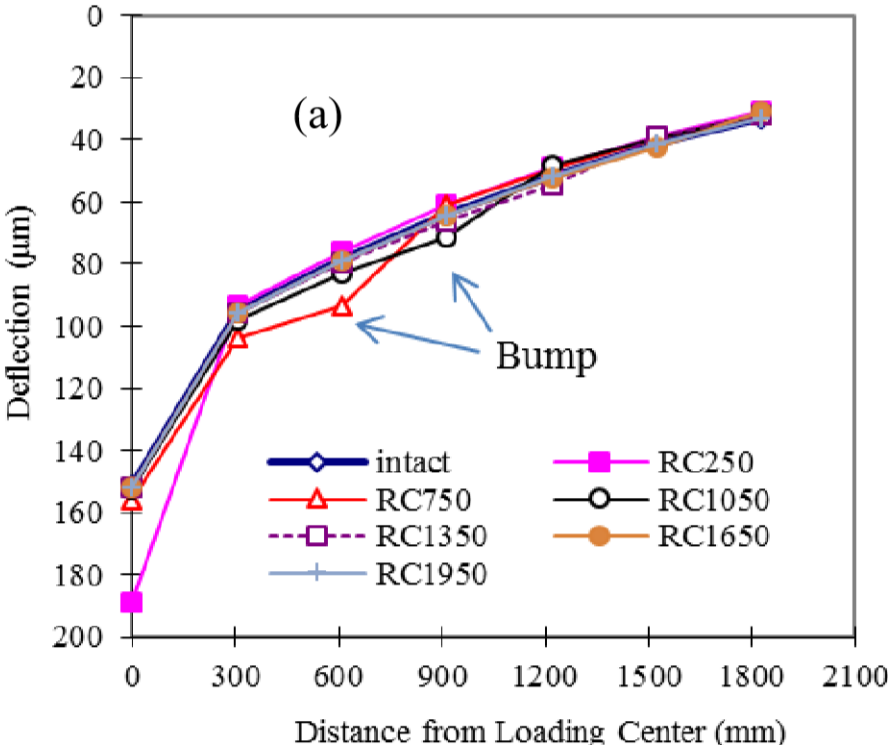

Figure 2.6 Deflection Basin with Significant Bump *(Xin et al., 2013)*.

The literature review reveals the need for more structural evaluation of CTB layers. Most structural evaluation studies are limited to FWD measurements, which indeed have high convergence error for CTB layers, or they lead to unjustified results. The concern about high convergence error has been reported by many studies *(Xie et al., 2015; Ozyildirim et al., 2017)* which can question the accuracy of structural evaluation for stabilized pavements.

Most of the studies used Gauss-Newton or other traditional optimization techniques to obtain the elastic modulus for each layer. While these traditional methods work well with conventional flexible pavements, they cannot necessarily converge well for all optimization problems. Fortunately, with the advance of Artificial Intelligence (AI) and Machine Learning methods, one can optimize a problem numerically with astonishing accuracy. Pavement engineering has not been an exception to use AI to address its challenging issues. AI methods have been used extensively to address complicated problems in the field of pavement engineering *(Leiva et al., 2017).* Feed-forward neural network (FNN) is the most common AI technique used in pavement engineering that belongs to the family of Artificial Neural Networks (ANN). ANN systems are computing systems vaguely inspired by the biological neural networks that constitute brains. Such systems "learn" to perform specific tasks by considering examples, generally without being programmed with task-specific rules. Figure 2.7 illustrates a simple FNN architecture for regression task with four distinct outputs.

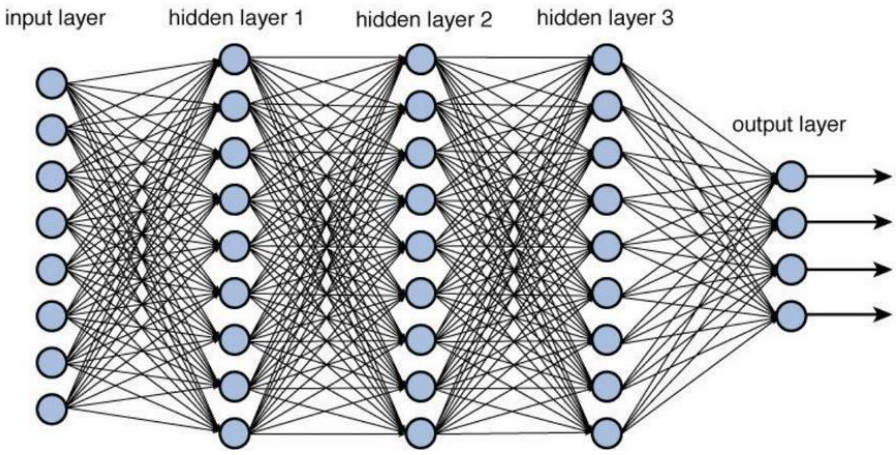

Figure 2.7 Feed-Forward Neural Network Architecture (https://medium.com).

Leiva et al. (2017) developed an FNN model to predict pavement layer moduli for full bond and full slip layer interface conditions. The FNN model was used to estimate the moduli of several NCAT Test Track structural sections. The results indicated that warm mix asphalt sections had lower moduli compared to the control section. Also, sections containing reclaimed asphalt pavement (RAP) had relatively higher moduli. They showed that in general the backcalculated layer moduli using the conventional optimization method had higher error compared to FNN models *(Leiva et al., 2017)*. Figure 2.8 demonstrates the correlation between asphalt concrete (AC) modulus backcalculated using feed-forward neural network and the backcalculated values obtained from EVERCALC. The R-squared is close to 1.0 suggesting the strong correlation between the two methods.

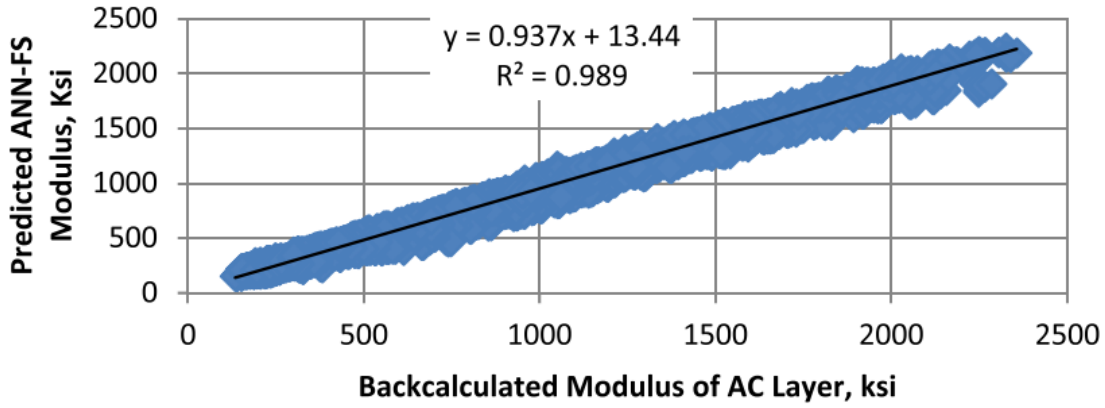

Figure 2.8 The Correlation Between Backcalculated VS FNN Predicted Moduli *(Leiva et al., 2017)*.

This study clearly showed the power of neural network models to estimate the pavement moduli. In another study, Sharma and Das investigated the moduli of 3-layer flexible pavement using artificial neural network. A dataset with 6000 deflection basins was generated using multi-layer elastic program. They concluded that having one hidden layer with 10 neurons would suffice to get acceptable results *(Sharma & Das, 2008).*

Since backcalculation of pavement layer moduli is an ill-posed inverse problem which involves searching for the optimal combination of pavement layer modulus solutions in a multimodal, complex search space, some researchers have gone one step further and used more advanced techniques and algorithms. Gopalakrishnan *(2010)* implemented a hybrid neural network for obtaining more robust pavement moduli. In Gopalakrishnan's study, Particle Swarm Optimization which is a population-based stochastic optimization technique inspired by social behavior of bird flocking or fish schooling was coupled with neural network which was proven to be effective and efficient approach to reach the global optimum *(Gopalakrishnan, 2010)*. Although these methods could be used as another tool for backcalculation of pavement modulus, they did

not necessarily provide a superior performance over traditional methods. This could be the reason for popularity of tradition methods in routine projects.

2.3. Summary

The literature review on stabilized foundation pavements reveals that most studies on these pavements were performed with the focus on material characterization, and less attention has been paid to structural investigation of these pavements.

To fill this gap, NCAT started a structural study on a stabilized pavement section (section S12) which was instrumented with pressure and strain sensors to characterize its behavior over time. The stabilized section was compared and contrasted with a similar pavement section but, with an aggregate base course (section N4). The study showed that section S12 had exhibited excellent performance over the research cycle period. Also, the analysis of in-place pavement sensors revealed that section S12 could be considered a perpetual pavement section since its strain distribution was less than the control distribution. However, section N4 exceeded the control strain distribution and was not considered as perpetual according to the conventional criteria *(West et al., 2019).*

In addition to scarcity of structural studies on stabilized pavements, the majority of such studies used FWD as the primary tool for their investigation which is itself prone to error for stiff pavements, as explained in the previous section. The main goal of this study is to provide a fundamental investigation of the structural behavior of stabilized pavement sections through embedded instrumentation, modeling, and FWD testing followed by backcalculation.

CHAPTER 3

TEST FACILITY AND TEST SECTIONS

3.1. Test Facility

The NCAT Test Track is a full-scale, accelerated closed-loop pavement testing facility in Opelika, Alabama. It consists of 1.7-mile oval track which is divided into 46 sections test sections, each two hundred feet long, that are designed to address the research needs of the section's sponsors. Established in 2000, numerous flexible pavements have been studied for construction factors, mix design, structural responses, and surface characteristics. The test sections are generally categorized as either structural or non-structural. The non-structural sections are used for surface mixture evaluation and pavement perseveration, while the structural sections are instrumented with asphalt strain gauges, earth pressure cells and temperature sensors for collecting structural pavement behavior over time. Figure 3.1 shows the Test Track facility.

A research cycle at the Test Track includes a year of forensic investigations of the previous research cycle and construction of new sections for the next cycle, followed by two years of trafficking and performance monitoring. Truck traffic is applied to the pavement sections 5 days a week, resulting in approximately10 million equivalent single axle loads (ESALs) being applied over the two-year trafficking portion of the research cycle (*Timm & Tutu, 2017*).

Figure 3.1 NCAT Pavement Test Track.

3.2. Pavement sections

As stated in chapters one and two, the primary purpose of this study was to evaluate fundamental behavior of stabilized pavements through studying the structural behavior of the stabilized foundation section (S2) at the Test Track. The stabilized foundation section (S2) was constructed in 2018 for MDOT to investigate the performance, structural response, and overall quality of this pavement under accelerated truck loads. To obtain enough knowledge about the differences and similarities of stabilized pavements with other pavement types, three additional full-scale sections including the Cold Central Plant Recycling (CCPR) section (N4), the CCPR with stabilized foundation (S12), and the thick-lift section (S9) were also examined, and their results were compared and contrasted. However, since the focus of this study is on the stabilized foundation section (S2), more details on construction and instrumentation of this section are provided here while other sections are briefly introduced. The details on the CCPR (N4), and the CCPR with stabilized foundation (S12) sections are documented by Diaz *(2019)* while further details of the thick-lift section (S9) are provided by McCarty *(2020)*.

While the stabilized foundation section (S2) and the thick-lift section (S9) were constructed in 2018 for the 2018 Test Track cycle, the CCPR (N4) and the CCPR with stabilized foundation (S12) sections were part of 2012 and 2015 experiments that have continued into the 2018 research cycle and were subjected to over 20 million ESALs through those experiments. Thus, in total considering the 2018 research cycle, the CCPR (N4) and the CCPR with stabilized foundation (S12) sections have experienced almost 30 million ESALs while the thick-lift section (S9) and the stabilized foundation section (S2) have experienced about 10 million ESALs with the completion of traffic in February 2021.

3.3. Cross sections

The stabilized foundation section (S2) consists of cement and lime treated layers underneath a multi-lift asphalt concrete (AC) layer. A key feature of the MDOT section was a soil imported from Mississippi to replicate often-encountered challenging soil conditions. To monitor and investigate the structural integrity and overall health of the pavement section over time, and to measure the horizontal bending strain under traffic, twelve asphalt strain gauges (ASGs) were placed at the AC/base course interface. Also, three earth pressure cells (EPCs) were installed on top of the CTB, LTS, and MS soil, respectively, to measure vertical compressive stresses transferred through the layers. Temperature probes were installed outside the edge stripe at the top, middle and bottom of the asphalt concrete and three inches into the CTB layer. This depth combination was selected to capture the thermal gradient through the depth of the AC and provide one temperature reading from the underlying layer. For the thick-lift section (S9), in addition to temperature probes and twelve strain gauges that were placed underneath the AC, two EPCs were

placed on the granular base layer to measure vertical compressive stresses transferred through the AC thick lift.

Figure 3.2 shows the as-built cross sections of the stabilized foundation section (S2) and the thick-lift section (S9) with depths and types of embedded instrumentation. Section S2 has 4 asphalt concrete lifts, a cement treated layer, a lime treated soil layer, and Mississippi subgrade that was placed on the top of native Test Track soil (not shown in Figure 3.2). In contrast, the thick-lift section (S9) had a single thick layer of AC on the top of granular base (GB) over the subgrade. The subgrade soil for the thick-lift section (S9) was native to the Test Track. Both sections used dense graded Superpave AC mixtures with unmodified binders. The key feature for the thick-lift section (S9) was the thick layer of AC that was placed and compacted in one lift (no multilayer application). One lift application removes the need for tack coat applications and can expedite the pavement construction for heavy traffic roads *(McCarty, 2020)*.

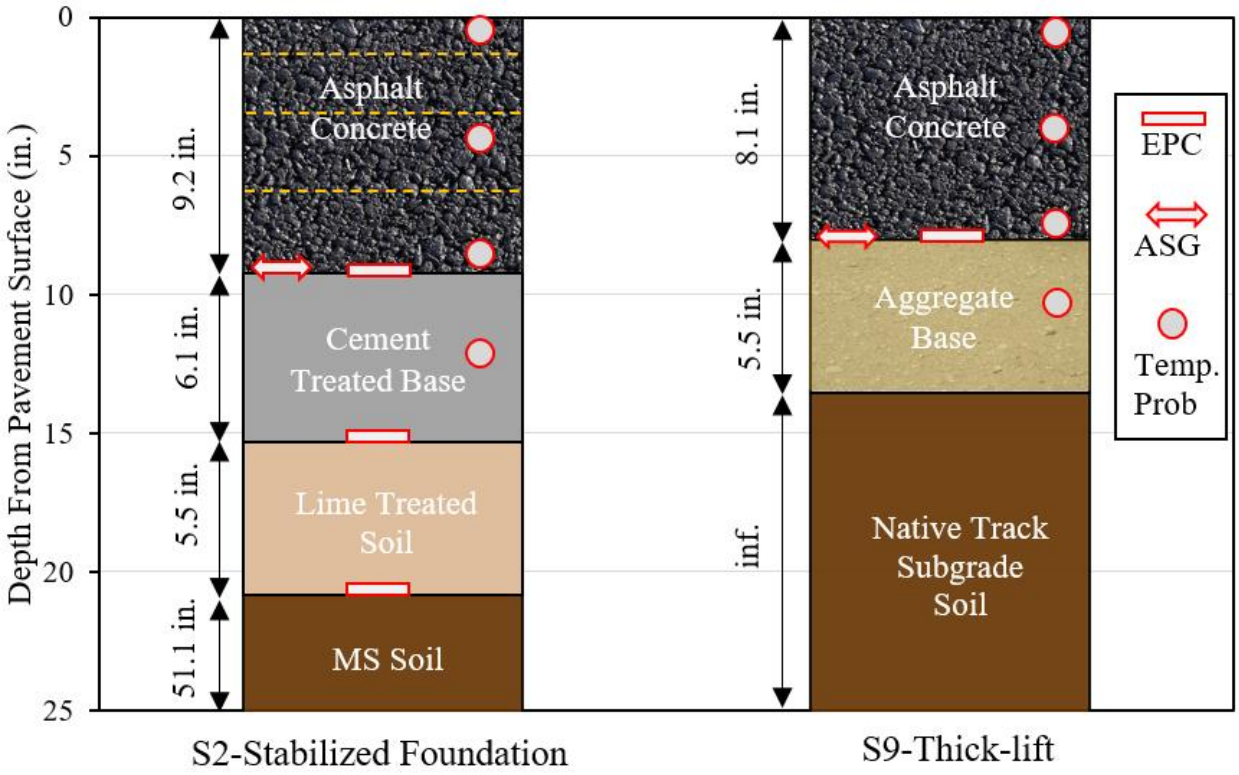

Figure 3.2 Sections S2 and S9 As-Built Thicknesses and Depth of Instrumentation.

Figure 3.3 shows the cross sections for the CCPR section (N4) and the CCPR with stabilized foundation section (S12). The two sections consisted of two asphalt concrete layers placed on similar CCPR material, with the exception that the CCPR with stabilized foundation section (S12) contained a cement treated base as a base layer. Both sections featured Stone-Matrix Asphalt (SMA) surface and Superpave dense-graded AC layers above the CCPR layer. While the CCPR section (N4) was constructed on top of a crushed granite aggregate base layer, the CCPR with stabilized foundation section (S12) was constructed on a CTB layer similar to the stabilized foundation section (S2).

The stabilization of the CTB was done in-place with a reclaimer in section S12 where approximately 6 inches of crushed granite aggregate base and 2 inches of the subgrade were treated in place with 4% Type II cement. The CCPR section (N4) and the CCPR with stabilized foundation

section (S12) were sponsored by Virginia Department of Transportation (VDOT) and were designed to determine the difference between aggregate base with 6 inches thickness and the CTB layers with 8 in. thickness.

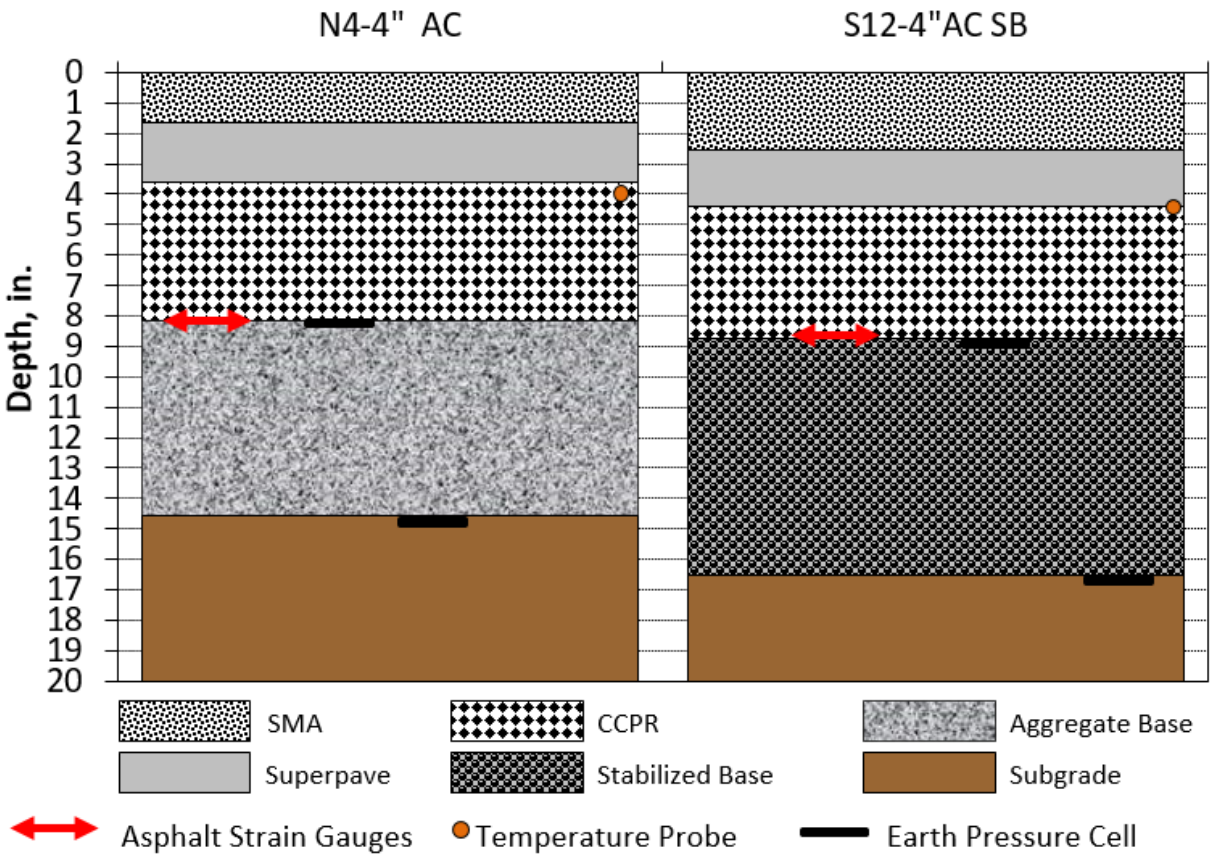

Figure 3.3 VDOT Experiment Average As-Built Thicknesses and Depth of Instrumentation *(Diaz, 2019).*

Six horizontal asphalt strain gauges oriented in the longitudinal direction (parallel to traffic) were placed at the bottom of the CCPR layer to capture bending of the asphalt-bound layers. Six vertical strain gauges were installed to capture vertical deflection of the asphalt bound layers. However, the vertical strain gauges were only functional for a short period of time (i.e., a few weeks), preventing the development of meaningful vertical strain data over time. Earth pressure cells were placed at the top of the base and subgrade layers to capture vertical pressures

transmitted through the sections. Temperature probes were installed after paving at the middle of the composite AC/CCPR to measure mid-depth temperature during testing. More information on VDOT sections is provided in *(Diaz, 2019)*. The following sections further discuss the construction details of the stabilized foundation section (S2), including instrumentation and construction practices.

3.4. **Pavement Instrumentation**

As shown earlier in Figure 3.2, the stabilized foundation section (S2) was equipped with response instrumentation to study its structural behavior over time. The instrumentation system developed in previous Test Track cycles had proven itself to be robust and effective *(Willis et al., 2009)*. Therefore, a similar instrumentation scheme was used for the stabilized foundation section (S2) with a few adjustments. This approach also helped to maintain the continuity of the current research study with section the CCPR with stabilized foundation section (S12) featuring cement treated base for possible cross comparisons. Detailed descriptions of earlier instrumentation efforts have been previously documented in *(Willis et al., 2009)*. The instrumentation modifications for the 2018 Test Track research cycle included adding local calibration for the asphalt strain gauges and modifying the arrangement of the gauges, which will be further discussed in this section.

Figure 3.4 illustrates the plan view arrangement where 12 asphalt strain gauges and one pressure plate were placed on top of the CTB at the bottom of the asphalt concrete. The two other pressure plates were installed on top of lime treated soil and the Mississippi subgrade soil (MS soil). In total, 15 dynamic response gauges were embedded into the section. The strain gauges were Geocomp's 4" x 6" 2013 model having a modulus of less than asphalt concrete to prevent locally reinforcing the pavement layer. The earth pressure plates were Geokon's model 3500-2-

250KPA sensor. As shown in Figure 3.4, the strain gauges are labeled 1 through 12 while pressure plates are identified as 13 through 15, which were placed on top of the CTB, LTS, and MS soil, respectively. The installed temperature probes were Campbell-Scientific's 108-U-L30-PT model with type J thermocouples. Figure 3.5 shows a picture of each instrumentation used in this study.

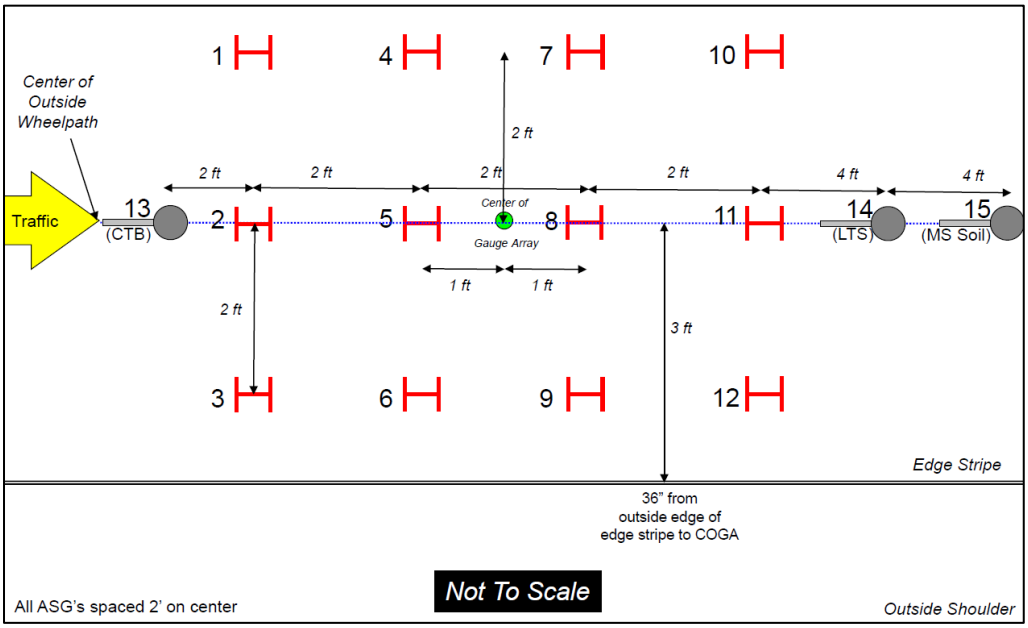

Figure 3.4 The Stabilized Foundation Section (S2) Gauge Arrangement.

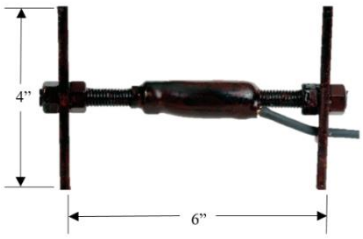

a) Geocomp ASG

c) Geokon EPC

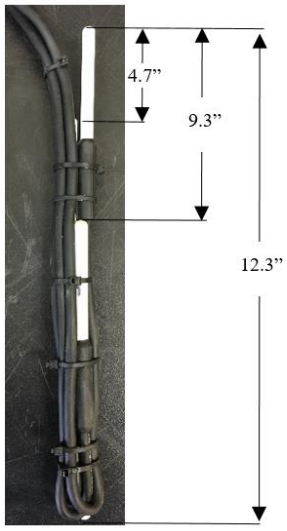

b) Temperature Probes

Figure 3.5 The (a)ASG, (b)EPC, and (c)Temperature Probes Used in this Research.

3.4.1. Calibration Procedure

3.4.1.1. Asphalt Strain Gauges

The asphalt strain gauge local calibration procedure was newly added to Test Track instrumentation preparation protocols to ensure the quality and functionality of strain gauges while providing local calibration factors for each gauge. The procedure started with a series of checks, followed by applying known strains and measuring the change in voltage to determine gauge-specific calibration factors. Each step of the process is detailed below.

Initially, the resistance of each strain gauge was checked against the standard value of 350 Ω to ensure the functionality of the strain gauges before any further evaluation. The strain gauges were then connected to the data acquisition system (DATAQ) to record their baseline voltages in an unloaded state. Some of the strain gauges showed an initial baseline drift once they were wired into the DATAQ. However, after 30 seconds to 1 minute warm-up period, the baseline values became stable. Each strain gauge was given enough warm-up period to ensure the stability of the baseline before proceeding to next calibration step. Then, as an additional initial check, the gauges were pulled and pushed by hand to ensure the gauges responded properly to tension and compression, respectively. Two of the gauges subjected to these tests did not pass and were replaced by the manufacturer.

Once basic functionality was established, each strain gauge was mounted into a calibration jig as shown in Figure 3.6. A mounted gauge was subjected to a small pre-tensile strain to remove any possible slack between the mounting brackets and the strain gauge. Then, the inside-to-inside length of both sides of the strain gauges were determined by a digital caliper. Since the baseline had been changed due to the pre-strain, a potentiometer was attached and used to adjust the baseline of the strain gauges back to the original baseline recorded under the unloaded state. The

strain gauge was then pulled into tension by approximately 0.02 mm increments using the hand crank on the calibration jig until the DATAQ read approximately a maximum excitation of +5V. The ASG was then relieved from tension by increments of 0.02 mm until the displacement decreased to 0 mm. The process of loading and unloading was repeated as a precision check. Also, any possible drift in the baseline as a result of strain loadings and unloading were monitored.

Finally, the measured voltage was plotted against the calculated microstrain (applied displacement divided by the average initial length of the gauge) and a linear trend line was fitted to determine the calibration factor. Figure 3.7 shows an example of calibration graph for the stabilized foundation section (S2) where the resulting gauge factor is 394.43 με/V. All calibration factors are tabulated in Table 3.1.

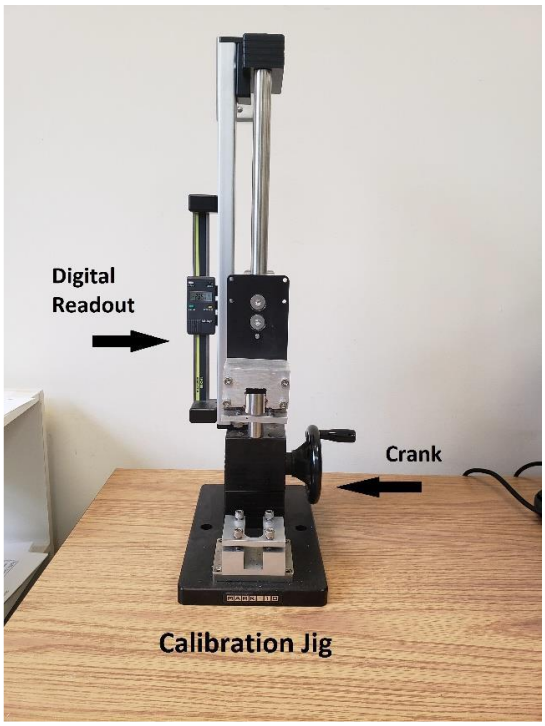

a) ASG Calibration Jig

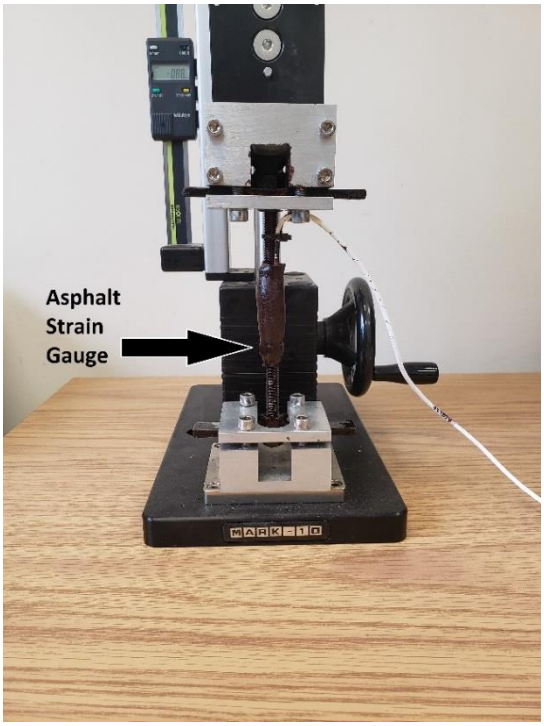

b) Calibration Jig with Strain Gauge

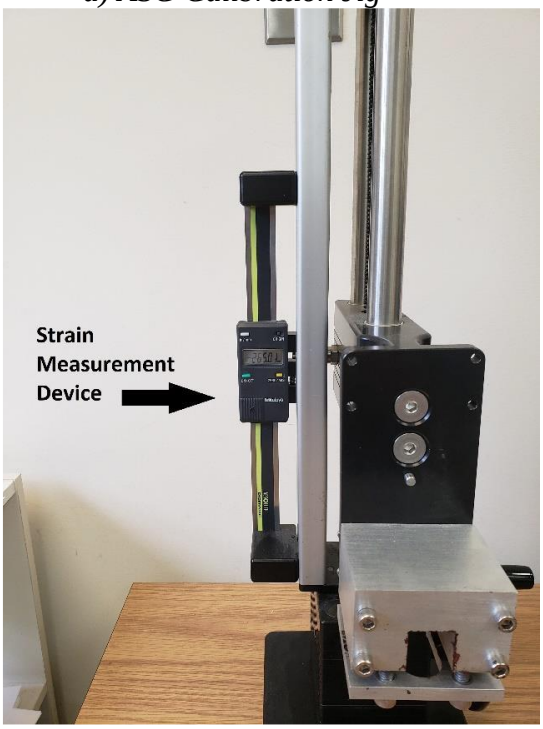

c) Strain Measurement Device

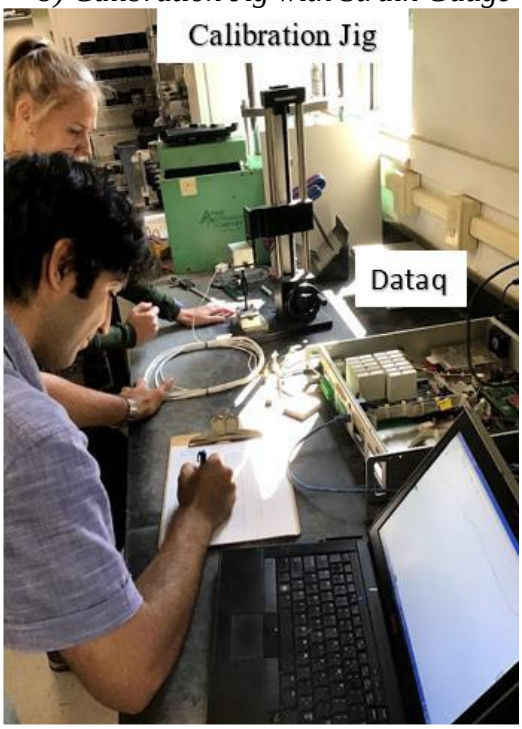

e) ASG Calibration Set-Up

Figure 3.6 ASG Calibration Jig.

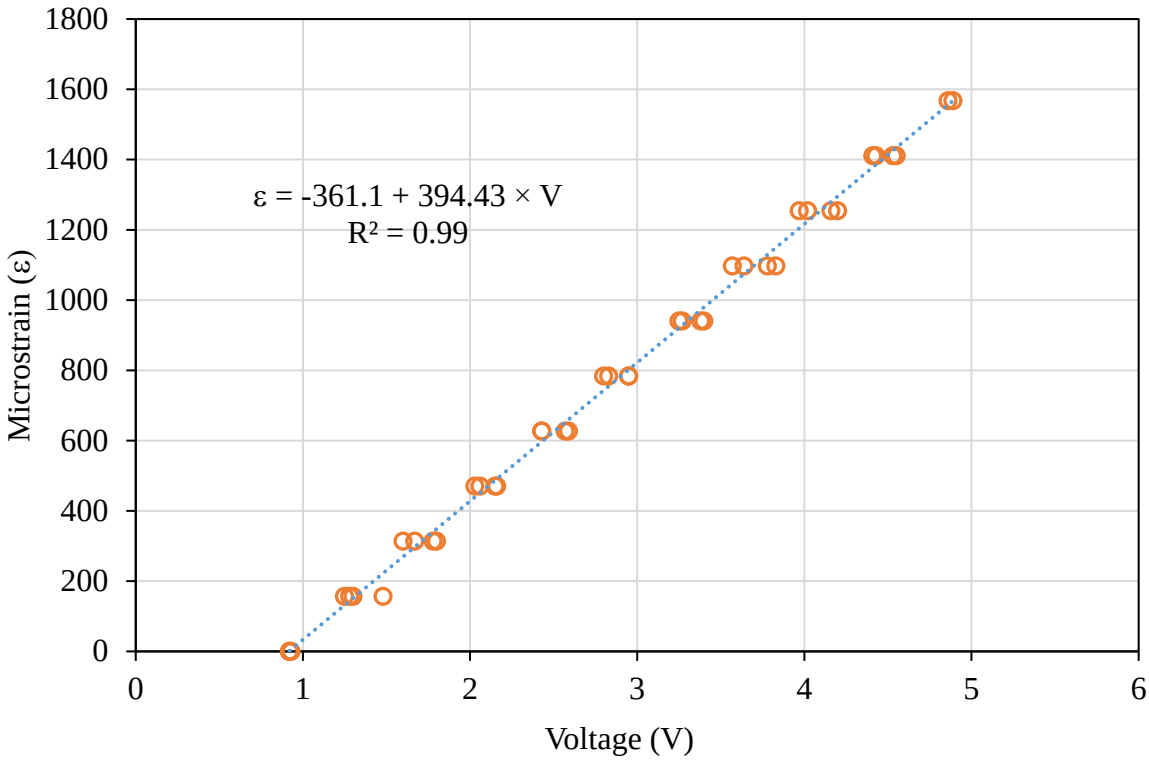

Figure 3.7 ASG Calibration Graph (GeoComp ID: 1).

Table 3.1 The Stabilized Foundation Section (S2) Gauge Factors

Channel	GeoComp ID	Baseline Voltage	Label	Gauge Factor (microstrain/Volt)
1	18	-2.14	S2-1	447.89
2	17	1.55	S2-2	411.64
3	34	-1.83	S2-3	425.64
4	22	1.46	S2-4	477.47
5	5	-1.11	S2-5	391.89
6	15	1.11	S2-6	413.39
7	38	0.07	S2-7	408.51
8	11	0.89	S2-8	415.05
9	37	0.11	S2-9	399.13
10	1	0.76	S2-10	394.43
11	4	0.33	S2-11	410.99
12	19	0.34	S2-12	425.48

3.4.1.2. Earth Pressure Cell:

The earth pressure cells used in this study were similar to the ones used in previous Test Track research cycles (*Timm, 2009; Timm et al., 2004*). Hence, the same calibration procedure was used to check the functionality and accuracy of pressure plates. A custom-built chamber capable of accommodating six pressure plates was used for calibration of pressure plates (*Timm, 2009*). All pressure plates were placed into the chamber (Figure 3.8a), and the chamber was filled with water. Then, the baseline values for each pressure plate were read and recorded using DATAQ while no extra pressure was added to the system. The chamber was then sealed by placing the top lid onto the rubber gasket and tightened with bolts as shown in Figure 3.8b. The holes on the side of the chamber for feeding out the wires were also sealed by taping the wires to obtain an air and water tight chamber. Then, an adjustable pressure regulator was used to pressurize the chamber up to 25 psi at 5 psi increments. To ensure the pressures plates were responding in the same manner with either increasing or decreasing pressure, the pressure was also relieved at 5 psi increments until 0 psi was again reached. The whole procedure was repeated to ensure the precision of the results. The applied pressure was measured via an external pressure gauge (Figure 3.8d) and used to correlate the voltage readings to pressure measurements. Figure 3.9 displays the results of calibration process for one of the pressure plates. Pressure plates that had linear trends and were consistent with manufacturer calibration line were deemed acceptable. Unlike strain gauges, all pressure plates had satisfactory results. Calibration results are presented in Table 3.2.

a) Calibration Chamber

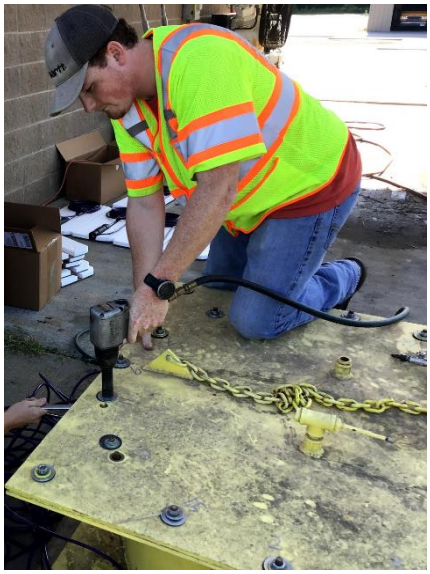

b) Sealing the chamber

c) EPC Calibration Set-Up

d) Omega Pressure Device

Figure 3.8 EPC Calibration Device

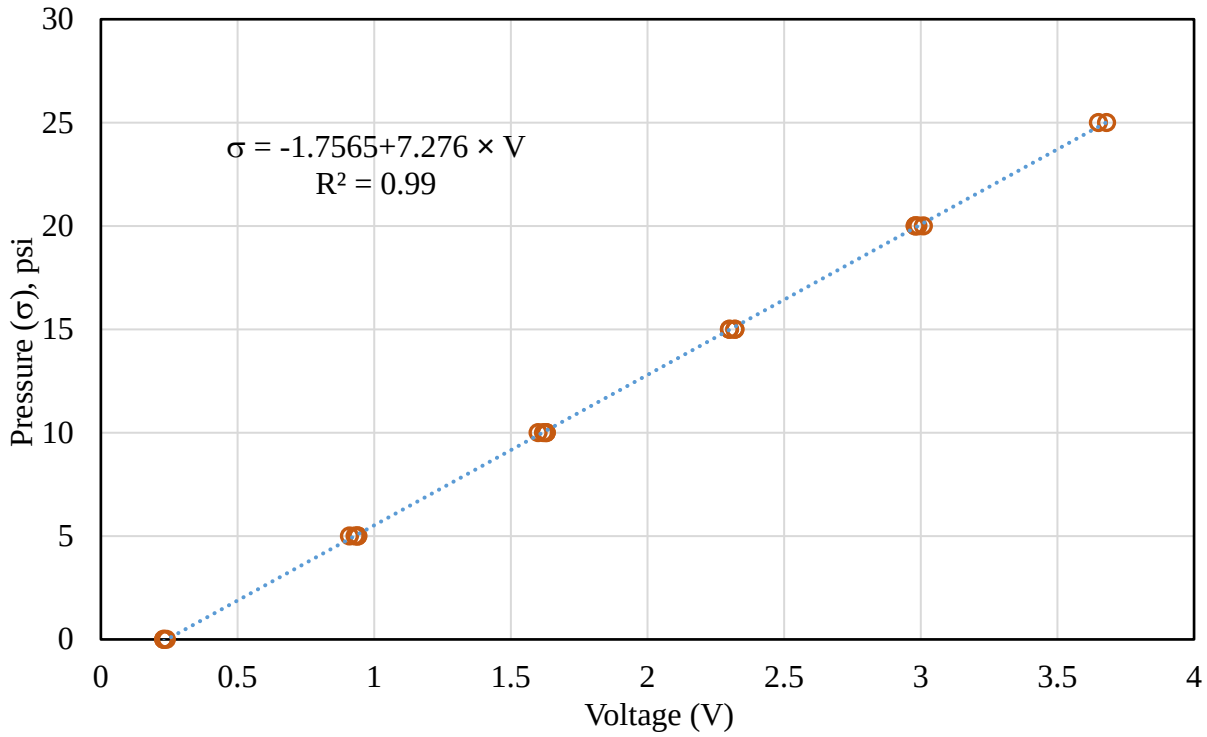

Figure 3.9 EPC Calibration Results for Section S2.

Table 3.2 S2 EPC Calibration Factors

Section-Gauge	Track Calibration, psi/Volt
S2-13	7.2760
S2-14	7.2222
S2-15	7.2653

3.5. The Stabilized Foundation Section (S2) Construction

3.5.1. Subgrade Construction

As mentioned earlier, the stabilized foundation section (S2) was sponsored by MDOT to replicate their typical pavements where challenging soil condition often exist. To simulate the weak subgrade support condition in Mississippi, full depth removal of the previous pavement section and the native Test Track soil were required to provide enough depth for Mississippi subgrade soil to be placed.

Construction of the stabilized foundation section (S2) began on April 30, 2018 by milling and excavation of the existing pavement layers and native Test Track soil. In total, approximately six feet of existing material was removed from the previous section which included asphalt concrete layers, base course layers, and native Test Track soil. Figure 3.10a shows the full excavation. As Figure 3.10 shows the shoulder was left in place since a large amount of material had to be replaced and the shoulder area was not included in the research study. Figure 3.10a also shows the location of a drainage outlet that was provided to minimize water kept in the section. To provide more protection for the section against water during construction, the pit was covered with tarp (Figure 3.10b) during rainy days. The accumulated water on the tarp was continuously pumped out to reduce the water infiltration into the section. After the rain, the section was exposed to sunlight and wind by removing the tarp to speed the drying process (Figure 3.10).

MS soil was then hauled to the Test Track and placed and compacted in eight lifts with total thickness of approximately 56 inches. The MS soil was classified as A6 under AASHTO M145 classification and CL under ASTM D2487. The amount of material passing the sieve #200 was 93% with 68% silt and 24% clay according to AASHTO T88 specification.

The laboratory density was determined to be 107.8 pcf for all subgrade lifts. The field minimum acceptable compaction level was set to 98% of laboratory density for the top 36 inches of subgrade soil and 95% for deeper layers. The results of laboratory and target densities along with field densities and field moisture content for each lift are presented in Table 3.3**.** As shown, all field densities were higher than the required target densities and were considered acceptable. Thus, the compaction for all layers met MDOT specifications.

a) Excavated Pit

c) Subgrade Tarp Protection.

d) Subgrade Sun Drying

Figure 3.10 Excavated pit and Protection Methods of Section S2

Table 3.3 Laboratory, Target, and Field Densities of MS soil

Lift No.	Lab. Density, pcf	Target Density, pcf	Field Density, pcf	Field Moisture Content, %
Lift 1	107.8	102.4	111.2	15.3
Lift 2	107.8	102.4	111.1	15.7
Lift 3	107.8	105.6	109.6	17.4
Lift 4	107.8	105.6	110.3	17.5
Lift 5	107.8	105.6	111.8	16.5
Lift 6	107.8	105.6	110.1	16.6
Lift 7	107.8	105.6	110.0	16.1
Lift 8	107.8	105.6	110.7	15.1

Mississippi subgrade was initially compacted six inches above its original grade since the top six inches of soil was to be scarified, mixed, and modified with hydrated lime. A nuclear density gauge was used to obtain moisture content and density of field material during construction while the total station surveying method was used to obtain the information about thicknesses of each lift.

3.5.2. Lime Treated Soil Construction

After the MS soil was placed and compacted, lime stabilization began. Dry hydrated lime was selected over slurry and quicklime applications due to easier and faster application. Dry hydrated lime was delivered to the project in a self-unloading transport truck and was mixed with the top six inches of MS soil using a milling machine with the conveyor system turned off. To ensure that right amount of lime was applied to the section, small cloths of known area and weight were placed on the surface for later verification (Figure 3.11b). However, since the length and width of the section was known, and the truck load weight was predetermined, the possibility for error in the lime application was very small. No soil scarification was applied prior to the application of lime which provided a smoother surface for the truck to apply lime uniformly. After mixing 4.0% of lime by dry weight of soil, the material was compacted with a steel-wheel roller and brought to

proper grade and cross-slope with a motor grader. Finally, following the clipping of the surface, a prime coat (NTSS-1HM anionic asphalt emulsion) sealed the layer to prevent any possible loss of moisture. The prime coat was sprayed at the rate of 0.2 gal/sy and the dilution rate of 60% binder and 40% water. A 10-day mellowing period was allowed for the lime treated layer to provide sufficient time for chemical reactions to take place before placing the dirty-sand base which was then treated two days later with cement to form the CTB.

a) Self-unloading for lime application

b) Verification Cloth

c) Uniform Application of Lime

d) Mixing Soil and Lime Together

Figure 3.11 Preparation and Construction of the Lime Treated Layer

The LTS was designed to obtain a soaked California Bearing Ratio (CBR) of 20% after seven days of protected curing. The field dry density of LTS was 100.1 pcf with moisture content of 15.8% at the time of construction. The explained construction steps are shown in Figure 3.12. Following the construction of this layer, the first pressure plate was installed on top of subgrade by locally removing six inches of LTS materials. The instrumentation details are provided in section 3.6.

a) LTS Compaction *b) LTS Clipping and Grading*

c) LTS Prime Coating

Figure 3.12 Finalizing the Construction of the Lime Treated Layer

3.5.3. Cement Treated Base Construction

The construction of the cement treated layer was similar to the lime treated layer. The only difference was the material being used in which the dirty-sand hauled from Mississippi State was mixed with 5.1% cement by dry weight of the dirty sand. Type I Portland cement met ASTM C150 specifications was used. Table 3.4 summarizes the mixture and design properties of the soils used in section S2. As shown in Table 3.4, dirty sand was classified as SM according to ASTM D2487 classification while the subgrade was classified as CL. The CTB was designed in the laboratory to meet the minimum of 300 psi compressive strength at 14 days of curing.

The soil and the cement were mixed together by a milling machine with the conveyor turned off and no external water was added to the cement and soil during the mixing process. The layer compacted using a rubber tire roller and came to the required grade through the application of a motor grader. Similar to the lime treated layer, the prime coat was used to seal the top surface to prevent any loss of moisture necessary for cement hydration. The EPR-1 prime coat with the rate of 0.2 gal/sy and the dilution ratio of 60% tack and 40% water was used. The curing time for this layer was two weeks. Figure 3.13 summarizes the construction steps for this layer.

The instrumentation of second pressure plate on top of LTS followed the construction of CTB layer. This was achieved by locally removing six inches of CTB materials to access the interface of LTS and CTB layers and placing pressure plate into the cavity. Later, strain gauges and the last pressure plate at the interface of AC and CTB layers were installed in this layer. The instrumentation details are fully discussed in section 3.6.

Table 3.4 Soil and Mixture Design Properties of section S2 *(Sullivan, 2021)*

Soil Property	Subgrade	Base (dirty sand)
Liquid Limit	39	---
Plastic Limit	18	---
Plasticity Index	21	Non-Plastic
% Passing No. 4	99	100
% Passing No. 10	98	99
% Passing No. 40	98	91
% Passing No. 60	97	72
% Passing No. 200	93	16
AASHTO T88 % Silt	68	7
AASHTO T88 % Clay	24	8
AASHTO M145 Classification	A6(20)	A2-4
ASTM D2487 Classification	CL	SM
Untreated Max γ_d (g/cm^3)[a]	1.73	1.76
Untreated OMC (%)[a]	16	13
Design L_w or C_w[b]	4.0	5.1
Treated Max γ_d (g/cm^3)[c]	1.62	1.83
Treated OMC (%)[c]	17	13

Note: Max γ_d = maximum dry density; OMC = optimum moisture content

[a] *Determined by AASHTO T 99.*

[b] *Determined by Mississippi Test Method 27 and 25, respectively.*

[c] *Determined by AASHTO T134 with soil-lime mixture tested in the same manner.*

3.5.4. Asphalt Concrete Construction for section S2

The stabilized foundation section (S2) was overlaid with four layers of asphalt concrete. The first layer was placed on October 4th, 2018 over the CTB layer with target thickness of three inches. On the day of construction, the 24 hour high and low temperatures were 90°F and 71°F, respectively. The asphalt plant used for the construction was the East Alabama Paving Company plant, located six miles away from Test Track at Opelika, Al. All four layers of asphalt concrete were non-modified asphalt mixtures with the binder grade of PG 64-22 (or PG 67-22), typically in use in the State of Mississippi. Table 3.5 shows the average as-built and as-designed thicknesses for the asphalt concrete layers.

a) Application of Cement

b) Mixing Cement and Soil

c) Compaction of the Layer

d) Sealed Surface with Prime Coat

Figure 3.13 Steps in Construction of Cement Treated Base.

Table 3.5 As-designed and As-built Thicknesses for Asphalt Concrete Layers (Section S2)

Layer Names	As-designed Thickness	As-built Thickness
Layer 1 (bottom layer, Sublot 4)	3.0 inches	3.08 inches
Layer 2 (intermediate layer, Sublot 3)	3.0 inches	2.80 inches
Layer 3 (intermediate layer, Sublot 2)	2.0 inches	2.08 inches
Layer 4 (top layer, Sublot 1)	1.5 inches	1.29 inches

The plant configuration setting for all four layers is provided in Table 3.6. The plant configuration adds up to around 105% for all four layers because East Alabama Paving Company

operates their plant based on aggregate weight and not based on the total mixture weight *(McCarty, 2019)*. The results adds-up to 100% for total aggregate weight as shown in Table 3.6.

The as-built aggregate gradation for all four asphalt concrete lifts is provided in Figure 3.14. The bottom two lifts were designed to contain coarser particles than the top two lifts. The target Nominal Maximum Aggregate Size (NMAS) for the two bottom lifts (lifts one and two) was 19 mm (3/4”). However, quality control results indicated that slightly finer materials with NMAS of 12.5 mm (1/2”) was being placed during construction. The target and as-built NMAS for the third and fourth (top) lifts were 12.5 mm (1/2”) and 9.5 mm (3/8”), respectively. In addition to aggregate gradation, as-built volumetric properties and densities of asphalt concrete layers are presented in Table 3.9. Further details of asphalt concrete material properties are provided in the Appendix A.

Table 3.6 S2 Plant Configuration Settings

Material,	Lift 1 (bottom)	Lift 2	Lift 3	Lift 4 (top)
Binder Content, %	4.5	4.5	4.9	5.1
MS Coarse Sand, %	10.0	7.0	6.0	6.0
MS -5/8" Crushed Gravel, %	25.0	40.0	44.0	52.0
MS #67 Fullen Dock Limestone, %	15.0	16.0	0.0	0.0
MS #10 Fullen Dock Limestone, %	19.0	6.0	0.0	0.0
MS #8 Vulcan Limestone, %	0.0	0.0	12.0	12.0
MS #10 Vulcan Limestone, %	0.0	0.0	7.0	9.0
MS Coarse RAP, %	20.0	20.0	10.0	0.0
MS Fine RAP, %	10.0	10.0	20.0	20.0
Hydrated Lime, %	1.0	1.0	1.0	1.0

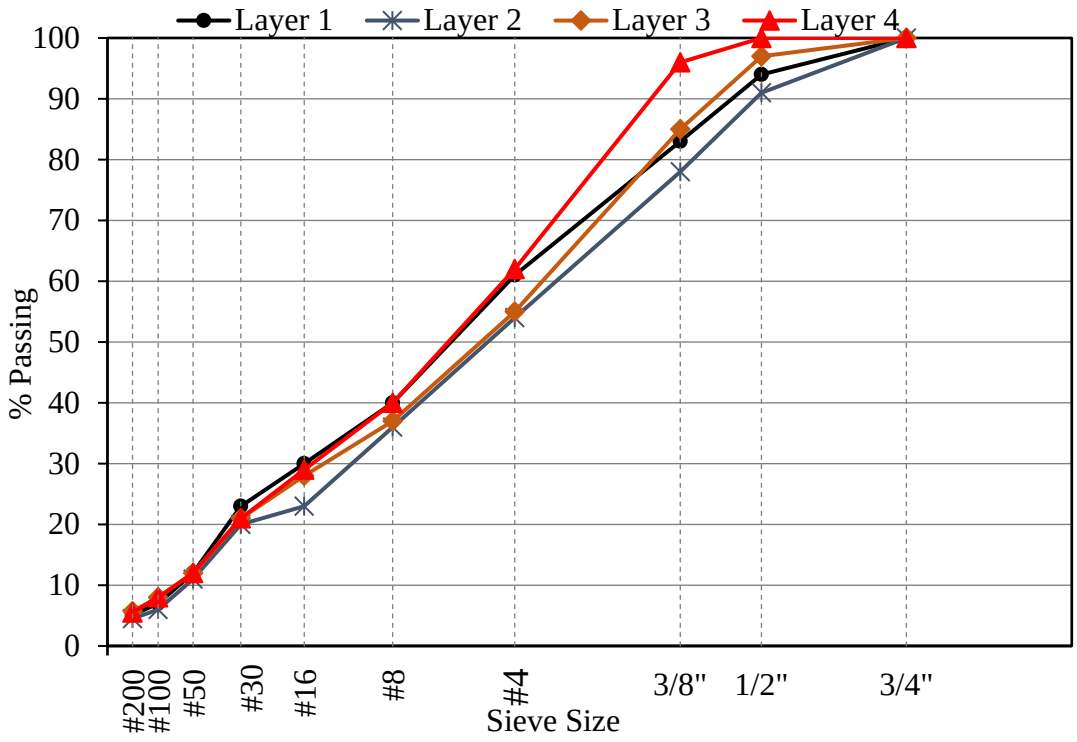

Figure 3.14 Aggregate Gradation for Asphalt Concrete Layers (Section S2).

Table 3.7 As-built Volumetric Properties for the stabilized foundation section (S2)

Properties	Layer 1	Layer 2	Layer 3	Layer 4
Binder Content, %	4.5	4.5	4.9	5.1
Effective Binder Content (Pbe), %	4.1	4.0	4.4	4.5
Dust-to-Effective Binder Ratio	1.2	1.1	1.3	1.2
RAP Binder Replacement, %	30	31	33	22
Rice Gravity (Gmm)	2.453	2.438	2.436	2.414
Bulk Gravity (Gmb)	3.387	2.381	2.377	2.349
Air Voids (Va), %	2.7	2.3	2.4	2.7
Aggregate Gravity (Gsb or Gse)	2.588	2.572	2.588	2.563
VMA, %	12	12	12	13
VFA, %	78	80	81	79

Prior to the application of the first asphalt layer, the transition zones leading in and out of the section as well as the vertical edges were covered with binder to prevent any possible slippage between the new and existing pavement. All pavement sensors were covered by the asphalt concrete mixtures sieved through a #4 screen before the application of the first layer to prevent

any damage. A more detailed discussion on pavement instrumentation is provided in section 3.6. Construction images of asphalt mixture application for the stabilized foundation section (S2) are provided in Figure 3.15. All four layers were placed with a RoadTec paver and brought to the required compaction level. The compaction level for each layer is provided in Table 3.8. Each layer was compacted individually with three roller types including a breakdown roller, a rubber tire roller, and a steel finishing roller. The tack coat used for layer interfaces was NTSS-1HM with undiluted target tack rate of 0.70 (gal/sy).

a) AC Placement on CTB Layer

b) AC Layer Before Compaction

c) Placement of intermediate AC mixtures

d) Finalizing S2 Construction (top layer)

Figure 3.15 Construction Images of Asphalt Layers for Section S2.

Table 3.8 Average measured mat compaction

Properties	Layer 1	Layer 2	Layer 3	Layer 4
Compaction level, % G_{mm}	93.7	95.6	93.2	92.3

The initial International Roughness Index (IRI) immediately after construction was 58.0 in/mile. Considering the IRI threshold value of 170 in/mile, the pavement fell into the accepted category. The panorama image of finished surface of the pavement is provided Figure 3.16.

Figure 3.16 Final View of Section S2 (Panorama Image).

3.6. Instrumentation Process for Section S2

3.6.1. Pressure Plate Installation for Mississippi Subgrade

As mentioned in section 3.5, the instrumentation of the first pressure plate had begun once the construction of LTS was completed. The instrumentation process mirrored the procedure that were used in the previous Test Track research cycle (Willis et al. 2009). To begin with, the location and the alignment of the pressure plate were specified and marked based on its location, shown earlier on Figure 3.4**,** to provide enough depth for pressure plate to be placed on top of the MS subgrade soil, a small cavity was excavated locally by removing almost six inches of LTS material (Figure 3.17b). Then, a 3/8-in. flexible conduit was used to protect the wire of the pressure plate to prevent any possible pinch or cutting by aggregate during the placement of the second layer. The cavity

was filled with a layer of -#8 material followed by a thin application of -#16. The sieved material was taken from current layer to preserve material uniformity. Then, the pressure plate was placed on top of the sieved material, and then the -#16 material covered the pressure plate followed by the application of - #8. The pressure plate was therefore enveloped with materials passing a #16 sieve.

The use of relatively finer materials ensured no large aggregate would come in direct contact with the pressure plate. Care was taken to ensure the pressure plate was completely level since any possible small tilt would alter the pressure readings. In addition, shallow trenches were dug to accommodate the wires and flexible conduit. The soils in trenches and cavities were compacted by hand to minimize the disturbance of the section and to maintain uniformity.

a) Flexible Conduit b) EPC Installation

Figure 3.17 EPC Installation Process for MS Soil.

3.6.2. Pressure Plate Installation for Lime Treated Soil

The pressure plate installation process for LTS began once the construction of CTB layer was completed. The installation mirrored the process explained earlier for MS soil where a small cavity was dug by removing almost six inches of CTB materials to access the top of lime treated soil. Then the pressure plate was placed on top of fine materials to avoid any possible direct contact with large aggregates. Similar to the Mississippi soil instrumentation, all trenches and cavities filled with the same layer materials to preserve uniformity and hand compacted with marshal hammer (Figure 3.18). In addition, a small copper plate was embedded at the interface of CTB and LTS layers to help future detection of layer thicknesses using ground penetrating radar (Figure 3.18c).

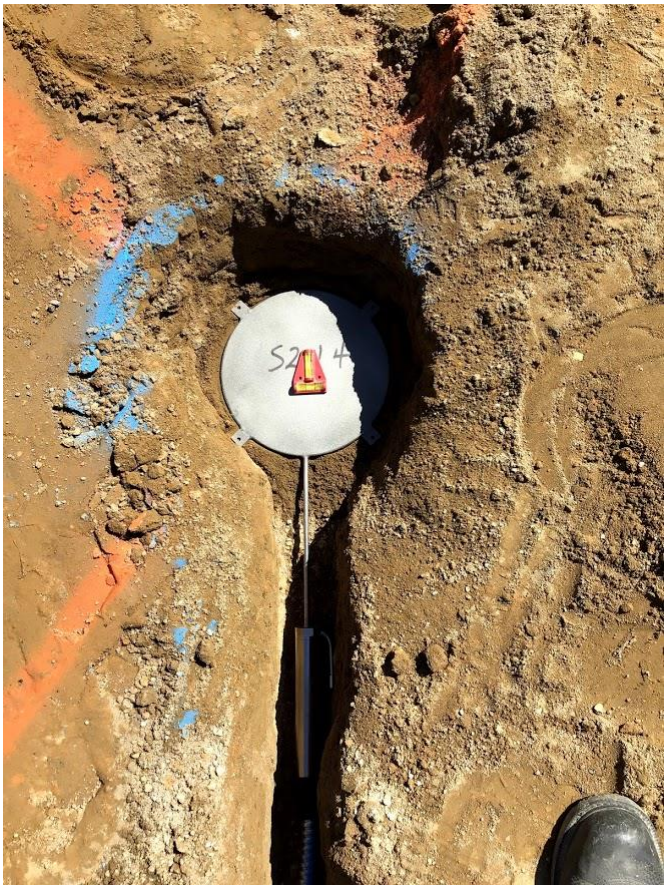

a) pressure plate installation

b) hand compaction of the materials

c) copper plate

Figure 3.18 Lime Treated Soil Instrumentation.

3.6.3. Pressure Plate and Strain Gauge Installation for Cement Treated Base

The instrumentation for this layer included one pressure plate and 12 asphalt strain gauges. The procedure for installation of the pressure plate was very similar to the installation procedure for LTS and Mississippi subgrade. However, this time a shallower cavity was dug to just have the pressure plate just flush with cement treated layer as shown in Figure 3.19. Unlike the other two layers, the cables were not buried into the layer to preserve the integrity of CTB.

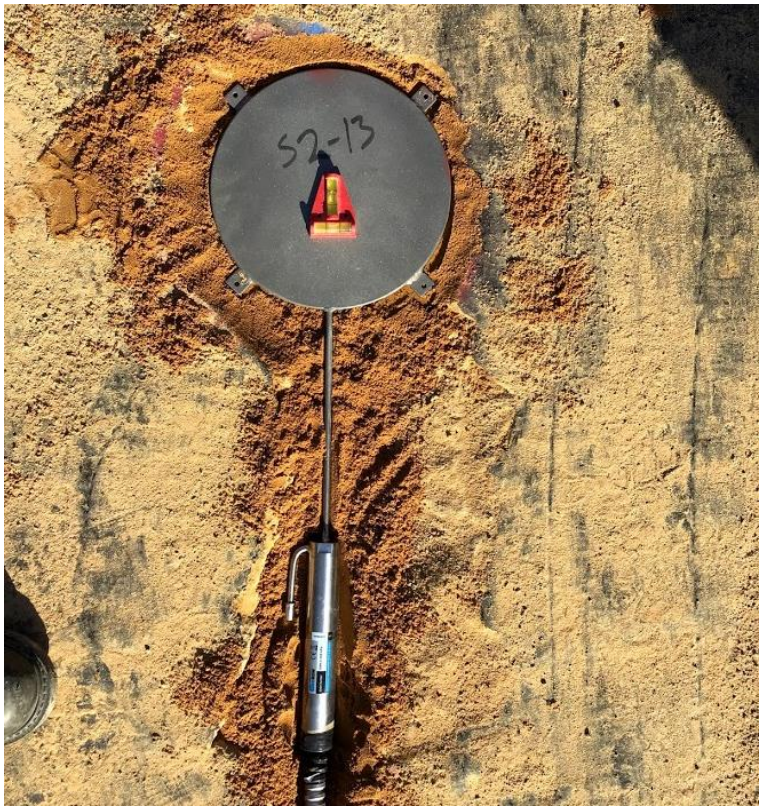

Figure 3.19 Pressure Plate for Cement Treated Base.

The installation procedure of asphalt strain gauges was almost identical to installation procedure of previous Test Track research cycles. However, in this research cycle, only longitudinal strain gauges were used since the previous studies at Test Track had shown that

longitudinal strain gauge measurements were usually 36% higher than transverse gauge measurements (*Timm and Priest, 2008; Priest and Timm, 2006*).

The installation procedure started with surveying the relative location of strain gauges on the test section and painting the locations by forming a grid. Figure 3.20a shows the grid in which the intersection of the stripes determined the location of each strain gauge. The location of the stripes was determined by surveying so that the center of strain gauges matched the center of outside wheel path. All strain gauge wires were threaded through a ½ inch flexible conduit (Figure 3.20b). In addition, plastic grommets were used at each end of the flexible conduit to prevent any possible damage to wires. The wires of strain gauges were not buried into the layer to avoid further disturbance of the cement treated layer. Finally, all strain gauges were covered with plastic tarp and protected until the paving with asphalt concrete.

a) Grid for the ASGs *b) Positioning the ASGs*

Figure 3.20 Installation of Strain Gauges for the Last Layer.

Just before the placement of the asphalt concrete, the strain gauges were tacked to the base course by asphalt binder mixed with sand as shown in Figure 3.21. The direction of each strain gauges was carefully adjusted during the application of the tack binder. Then, a small batch of asphalt concrete obtained from the material transfer vehicle and sieved through a #4 screen was

used to cover and protect the gauges and wires from the paving and compaction equipment (Figure 3.22a). A 1ft×1ft steel tamping plate was used to gently compact the asphalt materials through kneading action without applying any impact. The surface of the tamping plate was pre-heated to prevent any loss of temperature and prevent sticking of the asphalt to the plate. Once all the sensors were covered with sieved asphalt concrete, the paver proceeded forward and laid down the first lift (Figure 3.22b). The paving crew was directed not to make turns over the gauges or stop on top of embedded sensors to avoid any possible damage. The sensors were monitored continuously during the application of first lift as well as subsequent lifts.

a) Tacking Strain Gauges to the Base *b) The Final Array of Strain Gauges*

Figure 3.21 Tacking and Positioning ASGs Prior to Asphalt Layer Implementation

c) Final Protection of Strain Gauges *d) Paver Approaching Protected Gauges.*

Figure 3.22 Last Stage in Instrumentation Prior to Asphalt Layer Implementation.

During and after construction, the basic functionality of all instrumentations was validated. The pavement sensors were used in this study to obtain fundamental understanding of how section S2 behaves under truck loading and over time. The discussion about pavement response over time using pavement instrumentation is provided in Chapter 5.

CHAPTER 4

LABORATORY CHARACTERIZATION

This chapter provides laboratory characterization of AC, CTB, and LTS used for the stabilized foundation section (S2). While the asphalt concrete results were obtained internally at NCAT laboratory, the MS Soil, CTB, and LTS laboratory tests were performed and analyzed by Mississippi State University *(Sullivan, 2021)*. Asphalt material property and performance testing were conducted on plant-produced, lab-compacted specimens as part of routine testing at the Test Track.

4.1. Asphalt Concrete Laboratory Results

This section discusses the laboratory test results of the AC materials for the stabilized foundation section (S2). Some of the data will be compared against the thick-lift pavement section (S9) to provide a basis for comparison and to acquire more information about the similarities and differences of the sections through direct comparison. The test results presented include dynamic modulus, beam fatigue, IDEAL-CT, and Hamburg Wheel Track Testing.

4.1.1. Dynamic Modulus

Dynamic modulus (E*) is a fundamental material property for evaluating asphalt mixture properties which is used for performance prediction and M-E pavement design *(Nakhaei et al., 2018; Ziari et al., 2019; Ziari et al., 2016).* To perform the test, plant produced, lab compacted

samples were prepared with small geometry according to AASHTO PP 99-19 and as shown in Figure 4.1. Initially, asphalt samples were prepared in accordance with AASHTO T 312. The samples were compacted to the height of 7.09 in. (180 mm) or higher. The locations of the specimens were marked before coring out the samples similar to Figure 4.1a. The samples were cored with diameter of 1.5 in. (38 mm) from the main sample, and both ends of the core samples were sawed to obtain the height of 4.33 in. (110 mm). Small sample geometry is the preferred method for dynamic modulus testing since it reduces the amount of material required for testing *(Bowers et al., 2015)*.It was also shown that small scale samples produce comparable results to large scale samples *(Li and Gibson, 2013).*

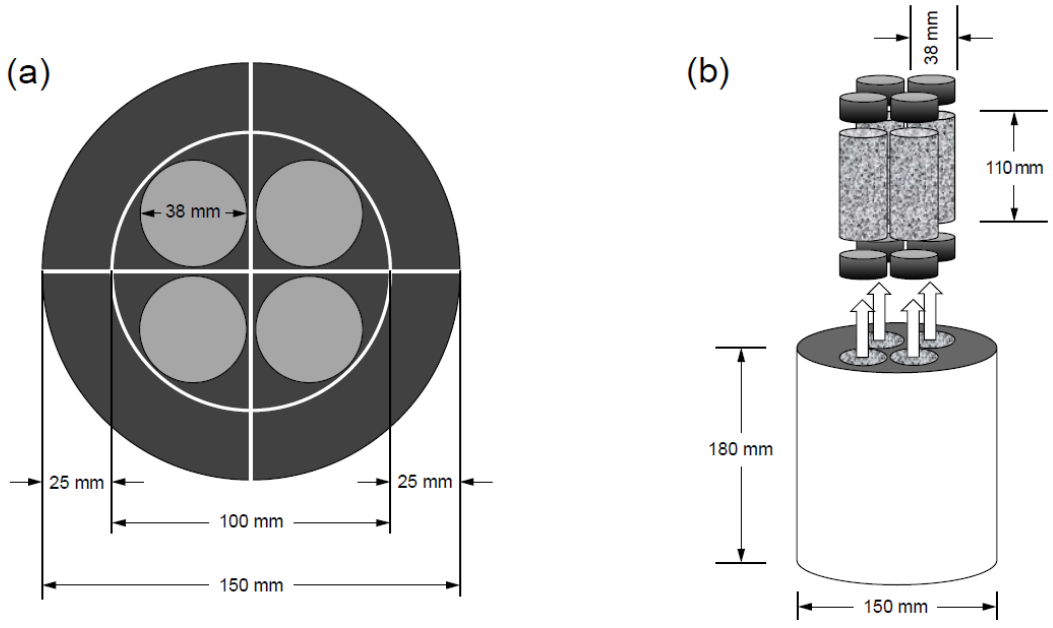

Figure 4.1 Schematic of Dynamic Modulus Specimens (obtained from AASHTO PP 99-19).

The Maximum Specific Gravity (G_{mm}) and Bulk specific gravity (G_{mb}) were measured according to AASHTO T 209 and AASHTO T 166. From G_{mm} and G_{mb} values, the air voids of the Superpave gyratory samples (SGC) were determined. The target air void content for SGC sample was set such that the small geometry samples achieved 7.0 ±0.5% air voids.

Once the samples were prepared, they were tested according to AASHTO TP 132-19. The samples were tested by Asphalt Mixture Performance Tester (AMPT) which is a computer-controlled hydraulic testing machine capable of applying cyclic load over a wide range of temperature and frequencies. With AMPT equipment, the cylindrical specimens were subjected to controlled haversine compressive stresses of various frequencies. The applied stresses and resulting axial strains were measured as a function of time and used to calculate dynamic modulus.

Table 4.1 tabulates the data at the three temperatures and frequencies used in the testing. The same information is shown graphically in Figure 4.2 which illustrates the master curves generated from the test data following AASHTO R 84-17. As the graph illustrates, the stiffness at lower frequencies for intermediate layers were higher than the surface and bottom layers. In particular, the surface mixture had the lowest stiffness at lower frequencies. Thus, the intermediate layers are expected to be more resistant to permanent deformation. On the other hand, modulus values for higher frequencies approached to similar values. Figure 4.3 shows the dynamic modulus master curve for the Thick-lift pavement section (S9). The results indicate that the dynamic modulus at lower frequencies is lower for this section compared to the stabilized pavement section (S2) but they both seemed to have similar moduli at higher frequencies.

Table 4.1 Section S2 Dynamic Modulus Test Data

			E Avg (MPa)*				*E* Avg (ksi)*			
Temp (°C)	*Temp (°F)*	*Freq (Hz)*	*S2-4 (Surface)*	*S2-3*	*S2-2*	*S2-1 (Base Mix)*	*S2-4 (Surface)*	*S2-3*	*S2-2*	*S2-1 (Base Mix)*
4	39.2	10	18,012	19,927	19,342	18,049	2,612	2,890	2,805	2,618
4	39.2	1	14,775	16,939	16,327	14,929	2,143	2,457	2,368	2,165
4	39.2	0.1	11,442	13,680	13,130	11,656	1,660	1,984	1,904	1,691
20	68	10	10,638	12,400	11,878	10,770	1,543	1,798	1,723	1,562
20	68	1	7,192	8,823	8,436	7,399	1,043	1,280	1,224	1,073
20	68	0.1	4,276	5,580	5,404	4,514	620	809	784	655
40	104	10	3,459	4,139	4,165	3,709	502	600	604	538
40	104	1	1,605	1,985	2,156	1,810	233	288	313	263
40	104	0.1	647	815	987	778	94	118	143	113

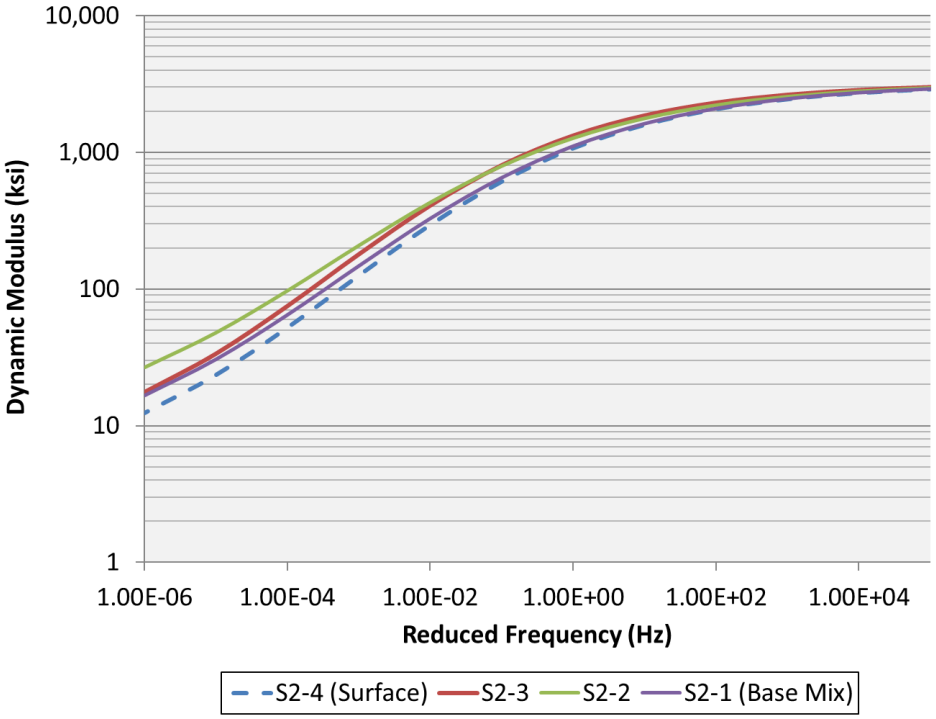

Figure 4.2 Stabilized Foundation Section Dynamic Modulus Master Curves.

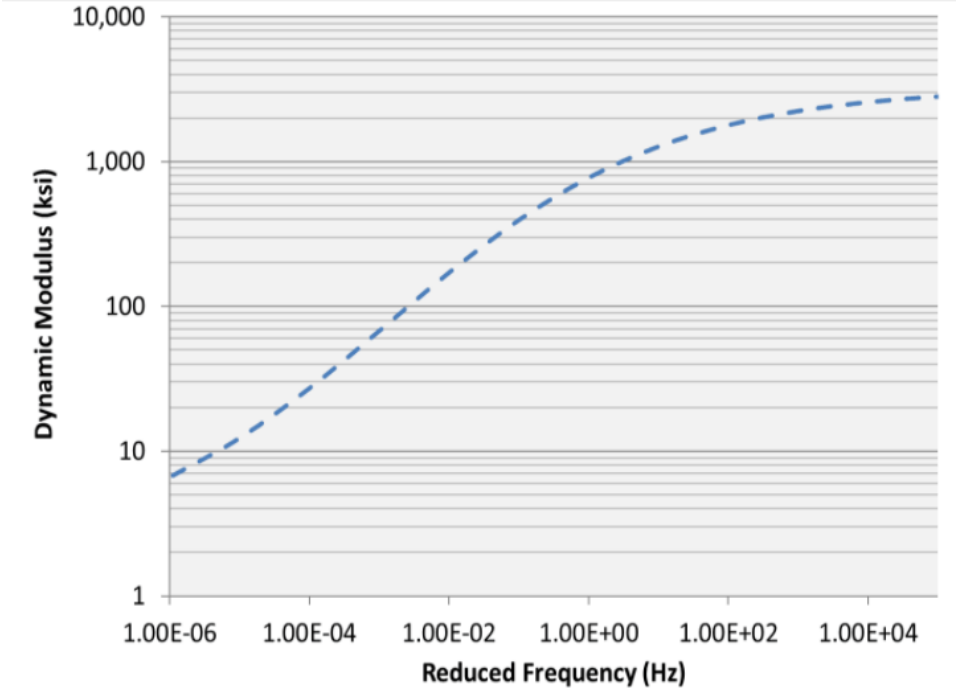

Figure 4.3 Thick-Lift Section Dynamic Modulus Master Curves.

4.1.2. Beam Fatigue Test

The fatigue test is used to characterize the fatigue life of asphalt mixtures at intermediate pavement temperatures *(Nakhaei et al., 2020)*. This test can provide insight and estimates of asphalt mixture fatigue life under repeated traffic loading. In this test, an asphalt concrete beam is subjected to repeated bending load until its initial stiffness reduces to a certain threshold. The number of loading cycles to reach the threshold (or at failure) is recorded and plotted against the strain value.

Bending Beam Fatigue Testing of the base mix (S2-1) followed AASHTO T 321-17 with specimens compacted with target air voids of 7% and tested at three target strain levels (300, 400 and 600 microstrain). The results with three replicates are shown in Table 4.2 and shown graphically in Figure 4.4. To provide a basis of comparison the results for the thick-lift pavement section (S9) are also plotted in Figure 4.4. It appeared that the mixture placed for the thick-lift pavement section had better fatigue resistance. As an example, with 400 microstrain applied loading, the stabilized section (S2) failed on average after 100,000 cycles while the thick-lift pavement section failed after 500,000 cycles, which is five times higher than the stabilized foundation pavement (S2). However, bottom-up fatigue cracking may not be a concern for the section with stabilized foundations since the in situ strain levels are much lower than the thick lift section.

The stabilized foundation section (S2) experienced 10 million ESALs during the 2018 research cycle with no apparent bottom-up cracking. Due to the low strain levels at the bottom of the AC, bottom-up fatigue is unlikely to occur in this section. However, as will be discussed in later chapters, further trafficking may initiate middle-up cracking in the section.

Table 4.2 Section S2 Base Mix Bending Beam Fatigue Test Data

Sample ID	Sample Air Voids (%)	Initial Beam Stiffness (MPa)	Initial Beam Stiffness (ksi)	Cycles to Failure (Peak Mod x Cycles)	Peak-to-Peak On-Specimen Microstrain
12	7.4	7,888	1,144	891,250	300
14	7.3	7,536	1,093	940,444	300
15	7.3	7,821	1,134	607,202	300
7	7.6	10,613	1,539	38,904	400
9	6.8	7,942	1,152	141,796	400
10	7.1	8,283	1,201	49,545	400
2	7.1	7,724	1,120	12,956	600
5	7.0	7,642	1,108	8,175	600
8	7.0	7,988	1,159	3,905	600

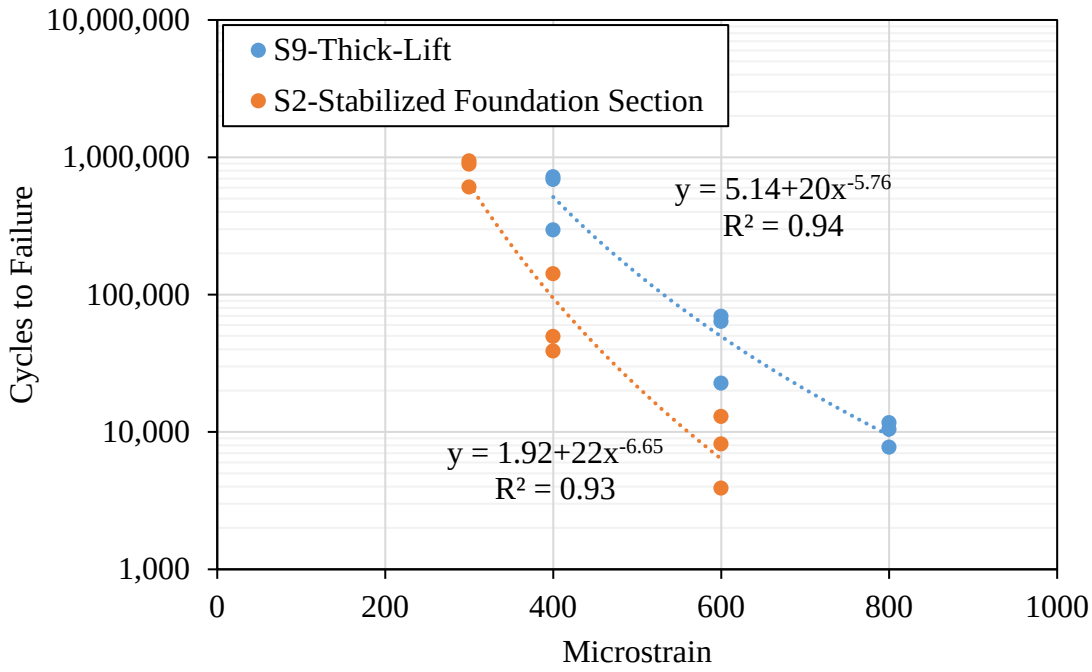

Figure 4.4 Bending Beam Fatigue Transfer Function for Stabilized Foundation (S2) and Thick-Lift Pavement Sections.

From dynamic modulus and beam fatigue data it can be concluded that asphalt material for the stabilized foundation section (S2) was stiffer than the asphalt material for the thick-lift pavement section (S9). Thus, considering the same level of strain and stress in the field, the stabilized section is more prone to cracking and less to rutting compared to the thick-lift section

(S9). However, Chapter 5 shows the strain readings of the stabilized foundation section is much lower than the thick-lift section. Again, these two sections were not part of the same experiment, but comparing the results helped gain insight about the behavior of each section.

4.1.3. IDEAL-CT Testing

Due to increased use of recycled material in asphalt pavements, some pavements are becoming more susceptible to cracking. The indirect tensile asphalt cracking test (IDEAL-CT) was developed in response to the urgent need for a practical cracking test for routine use in mix-design and quality control. The IDEAL-CT is simple (no cutting or notching is needed), practical, and efficient (test completion less than 1 min) which can be performed with regular indirect tensile strength test equipment *(Zhou et al., 2017)*. Figure 4.5 shows the schematic setup for IDEAL-CT test along with load cells and linear variable differential transformers (LVDTs). To perform this test, each cylindrical specimen was centered in the fixture and the load was applied such that a constant load-line displacement (LLD) of 50 ± 2.0 mm/min was obtained and maintained during the test duration. Both LLD and load for each specimen were used to calculate CT_{index}.

The cracking index of the surface mix (S2-4) was determined following ASTM D8225-19. Six specimens were compacted to a target air void content of 7.0 ±0.5% and the results are shown in Table 4.3. There is active research regarding minimum CT Index values for use in balanced mix design. One commonly cited specification from the Virginia DOT requires a CT_{Index} exceeding 70 to avoid surface cracking problems *(VDOT, 2020)*. However, some mixes previously placed on the Test Track with CT_{Index} values in the 30s also performed well, though they were placed on the existing AC layer *(West et al., 2018)*. The CT_{Index} values highlighted in Table 4.3 are below even this lower threshold so top-down cracking may become an issue in the next test

cycle, though not evident through the first two years and 10 million ESALs of trafficking. The results from IDEAL-CT confirmed the previous findings from dynamic modulus and beam fatigue testing that the asphalt mixture for this section was stiff and prone to cracking.

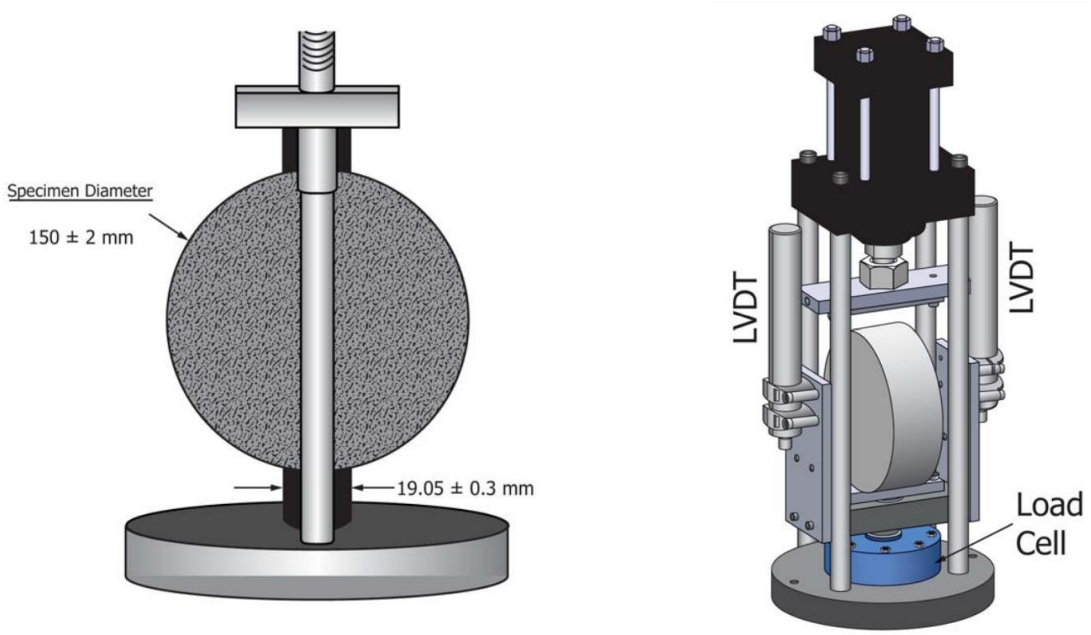

Figure 4.5 IDEAL-CT Setup Schematic (Obtained from ASTM D8225-19).

Table 4.3 Stabilized Foundation (S2) Surface Mix Ideal CT Test Data

Sample ID #	1	2	3	4	5	6
Air Voids	7.1	6.7	6.8	6.9	7	7.1
Thickness (mm)	62	62	62	62	62	62
Diameter (mm)	150	150	150	150	150	150
Test Temperature	25C	25C	25C	25C	25C	25C
CT Index	**25.2**	**19.3**	**23.4**	**17.9**	**18.8**	**24.3**
Peak Load (lbs)	4612.5	4731.4	4731.6	4678.7	4809.3	4681.9
Fracture Energy (J/m2)	8429.9	8155.6	8907.9	7949.2	8257.8	8538.1
Post Peak Slope (kN/mm)	7.39	8.486	8.018	8.853	8.556	7.619
Displacement @75% (mm)	3.307	3.015	3.162	2.987	2.918	3.25

Note: Loading rate = 50 mm/min

The IDEAL-CT results for the thick-lift pavement section (S9) is provided in Table 4.4 for comparison with the stabilized foundation section (S2). The values are on average three times higher than those for stabilized foundation section confirming the findings from dynamic modulus and beam fatigue testing that stabilized foundation layer has stiffer AC material and thus more susceptible to cracking.

Table 4.4 Stabilized Foundation (S2) Surface Mix Ideal CT Test Data

Sample ID #	1	2	3	4	5	6
Air Voids	7.0	6.7	7.1	7.0	7.1	7.3
Thickness (mm)	62.0	62.0	62.0	62.0	62.0	62.0
Diameter (mm)	150.0	150.0	150.0	150.0	150.0	150.0
Test Temperature	25C	25C	25C	25C	25C	25C
CT Index	**64.5**	**50.0**	**58.8**	**55.2**	**59.2**	**57.5**
Peak Load (lbs)	3536.2	3690.7	3603.7	3498.6	3565.3	3415.5
Fracture Energy (J/m2)	8405.9	8554.00	8702.2	8250.3	8624.6	8332.9
Post Peak Slope (kN/mm)	3.915	4.8	4.361	4.3	4.1	4.272
Displacement @75% (mm)	4.506	4.2	4.42	4.3	4.2	4.418

4.1.4. Hamburg Wheel Track Testing

The Hamburg wheel tracking test (HWTT) has been extensively used by state agencies and industry for identifying mixtures which are prone to rutting and/or moisture damage. The HWTT includes testing a submerged, compacted asphalt mixture in a reciprocating rolling-wheel device. Test samples can be slabs, SGC samples, or field cores.

For this study, two plant produced, lab compacted samples with 6.0 inch diameter were fabricated following AASHTO T312 to a target air void content of 7.0±0.5%. Then rutting susceptibility of the surface mix was measured with the Hamburg Wheel Track Testing device according to AASHTO T324-19. The measured profile data are shown in Figure 4.6 and Figure 4.7 and the summary results are presented in Table 4.5. Similarly, there is a range of published thresholds for acceptable Hamburg test results *(West et al., 2018).* A mix with an unmodified

binder is expected to have less than 12.5 mm of rutting after 10,000 or 15,000 wheel passes. The maximum rutting in Table 4.5 is well below this threshold. Furthermore, the mixture had no stripping problems as it achieved over 20,000 passes with no stripping evident.

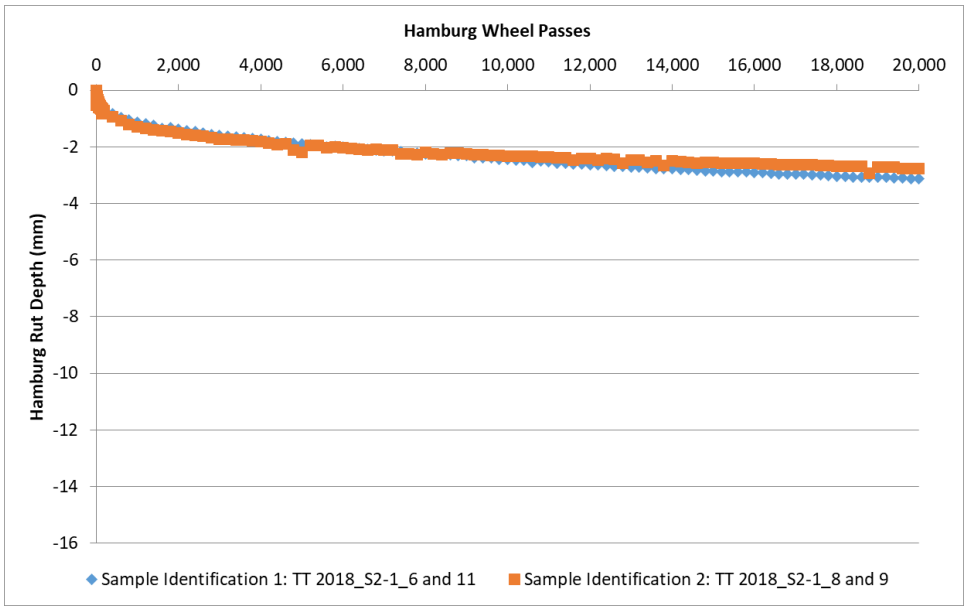

Figure 4.6 Stabilized Foundation (S2) Surface Mix Hamburg Wheel Track Testing Minimum Profile Values.

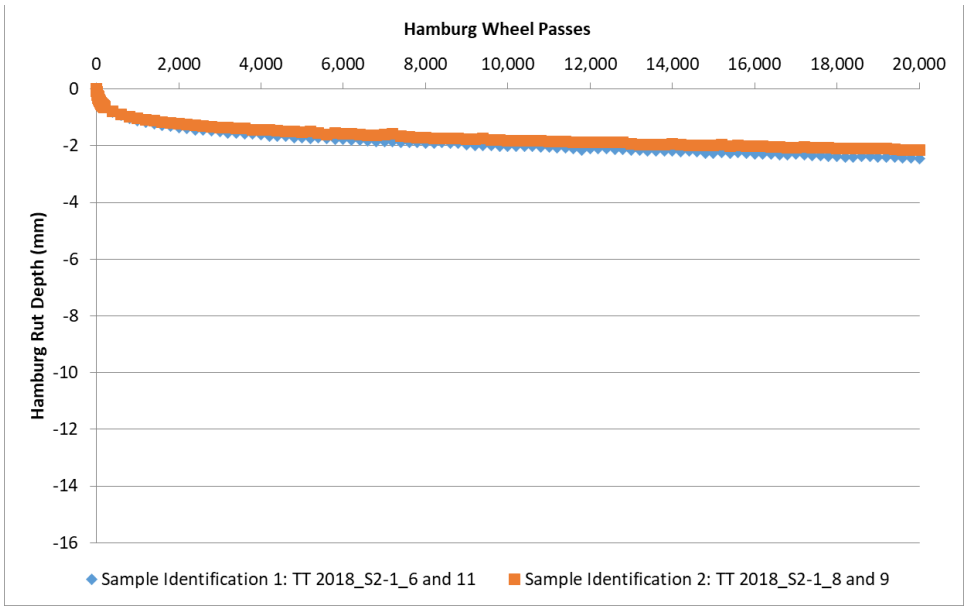

Figure 4.7 Stabilized Foundation (S2) Surface Mix Hamburg Wheel Track Testing Center Profile Values.

Table 4.5 Section S2 Surface Mix Hamburg Wheel Track Testing Summary

Parameter	Replicate 1	Replicate 2
Sample 1 ID	6	8
Sample 2 ID	11	9
Sample 1 Va (%)	7.1	7.2
Sample 2 Va (%)	7.1	7.2
Max Rut - 10k passes (mm)	2.45	2.33
Max Rut - 20k passes (mm)	3.14	2.78
Passes to 12.5 mm Rut	>20,000	>20,000
Approximate Stripping Inflection Point (passes)	>20,000	>20,000

4.2. **Properties of Foundation Layers**

This section provides the laboratory testing results conducted on Mississippi subgrade, lime treated soil, and cement treated base materials. The results presented in this document were collected and analyzed by Mississippi State University research team and only reported in this document. Interested readers may refer to *(Sullivan, 2021)* for additional information.

4.2.1. Subgrade

The Mississippi subgrade was brought to the project from Mississippi. The engineering properties of the Mississippi subgrade soil are presented in the Table 3.4. As shown, the subgrade soil is highly plastic with plasticity index of 21. Having high plasticity index for subgrade soil is one of the reasons that the Mississippi DOT uses stabilized pavement layers for highway construction. The Atterberg limits were obtained following the ASTM D4318. In addition, according to AASHTO M145 classification, the subgrade was classified as A6(20) and CL based on ASTM D2487 classification method. The percent passing sieve number 200 was 93% which indicated the weak subgrade support for the stabilized foundation section (S2).

Table 4.6 Mixture Design Properties of Mississippi Subgrade for Section (S2)

Soil Property	Subgrade
Liquid Limit	39
Plastic Limit	18
Plasticity Index	21
% Passing No. 4	99
% Passing No. 10	98
% Passing No. 40	98
% Passing No. 60	97
% Passing No. 200	93
AASHTO T88 % Silt	68
AASHTO T88 % Clay	24
AASHTO M145 Classification	A6(20)
ASTM D2487 Classification	CL
Untreated Max γ_d (g/cm^3)[a]	1.73
Untreated OMC (%)[a]	16
Design L_w or C_w[b]	4.0
Treated Max γ_d (g/cm^3)[c]	1.62
Treated OMC (%)[c]	17

Note: Max γ_d = maximum dry density; OMC = optimum moisture content

[a] *Determined by AASHTO T 99.*

[b] *Determined by Mississippi Test Method 27 and 25, respectively.*

[c] *Determined by AASHTO T134 with soil-lime mixture tested in the same manner.*

4.2.2. Lime Treated Soil

The top 6 inches of the subgrade soil was modified with 4% lime. The maximum density of 106.0 PCF was obtained at 16.6% optimum moisture content as shown in Figure 4.13. Table 4.7 shows the California Bearing Ratio (CBR) values for the lime treated soil. The values are provided for immediate and one day mellow period.

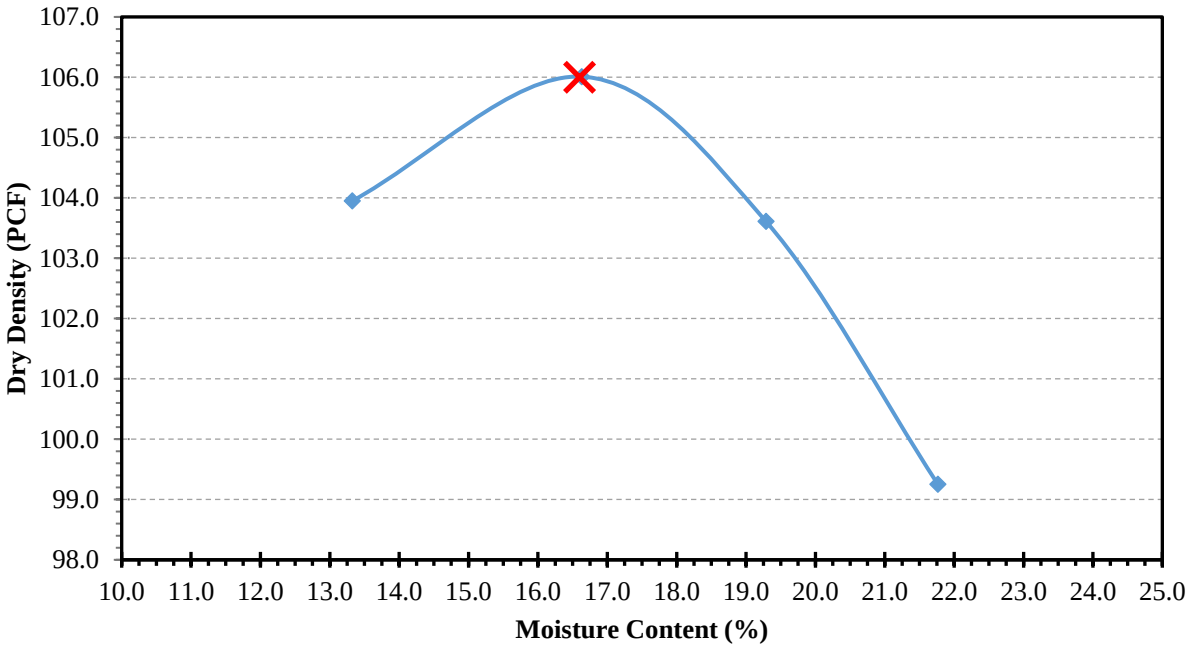

Figure 4.8 Optimum Moisture Content Graph for Lime Treated Soil with 4.0% Hydrated Lime (obtained from *(Sullivan, 2021)*).

Table 4.7 Laboratory CBR values for Lime Treated Soil *(Sullivan, 2021)*

Submerged Time (days)	Target Moisture Content (%)	Immediate/ 1 day Mellow	CBR
4	16.6	Immediate	73
4	16.6	Immediate	72
4	16.6	Immediate	76
4	18.6	1 Day Mellow	37
4	18.6	1 Day Mellow	46
4	18.6	1 Day Mellow	41

**Load rate=0.05 in. /min, lime content=4.0%, compaction effort=56 blows/lift*

As mentioned in Chapter 3, each section at the Test Track is 200 ft long where the first and last 25 feet are transition zones from which no data are normally collected. To perform the quality control during the construction, samples were taken along the outer edge of the pavement and approximately 1 foot away from the pavement white stripe *(Sullivan, 2021)*. Figure 4.9 shows the sampling locations from this section which are represented by dots on the top of the image. Samples were taken from each location to fabricate Plastic Mold compaction Device (PM) of size

3x6 and 4x8 according to AASHTO PP92-19. Unconfined compressive strength (UCS) of soil-lime materials was obtained according to ASTM D5102-96 along with their elastic modulus (E) following the ASTM C469 after 7, 14, 28, 180 days of curing.

The results are presented in Table 4.8. The average elastic modulus ranged from 30.1 ksi to 326.12 ksi with overall average of 156.1 ksi and coefficient of variation (COV) of 67.75% for the soil-lime mixture. The UCS values ranged from 26.7 to 192 ksi with an average of 74.69 and COV of 54.14%. The values presented in Table 4.8 were for samples collected in the field and tested in the laboratory during different testing periods. However, another set of specimens was fabricated and tested in the laboratory. Focusing on samples that were cured 180 days, the average for lab fabricated lab tested samples was 366.6 ksi with standard deviation of 69.2 ksi and COV of 18.8%. The laboratory fabricated samples showed higher modulus and lower COV due to less variability in sample preparation compared to field samples.

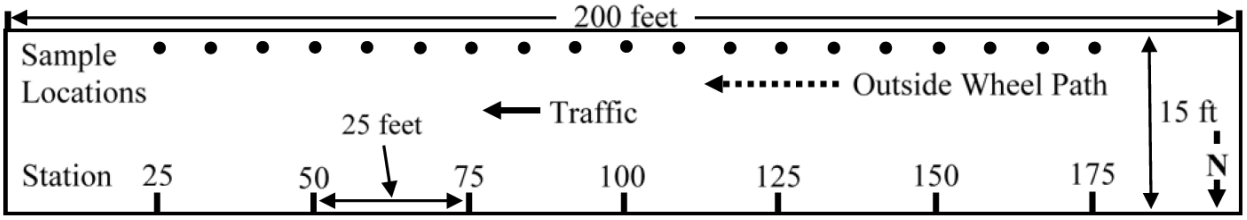

Figure 4.9 NCAT Test Section Sampling Layout (Obtained from *(Sullivan, 2021)*).

Table 4.8 Stabilized Foundation Pavement Section Lime Treated Lab Results *(Sullivan, 2021)*

Station	Specimen Type	t_{test} (days)	UCS (psi)	E (ksi)	Station	Specimen Type	t_{test} (days)	UCS (psi)	E (ksi)
175	PM 3x6	7	60.53	….	75	PM 4x8	28	72.19	….
175	PM 3x6	28	63.65	….	75	PM 4x8	28	74.70	181.66
175	PM 3x6	28	62.02	107.04	75	PM 4x8	180	191.97	326.12
175	PM 3x6	180	55.88	….	75	PM 3x6	180	145.25	….
175	PM 4x8	28	47.85	….	150	PM 3x6	7	57.04	….
125	PM 3x6	7	46.08	….	150	PM 3x6	7	47.63	….
125	PM 3x6	28	58.33	….	150	PM 3x6	7	51.69	….
125	PM 3x6	180	88.60	….	150	PM 3x6	28	….	….
125	PM 4x8	7	55.10	….	150	PM 3x6	28	59.48	….
125	PM 4x8	28	70.53	….	150	PM 3x6	28	80.05	66.78
125	PM 4x8	180	64.73	141.23	150	PM 3x6	28	….	….
50	PM 3x6	7	46.12	….	150	PM 3x6	28	62.43	80.92
50	PM 3x6	28	67.79	….	150	PM 3x6	28	….	….
50	PM 3x6	28	62.29	38.59	150	PM 3x6	180	156.31	302.38
50	PM 3x6	180	165.79	….	150	PM 3x6	180	163.09	305.24
50	PM 4x8	7	41.89	….	150	PM 3x6	180	170.01	….
50	PM 4x8	28	53.93	….	150	PM 3x6	180	….	….
50	PM 4x8	28	59.38	30.21	150	PM 3x6	180	….	….
50	PM 4x8	180	135.46	168.37	150	PM 3x6	180	….	….
25	PM 3x6	7	55.71	….	100	PM 3x6	7	32.67	….
25	PM 3x6	28	75.87	….	100	PM 3x6	28	40.74	….
25	PM 3x6	28	79.75	88.66	100	PM 3x6	180	102.27	….
25	PM 3x6	180	152.53	….	100	PM 3x6	7	29.89	….
25	PM 4x8	7	51.73	….	100	PM 3x6	28	40.57	….
25	PM 4x8	28	74.59	….	100	PM 3x6	180	80.24	….
25	PM 4x8	180	131.82	276.8	100	PM 3x6	7	26.66	….
75	PM 3x6	7	….	….	100	PM 3x6	28	37.97	….
75	PM 3x6	7	44.73	….	100	PM 3x6	180	89.81	….
75	PM 3x6	28	71.91	….	100	PM 4x8	28	41.79	….
75	PM 3x6	28	77.45	71.85	100	PM 4x8	28	40.45	….
75	PM 4x8	7	49.23	….	100	PM 4x8	28	41.68	….

Note: t_{test}=test time; ---=no data collected. PM3x6 were compacted by 5 blows while PM4x8 were compacted by 9 blows.

4.2.3. Cement Treated Base

The base soil was sampled from MDOT's Interstate 269 project in north Mississippi which represented a typical soil utilized for stabilization in Mississippi. Type I Portland cement meeting ASTM C150 specifications was used. The base consisted of six inches of silty-sand that was stabilized with 5.1% Portland cement to achieve minimum compressive strength of 300 psi after 14 days of curing. Table 4.9 shows the base material properties for the silty-sand used in this layer. The base material was classified as A2-4 and SM according to AASHTO M145 and ASTM D2487, respectively. Figure 4.10 shows the maximum dry density against moisture content for this material. The maximum dry density of 116.2 PCF was achieved at 11.3% moisture content.

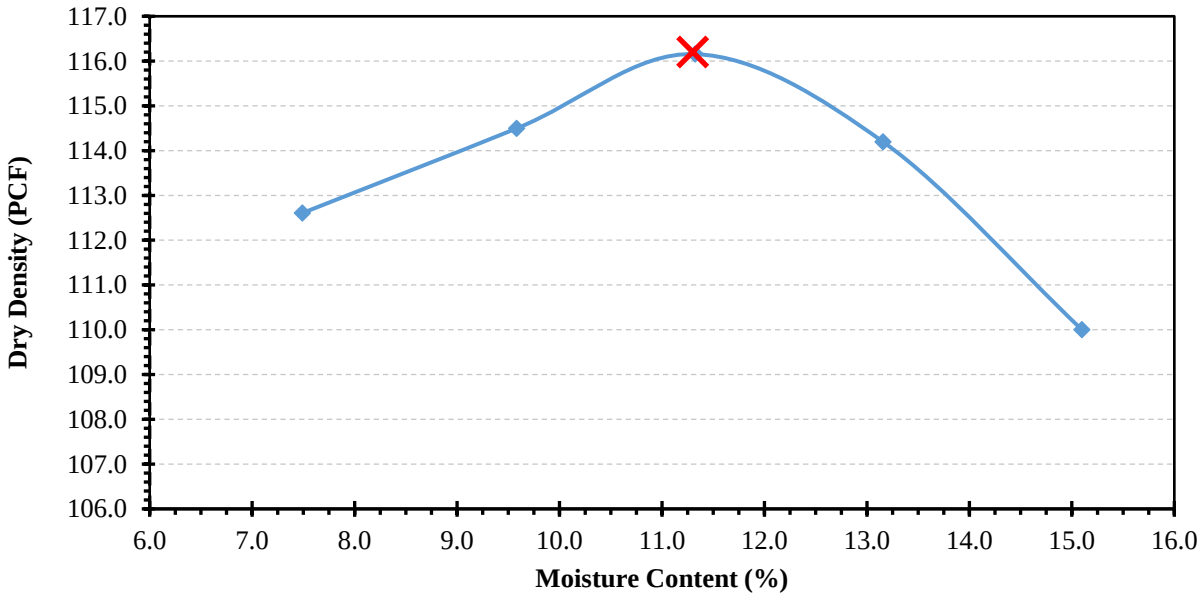

Figure 4.10 Optimum Moisture Content Graph for Silty-Sand with 5.1% Portland Cement.

Table 4.9 Mixture Properties of Base Material for Stabilized Foundation Section (S2)

Soil Property	Base (dirty sand)
Liquid Limit	---
Plastic Limit	---
Plasticity Index	Non-Plastic
% Passing No. 4	100
% Passing No. 10	99
% Passing No. 40	91
% Passing No. 60	72
% Passing No. 200	16
AASHTO T88 % Silt	7
AASHTO T88 % Clay	8
AASHTO M145 Classification	A2-4
ASTM D2487 Classification	SM
Untreated Max γ_d (g/cm^3)[a]	1.76
Untreated OMC (%)[a]	13
Design L_w or C_w[b]	5.1
Treated Max γ_d (g/cm^3)[c]	1.83
Treated OMC (%)[c]	13

Similar to lime treated samples, soil-cement samples were taken from each location (shown in Figure 4.9) to fabricate samples of size 3x6 and 4x8 according to AASHTO PP92-19. UCS of soil-cement materials (with no soaking period) was obtained according to ASTM D1633 in addition to their elastic modulus (E) following the ASTM C469 after 7, 14, 28, 180 days of curing. Although the Mississippi DOT designed UCS to meet the minimum of 300 psi after 14 days of curing using Proctor specimens, the PM samples are expected to achieve an UCS 10% less than proctor specimens; and therefore the expected UCS for PM device samples was decreased to 270 psi. Table 4.10 summarizes the results obtained from the Test Track locations. Table 4.10 and Figure 4.11 show the UCS results that are ranged from 97 to 221 psi with an overall average of 159 psi and COV of 23% for field samples.

Table 4.10 Stabilized Foundation Base Layer Results (Obtained From *(Sullivan, 2021)*)

Station	Specimen Type	γ_{dry} (pcf)	t_{test} (day)	UCS (psi)	E (ksi)	Station	Specimen Type	γ_{dry} (pcf)	t_{test} (day)	UCS (psi)	E (ksi)
25	PM3x6[5]	106.3	28	221	---	100	PM4x8[9]	110.9	7	121	---
33	PM3x6[5]	109.2	28	219	468	100	PM4x8[9]	110.9	7	130	329
41	PM3x6[5]	106.8	28	196	380	100	PM4x8[9]	110.8	7	120	182
50	PM3x6[5]	104.8	28	215	---	100	PM4x8[9]	110.6	28	163	---
58	PM3x6[5]	106.7	28	126	223	100	PM4x8[9]	111.3	28	155	301
66	PM3x6[5]	109.7	28	204	454	100	PM4x8[9]	110.5	28	133	283
75	PM3x6[5]	109.1	28	111	---	100	PM4x8[9]	109.6	180	200	---
83	PM3x6[5]	109.6	28	119	201	100	PM4x8[9]	109.6	180	247	859
91	PM3x6[5]	107.6	28	113	182	100	PM4x8[9]	108.7	180	196	438
100	PM3x6[5]	111.2	7	149	---	108	PM3x6[5]	107.8	28	146	564
100	PM3x6[5]	111.8	7	149	267	116	PM3x6[5]	107.6	28	169	330
100	PM3x6[5]	112.0	7	134	245	125	PM3x6[5]	108.0	28	183	---
100	PM3x6[5]	111.3	14	121	---	133	PM3x6[5]	108.4	28	132	216
100	PM3x6[5]	111.3	14	146	257	141	PM3x6[5]	108.8	28	127	260
100	PM3x6[5]	111.7	14	136	353	150	PM3x6[5]	109.3	28	168	---
100	PM3x6[5]	110.5	28	190	---	158	PM3x6[5]	106.8	28	97	349
100	PM3x6[5]	111.0	28	166	289	166	PM3x6[5]	108.3	28	106	251
100	PM3x6[5]	110.3	28	174	456	175	PM3x6[5]	108.9	28	189	---
100	PM3x6[5]	111.0	180	204	---						
100	PM3x6[5]	108.0	180	161	425						
100	PM3x6[5]	107.3	180	188	324						
100	PM3x6[5]	108.1	180	190	367						

Note: γ_{dry}=dry density; t_{test}=test time; ---=no data collected. PM3x6 were compacted by 5 blows while PM4x8 were compacted by 9 blows. Optimum moisture content was 13% for all samples.

At station 100, three PM3x6 and three PM4x8 samples were averaged to yield the value of 164 psi (shown in Figure 4.11). After 28 days of curing, all samples were below the expected design value of 270 psi which is shown by the red line in Figure 4.11. Lower values could be attributed to sample densities, construction factors, and sampling locations *(Sullivan, 2021)*. Figure 4.12 shows the UCS for station 100 over a range of testing times. For PM3x6 samples, compressive strength was the same for 7 and 14 days of curing and increased by 30 psi at 28 days and remained constant at 180 days. For the PM4x8 samples, the UCS increased gradually for different curing days. However, all samples were below the expected 270 psi UCS.

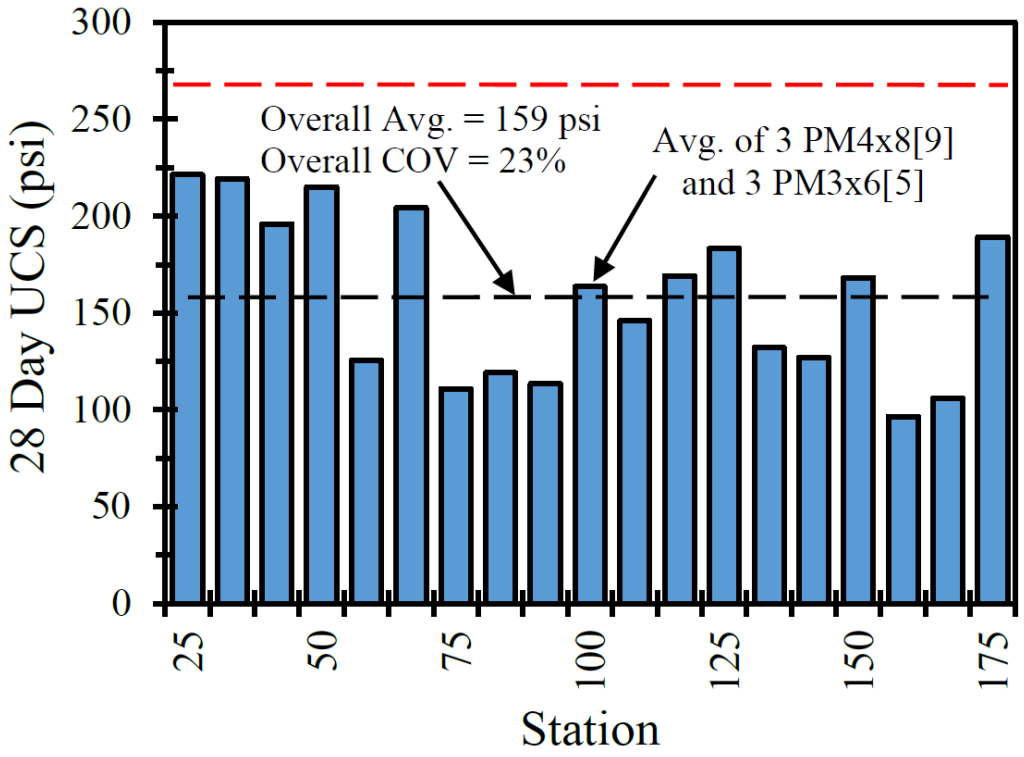

Figure 4.11 Unconfined Compressive Strength across all Stations at 28 days Obtained from *(Sullivan, 2021).*

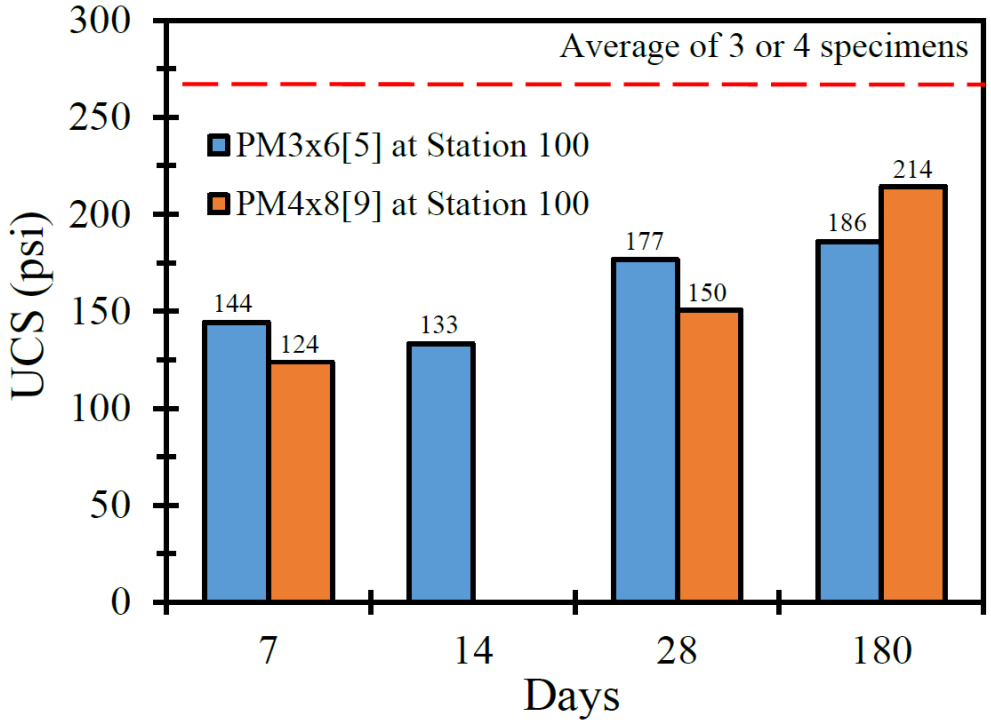

Figure 4.12 Unconfined Compressive Strength at Station 100 Over Time, Obtained from *(Sullivan, 2021).*

Figure 4.13 shows the relationship between elastic modulus and UCS for field samples. The data points were plotted between lines E=1200*UCS and E=4500*UCS with overall trend of E=2247*UCS. The average value for the field samples tested in the laboratory was 482.4 ksi with standard deviation of 215 ksi for samples cured for 180 days. Similar to LTS material, the laboratory fabricated, and tested samples had higher modulus and less variability. For laboratory fabricated samples cured for 180 days or 360 days, the average value obtained 1012.56 ksi with standard deviation of 294.56 ksi.

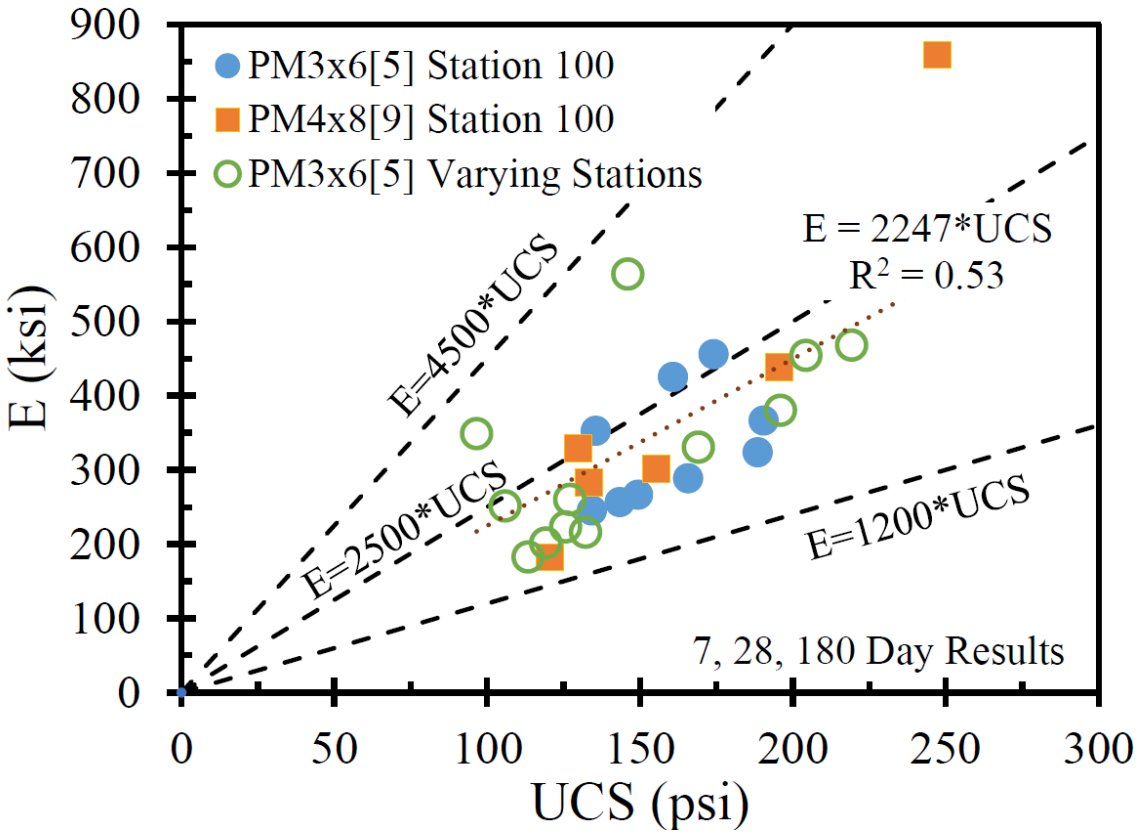

Figure 4.13 Relationship between UCS and Elastic Modulus for Stabilized Foundation Section (Obtained from *(Sullivan, 2021)*).

In summary, it was found that the dynamic modulus of the AC materials for the stabilized foundation section (S2) was higher compared to the thick-lift section (S9). Less tolerance to fatigue

cracking was also observed for the stabilized foundation section with better resistance to rutting. The field fabricated lab tested samples for LTS and CTB showed lower elastic modulus compared to lab fabricated lab tested samples. The curing was found to be effective for both stabilized layers even after 360 days of curing. The results indicated that laboratory elastic modulus for lime treated material had the expected value of 366.6 ksi for lab fabricated samples while this value for cement treated layer was about 3 times higher and at around 1012.56 ksi. Field modulus obtained through non-destructive testing will be discussed in Chapter 8, in which a comparison will be made between laboratory and backcalculated moduli of all materials. Chapter 5 provides a detailed discussion about the strain and stress responses of each pavement section.

CHAPTER 5

FIELD PERFORMANCE AND RESPONSE MEASUREMENTS

The NCAT Test Track is an accelerated pavement testing facility which produces 10 million ESALs within two years of truck trafficking. During the trafficking period, the performance of the test sections are evaluated with a diverse set of surface measurements. Additionally, the in situ responses of the structural sections are routinely measured using embedded stress and strain gauges and FWD testing. This chapter discusses the trafficking program along with the field performance of four pavement sections (S2, S9, S12, and N4) obtained from surface quality measurements and in-depth stress and strain measurements. As mentioned earlier in Chapter 3, while the stabilized foundation (S2) and the thick-lift (S9) pavement sections were built in 2018, the CCPR (N4) and the CCPR with stabilized foundation (S12) pavement sections were part of the 2012 research cycle that continued into the 2018 research cycle. The following section discusses trafficking program of 2018 research cycle as that was the main focus of this study. Further details on trafficking of previous research cycles can be found in *(Diaz, 2019)*. After discussion trafficking, field performance and structural pavement responses are presented.

5.1. Trafficking Program

Trafficking in the 2018 experiment was similar to previous research cycles where five triple flat-bed trailer trucks (Figure 5.1) circled the 1.7-mile oval Test Track in two separate shifts from 5:00 AM to 10:40 PM., Tuesday through Saturday. The trafficking began on November 26, 2018, and

ended February 27, 2021. The total traffic applied during 2018 research cycle was 10 Million ESALs.

During the test cycle, traffic operations were suspended on Mondays to conduct pavement surface studies as well as FWD testing. The primary surface performance measures were rutting, cracking, texture, and roughness. Rutting and International Roughness Index (IRI) were determined using the Dynatest Mark III profiler bar mounted on ARAN van (Figure 5.2). Crack mapping was conducted monthly with an in-house video system and unlike previous research cycles, the cracks were not highlighted with a paint pen in the field before obtaining video records.

In addition to surface measurements, the structural health of the sections was monitored on weekly basis under truck loading. Table 5.1 shows the type and frequency of the data collection activities. The structural and surface measurements of the four pavement sections (S2, S9, S12, N4) are further discussed below.

Figure 5.1 Triple-Trailer Truck Used for Accelerated Loading on the Test Track.

Figure 5.2 Profiler Used to Assess Ride Quality and Rutting Measurement

Table 5.1 NCAT Test Track Pavement Monitoring Plan

Activity	Sections	Frequency	Methods
Rut depth	all	weekly	Dynatest Mark III profiler bar, AASHTO R 48
Mean texture depth	all	weekly	Dynatest Mark III profiler bar, ASTM E1845
Mean texture depth	select	quarterly	CTM, ASTM E2157-09
International Roughness Index	all	weekly	ASTM E950, AASHTO R 43
Crack mapping	sponsored	Monthly	In-house video system
FWD	structured	3 times/mo.	AASHTO T 256-01
Stress/strain response to live traffic	structured	weekly	NCAT method
Pavement temperature at four depths	all	hourly	Campbell Sci. 108 thermistors
Pavement reflectivity/albedo	sponsored	quarterly	ASTM E 1918-06
Field permeability	OGFC/PFCs	quarterly	NCAT method
Core density	sponsored	quarterly	ASTM D979, AASHTO T 166
Friction	all	monthly	ASTM E274, AASHTO T 242
Friction	select	quarterly	DFT, ASTM E1911
Tire-pavement noise	all	quarterly	OBSI, AASHTO TP 76-11, CPX, ISO 11819-2, Absorption, ASTM E 1050-10

5.2. International Roughness Index

IRI was measured weekly for all sections using a Dynatest Mark III profiler. Figure 5.3 shows the IRI results over time for the stabilized foundation section (S2) and the thick-lift (S9) pavement sections that were built in 2018. Both measurements indicate no appreciable change in IRI values

in 2018 research cycle. In general, the stabilized foundation pavement (S2) had lower IRI values than the thick-lift section (S9) that could be attributed to difficulties in constructing the thick-lift pavement section. The stabilized foundation (S2) IRI measurements became slightly more stable with less scatter over time due to the application of traffic load. Also, there is a slight increase in IRI over time for this section.

Since the thick-lift (S9) AC layer was constructed in one lift (eight inches thick), it was determined that although the pavement did achieve adequate density, it had issues with smoothness *(McCarty, 2020)*. Based on past experience with this issue, the South Carolina DOT suggested diamond grinding to remedy the roughness issue. The diamond grinding reduced the initial roughness from 396.4 in/mile to around 100 in/mile. Because of the thick lift application, this section had higher as-built roughness compared to the stabilized foundation pavement (S2). However, both sections performed satisfactorily after experiencing 10 million ESALs. The IRI values for the CCPR (N4) and CCPR with stabilized foundation (S12) sections are not provided in this document but both sections had good roughness performance. Interested readers may refer to *(Diaz, 2019)* for more details.

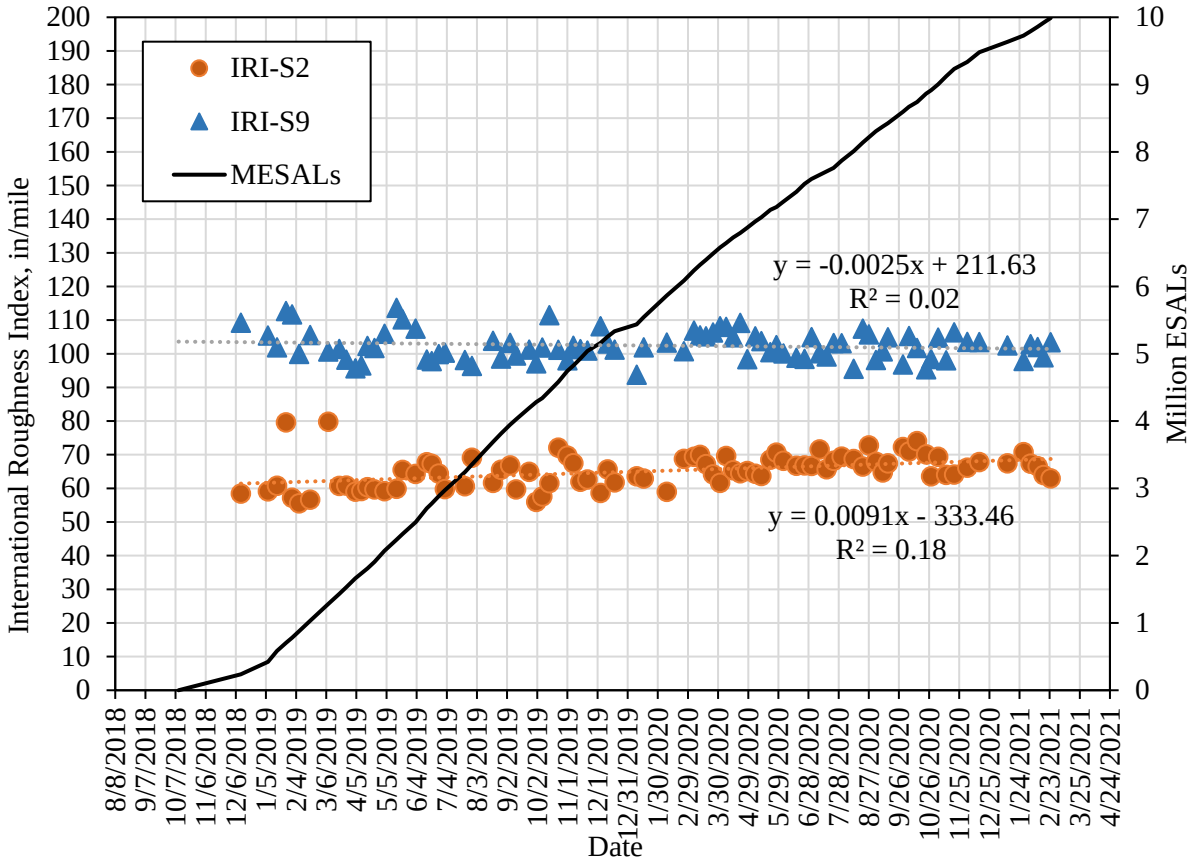

Figure 5.3 IRI Performance for the Thick-lift (S9) and the Stabilized Foundation (S2) Sections.

5.3. **Rutting Performance**

Figure 5.4 shows the rutting performance of the stabilized foundation (S2) and the thick-lift (S9) pavement sections. As shown, the rutting increased during the first warm season and then leveled off for both sections. There is an increase in rut depth of both sections toward the very end of the research cycle which is due to the change in data acquisition system and not the change in pavement rutting itself. The rutting measurements remained constant below 0.25 inches in general. The initial increase in rut depth could be explained by further compaction of the material in the early trafficking phase. The plateau behavior indicates that both sections were structurally stable with good rutting performance. Both IRI and rutting results met the construction standard specification for their state DOTs. In addition, the CCPR (N4) and CCPR with stabilized

foundation (S12) sections also performed satisfactorily in terms of rutting but their data is not shown in this document for brevity.

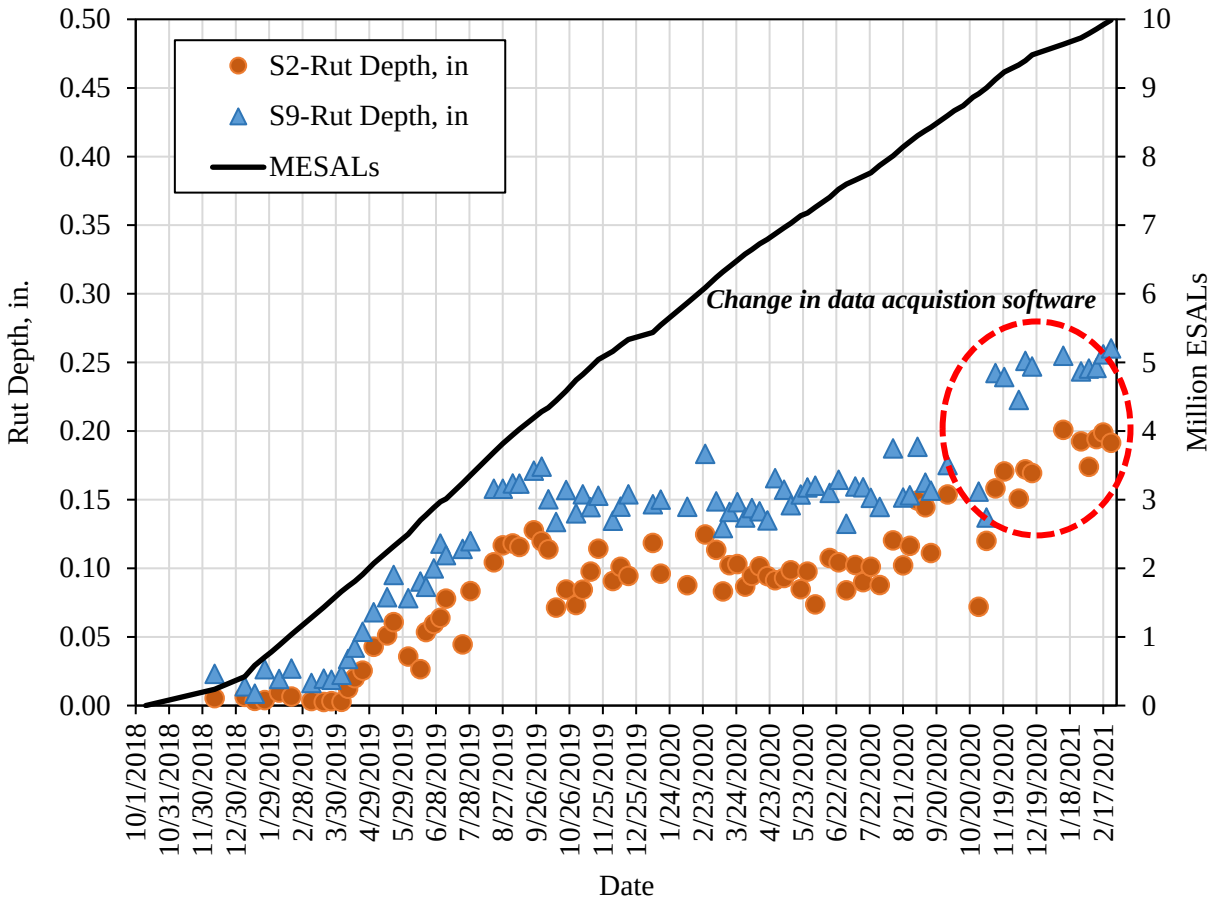

Figure 5.4 Rutting Performance of the Stabilized Foundation (S2) and Thick Lift (S9) Pavement Sections.

5.4. **Cracking Performance**

On weekly basis, the pavement sections were inspected to find cracks at the surface of the test sections. The stabilized foundation (S2) and the thick-lift (S9) pavement sections experienced about 10 Million ESALs by the end of 2018 research cycle and showed no signs of major cracking at the pavement surface. The stabilized foundation (S2) section had a few popouts in the surface. The popouts appears normally in rigid pavements but they can form in flexible pavements due to expansive aggregates, lack of adequate adhesion, or high stiffness of the binder. In Chapter 4, it

was shown that the asphalt material for this section is comparatively stiffer. In addition, the binder content of the field samples was determined to be smaller than the binder content defined in the mix design process. These factors can contribute to few popouts of this section. Some of the popouts were larger than others, but none of them was deemed to adversely affect the pavement performance. Figure 5.5 shows the surface of the stabilized foundation section (S2) and two of the popouts. A small amount of cracking was seen in the thick-lift section (S9), first observed in mid-December 2020 after approximately 9.4 million ESALs. The hairline cracks were aligned in the direction of travel and were at the edges of the wheelpath. At the end of trafficking, the cracking represented a total of 0.7% of the lane area or 1.1% of the wheelpath area. Figure 5.6 shows the surface of the thick-lift pavement section (S9) and a crack that appeared on this section. In general, regardless of the minor defects on the stabilized foundation (S2) and the thick-lift (S9) sections, they performed satisfactorily in 2018 research cycle.

Figure 5.5 The Surface of the Stabilized Foundation (S2). (a) Pavement Section Surface View, (b) & (c) Local Defects (Date Taken: 02/07/2021).

Figure 5.6 The Surface of Section S9. (a) Pavement Section Surface View, (b) Visible Cracks at S9 (Date Taken: 02/07/2021).

The CCPR sections (N4 and S12) originally built in 2012 experienced a total of about 30 Million ESALs by the end of 2018. Both sections exceeded the original ESALs designs with no visible cracking in the first two research cycles. The CCPR with stabilized foundation (S12) pavement section showed no signs of visible cracks by the end of 2018 research cycle. Figure 5.7 shows the surface of the CCPR with stabilized foundation (S12) pavement section.

Figure 5.7 The Surface of the CCPR with stabilized foundation Section (S12). (a) Pavement Section Surface View, (b) A Random Location at S12 (Date Taken: 02/07/2021).

Minor cracking (low severity) was observed in the CCPR section (N4) near the end of the third test cycle on January 25, 2021 after the application of 29.6 million ESALs. The cracking was confined to the outside wheelpath, was primarily transverse to the direction of travel (though there were some interconnecting longitudinal cracks), and was spread evenly along the length of the section. The cracks were relatively tight and there was no evidence of pumping or fines at the surface. Subsequent inspections on later dates revealed much less cracking, which did not appear to progress or worsen during the last 400,000 ESAL applications. As of February 15, 2021 (29.9 million ESALs) there was 0.5% of the lane area cracked and 0.1% of the wheelpath area cracked as determined from inspection of high-resolution crack mapping images. The severity and extent of cracks did not consider to have a major impact on the CCPR (N4) performance. This pavement section continued to perform satisfactorily in the last two months of 2018 research cycle. Figure 5.8 and Figure 5.9 show the section surface view and two sample images of the cracks at the surface of the CCPR section (N4) along with enhanced photos to aid the detection of the cracks.

Figure 5.8 The View of the CCPR (N4) Surface Pavement Section (Date Taken: 01/25/2021).

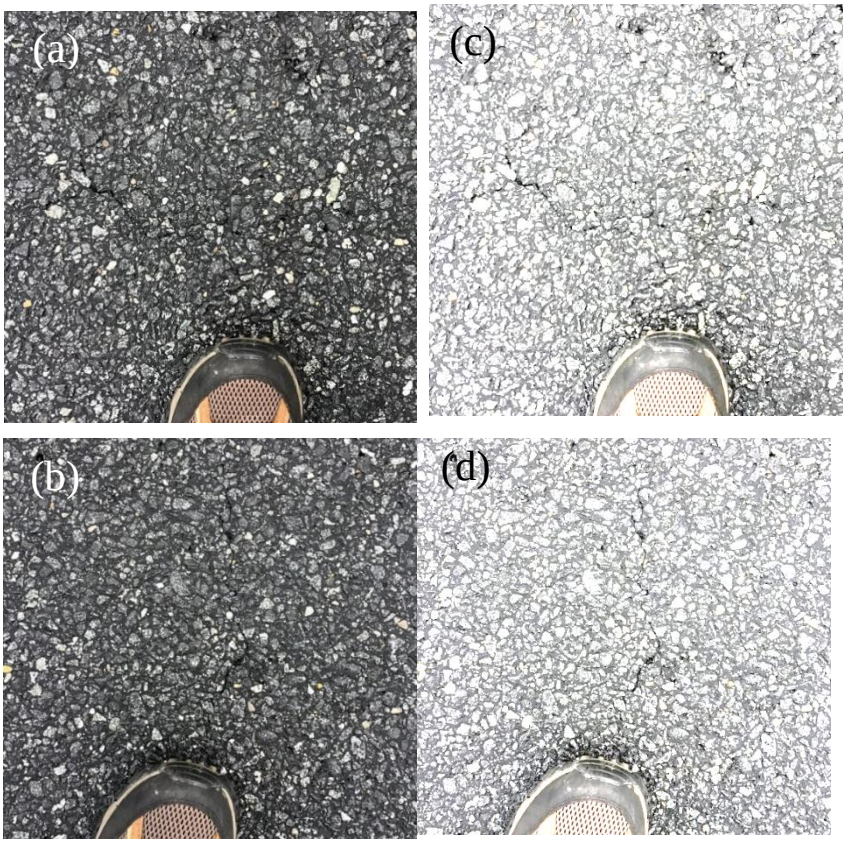

Figure 5.9 The Surface of the CCPR (N4) Pavement Section. (a) & (b) Surface Cracks at N4, (c) & (d) Enhanced Photo of the Surface Cracks (Date Taken: 01/25/2021).

5.4.1. Structural Pavement Response

One of the main objectives of this study was to explore the fundamental assumptions that governs the structural design of stabilized foundation pavement sections. This was partly accomplished through direct field stress/strain measurements under truck traffic and FWD loading. This section compares and contrasts the stabilized foundation (S2) section structural response with the other three pavement sections at the Test Track.

5.4.2. Individual Truck Response

Figure 5.10 and Figure 5.11 illustrate measured responses for the stabilized foundation (S2) and the thick-lift (S9) pavement sections, respectively, under the standard eight-axle triple-trailer truck

at the Test Track for specific stress and strain sensors. In the figures, the steering axle event is the first significant spike on the left followed by the drive tandem axle and 5 trailing single axles. The effect of temperature on vertical stress readings for both sections is shown in Figure 5.10 where the response clearly increased due to temperature rise in the summer. It can be seen that the magnitude of the stress response is somewhat similar between the two sections regardless of their differences in material, structure, and pavement temperature. Winter strain response for both sections (Figure 5.11) followed the same behavior where the strain response magnitude was fairly similar in both sections. In addition, the strain at the AC bottom was in tension for both sections, as expected, and in agreement with conventional mechanistic-empirical analysis. While strain results are presented only for specific sensors for the sake of brevity, other sensors had very similar behavior. Also, all strain gauges at the bottom of AC were longitudinal (parallel to traffic) since previous NCAT studies had shown that longitudinal strains were about 36% higher than transverse strain measurements *(West et al., 2019)*.

In the summer, the strain response for the thick-lift section (S9) increased due to increased temperature. This observation matched other flexible pavement behavior at the Test Track *(Tran et al., 2015)*. It also confirmed the well-stablished premise that the strain at the bottom of AC experiences tension, and the response magnitude increase with the increase in temperature (causing a reduction in AC modulus).

In contrast, the stabilized foundation section (S2) exhibited a fundamentally different strain response from that of the thick lift section (S9) and other flexible pavements. Counterintuitively, the strain response magnitude decreased in the summer and the strain switched to predominantly compression. The compressive strain response at the bottom of AC contradicts the well-established premise that the bottom of AC is in tension. This interesting behavior suggests that stabilized

foundation pavement sections can behave fundamentally differently than other conventional flexible pavements. This behavior was observed with repeated measurements and from all working strain gauges at elevated pavement temperatures (> 80 °F), which eliminated the possibility of observing abnormal behavior or sensor error, but rather indicated the fundamental behavior of this section.

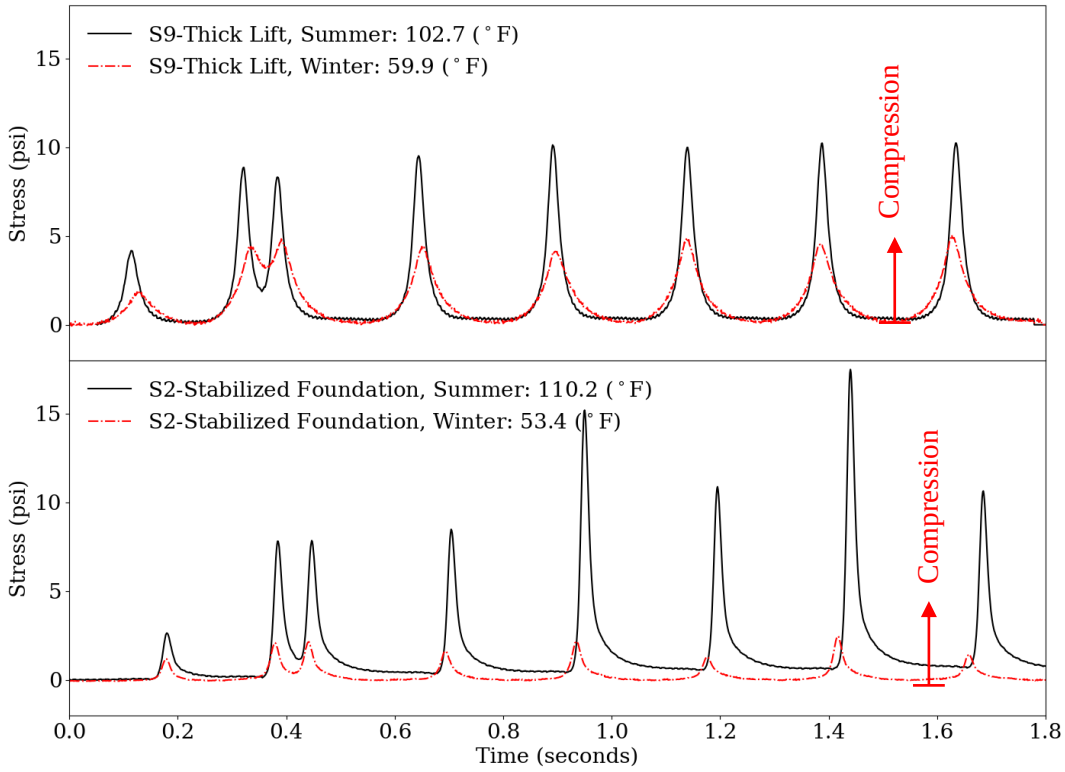

Figure 5.10 Measured Stress Events under Truck Loading for Sections S2 and S9.

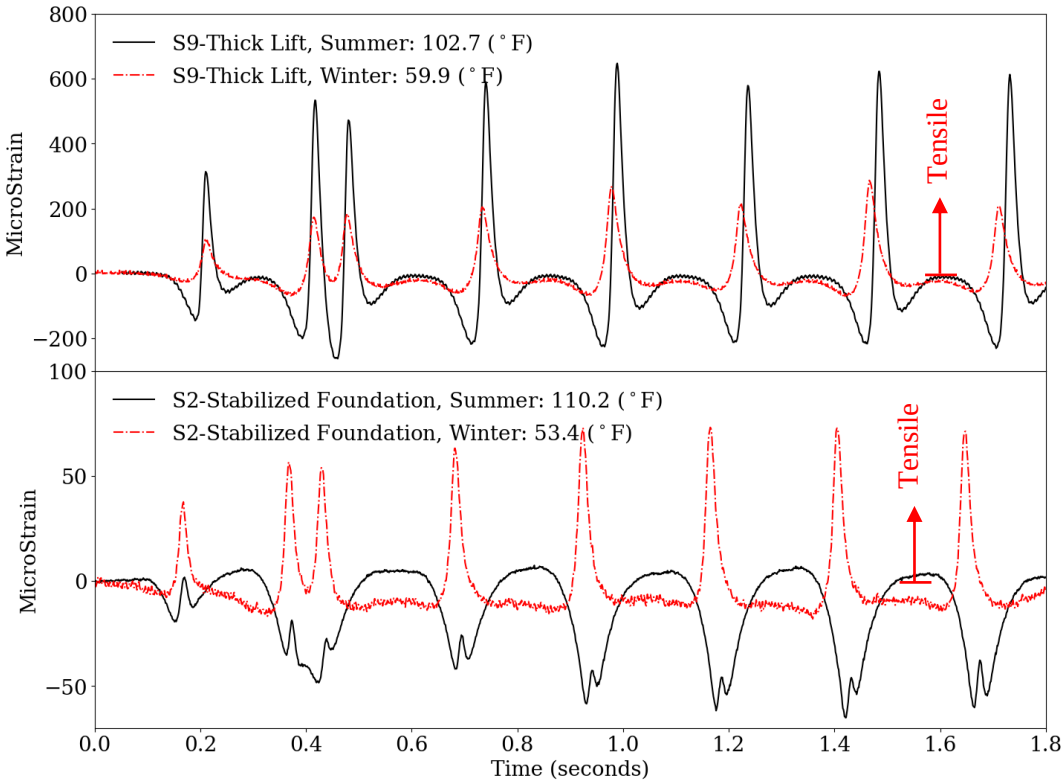

Figure 5.11 Measured Strain Events under Truck Loading for Sections S2 and S9.

Since the behavior of the stabilized foundation (S2) section was not expected and contradicted the common premise that the maximum tensile strain occurs at the bottom of AC layer, further investigation was conducted on individual truck loading for the CCPR (N4) and CCPR with stabilized foundation (S12) sections. Again, the CCPR with stabilized foundation section (S12) featured a cement stabilized layer while the CCPR section (N4) placed on top of crushed granite materials. Figure 5.12 and Figure 5.13 show the pavement stress and strain responses under individual truck loading, respectively. In the figures, the steering axles, drive tandem axles, and 5 trailing axles are presented as individual spikes in the sensor baselines. Similar to the stabilized foundation (S2) and the thick-lift pavement (S9) sections, the CCPR sections (N4 and S12) showed a decreased in stress response as the temperature dropped from summer to winter

(Figure 5.12). However, the drop in stress response for the CCPR with stabilized foundation (S12) was more pronounced which closely followed the behavior of the other stabilized section (S2). The reduction in pavement response is related to the increase in AC modulus at lower temperatures.

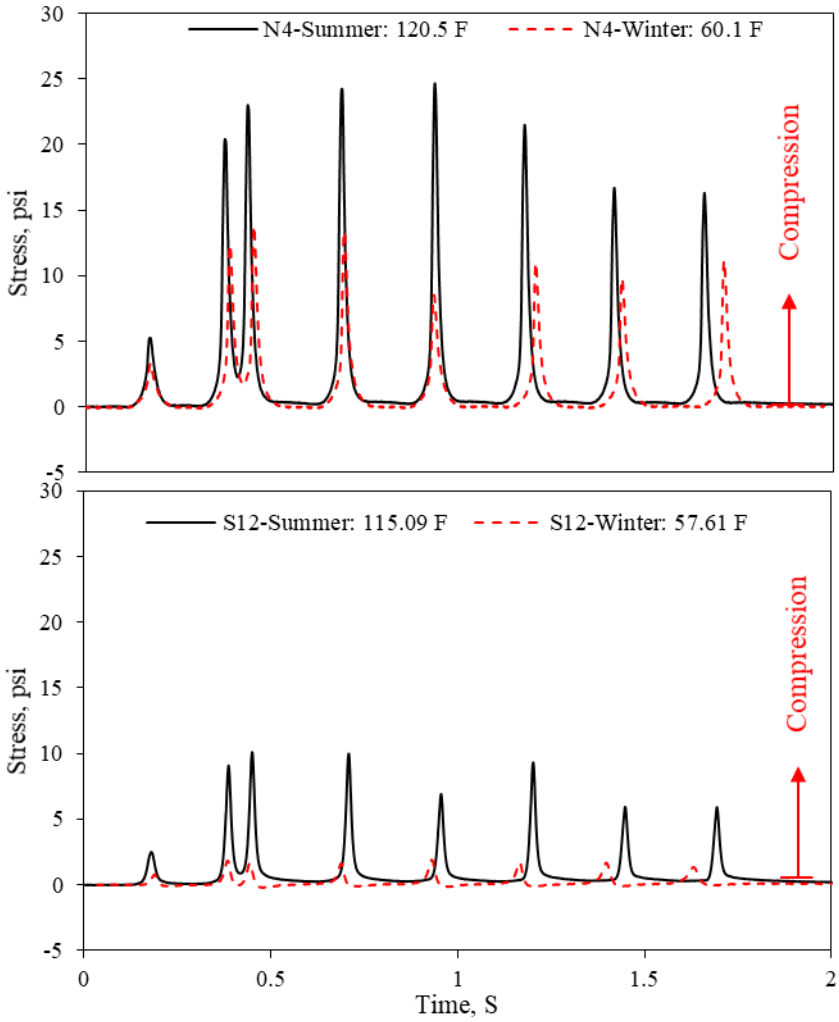

Figure 5.12 Measured Stress Events under Truck Loading for CCPR (N4) and CCPR with stabilized foundation (S12) Sections.

Figure 5.13 illustrates the strain response for the CCPR sections (N4 and S12) under dynamic truck loading. The response for both sections reduced as the temperature dropped due to stiffening effect of asphalt concrete layer. However, the drop in strain response from summer to

winter was more pronounced for the CCPR section (N4) compared to the stabilized foundation section (S12). Unlike the other stabilized section (S2) in which the strain response in warm seasons unexpectedly flipped into predominantly compressive strain (Figure 5.11), the response for the CCPR with stabilized foundation section (S12) remained predominantly tensile regardless of pavement temperature. For thick-lift (S9), CCPR with stabilized foundation (S12), and CCPR (N4) sections' summer responses, the flexible pavements squeezed into compression as the moving load approached the sensors, followed by a predominantly tensile peak when the axle was on top of the strain sensor, followed by compression again as the axle passed the sensor. The stabilized foundation pavement (S2) behaved exactly similar to other sections but with a reversed sign in the summer. The shape of the winter response of the two non-stabilized sections (N4 and S9) was similar to their summer response where the pavements went into compression, followed by tension, and then compression as a truck approached and passed the sensors. Likewise, the CCPR with stabilized foundation section (S12) squeezed into compression followed by a predominantly tensile strain peak; however, in winter the strain sensor did not experience a compression mode as the truck left the sensor and the latter portion of the signal for each axle gradually transitioned to the baseline (Figure 5.13). The reason for the different behavior in the CCPR with stabilized foundation is not clear but could be attributed to different viscoelastic response of this section. In general, compared to other pavement sections, the stabilized foundation pavement (S2) had more symmetric strain response in winter for each axle load suggesting a more elastic behavior.

In summary, the strain response for the stabilized foundation pavement (S2) contradicted the existing premise that the bottom of AC layer always experiences tension. The reason that this section did behave differently than other sections will be further discussed in the rest of this dissertation.

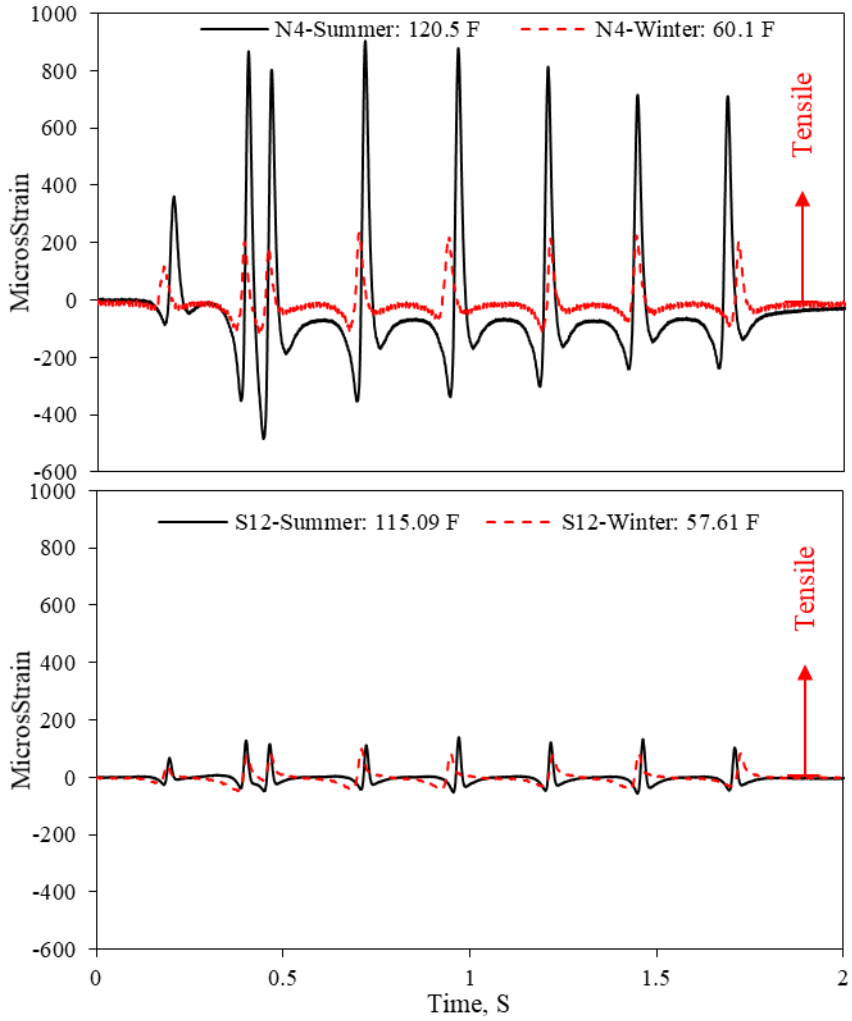

Figure 5.13 Strain Events under Truck Loading for the CCPR (N4) and CCPR with stabilized foundation (S12) sections.

5.4.3. Direct Sensor Responses under FWD Measurements

Since the behavior of the stabilized foundation pavement (S2) was inconsistent with the current state-of-the-practice and common understanding of M-E analysis, in which the bottom of AC is assumed to be in tension, further investigation was made with FWD testing. In this investigation, FWD tests were conducted directly on top of all embedded strain and stress gauges for pavement sections on five different dates (shown in Table 5.2) to capture different range of temperatures.

Table 5.2 FWD Experiment on Stress/Strain Gauges

Date	Section	Mid-depth Temperature Range
March 02, 2020	S2	50-60 °F
May 04, 2020	S2	90-110 °F
May 18, 2020	S2, S9	85-95 °F
July 20, 2020	S2, S9, N4, S12	100-120 °F
February 01, 2021	S2, S9, N4, S12	50-60 °F

The vertical surface deflections were recorded by 9 geophones mounted on the FWD device while in situ strain/stress responses were measured simultaneously by embedded strain/stress sensors. In this chapter, the results for the last two dates of FWD testing on top of gauges are provided for the sake of brevity which represent warm and cold weather. The results from all dates were consistent with the presented results and are not provided in this document. For the last two dates (July 20, 2020, and February 01, 2021), three replicates of the 12-kip FWD load level were generated on each sensor and surface deflections were recorded while in-depth strain/stress responses were obtained from embedded instrumentation. This process was repeated for each working sensor in each section.

Figure 5.14 illustrates the stress and strain responses under FWD loading for the stabilized foundation pavement (S2) for summer and winter responses. Although three replicates were used at each test location, Figure 5.14 only depicts the results for one replicate of the 12-kip load event. In this figure, the first FWD load drop is clearly identifiable which is followed by a sequence of load resonance that is captured by the pavement sensors. The strain in the winter is dominantly in tension at the bottom of AC (Figure 5.14c) while the stress response is largely in compression (Figure 5.14a). The stress response increased in the summer significantly which was expected since the AC modulus reduces as temperature increases. This again confirms the general premise in pavement sections that the bottom of AC should be in tension and decrease in modulus should

increase the pavement response. On the other hand, the strain response in the summer (Figure 5.14d) was not expected since the strain gauge at the bottom of AC recorded dominantly compressive horizontal strain. This interesting observation contradicted the normal assumption that the bottom of AC should experience horizontal tensile strain but was consistent with measurements made under truck loading depicted in Figure 5.11. Although Figure 5.14 provides only the response of strain gauge 11 (S2-11 in the figure), all other measurements on different strain gauges followed the same trend in which the strain at the bottom of AC layer was observed to be in compression.

To investigate the stabilized foundation (S2) section's interesting behavior, similar FWD testing was conducted on the same dates on the thick lift section (S9), the CCPR with stabilized foundation (S12) section, and the CCPR section (N4). The thick-lift (S9) and the CCPR (N4) sections were built on top of non-stabilized base layers while the other two sections featured a stabilized base layer. Figure 5.15, Figure 5.16, and Figure 5.17 show the summer and winter stress and strain responses of the CCPR with stabilized foundation (S12), the thick-lift (S9), and the CCPR (N4) sections under FWD loading, respectively. The stress response for these three sections mimicked the stabilized foundation (S2) stress response but with slightly smaller or larger magnitudes. Among all sections, the CCPR with stabilized foundation section (S12) had lowest stress measurements both in summer and winter. Also, the stress response for the stabilized foundation section (S2) was slightly higher than the thick-lift section. However, in general, the response for all sections were similar.

Conversely, the strain response at the bottom of AC layer under 12-kip loading were significantly different among sections. In winter, the stabilized foundation pavement (S2) had the lowest tensile strain followed by the CCPR with stabilized foundation (S12) section. This further

demonstrates effectiveness of stabilized pavement sections to reduce tensile strain at the bottom of AC layer. The two non-stabilized sections, the thick-lift (S9) and the CCPR (N4) sections, had about six- and ten-times higher magnitude in tensile strain levels in winter compared with the stabilized foundation pavement (S2). Higher stiffness provided by the stabilized base foundation was the main reason for observing smaller strain response in winter.

In summer, the non-stabilized sections (N4 and S9) had also higher tensile strain readings and, as explained earlier, the stabilized foundation (S2) pavement response flipped into a predominantly compressive mode. The data presented in Figure 5.14 through Figure 5.17 is summarized in Table 5.3 where the peak value of stress and strain responses for summer and winter responses are presented. This table clearly shows that the stabilized foundation pavement (S2) did not follow the behavior of other pavement sections in the summer. However, the other three sections followed the well-stablished premise that the strain at the bottom of AC is in tension. Based on individual truck and FWD loading, it was found that although both stabilized foundation section (S2) and the CCPR with stabilized foundation section (S12) featured a cement treated layer, their behavior could be different. In particular, the behavior of the CCPR with stabilized foundation section (S12) resembled the flexible pavements more due to tensile strain at the bottom of AC layer, while the stabilized foundation section (S2) had a flipped response in the summer. The reason for S2's behavior was higher stiffness of the base materials compared to S12 that will be explained thoroughly on Chapter 7.

In general, the similarity in stress response magnitude and the big difference in horizontal strain at the bottom of AC suggests that stabilized foundation pavement sections could outperform flexible pavements based on bottom-up fatigue criterion. But what if the maximum tensile strain occurs somewhere other than the bottom of AC in stabilized foundation pavements? To answer this question, further investigation was conducted which is presented in the rest of this dissertation.

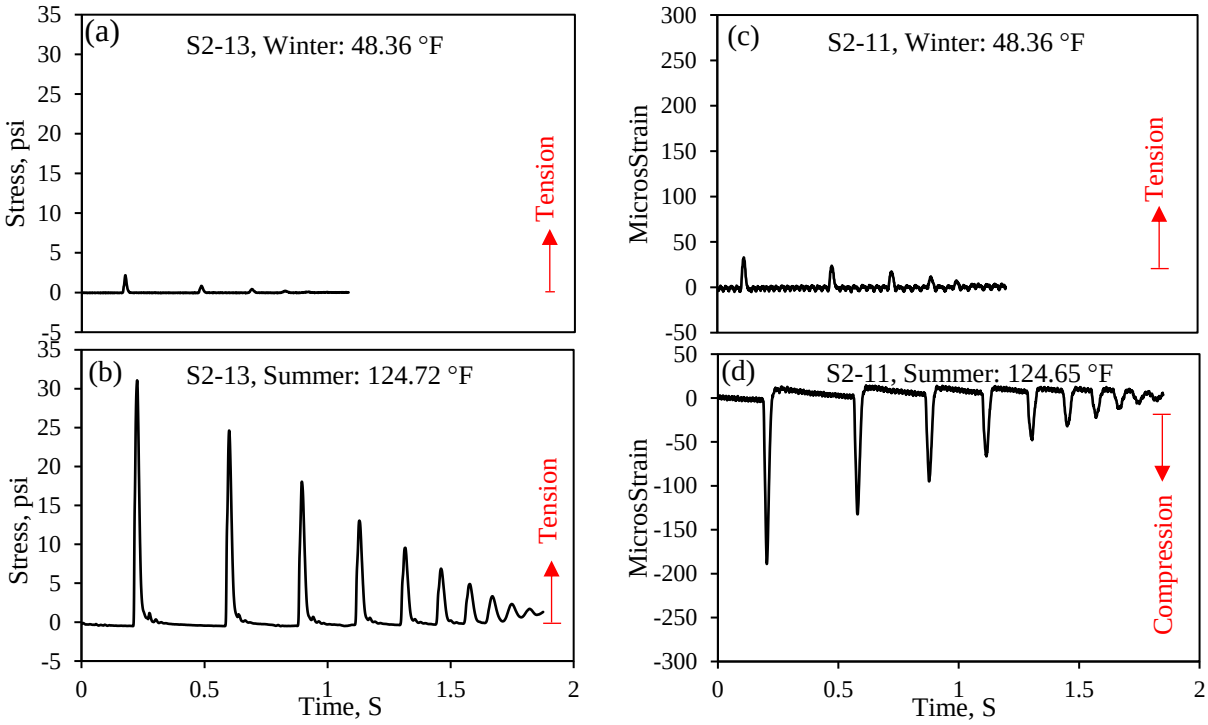

Figure 5.14 Measured Responses under FWD Loading for the Stabilized Foundation Section (S2). (a), (b) stress responses in winter and summer; (c), (d) strain responses in winter and summer.

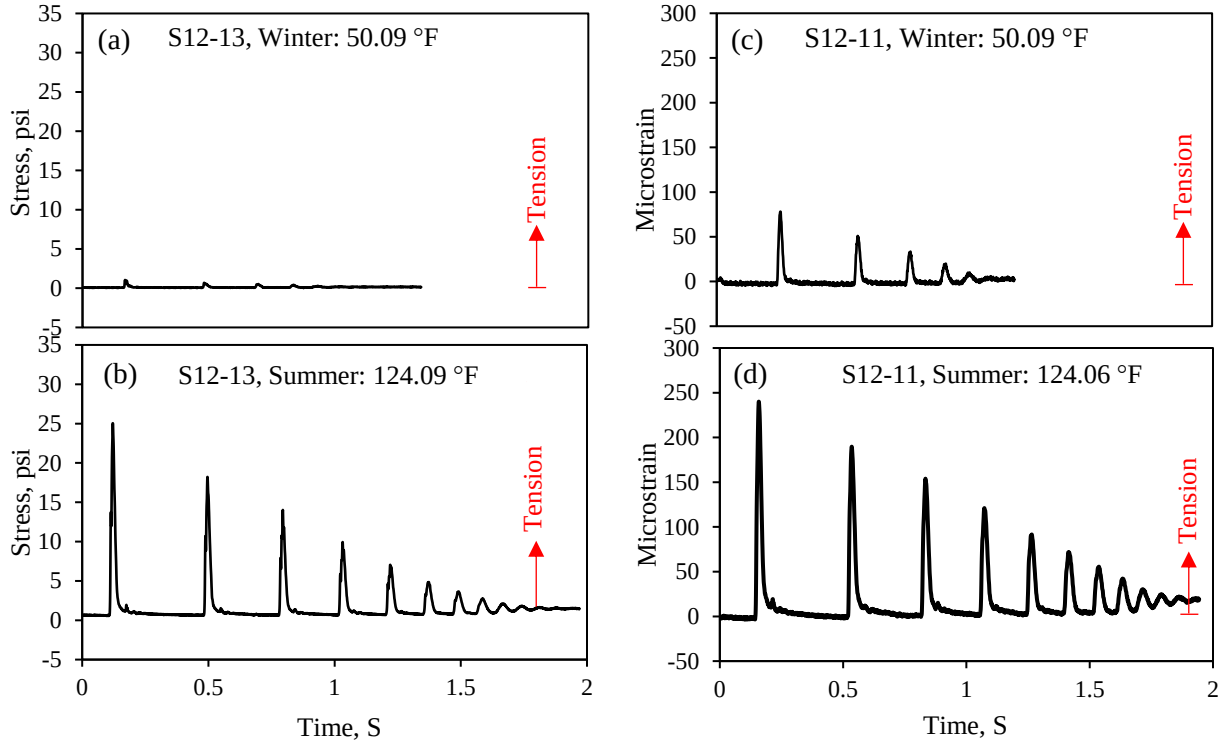

Figure 5.15 Measured Responses under FWD Loading for CCPR with stabilized foundation Section (S12). (a), (b) Stress Responses in Winter and Summer; (c), (d) Strain Responses in Winter and Summer.

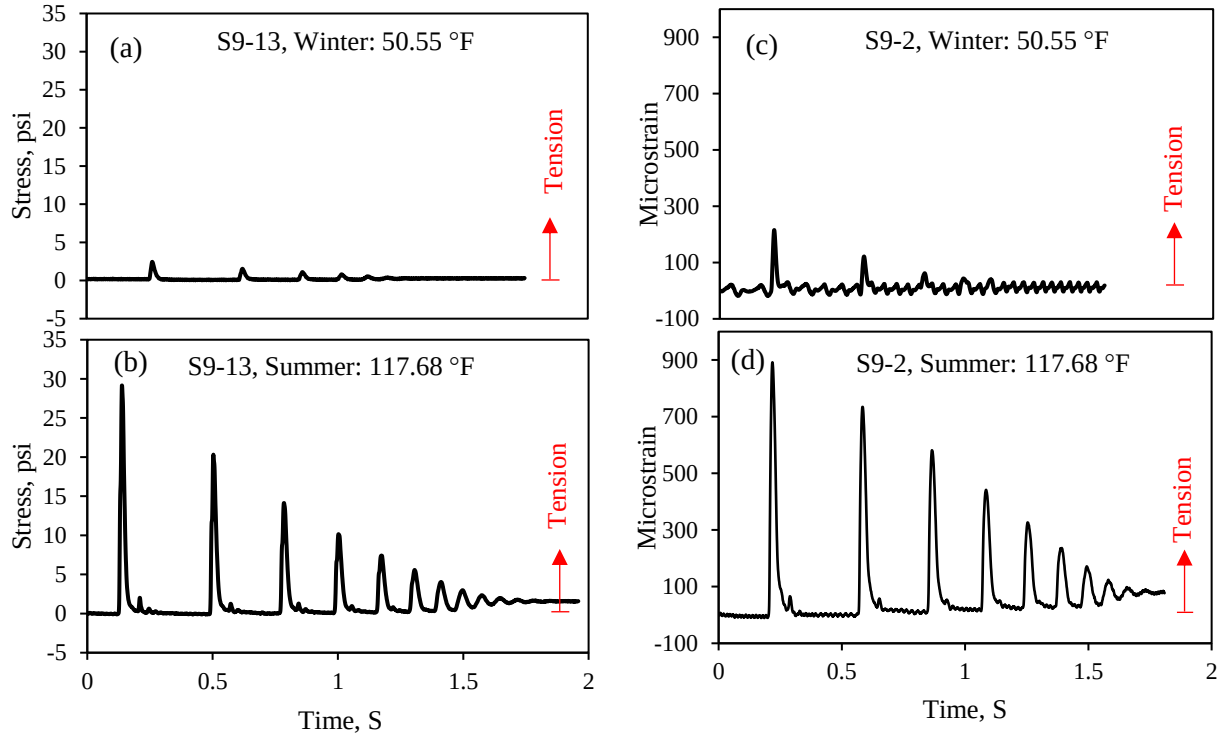

Figure 5.16 Measured Responses under FWD Loading for the Thick-lift Section (S9). (a), (b) Stress Responses in Winter and Summer; (c), (d) Strain Responses in Winter and Summer.

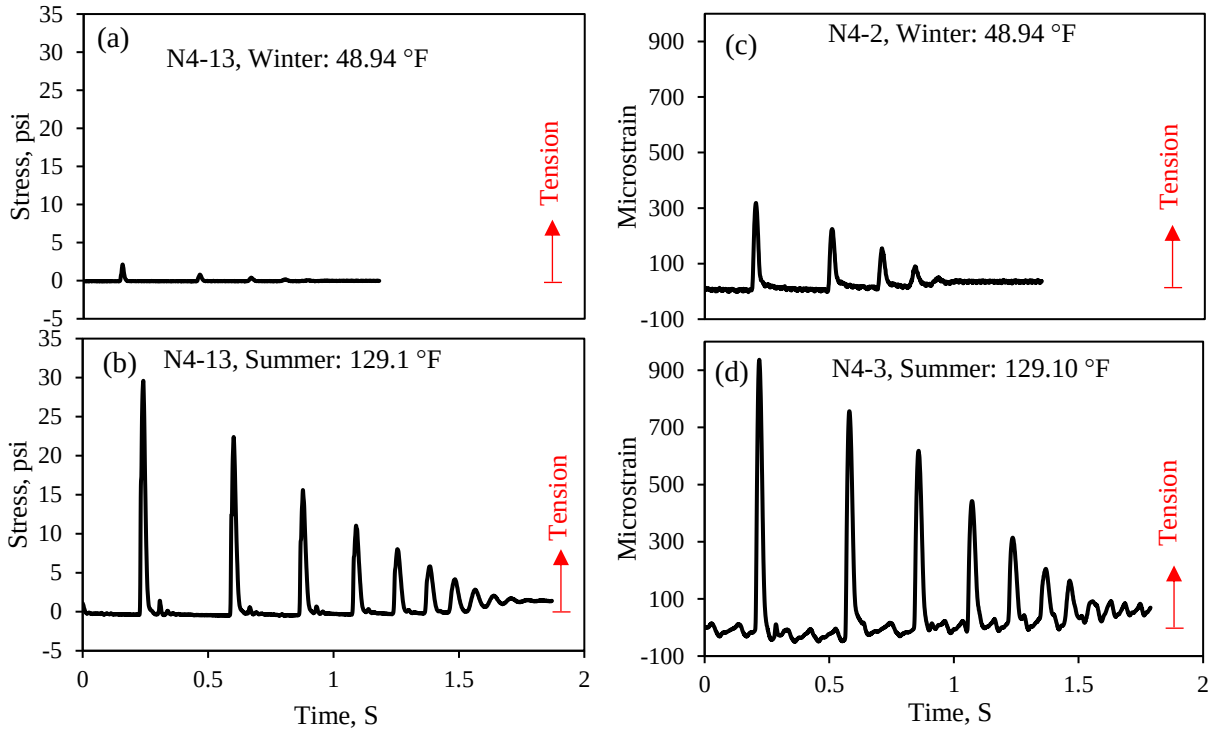

Figure 5.17 Measured Responses under FWD Loading for CCPR Section (N4). (a), (b) Stress Responses in Winter and Summer; (c), (d) Strain Responses in Winter and Summer.

Table 5.3 Peak Stress/Strain at the Bottom of AC under FWD loading.

	Stress, psi		**Microstrain**	
Sections	Winter	Summer	Winter	Summer
Stabilized foundation (S2)	2.2	31.1	32.9	-188.9
CCPR Stabilized (S12)	1.0	25.0	78.1	240.1
Thick lift (S9)	2.5	29.2	215.3	891.4
CCPR (N4)	2.1	29.6	318.5	936.7

5.4.4. Stress and Strain Measurements Over Time

Since the response of the stabilized foundation section (S2) was not initially expected, further investigation was made by exploring stress and strain responses under the Test Track vehicles collected over time for all sections. For the thick-lift (S9) and stabilized foundation (S2) pavement sections, the pavement response data and pavement temperatures were collected weekly under live

truck traffic load from November 26, 2018 through the end of February, 2021. The collection was alternated between mornings and afternoons to capture daily temperature fluctuations in addition to seasonal trends. Figure 5.18 and Figure 5.19 show the maximum pavement responses under single axles and temperature trends versus date. Figure 5.18 clearly shows the base stress response increasing over time with a general increase in temperature. The short-term cycling results from alternating morning and afternoon collection cycles to capture the daily temperature fluctuation in addition to the longer-term seasonal trends. The mid-depth temperatures at the AC/base interface are nearly the same between the sections but the stress is higher in the stabilized foundation section (S2). The stabilized foundation section had even a thicker AC layer, and yet yielded higher stress levels. This is due to the stiff underlying layer that cause an increase in stress levels in upper layers which will be discussed in Chapter 7.

Figure 5.19 shows a similar trend for the thick-lift section (S9) where the tensile microstrain correlates well to changes in mid-depth temperature. However, the strain response for the stabilized foundation pavement (S2) showed a fundamentally different response than S9 as noted previously under dynamic and FWD loading. The tensile strain responses were relatively insensitive to changes in pavement temperature. It even appears that tensile strain could be decreasing with temperature over time in the stabilized foundation pavement (S2). Figure 5.19 includes only tensile microstrain readings. In winter, this includes the peak values of the stress wave but in summer it includes the small upticks in the positive tensile zone and not the peaks since the signal is flipped. Thus, from the whole dynamic response in the summer, only those small upticks in the tensile zone are collected to represent the graph which explains the insensitivity to temperature. More explanation will be provided later in this chapter.

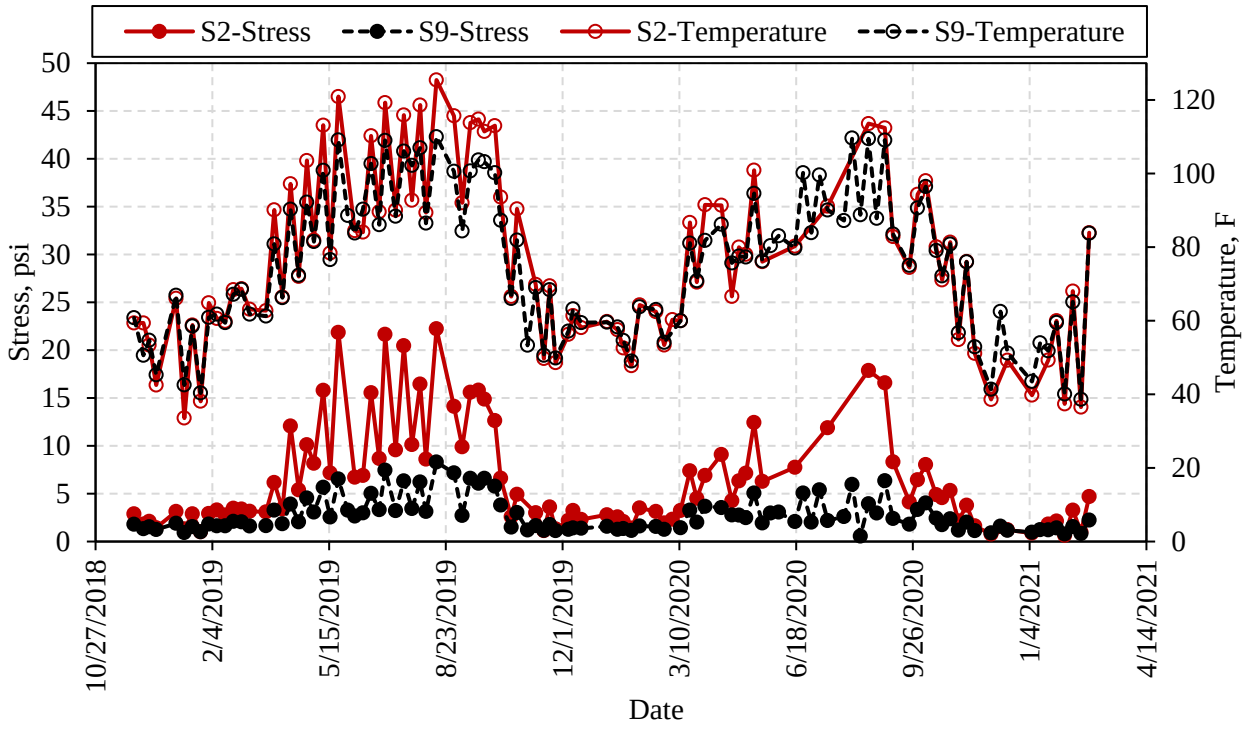

Figure 5.18 Stress Response and Temperature for Stabilized Foundation Section (S2) and the Thick-Lift Section (S9).

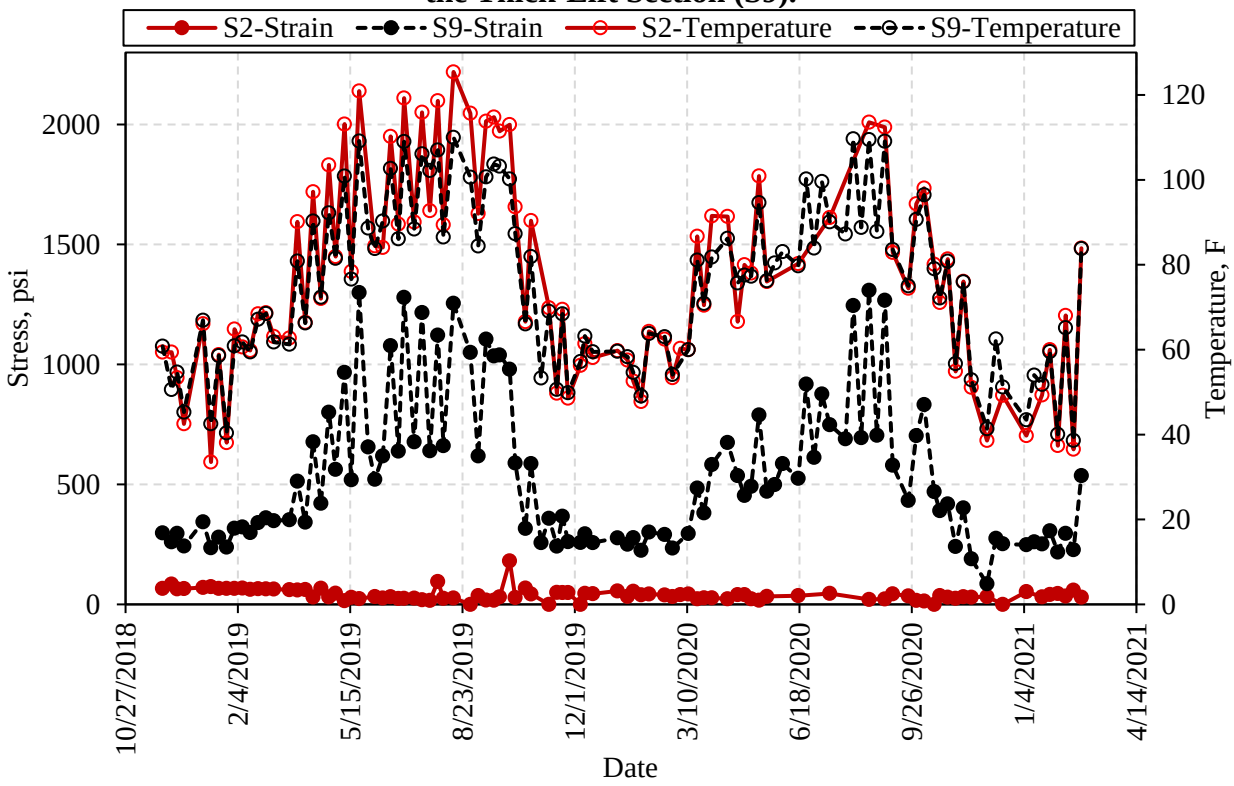

Figure 5.19 Strain Response and Temperature for Stabilized Foundation Section (S2) and the Thick-Lift Section (S9).

The same data were generated again considering the AC temperature. Figure 5.21 show the stress and strain responses of the stabilized foundation (S12) and the thick-lift flexible (S9) pavement sections versus mid-depth temperature. Similar to previous graphs, each data point in the graph represents 95th percentile compressive stress (Figure 5.21) or tensile strain (Figure 5.21) measurements in each section on each date. As shown in Figure 5.21, there exists an exponential relationship between stress response and temperature for the thick-lift section (S9) which is in good agreement with the CCPR sections (N4 and S12) as well as previous research studies at NCAT *(West et al., 2019).* It confirms the strong influence of temperature on stress response resulting from the change in AC modulus.

On the other hand, the tensile strain response for the stabilized foundation section (S2) showed a fundamentally different behavior than the thick-lift pavement section (S9) and other conventional pavements. As shown in Figure 5.21, the tensile horizontal strain response at the bottom of AC decreased with the increase in temperature. This again shows that the stabilized foundation section (S2) was not sensitive to temperature changes.

To create Figure 5.21, only horizontal tensile strains were extracted from the database because it was originally premised that the bottom of AC would experience predominantly tensile strains similar to the CCPR sections and other flexible pavements. Given the previous finding that the bottom of AC in the stabilized foundation section can experience compression, the strain measurement was investigated more closely. This time, 95th percentile compressive responses on each day were extracted from the database. Figure 5.22 depicts compressive and tensile strain at the bottom of AC with respect to temperature in one graph where negative response represents compression. The compressive strain in the stabilized foundation pavement (S2) follows a negative exponential trend that resembles the thick-lift (S9) tensile strain trend but with a reversed sign.

Even the exponential power for the trend lines of both sections are similar with high coefficients of determination (R-square > 0.8). Figure 5.22 also suggests that the stabilized foundation section experiences two different strain modes depending on pavement temperature. At lower temperatures (less than 75°F), the pavement strain response at the bottom of AC is dominantly tensile. In fact, the absolute strain response for compressive mode is lower than the absolute value for tensile mode, making the strain wave under moving load dominantly tensile. However, the strain response converts to dominantly compressive mode at higher temperatures (above 75°F). In other words, 75°F is the critical temperature at which the strain readings change from dominantly tensile mode to dominantly compressive mode for this section. This further confirms the findings of Figure 5.11 and Figure 5.14 where winter response under moving load was predominantly in tension, but summer response was primarily in compression.

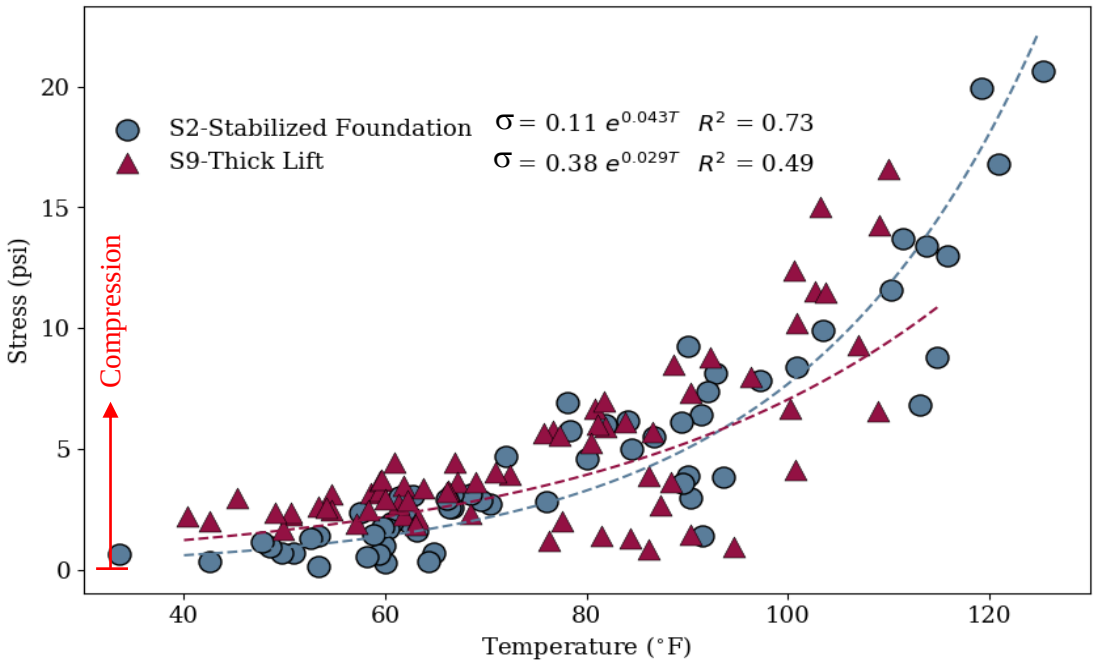

Figure 5.20 Measured Stress Responses for Sections S2 and S9 *(Nakhaei and Timm, 2021)*.

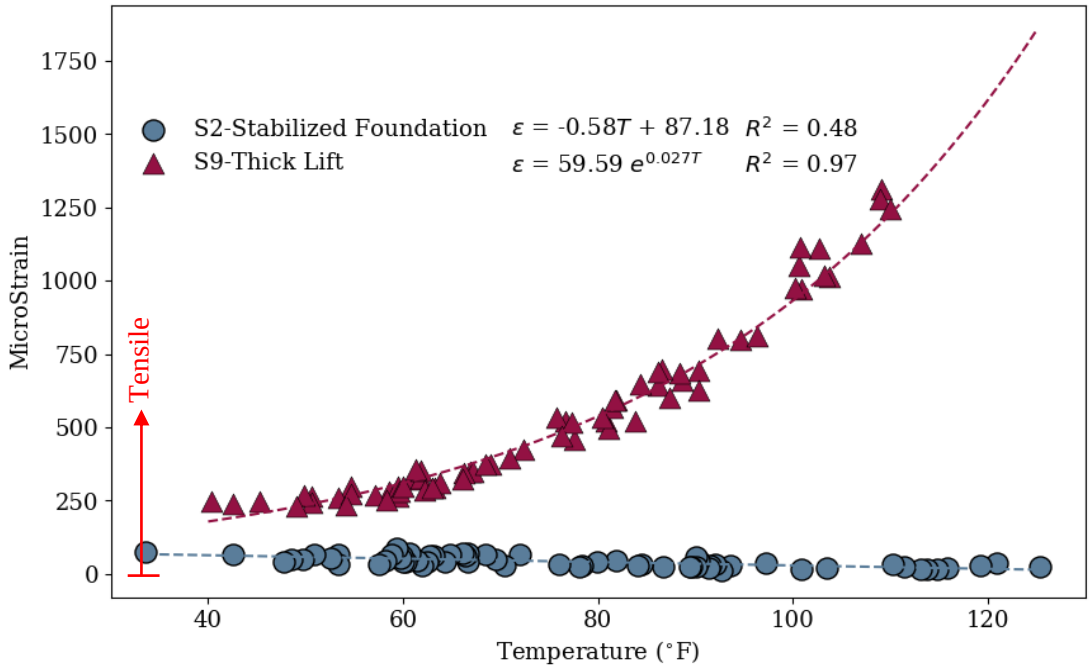

Figure 5.21 Measured Strain Responses for Sections S2 and S9 *(Nakhaei and Timm, 2021)*.

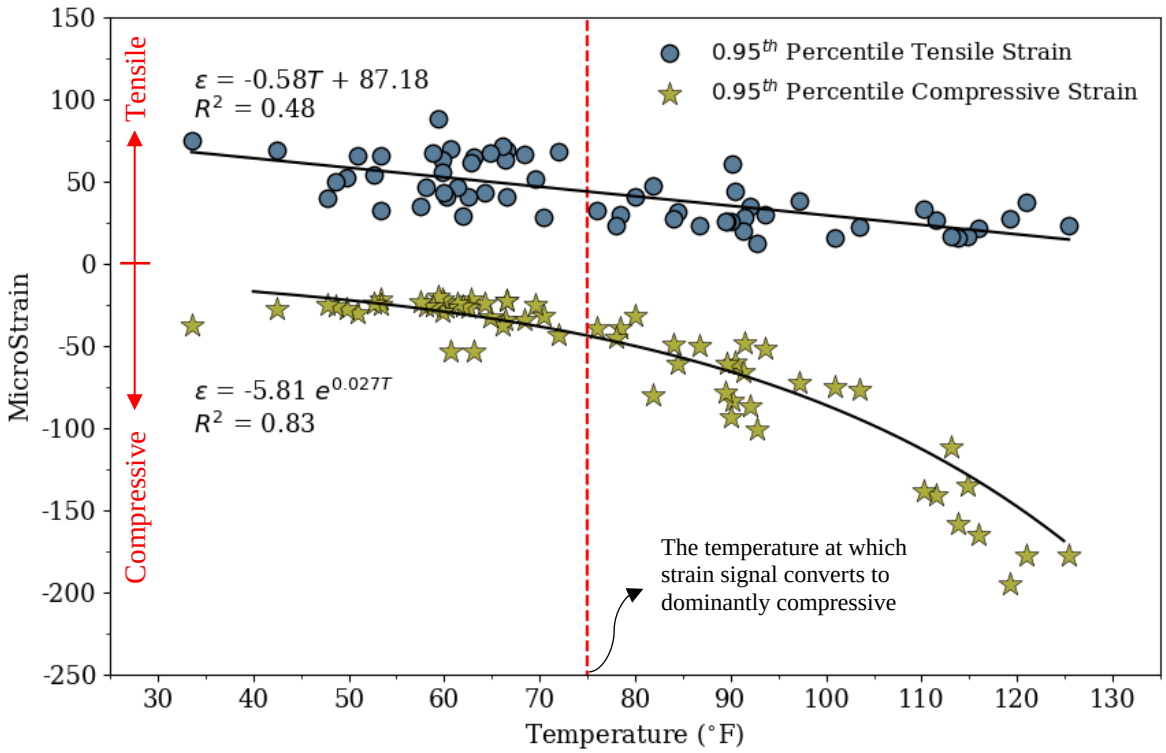

Figure 5.22 Measured tensile and compressive strain responses for section S2 *(Nakhaei and Timm, 2021)*.

Figure 5.23 shows the strain response versus the measurement dates for CCPR (N4) and CCPR stabilized (S12) pavement sections for the last three research cycles at the Test Track. Each data point in the graph represents 95th percentile tensile strain measurements from single axles in each section on each date. The large gaps in the data represent the breaks between research cycles and when there was no trafficking on the pavement sections. This figure shows the cyclic behavior of strain responses for both sections, where the response increased in warm seasons and decreased in cold seasons. The cyclic behavior was more pronounced for the CCPR section (N4) than CCPR with stabilized foundation section (S12) which was less sensitive to temperature. The insensitivity to temperature for CCPR with stabilized foundation section (S12) can be attributed to the stabilized foundation layer that provided restraint under the AC layer causing the AC to bend less similar to the stabilized foundation section (S2). The graph also shows that the maximum strain response in warm seasons increased for the CCPR section (N4) in the 2018 research cycle (cycle 3) compared to the previous research cycles suggesting damage accumulation to the pavement section. The strain data measurements indicated the possibility for crack and damage long before any cracks were appeared at the surface of this section.

Figure 5.24 shows the same set of strain gauge measurements but this time strain measurements were plotted versus mid-depth temperature of the AC layer. The graph confirms that the CCPR section (N4) was more sensitive to pavement temperature compared to CCPR with stabilized foundation section (S12). As shown, the data are more scattered for the CCPR section (N4) which could indicate the possibility of damage to the pavement section. To study which research cycle contributes the most to the scattered observations in the CCPR section (N4), the strain and stress responses were color coded based on each research cycle and depicted versus temperature again (Figure 5.25 and Figure 5.26). Figure 5.25 and Figure 5.26 suggest that there is

an upward trend in the strain and stress measurements moving from cycle 1 to cycle 3 (the most recent). While the difference between cycle 1 and 2 is only significant at higher temperatures in both figures, there is an upward trend in cycle 3 response in all temperatures. Thus, the data suggested that the pavement experienced more damage at the last research cycle which was later appeared as the form of cracks at the surface of the CCPR section as discussed in section 5.4. This analysis clearly demonstrates the ability of pavement instrumentation to show evidence for pavement damage before any damage appears at the surface.

Similar to the stabilized foundation section (S2), the 95th percentile compressive and tensile strain were plotted for the CCPR with stabilized foundation section (S12) section to investigate if this section also followed the same behavior. Figure 5.27 illustrates the same behavior for the CCPR with stabilized foundation section with both tension and compression following exponential trend with opposite signs. However, unlike section S2, the magnitude of tension always exceeds the compression in this section. This again could be attributed to different stiffness of the base material between the two sections which will be further discussed in Chapter 7.

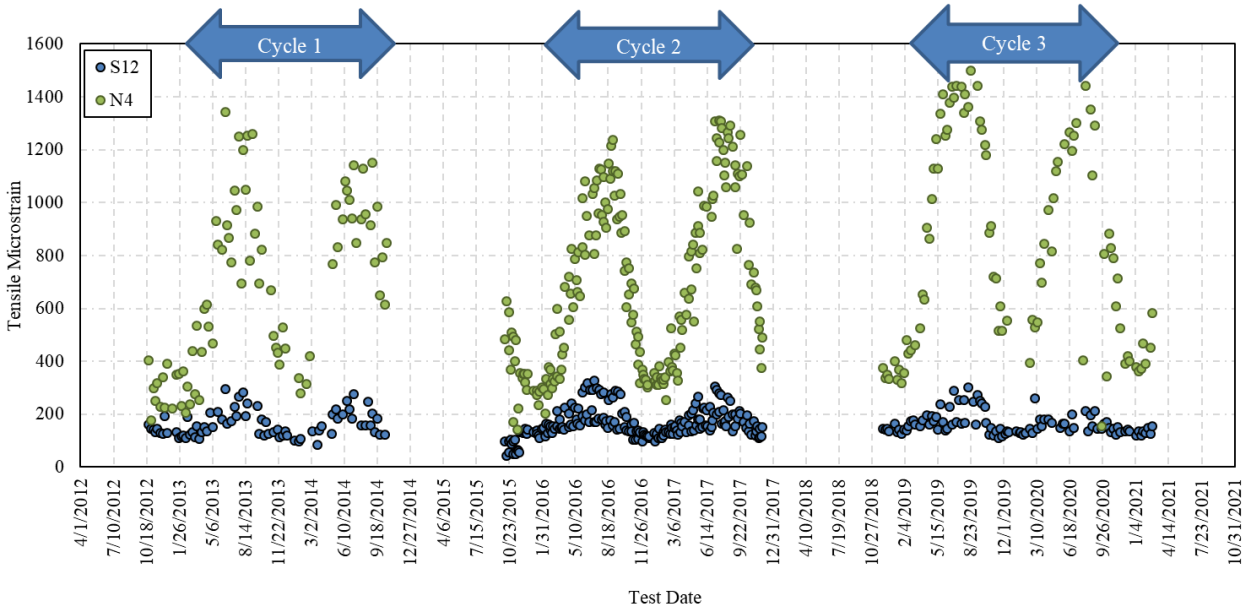

Figure 5.23 Cyclic Strain Measurements for CCPR (N4) and CCPR Stabilized (S12) Sections *(Timm et al., 2020)*.

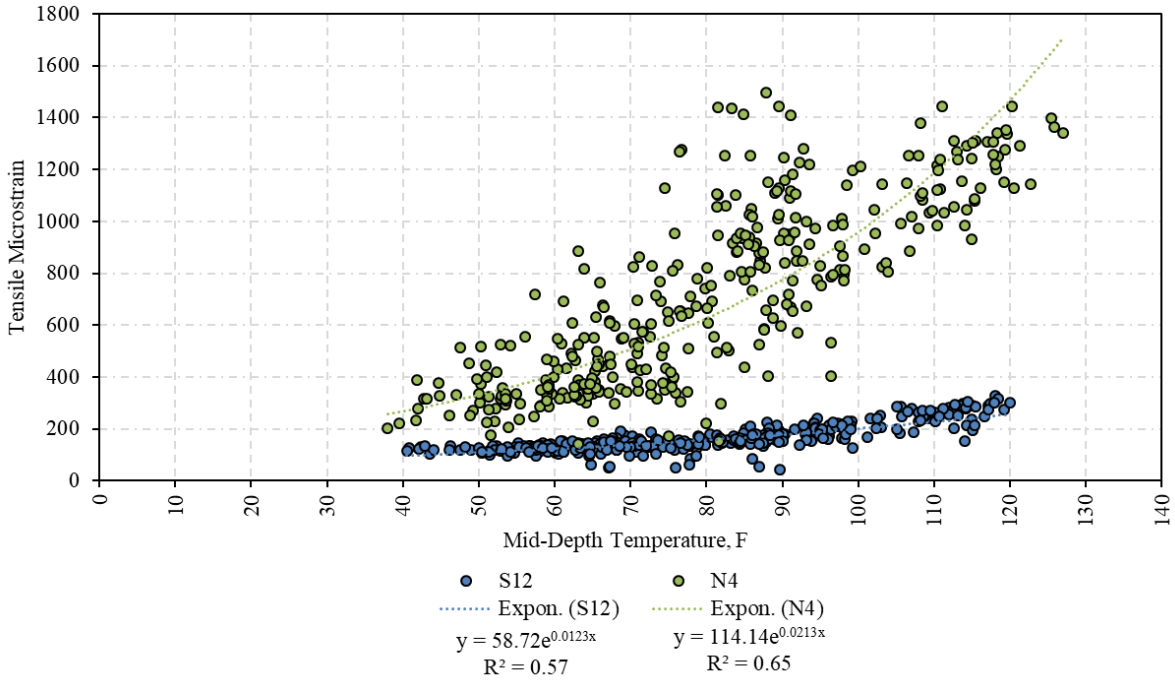

Figure 5.24 Strain Response for the CCPR (N4) and CCPR Stabilized (S12) Sections versus Temperature *(Timm et al., 2020)*.

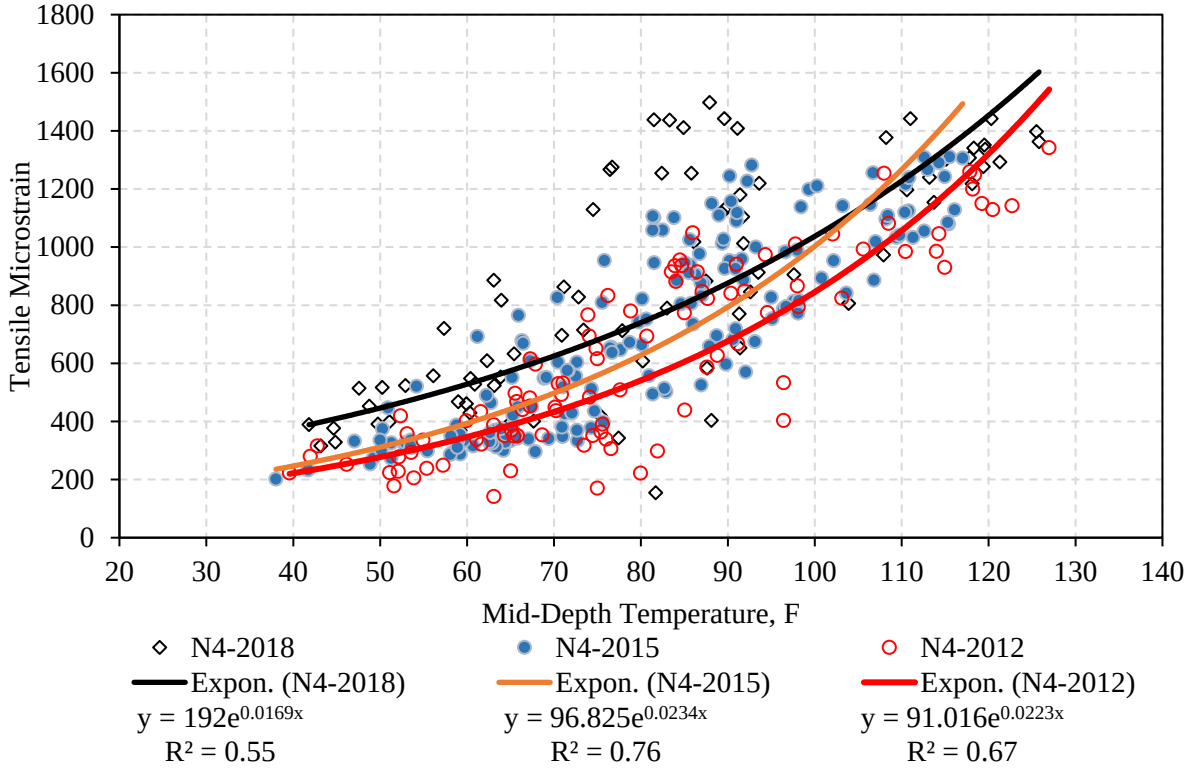

Figure 5.25 The Strain Response for the CCPR Section (N4) for the Three Research Cycles *(Timm et al., 2020)*.

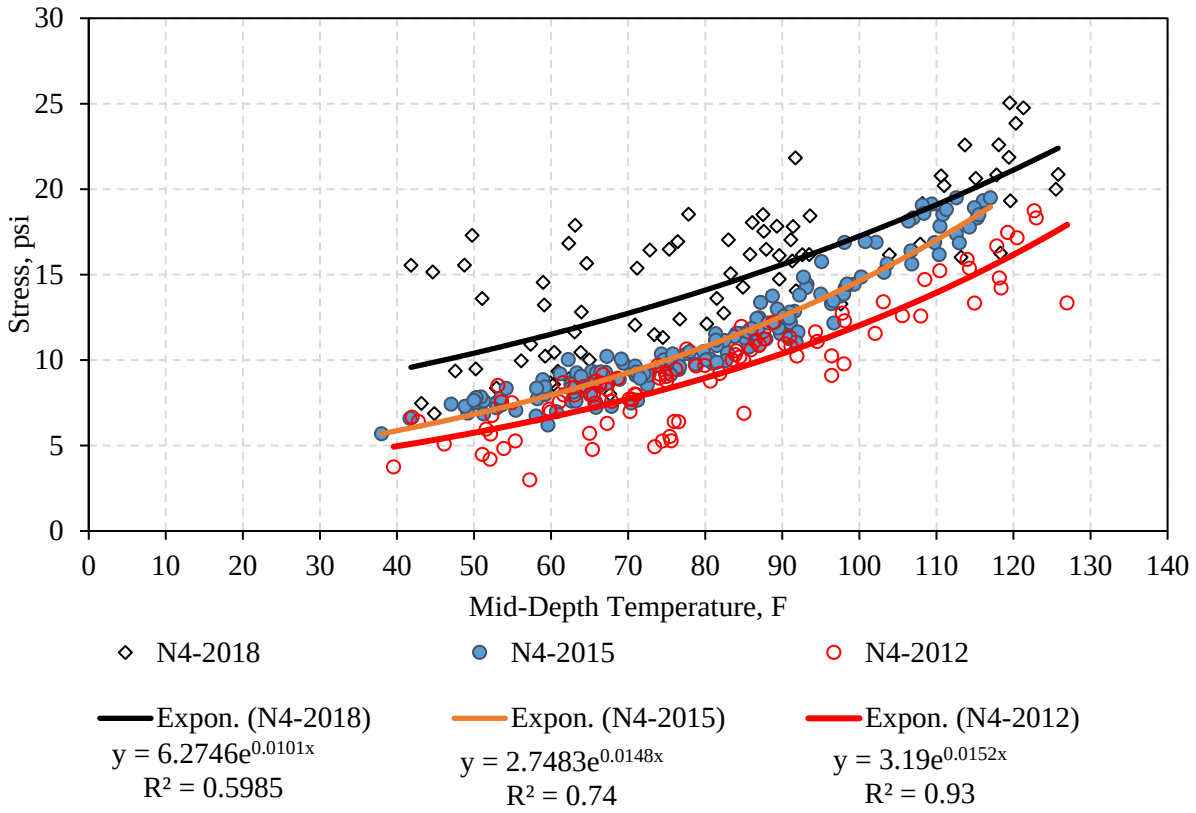

Figure 5.26 The Stress Response for the CCPR Section (N4) for the Three Research Cycles.

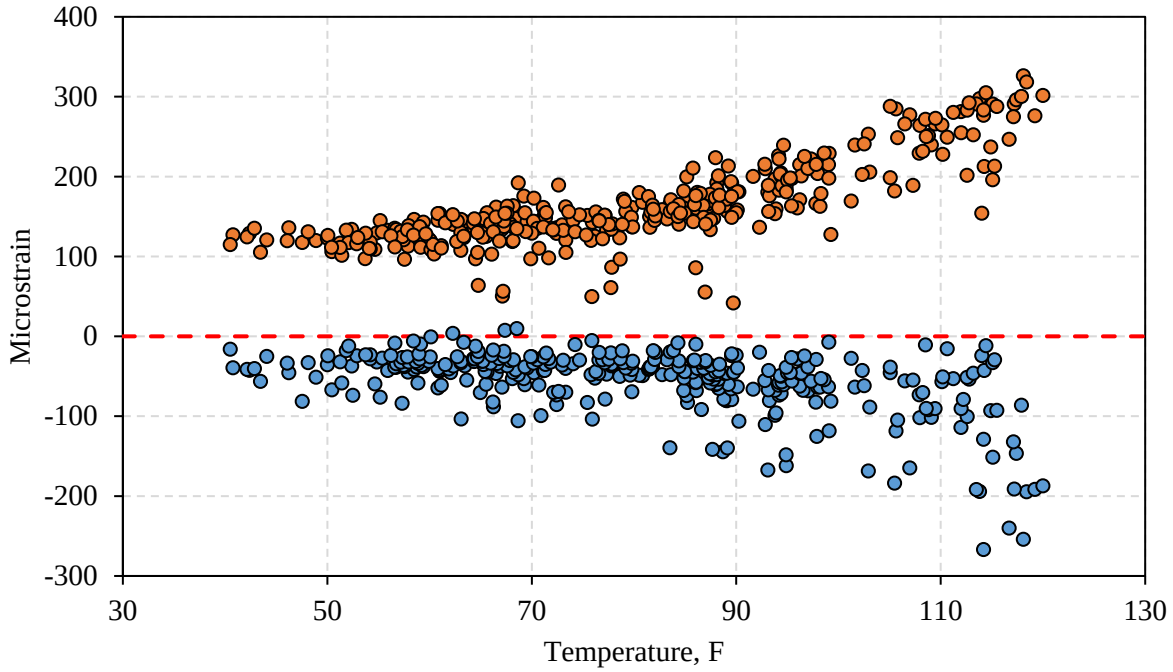

Figure 5.27 The 95th Percentile Tensile and Compressive Strain versus Temperature for CCPR with stabilized foundation section (S12).

In summary, the strain responses measured over time suggested a fundamentally different behavior for the stabilized foundation pavement section (S2). The measurements indicated that the stabilized foundation section can experience compressive strain at the bottom of the AC layer. But does the pavement simulation suggest the same? To answer this question, further analysis was conducted by simulating the pavement sections using MASTIC program. MASTIC was specifically developed for this research study and Chapter 6 discusses its development. Chapter 7 discusses the simulation results of the pavement sections using MASTIC and whether simulation and measurements were in agreement.

CHAPTER 6

A NEW MULTILAYER SIMULATION PROGRAM

For more than 50 years the multilayer elastic theory has successfully been applied for structural analysis of flexible pavements. Many computer software packages have been developed based on multilayer elastic theory *(Khazanovich and Wang, 2007)*. This chapter introduces the fundamental theory behind the implementation of layered elastic theory first proposed by Burmister *(1944)*. This chapter derives the equations for determining the stresses, strains, and displacements in a multilayer system under a circular loaded area. Those equations were used to develop the forward and backward solutions of a new computer program "MASTIC". MASTIC is short for Matlab-Elastic program since the program was originally developed in Matlab. The Python version of MASTIC was also developed with the same principals. MASTIC was specifically developed for this study to obtain forward and backward solutions of an elastic system under circular loading. Unlike WESLEA and many other similar multilayer elastic programs that can analyze up to certain number of pavement layers (e.g. 5 layers), MASTIC has no limitation on the number of layers. This program can handle partial friction between the layer interfaces while most programs such as WESLEA can consider only fully bonded or unbonded conditions. This chapter demonstrates that MASTIC can outperform EVERCALC for backcalculation of FWD data for complex pavement systems, and thus was used extensively in this study to evaluate the stabilized foundation pavement section (S2). In addition, MASTIC incorporates several advanced optimizations which can be changed by user to arrive at more optimum solutions.

6.1. **Layered Elastic Theory**

A simple way to characterize the behavior of a flexible pavement under a load is to consider it as a homogeneous half-space. The half-space system can be solved for stress, strain, and deflection under concentrated load based on Boussinesq theory (*Huang 2004*). Figure 6.1 shows a homogeneous half-space with elastic modulus *E* and a Poisson's ratio ν subjected to a circular load with radius *a* and uniform pressure *q*. A small element with center at a distance *z* below the surface and *r* from the axis of symmetry is shown. While the Boussinesq theory was an effective solution for pavement system with similar modular ratio for all layers, it could not properly estimate the pavement responses within a layered system with significantly different material properties. Thus, a multi-layer elastic solution was introduced by Burmister, who developed analytical solutions for a two layered system and later extended them to a three-layered system *(Burmister, 1944, 1955)*. Over the years, the theory was extended for an arbitrary number of layers *(Khazanovich, and Wang. 2007)*.

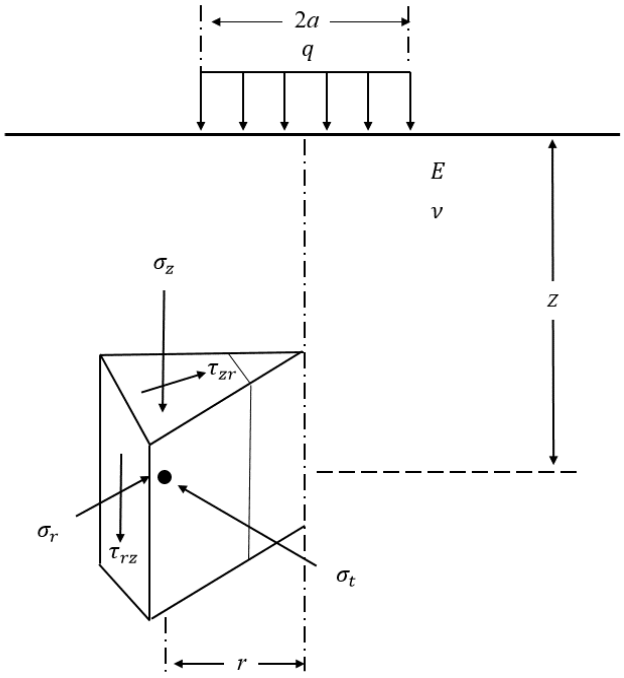

Figure 6.1 Stress Component under axisymmetric loading for elastic half space system.

The solution of multi-layer elastic theory, developed by Burmister, involves the following steps *(Khazanovich, and Wang. 2007)*:

1. Presenting pavement responses in terms of Burmisters biharmonic functions (ϕ).
2. Assembling boundary conditions.
3. Applying Hankel transform to the boundary conditions.
4. Solving a system of linear equations to determine the coefficients of Burmister's functions.
5. Performing an inverse Hankel transform to determine stresses, strains, and deflections.

Burmister's equations were formed assuming that asphalt pavement does not have any bending moment carrying capacity. Thus, the governing equations which were developed to estimate stresses in asphalt pavements did not contain any bending moment term. In the following sections, the essential equations for solving a multi-layered elastic system under circular load is presented.

6.2. **Multilayer Elastic Theory Essential Equations**

To solve for a multi-layered system, a stress function ϕ that satisfies the differential Equation (6.1 can be assumed for each layer.

$$\nabla^4\phi = 0 \tag{6.1}$$

For systems with an axially symmetrical stress distribution, we have:

$$\nabla^4 = \left(\frac{\partial^2}{\partial r^2} + \frac{1}{r}\frac{\partial}{\partial r} + \frac{\partial}{\partial z^2}\right)\left(\frac{\partial^2}{\partial r^2} + \frac{1}{r}\frac{\partial}{\partial r} + \frac{\partial}{\partial z^2}\right) \tag{6.2}$$

in which r and z are cylindrical coordinates for radial and vertical directions, respectively (as shown in Figure 6.1). Having the stress function (ϕ), one can find the stress and displacement within pavement system by the following equations:

$$\sigma_z = \frac{\partial}{\partial z}\left[(2-\nu)\nabla^2\phi - \frac{\partial^2\phi}{\partial z^2}\right] \tag{6.3}$$

$$\sigma_r = \frac{\partial}{\partial z}\left[\nu\nabla^2\phi - \frac{\partial^2\phi}{\partial r^2}\right] \tag{6.4}$$

$$\sigma_t = \frac{\partial}{\partial z}\left[\nu\nabla^2\phi - \frac{1}{r}\frac{\partial\phi}{\partial r}\right] \tag{6.5}$$

$$\tau_{rz} = \frac{\partial}{\partial r}\left[(1-\nu)\nabla^2\phi - \frac{\partial^2\phi}{\partial z^2}\right] \tag{6.6}$$

$$\omega = \frac{1+\nu}{E}\left[(1-2\nu)\nabla^2\phi + \frac{\partial^2\phi}{\partial r^2} + \frac{1}{r}\frac{\partial\phi}{\partial r}\right] \tag{6.7}$$

$$u = -\frac{1+\nu}{E}\left[\frac{\partial^2\phi}{\partial r\,\partial z}\right] \tag{6.8}$$

where σ_z, σ_r, σ_t, and τ_{rz} represent vertical, radial, tangential, and shear stresses, respectively. The vertical and horizontal deflections are defined as ω and u, respectively. ν represents Poisson's ratio and E is elastic modulus. The load is applied over a circular area with a radius of a and intensity of q. Equation (6.1 is a fourth-order differential equation which requires determining four constants of integration that can be determined from the boundary and continuity conditions to calculate the stress, strain, and displacement. In addition to original parameters, to avoid numerical instability, this study used the variable transformations of $\rho = r/H$ and $\lambda = z/H$. Here H is the vertical distance from the surface to the upper boundary of the lowest layer (or simply total pavement thickness). The stress function for the *i*th layer which satisfies Equation (6.1 can be found using the following equation:

$$\phi = \frac{H^3 J_0(m\rho)}{m^2}\left[A_i e^{-m(\lambda_i-\lambda)} - \mathrm{B}_i e^{-m(\lambda-\lambda_{i-1})} + C_i m\lambda e^{-m(\lambda_i-\lambda)} - D_i m e^{-(\lambda-\lambda_{i-1})}\right]. \quad (6.9)$$

Where J_0 is the Bessel Function of the first kind and order 0; m is the Henkel parameter (or the domain on which the integral is solved). A, B, C, and D are constants of integration to be determined from the boundary condition and continuity equations. The subscript *i* varies from 1 to n which refers to corresponding quantities to the *i*th layer. Having the stress function known, the following equations can be obtained by substituting Equation (6.9 into Equations (6.2 through (6.7.

$$(\sigma_z{}^*)_i = -mJ_0(m\rho)\{[A_i - C_i(1-2v_i-m\lambda)]e^{-m(\lambda_i-\lambda)} + [B_i + D_i(1-2v_i+m\lambda)\,]e^{-m(\lambda-\lambda_{i-1})}\} \quad (6.10)$$

$$(\sigma_r{}^*)_i = [mJ_0(m\rho) - \frac{J_1(m\rho)}{\rho}]\{[A_i + C_i(1+m\lambda)]e^{-m(\lambda_i-\lambda)} + [B_i - D_i(1-m\lambda)]e^{-m(\lambda-\lambda_{i-1})}\} + 2v_i m J_0(m\rho)[C_i e^{-m(\lambda_i-\lambda)} - D_i e^{-m(\lambda-\lambda_{i-1})}] \quad (6.11)$$

$$(\sigma_t{}^*)_i = \frac{J_1(m\rho)}{\rho}\{[A_i + C_i(1+m\lambda)]e^{-m(\lambda_i-\lambda)} + [B_i - D_i(1-m\lambda)]e^{-m(\lambda-\lambda_{i-1})}\} + 2v_i m J_0(m\rho)[C_i e^{-m(\lambda_i-\lambda)} - D_i e^{-m(\lambda-\lambda_{i-1})}] \quad (6.12)$$

$$(\tau_{rz}{}^*)_i = -mJ_1(m\rho)\{[A_i + C_i(2v_i+m\lambda)]e^{-m(\lambda_i-\lambda)} - [B_i + D_i(2v_i-m\lambda)\,]e^{-m(\lambda-\lambda_{i-1})}\} \quad (6.13)$$

$$(\omega^*)_i = -\frac{1+\nu_1}{E_i}J_0(m\rho)\{[A_i - C_i(2-4v_i-m\lambda)]e^{-m(\lambda_i-\lambda)} - [B_i + D_i(2-4v_i+m\lambda)\,]e^{-m(\lambda-\lambda_{i-1})}\} \quad (6.14)$$

$$(\omega^*)_i = -\frac{1+\nu_1}{E_i}J_0(m\rho)\{[A_i - C_i(2-4v_i-m\lambda)]e^{-m(\lambda_i-\lambda)} - [B_i + D_i(2-4v_i+m\lambda)\,]e^{-m(\lambda-\lambda_{i-1})}\} \quad (6.15)$$

$$(u^*)_i = \frac{1+\nu_i}{E_i} J_1(m\rho)\{[A_i + C_i(1+m\lambda)]e^{-m(\lambda_i-\lambda)} + [B_i - D_i(1-m\lambda)\,]e^{-m(\lambda-\lambda_{i-1})}\} \quad (6.16)$$

In the above equations, J_1 is a Bessel function of the first kind and of order one. The subscript outside the parenthesis corresponds to the *i*th layer, counting from top to bottom. The above pavement responses are not the actual stresses and displacements due to a uniform load *q*, but are those due to a vertical load of $-mJ_0(m\rho)$. The Hankel transform method is used to obtain pavement responses due to a constant load *q*. The Hankel transform of such loading is:

$$\bar{f}(m) = \int_0^{\alpha} qpJ_0(m\rho)d\rho = \frac{q\alpha}{m} J_1(m\alpha) \quad (6.17)$$

where $\alpha = a/H$. The Henkel inversion of the Equation (6.17 is obtained using Equation (6.18:

$$\bar{f}(m) = \int_0^{\infty} \bar{f}(m) m J_0(m\rho)\, dm = q\alpha \int_0^{\infty} J_0(m\rho)\, J_1(m\alpha)\, dm \quad (6.18)$$

.

Now, any pavement response in equations (6.11 through (6.16 can be solved for a uniform load *q* via equation (6.19:

$$R(r,z) = \int_0^{\infty} \frac{R^*}{m} J_1(m\alpha)\, dm \quad (6.19)$$

where R^* is any pavement response under $-mJ_0(m\rho)$ loading. The analysis of a multi-layer elastic system can be summarized into the following steps *(Huang 2006):*

1. Successive values of *m*, from 0 to a rather large positive number are assigned until *R* in Equation (6.19 converges.
2. For each value of *m*, the constants of integration, A_i , B_i , C_i and D_i are determined from the boundary and continuity conditions.
3. A_i , B_i , C_i and D_i constants are plugged into equations (6.10 through (6.16 to obtain *R**.
4. *R* is then solved using Equation (6.19 by a numerical integration method.

The improper integral in Equation (6.19 should be evaluated numerically. Since solving to infinity is not feasible in computers, a general approach is to break down the interval into subintervals and then solve each interval numerically until the integral converges. It has been shown that if the subintervals are selected to be the successive zeros of the Bessel functions, the results are more satisfactory. In particular, Huang *(2004)* suggested that for the numerical integration, the zeros of $J_0(m\rho)$ and $J_1(m\rho)$ are first determined, and the integral between these two zeros is evaluated by a four-point Gaussian formula. Also, since the first cycle of integration must be finely divided, especially when ρ is large, the interval between 0 and the first zero of J_0 which is 2.40483, is sub-divided into six intervals, and that between 2.40483 and 3.83171, which is the first zero of J_1, is subdivided into two intervals. The integral for each subinterval is also evaluated by the four-point formula. More details about solving the numerical integral will be provided later in this chapter.

To obtain the pavement responses, it is still needed to obtain constants of integration from the boundary conditions. At the top surface where *i* = 1 and $\lambda = 0$, the boundary condition can be written as:

$$(\sigma_z{}^*)_i = -mJ_0(m\rho) \tag{6.20}$$

$$(\tau_{rz}{}^*)_i = 0 \tag{6.21}$$

Equation (6.20 is simply obtained by substituting the value of 1.0 in place of all parameters in curly brackets in equation (6.10. This means that the vertical pressure under the load is equal to $-mJ_0(m\rho)$. Also shear stress is assumed to be zero under the load contact. These two equations result in two boundary conditions:

$$\begin{bmatrix} e^{-m\lambda_1} & 1 \\ e^{-m\lambda_1} & -1 \end{bmatrix} \begin{pmatrix} A_1 \\ B_1 \end{pmatrix} + \begin{bmatrix} -(1-2\nu_1)e^{-m\lambda_1} & 1-2\nu_1 \\ 2\nu_1 e^{-m\lambda_1} & 2\nu_1 \end{bmatrix} \begin{pmatrix} C \\ D_1 \end{pmatrix} = \begin{pmatrix} 1 \\ 0 \end{pmatrix} \tag{6.22}$$

For the case of a fully bonded condition, it is assumed that the vertical stress, shear stress, vertical displacement, and radial displacement are the same for every point along the interface. Therefore, when the $\lambda = \lambda_i$, the continuity conditions are:

$$(\sigma_z^*)_i = (\sigma_z^*)_{i+1} \tag{6.23a}$$

$$(\tau_{rz}^*)_i = (\tau_{rz}^*)_{i+1} \tag{6.23b}$$

$$(\omega^*)_i = (\omega^*)_{i+1} \tag{6.23c}$$

$$(u^*)_i = (u^*)_{i+1} \tag{6.23c}$$

.

If system responses satisfy the boundary conditions, then the Hankel transforms of these responses also satisfy the Hankel transform of the boundary conditions. Conversely, if the Hankel transforms of the boundary conditions are satisfied by the Hankel transforms of the system responses, then the boundary conditions themselves are satisfied by the original system responses. In other words, the set of boundary condition in equations (6.23a through (6.23c does not have to be written for the response under the uniform load *q*, but just for R^*. Simply stated, the above equations result in four equations which is provided in the following matrix form:

$$\begin{bmatrix} 1 & F_i & -(1-2\nu_i - m\lambda_i) & (1-2\nu_i + m\lambda_i)F_i \\ 1 & F_i & 1+m\lambda_i & -(1-m\lambda_i)F_i \\ 1 & -F_i & 2\nu_i + m\lambda_i & (2\nu_i - m\lambda_i)F_i \\ 1 & -F_i & -(2-4\nu_i - m\lambda_i) & -(2-4\nu_i + m\lambda_i)F_i \end{bmatrix} \begin{Bmatrix} A_i \\ B_i \\ C_i \\ D_i \end{Bmatrix} \tag{6.24}$$

$$= \begin{bmatrix} F_{i+1} & 1 & -(1-2\nu_{i+1} - m\lambda_i)F_{i+1} & 1-2\nu_{i+1} + m\lambda_i \\ R_iF_{i+1} & R_i & (1+m\lambda_i)R_iF_{i+1} & -(1-m\lambda_i)R_i \\ F_{i+1} & -1 & (2\nu_{i+1} + m\lambda_i)F_{i+1} & 2\nu_{i+1} - m\lambda_i \\ R_iF_{i+1} & -R_i & -(2-4\nu_{i+1} - m\lambda_i)R_iF_{i+1} & -(2-4\nu_{i+1} + m\lambda_i)R_i \end{bmatrix} \begin{Bmatrix} A_{i+1} \\ B_{i+1} \\ C_{i+1} \\ D_{i+1} \end{Bmatrix} \quad .$$

In the above matrix:

$$F_i = e^{-m(\lambda_i - \lambda_{i-1})} \tag{6.25}$$

$$R_i = \frac{E_i}{E_{i+1}} \frac{1+\nu_{i+1}}{1+\nu_i} \tag{6.26}$$

Another set of boundary conditions can be obtained at the depth of infinity since stresses and displacements must vanish as λ approaches to infinity thus for lowest layer where *i*=*n*:

$$A_n = C_n = 0 \tag{6.27}$$

For an *n*-layer system, there are 4*n* constants of integration (four constants for each layer). However, constants $A_n = C_n = 0$ and thus are known. In addition, two more constants can be obtained from equations (6.20 and (6.21. The remaining $4(n-1)$ equations can be found from the matrix (6.24. If the *i*th interface is unbonded, the continuation of shear stress and radial displacement must be replaced by zero shear stress on both side of the interface:

$$(\sigma_z^*)_i = (\sigma_z^*)_{i+1} \tag{6.28a}$$

$$(\omega^*)_i = (\omega^*)_{i+1} \tag{6.28b}$$

$$(\tau_{rz}^*)_i = 0 \tag{6.28c}$$

$$(\tau_{rz}^*)_{i+1} = 0 \tag{6.28c}$$

. Thus, the boundary condition matrix would be:

$$\begin{bmatrix} 1 & F_i & -(1-2\nu_i - m\lambda_i) & (1-2\nu_i + m\lambda_i)F_i \\ 1 & F_i & 1+m\lambda_i & -(1-m\lambda_i)F_i \\ 1 & -F_i & 2\nu_i + m\lambda_i & (2\nu_i - m\lambda_i)F_i \\ 0 & 0 & 0 & 0 \end{bmatrix} \begin{Bmatrix} A_i \\ B_i \\ C_i \\ D_i \end{Bmatrix} \tag{6.29}$$

$$= \begin{bmatrix} F_{i+1} & 1 & -(1-2\nu_{i+1} - m\lambda_i)F_{i+1} & 1-2\nu_{i+1} + m\lambda_i \\ R_i F_{i+1} & R_i & (1+m\lambda_i)R_i F_{i+1} & -(1-m\lambda_i)R_i \\ 0 & 0 & 0 & 0 \\ F_{i+1} & -1 & (2\nu_{i+1} + m\lambda_i)F_{i+1} & 2\nu_{i+1} - m\lambda_i \end{bmatrix} \begin{Bmatrix} A_{i+1} \\ B_{i+1} \\ C_{i+1} \\ D_{i+1} \end{Bmatrix} .$$

Equation (6.29 can be used for any interface that is not bonded. If one wants to apply partial friction method, then the shear stress can be written as follows:

$$(\tau_{rz}^*)_i = k_i(u_i^* - u_{i+1}^*) \quad (6.30)$$

where k is the interface model stiffness. This model describes both fully bonded and fully unbonded interface conditions, as well as a wide range of intermediate conditions. All three conditions have been taken into account in MASTIC development. However, deploying a partial friction method in MASTIC is more time consuming compared to a bonded condition, especially for backcalculation process, and thus, should be used when necessary.

6.3. **Precision Improvement**

One of the often-encountered problems of implementing multi-layer elastic theory is the numerical evaluation of the inverse Hankel transform of the layered elastic solutions which sometimes leads to overflow/underflow problem for computers which consequently leads to inaccurate calculation of pavement responses at some points, especially at points near the surface. The imprecision occurs when a computer attempts to handle the numbers that are too small or large for it. Every computer has a well-defined range of values. If during execution of a program it arrives at a number outside this range, it will experience an overflow/underflow problem and truncates the digits that are beyond its precision.

This problem is significant for calculating the pavement responses at the top surface of the top layer and especially when the radial offset value is large due to low convergence rate of the numerical integration. This problem has been recognized in the past by developers of layered elastic programs. As an example, JULEA provides evaluations only for points located at the top layer that are deeper than 0.2 load radius below the surface (Khazanovich and Wang 2007). In the latest version, JULEA uses a correlation for predicting the response in the surface. In KENPAVE, the coordinates of the system are adjusted and normalized based on the tire radius and total

pavement thickness to increase the precision and avoid underflow problem. However, the problem may still be persistent when higher precision is needed for the surface response and when the radial offset is large. The best approach to overcome this problem was proposed by Khazanovich and Wang *(2007)* in which they added and subtracted a solution for the elastic half-space with the same properties as the properties of the top layer. They showed this method can enhance the convergence of the improper integral. For development of MASTIC, this study made use of variable transformation along with a simple method that was introduced in this study to increase the accuracy of numerical integration and will be discussed further below.

As mentioned before, the solution for layered elastic media, subjected to circular load with radius *a*, has the form of Equation 6.19. This equation can be re-written as the form ofEquation (6.31:

$$R_i(r,z) = \int_0^\infty f_i(\mu_i, E_i, z, m)\ J_1(ma)\, J_k(mr)\, dm \tag{6.31}$$

where $f_i(\mu_i, E_i, z, m)$ is a function of the boundary conditions and response type with $k = 0$ or 1, depending on the response type. As mentioned earlier, the improper integral in Equation (6.19 or (6.31 should be evaluated numerically. The function in Equation 6.31 can be represented as a product of two functions: function $f_i(\mu_i, E_i, z, m)$ and the product of two Bessel functions ($J_1(ma)\, J_k(mr)$). Khazanovich and Wang *(2007)* showed the $f_i(\mu_i, E_i, z, m)$ is a relatively monotonic term, though it is computationally expensive to solve since it requires solving the system of equations for boundary conditions at each point or at each "*m*". However, the multiplication of the two Bessel functions ($J_1(ma)\, J_k(mr)$) is highly oscillatory, but it does not cause computational difficulties.

The oscillatory nature of the Bessel functions product can decrease the precision of the calculation since the integral shown in Equation (6.31 will converge only when large values of

"*m*" are selected. The choice of large values of "*m*" will lead to overflow/underflow problem when solving for system of equations for boundary conditions. Also, it will lead to additional computational overhead since the boundary condition matrix becomes singular with values reaching close to zero. In fact, high values of "*m*" will cause some of the boundary condition internal values to get extremely close to zero which subsequently makes the matrix inversion close to singular which decreases the precision and increases the run time. Farther away from the extreme values, the program performs faster. Studies have shown that this problem only exists for the top surface of the top layer which becomes more pronounced when higher radial offset "*r*" is selected. Figure 6.2 visually explains this problem. In this figure, the vertical axis is radial strain with the actual value of zero, and horizontal axis is Henkel parameter "*m*".

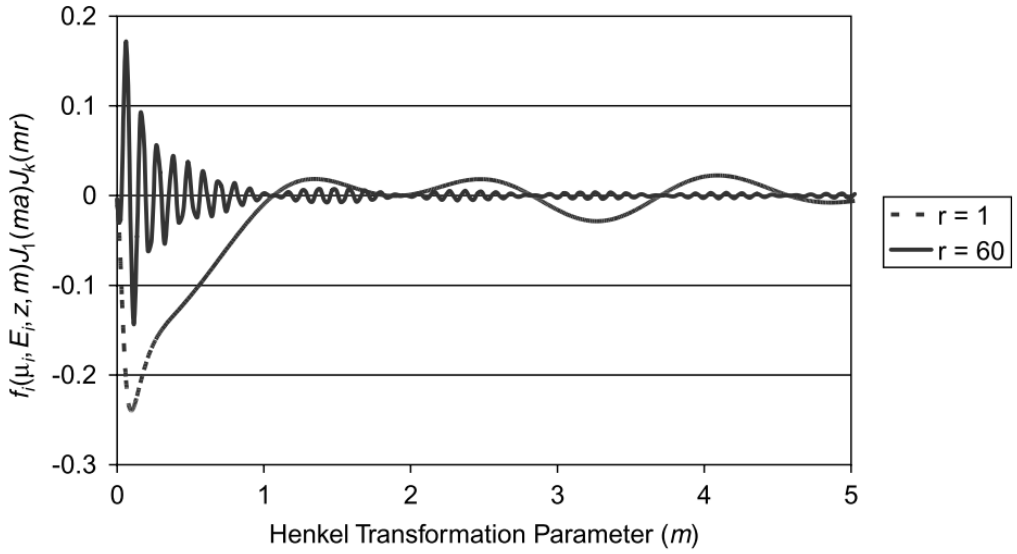

Figure 6.2 Effect of distances from load center on shape of function $f_i(u_i, E_i, z, m)\, J_1(ma)\, J_k(mr)$ for radial strains (Khazanovich and Wang 2007)**.**

Two radial distances are selected for comparison purposes in Figure 6.2. For the integral presented in Equation (6.31 to converge, larger values of "m" should be selected when choosing larger offsets, whereas smaller offsets (such as *r*=1) converges relatively fast. Larger selection of

"*m*" will lead to overflow/underflow problem when solving for the boundary condition which consequently decreases the precision. On the other hand, choosing lower values will also lead to lower accuracy since the integral is not yet converged and calculated values hover over the true value in an oscillatory manner. The next section will introduce a method to alleviate the issue.

6.3.1. Proposed Modification

A simple, and yet effective method is proposed in this study to mitigate the above problem. Considering the fact that the calculated $f_i(\mu_i, E_i, z, m)\ J_i(ma)\, J_k(mr)$ hovers over the true value, by knowing the lowest and highest peak values for the Henkel function in two consecutive oscillations, one can simply take the average of the highest and lowest peaks to arrive at the target value or close to target value. This average value should be close to the true value given the rate of decay for higher values of *r* is relatively small (low convergence rate). This technique can be also considered as a measure of model convergence. If the average value calculated from two consecutive oscillations is close to the low and high peak values, then the results deemed to converge otherwise "*m*" value should increase (while avoiding the overflow problem). Figure 6.3 explains this concept graphically. To demonstrate the veracity of MASTIC, this study will provide a comparison study between MASTIC, KENPAVE, and WESLEA. Figure 6.3 clearly shows that calculating the average of the two consecutive oscillation would lead to a better solution. This is true for all consecutive oscillations.

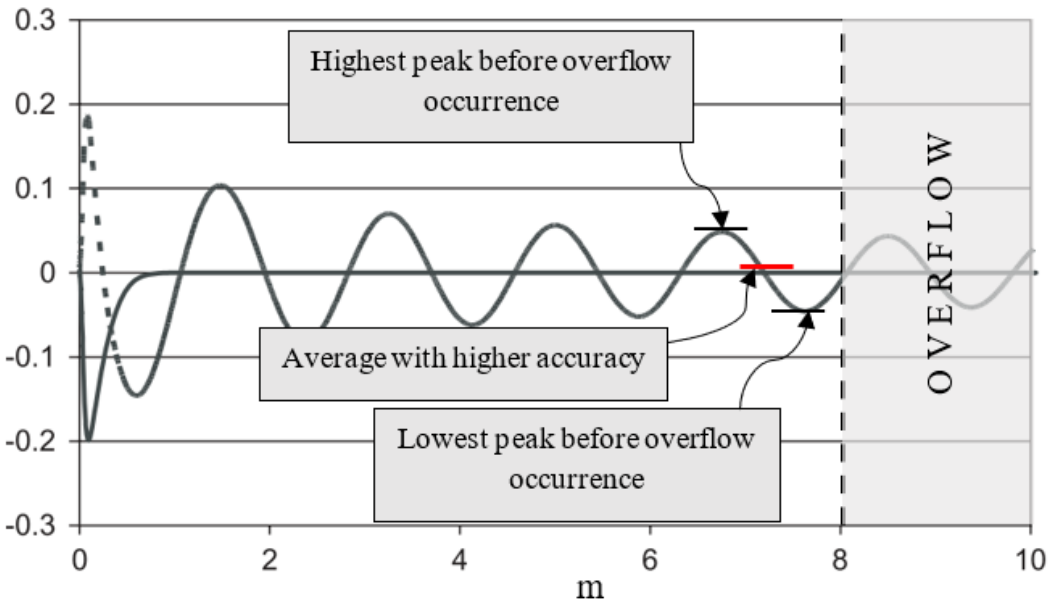

Figure 6.3 The Averaging Technique Proposed in this Study to Increase the Precision.

6.4. **Optimization Methods**

In general, by having a forward solution for the layered elastic theory, one can use an optimization technique to find the material properties. In particular, using a deflection basin measured by falling weight deflectometer device, it is possible to obtain a set of elastic moduli that matches the ones measured in the field under falling weight deflectometer loading.

Different optimization methods can lead to different results since the optimization task for finding elastic modulus is a non-convex optimization problem. The optimization technique that is generally used in FWD backcalculation process is Gauss-Newton optimization with constraints. The Gauss–Newton algorithm is generally used to solve nonlinear least squares problems. It is considered as the modification of Newton's method for finding a minimum of a function. Gauss-Newton's method can only be used to minimize a sum of squared function values. But compared

to Newton's method, it has the advantage that second derivatives, which can be challenging to compute, are not required.

Given m functions $r = (r_1, ..., r_m)$ that are often called residuals of n variables $\beta = (\beta_1, ..., \beta_n)$, with $m \geq n$, the Gauss–Newton algorithm iteratively finds the value of the variables that minimizes the sum of squares as shown in equation 6.32.

$$S(\beta) = \sum_{i=1}^{m} r_i^2(\beta) \tag{6.32}$$

Starting with an initial guess β^0 for the minimum, the method proceeds by the iterations using the Equation (6.33:

$$\beta^{(s+1)} = \beta^{(s)} - (J_r{}^T J_r)^{-1} J_r{}^T r\,(\beta^{(s)}) \tag{6.33}$$

Given r and β as column vectors, the entries of the Jacobian (J) matrix are:

$$(J_r)_{ij} = \frac{\partial r_i(\beta^{(s)})}{\partial \beta_j} \tag{6.34}$$

If $m = n$, the iteration simplifies to:

$$\beta^{(s+1)} = \beta^{(s)} - (J_r)^{-1} r\,(\beta^{(s)}) \tag{6.35}$$

which is a direct generalization of Newton's method in one dimension. In data fitting, where the goal is to find the parameters β such that a given model function $y = f(x, \beta)$ best fits some data points (x_i, y_i), the functions r_i are the residuals:

$$r_i(\beta) = y_i - f(x_i, \beta) \tag{6.36}$$

Then, the Gauss–Newton method can be expressed in terms of the Jacobian J_f of the function f as

$$\beta^{(s+1)} = \beta^{(s)} - (J_f{}^T J_f)^{-1} J_f{}^T r\,(\beta^{(s)}) \tag{6.37}$$

The elastic moduli are the betas (βs) in the above equations for which the algorithm searches. Most software packages only support one optimization method. For example, EVERCALC only

supports augmented Gauss-Newton optimization and user cannot change the optimization method. However, MASTIC provides several choices of searching algorithms. The default search algorithm is Interior-Point optimization which was proven to provide the best performance among other methods and will be discussed later. In addition, MASTIC can apply algorithms from simple Newton search to sequential quadratic programming (SQP). There is no limitation on the number of layers to be analyzed which can be useful for complex pavement structures. MASTIC can consider different configurations with infinite number of deflection readings while other programs such as EVERCALC generally limit the number of sensors to 10. This is particularly important for unconventional pavements where more sensors are possibly needed. The details of optimizers used in MASTIC are not discussed in this document for brevity but can be found elsewhere *(Anderson et al., 2000)*.

6.5. **Comparison of MASTIC with EVERCALC**

This section validates MASTIC forward and backward solutions with other well-established software.

6.5.1. Forward Solution

The MASTIC forward solution is compared against KENPAVE solution to ensure the accuracy of the MASTIC. KENPAVE results have already been validated through extensive research studies such as Advanced Models for Analytical Design of European Pavement Structures *(AMADEUS, 2000)*. Thus, comparing MASTIC with EVERCALC should suffice to establish the accuracy of the MASTIC program. Table 6.1 presents the pavement properties used for comparison. The data in this table are obtained from (*AMADEUS, 2000)* to provide additional cases for cross-comparison

with other programs, if one is to conduct further comparison (note that the values are converted from SI units). The cross section is relatively thick since the section was highly trafficked.

Table 6.1 Pavement Properties for Simulation

Layer	Thickness (in.)	Young's Moduli (ksi)	Poisson's ratio
1	10.23	725.19	0.35
2	19.68	29.01	0.40
3	infinity	7.25	0.45

* Pressure (q) = 145.039 psi, Tire Radius (a) = 5.94 in.

Figure 6.4 and Figure 6.5 show the vertical and horizontal strain distributions, respectively, for MASTIC and KENPAVE programs. In both cases, there is a good agreement between the strain distributions under the load center. The two programs show almost identical results except for the strain response at the top surface. As mentioned earlier, due to oscillatory nature of the Bessel Functions, the convergence rate is low at the surface and thus the solutions may lose the precision. Depending on the methods that were deployed by each program to overcome this issue, the results may differ from one program to another.

Figure 6.6 and Figure 6.7 present the pavement distribution for vertical and radial stresses, respectively, for both programs. The two programs have almost identical results for vertical stress response (Figure 6.6). From the boundry condition, the vertical pressure right underneath the load should equal the applied pressure which is properly given by both programs. However, there exists a small deviation at the surface radial stress between the two programs due to integration issue mentioned earlier. The same problem is seen in Figure 6.8 where the vertical deflection at the surface is slightly different in both programs. When processing the FWD results, the impercision in calculating deflection at the surface could potentially lead to erronous material properties. To investigate which program is providing more precise results at the surface, a third program, WESLEA, was used to simulate the same pavement cross section. The vertical deflections for

WESLA, MASTIC, and KENPAVE were compuated with different radial offsets at the surface. Figure 6.9 compares the result of all three programs where a close match was found between WESLEA and MASTIC. Since MASTIC takes the average of two consequtive Henkel function peaks, it is providing theoretically more precise results compared to other two programs. WESLEA results were found to be almost idential to MASTIC results at the surface.

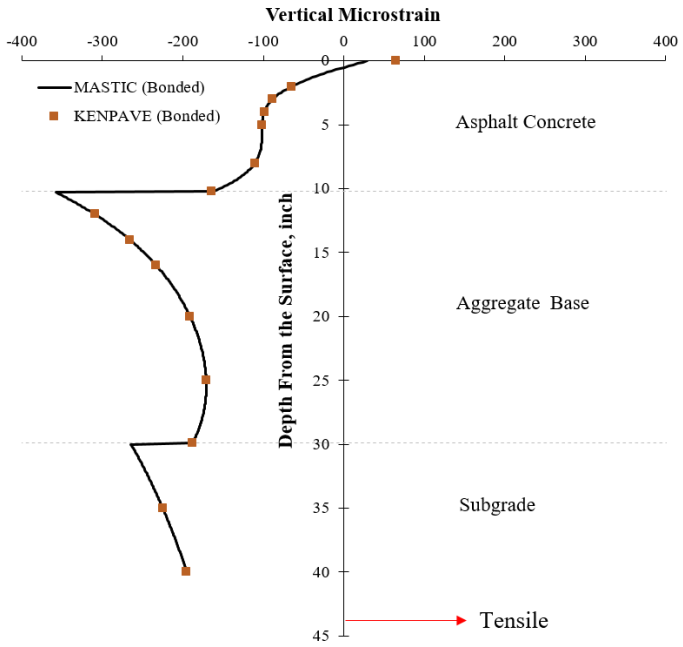

Figure 6.4 Vertical Strain Distributions for MASTIC and KENPAVE (r=0).

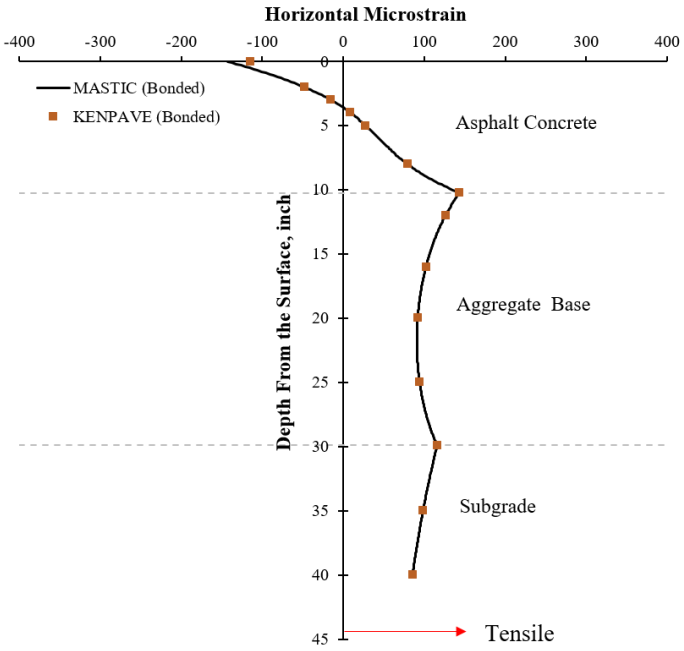

Figure 6.5 Horizontal Strain Distributions for MASTIC and KENPAVE (r=0).

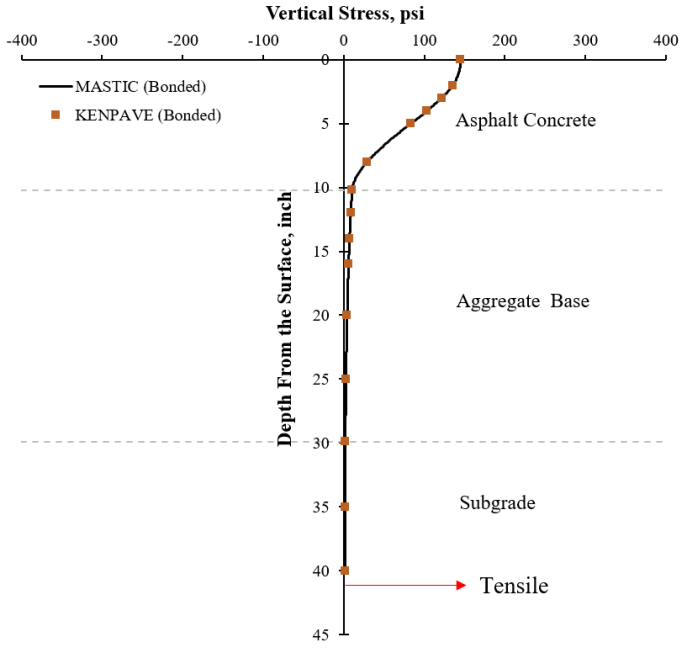

Figure 6.6 Vertical Stress Distributions for MASTIC and KENPAVE (r=0).

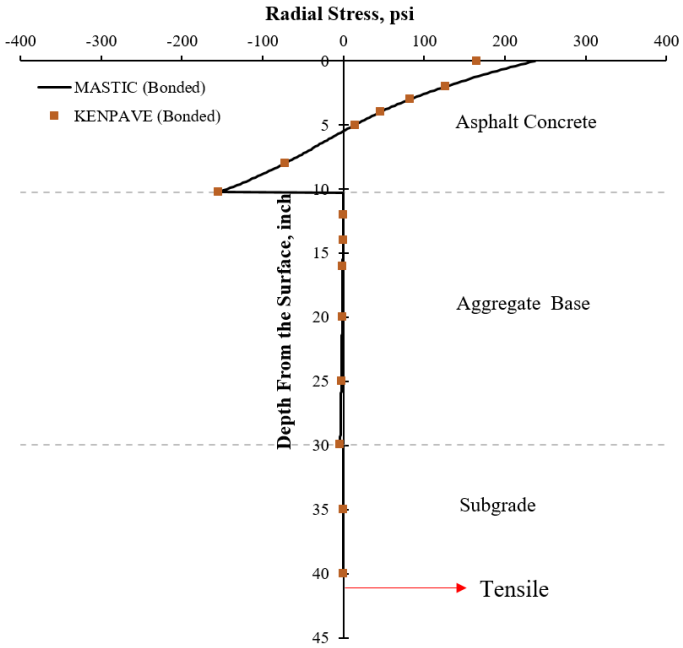

Figure 6.7 Radial Strain Distributions for MASTIC and KENPAVE (r=0).

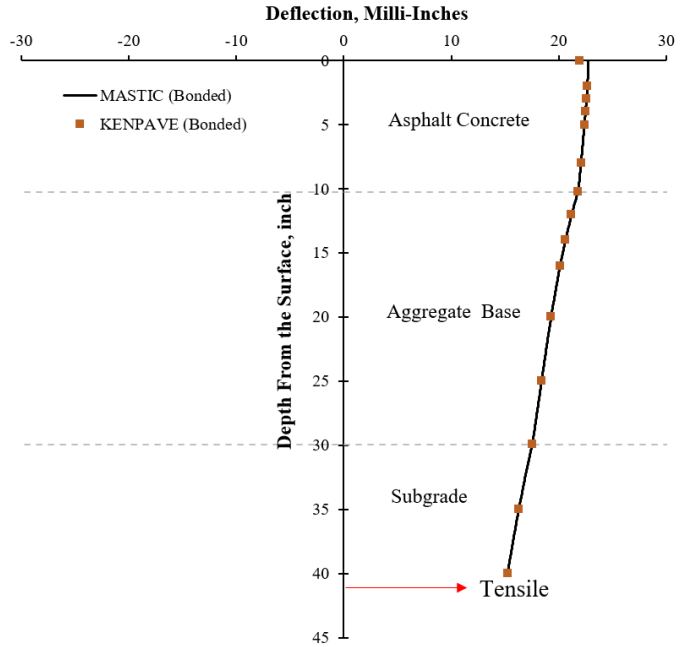

Figure 6.8 Vertical Deflection Distributions for MASTIC and KENPAVE (r=0).

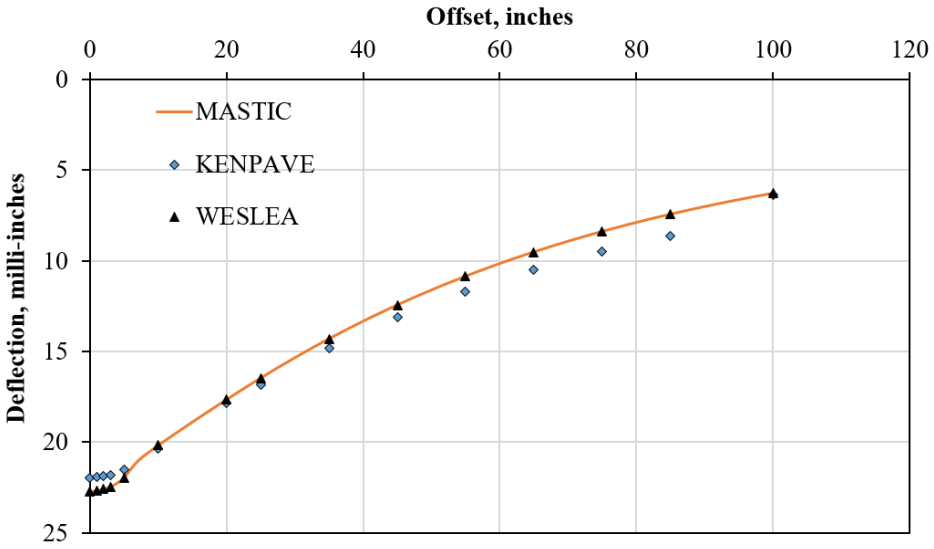

Figure 6.9 Deflection Basin for MASTIC, WESLEA, and KENPAVE (Z=0).

6.5.2. Backward Solution

The backward solution of MASTIC was compared against the EVERCALC program to ensure the basic functionality for backcalculating FWD data. To perform the comparison, the program outputs were compared for a conventional pavement section (Section N1) at the NCAT Test Track. An arbitrary date (12/03/2018) was chosen from the FWD database and backcalculation was performed using both programs with 747 deflection basins. The result of backcalculation for all basins are provided in Figure 6.10 through Figure 6.12. The pavement section was backcalculated assuming a three layer system. Both MASTIC and EVERCALC appears to have almost identical results for all deflection basins. Small variations can be explained by different optimization methods used in the programs and the different convergence level for the improper integral of the forward elastic solution. Although both programs provided almost identical results in a conventional pavement system with three layers, they may output different results for more complex structures with more than three layers. To investigate which program produces more accurate results, in the case of complex structures, a synthetic database composing of 100

randomly generated deflection basins was created. To create the database, the input values needed for multilayer elastic analysis were randomly generated between upper and lower values shown in Table 6.2. The load radius was considered to be 5.9 inches for all simulations. Next, given randomly generated elastic moduli, thicknesses, and loads, the deflection basins were generated for pre-defined radial offsets (0, 8, 12, 18, 24, 36, 48, 60, 72 inches) using the WESLEA program. These deflection basins were then used to backcalculate the elastic moduli using EVERCALC and MASTIC. Since the elastic moduli used for the deflection basin was known, each program was compared against the true elastic moduli to investigate their estimation capability.

Table 6.2 Inputs of Synthetic Database.

	AC	Base	Subbase	Subgrade
Modulus lower bound, ksi	80	10	10	10
Modulus Upper bound, ksi	3000	3000	1000	200
Thickness lower bound, in.	3	3	3	-
Thickness Upper bound, in.	20	10	10	-
Poisson's Ratio	0.35	0.2	0.4	0.45
Load Upper Bound, lb.			5000	
Load Upper Bound, lb.			20000	

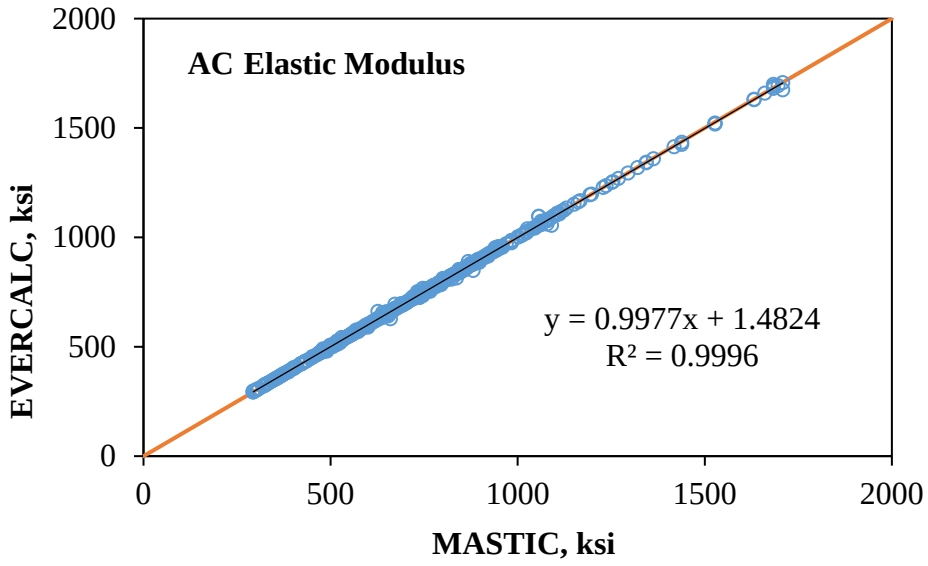

Figure 6.10 AC Elastic Moduli *C*omparison for Section N1 (12/03/2018).

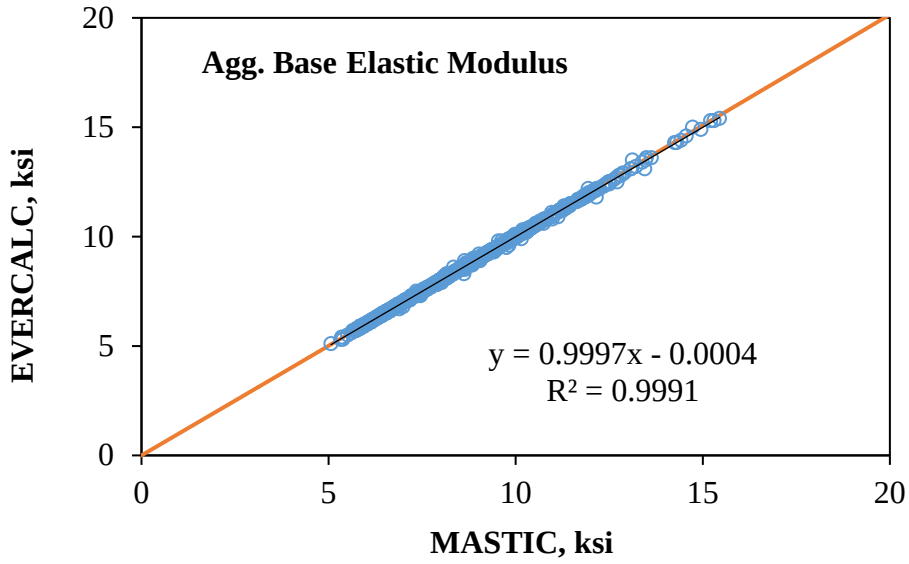

Figure 6.11 Base Course Elastic Moduli *C*omparison for Section N1 (12/03/2018).

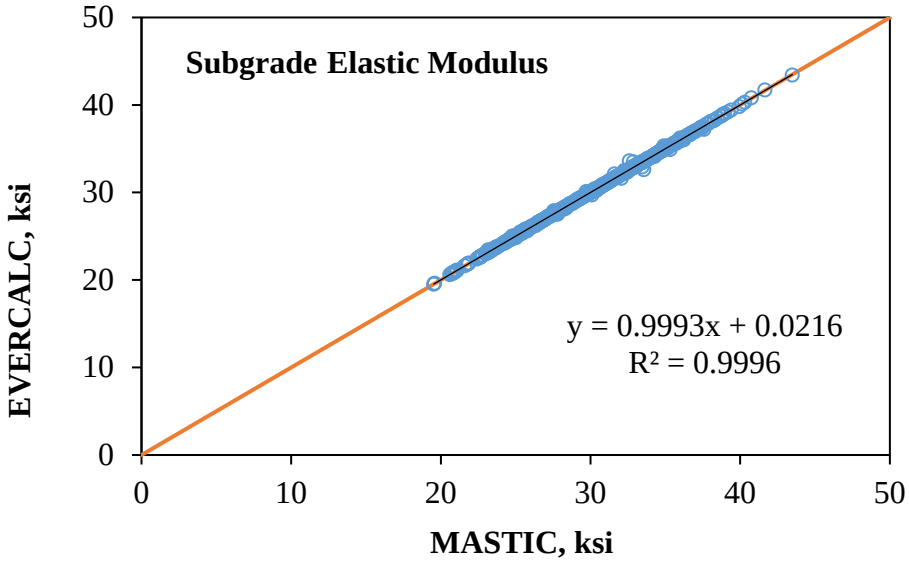

Figure 6.12 Subgrade Elastic Moduli *C*omparison for Section N1 (12/03/2018).

Figure 6.13 and Figure 6.14 present the result of backcalculation on the synthetic database for EVERCALC and MASTIC, respectively. EVERCALC showed good estimation results for AC and subgrade layers as evidence by high R square values. However, the program's results for the two intermediate layers were debatable. Aside from high variability in estimation of both layers'

moduli, it appeared that the moduli values for base and subbase were respectively under- and overestimated. In other words, the lower values of base were compensated by higher moduli of subbase, and vice versa. This emphasizes the fact that for sections with more than three layers, a more advanced optimization may be needed to achieve acceptable results.

Similarly, MASTIC results for AC and subgrade showed a good match with actual values. Compared to EVERCALC, the variability was smaller for AC and subgrade modulus estimation. The standard deviation of the difference of actual and estimated values are provided in Table 6.3. This table shows that for 100 randomly generated deflection basins, MASTIC outperformed the EVERCALC program in terms of variability since it has lower standard deviation in all moduli. MASTIC in particular output better estimations for the two intermediate layers as shown in Figure 6.14. In MASTIC simulation a default optimization method of "Interior-Point" was used which is different from EVERCALC optimization method. Similar to EVERCALC, the compensation effect can be seen from the two intermediate layers which sometimes is inevitable given the ill-posed nature of backcalculation optimization. This problem may be alleviated using global optimization techniques such as Genetic Algorithm methods; however, deploying such methods is significantly time consuming compared to traditional methods and there is no guarantee that the solution arrives at a global minimum.

Table 6.3 Standard Deviation for the Difference between Actual and Estimated Moduli

	AC	Base	Subbase	Subgrade
EVERCALC, ksi	454.19	922.83	417.15	11.41
MASTIC, ksi	201.43	342.93	228.60	2.69

In general, the pavement simulation results in this chapter showed that MASTIC produces almost identical results to other available well-established software programs such as WESLEA

and KENPAVE. Although the calculated results for pavement response at the surface were slightly different for MASTIC and EVERCALC, WESLEA and MASTIC showed consistent results at the surface. In theory, MASTIC should produce the most accurate results among the other two programs due to the modification used in the improper integral.

The backcalculation results of MASTIC demonstrated that this program could produce identical or more accurate estimation of the pavement system. In fact, due to a more advanced optimization technique used in MASTIC, this program can outperform EVERCALC in more complex pavement structures. However, it is possible to use similar optimization (Newton-Gausses) to achieve identical result with EVERCALC, if one wants to preserve consistency with historical data processed with EVERCALC.

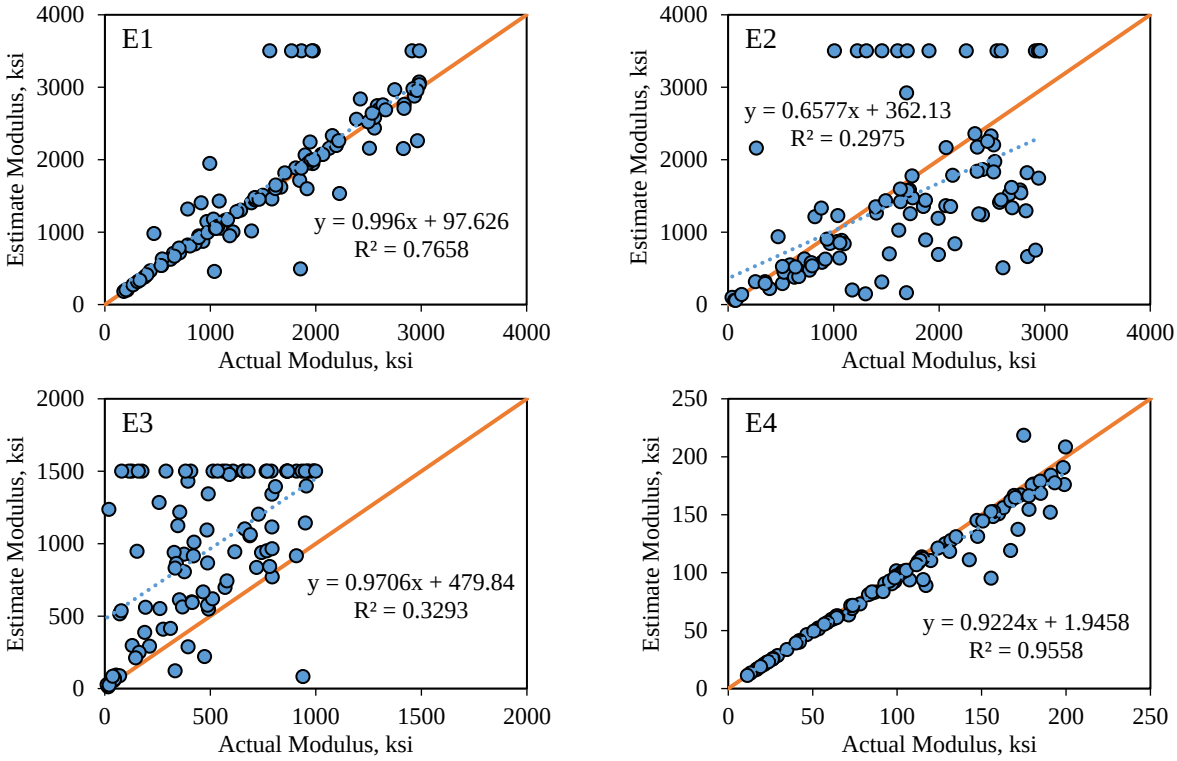

Figure 6.13 EVERCALC Backcalculation Results versus Actual Values.

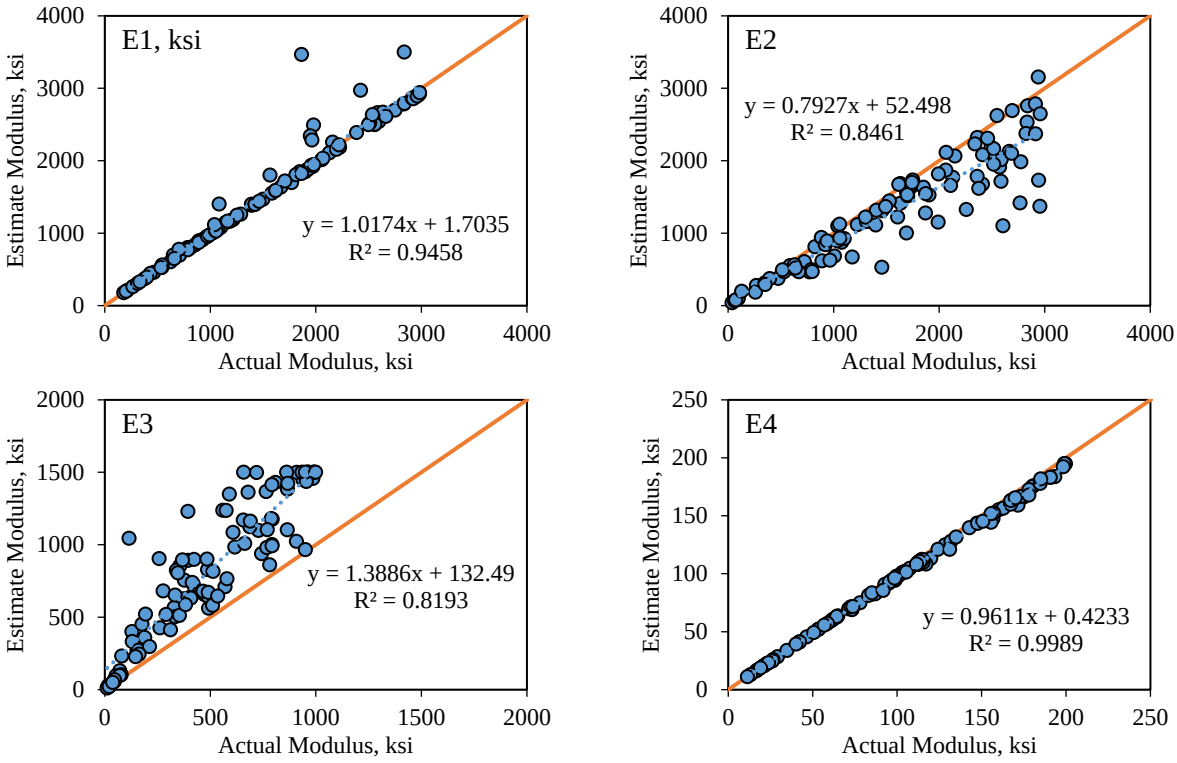

Figure 6.14 MASTIC Backcalculation Results versus Actual Values.

CHAPTER 7

PAVEMENT SIMULATION

As mentioned in Chapter 5, the direct strain and stress measurements at the Test Track suggested that there exists a fundamental difference in pavement responses of the stabilized foundation section (S2) compared to other conventional pavement sections. Thus, further investigation was made by simulating the four pavement sections under static and dynamic loading. The results of pavement simulations are presented in the following sections.

7.1. Static Pavement Simulation

The pavement sections were simulated to investigate their differences using the MASTIC simulation program. As discussed in Chapter 6, MASTIC was specifically developed for this research which uses the multilayer elastic theory. This program can perform various tasks such as calculating elastic response under static and dynamic load on multi-layer pavement structure and backcalculating pavement moduli under FWD loading events. Except for the stabilized foundation pavement (S2) that used MASTIC for backcalculation, backcalculation of the other sections were conducted with EVERCALC 5.0 software package. All backcalculation results are discussed in Chapter 8. Using conventional backcalculation software packages such as EVERCALC had been challenging for the stabilized foundation pavement (S2) due to presence of a very stiff cement treated layer. Issues with backcalculation of stabilized foundation pavements have also been reported by other researchers (Ozyildirim et al., 2017).

Using the backcalculation moduli as inputs to MASTIC, the pavement sections were simulated to investigate the differences in their behavior. The final input values for simulation are provided in Table 7.1. These values roughly represent the sectional moduli in winter and summer, but it is important to note that the purpose of these simulations was not to exactly replicate the pavement sections, but rather better understand the relative influence of material stiffness on pavement response, especially in the presence of a very stiff base layer. Table 7.1 presents the input values that were used for multi-layer elastic simulation which have been rounded off from actual backcalculated values. To simulate winter or summer conditions, the change in pavement temperature was simulated by the change in AC modulus. The two AC moduli values for each section represents summer (lower modulus) and winter (higher modulus) moduli.

Table 7.1 Simulated Pavement Section Properties

Section Name	Layers	Elastic Modulus (ksi)	Poison's Ratio	Thickness (in.)
Stabilized Foundation (S2)	Asphalt Concrete	2000 | 300*	0.35	9.2
	Cement Treated Base	2000	0.2	6.1
	Lime Treated Soil	100	0.4	5.5
	Mississippi Subgrade	30	0.45	inf.
Thick-Lift (S9)	Asphalt Concrete	2000 | 100*	0.35	8.1
	Aggregate Base	10	0.4	5.5
	Test Track Subgrade	30	0.45	inf.
CCPR (N4)	Asphalt Concrete	500 | 100*	0.35	8.2
	Aggregate Base	10	0.4	6.4
	Test Track Subgrade	30	0.45	inf.
CCPR with stabilized foundation (S12)	Asphalt Concrete	2000 | 300*	0.35	8.7
	Cement Treated Base	300	0.4	7.8
	Test Track Subgrade	30	0.45	inf.

** The value to the left represents winter (cold) and the value to the right represent summer (warm) moduli used for simulation. Tire pressure of 100 psi with tire radius of 5.9 inches used for all sections.*

Figure 7.1 illustrates the simulated horizontal microstrain versus depth for the thick-lift flexible pavement (S9). The thick-lift pavement acted like a conventional pavement section in

which the maximum horizontal strain occurred at the bottom of the AC. This is in good agreement with available literature and confirms previous Test Track findings on flexible pavement sections *(Ellison and Timm, 2011; Willis et al., 2011; Timm, 2009; Heitzman et al., 2019)*. It is generally believed that the maximum tensile strain causes bottom-up fatigue cracking in flexible pavement sections. Both summer (E1=100 ksi) and winter (E1=2000 ksi) response simulations showed that this section experienced maximum strain at the bottom of AC layer with smaller strain response in the winter due to stiffening effect of AC material. Also, the neutral axis in both simulations resided in the upper portion of the AC.

On the contrary, the analysis of the stabilized foundation pavement section (S2), simulated by assigning a very stiff base layer, revealed that the bottom of AC layer experienced dominantly compressive strain as opposed to tensile (Figure 7.2) in the summer when the AC modulus is low (E1=300 ksi). In summer, the maximum tensile strain occurred somewhere near the middle of AC layer instead of the bottom. The simulated compressive response at the bottom of the AC layer confirms the field strain measurements. The observation that the presence of a very stiff layer forces maximum horizontal strain to occur at shallower depth is important for several reasons. First, most M-E design methods only consider the bottom of the AC layer as the critical location for bottom-up fatigue cracking. Figure 7.2 and direct strain measurements on the stabilized foundation pavement section (S2) suggest that maximum tensile strain can occur somewhere other than the bottom of AC. Figure 7.2 also suggests that the fatigue cracking could actually initiate and propagate from near the mid-depth of the pavement section resulting in middle-up cracking. Also, when instrumenting pavement sections, the strain gauges are usually embedded at the bottom of the AC layer while the model suggests that maximum tensile response could occur somewhere other than the bottom. The compressive strain response at the bottom of the AC layer was already

observed through full scale field measurements as discussed in Chapter 5. Figure 7.2 also illustrates the simulated strain response for winter weather condition with relatively higher AC modulus (E1=2000 ksi). The analysis shows that in winter, the AC bottom is in tension which is consistent with the field measurements. A stabilized foundation section with higher AC modulus acts like a conventional flexible pavement with maximum tensile strain occurring at the bottom of the AC layer. The simulation of both low and high AC moduli confirmed the field measurements of the stabilized foundation pavement (S2) in summer and winter.

It is important to note that although the stabilized foundation pavement section (S2) was simulated as a 4-layer system, the maximum tensile strain can occur in any other pavement system with thick AC on top and stiff foundation underneath regardless of the pavement setting. In fact, a thick layer on top and a stiff foundation at the bottom are favorable conditions for maximum tensile strain to occur at shallower depth. Increases in either condition increases the possibility of maximum tensile strain to occur at shallower depths. Further discussion on this subject is provided in Section 7.2.

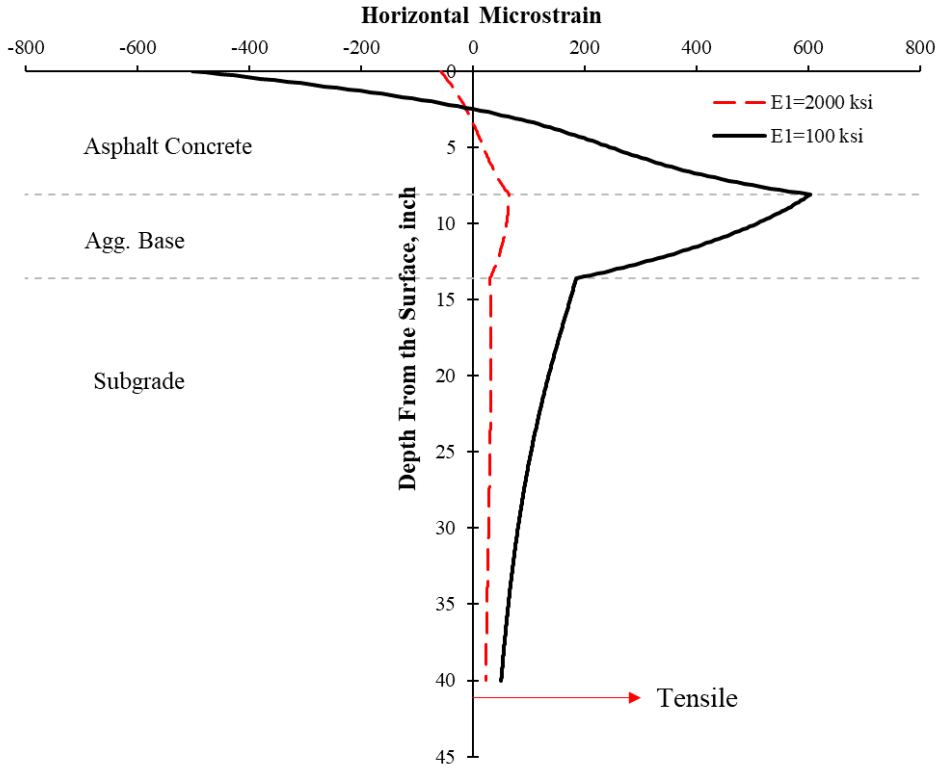

Figure 7.1 Strain Distribution of the Simulated Thick-Lift Section Pavement Section (S9).

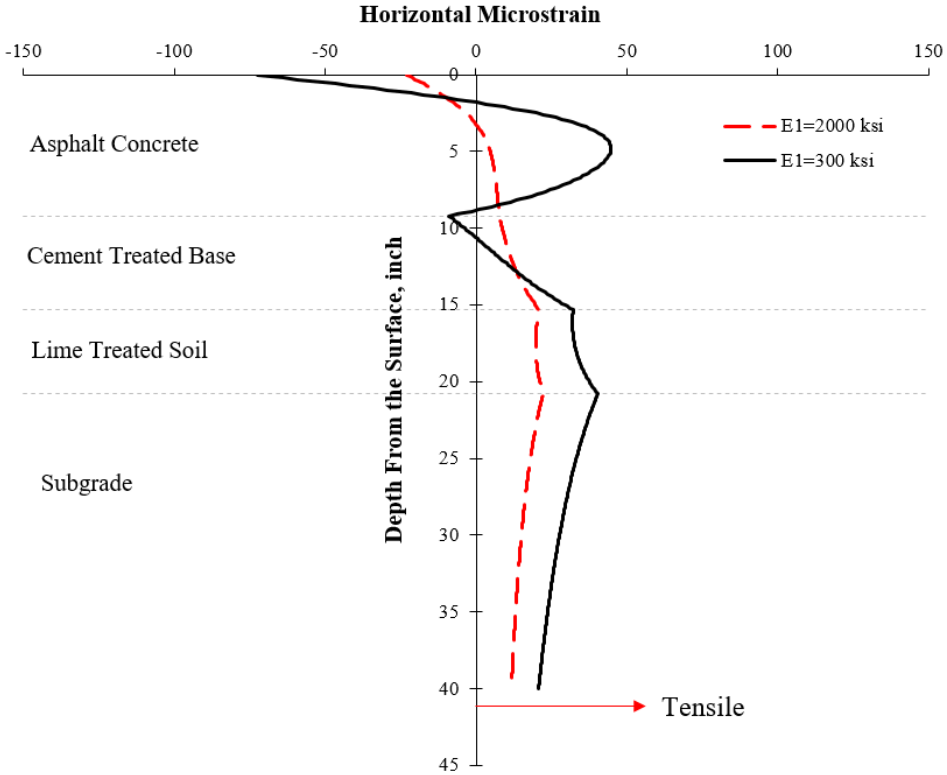

Figure 7.2 Strain Distribution of the Simulated Stabilized Foundation Section (S2).

To understand the unique behavior of the stabilized foundation pavement section (S2), the CCPR with stabilized foundation section (S12) was also simulated along with the CCPR section (N4). The comparison of the CCPR with stabilized foundation (S12) and the stabilized foundation pavement section (S2) was important since both sections featured a cement treated base which provided a base for comparison of the relative influence of the base stiffness. Figure 7.3 illustrates the analysis of the simulated CCPR with stabilized foundation section (S12). The simulated strain distribution for both summer (E1=300 ksi) and winter (E1=2000 ksi) indicate positive (tensile) strain at the bottom of AC layer which is consistent with field-measured data as discussed in Chapter 5. It is also interesting to note that for summer response (E1=300 ksi), the maximum tensile strain occurred near the bottom the AC and not necessarily at the bottom. The depth of simulated maximum tensile strain was determined to be 6.7 inches. This further highlights the fact that for stabilized pavement sections, the maximum tensile strain could occur somewhere other than the bottom of AC layer. As will be discussed in Section 7.2, given a thick AC layer, a higher ratio of base to AC modulus can trigger a condition where the maximum tensile strain resides somewhere other than the bottom of AC layer.

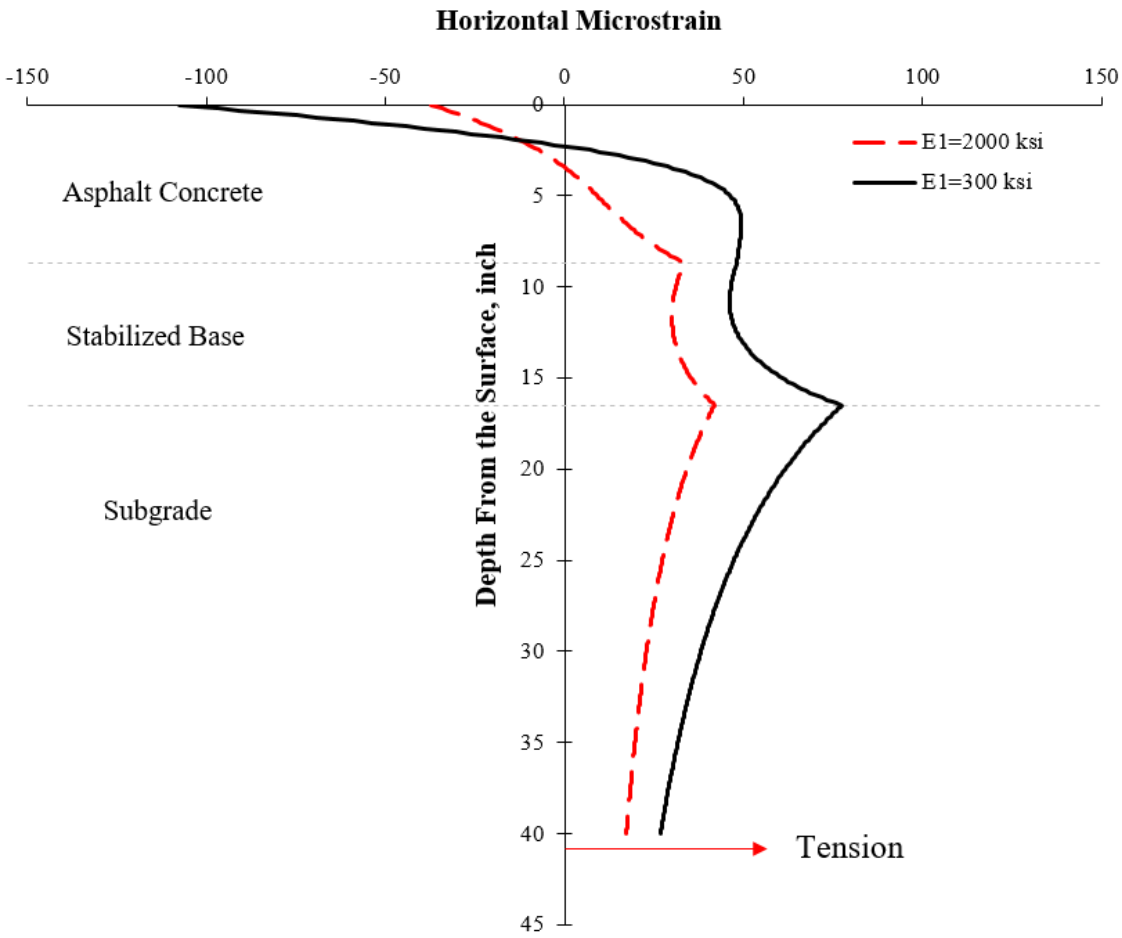

Figure 7.3 Strain Distribution of the Simulated CCPR with stabilized foundation Pavement Section (S12).

Figure 7.3 also suggests a peak tensile strain occurring at the bottom of the stabilized base layer regardless of the AC modulus. Its magnitude is higher in summer when the AC modulus is low. Given the fact that stabilized layers are not designed to tolerated high tensile strain levels, a peak tensile strain at the bottom of the stabilized layer can trigger bottom-up cracking that starts from the bottom of the base layer. This can be confused with shrinkage cracking which is a prevailing mode of failure for these sections. Thus, the design of the stabilized foundation sections should consider the fatigue cracking that can potentially start from the bottom of the stabilized layer.

To elaborate on the difference in simulated strain distribution in the stabilized foundation sections, the CCPR (N4) strain distribution was also investigated since this section was built to replicate the CCPR with stabilized foundation section (S12) but with crushed aggregate base. Figure 7.4 depicts the simulated strain distribution of the CCPR section (N4) for winter (E1=500 ksi) and summer (E1=100 ksi) conditions. It is important to note the moduli selected for N4 based on FWD backcalculation process is lower than other sections because this section experienced accumulated damage in 2018 research cycle. In addition, the top layer in layer in backcalculation process was considered to be the combination of AC and CCPR layer. As shown, the strain distribution of the CCPR section (N4) was very similar to the thick-lift pavement section (S9) since both sections featured crushed granite base materials. Similar to the thick-lift pavement section (S9), the simulated maximum tensile strain response for both summer and winter occurred at the bottom of AC layer which confirms the field measurements and the current state-of-the-art practice for the structural design of asphalt pavements.

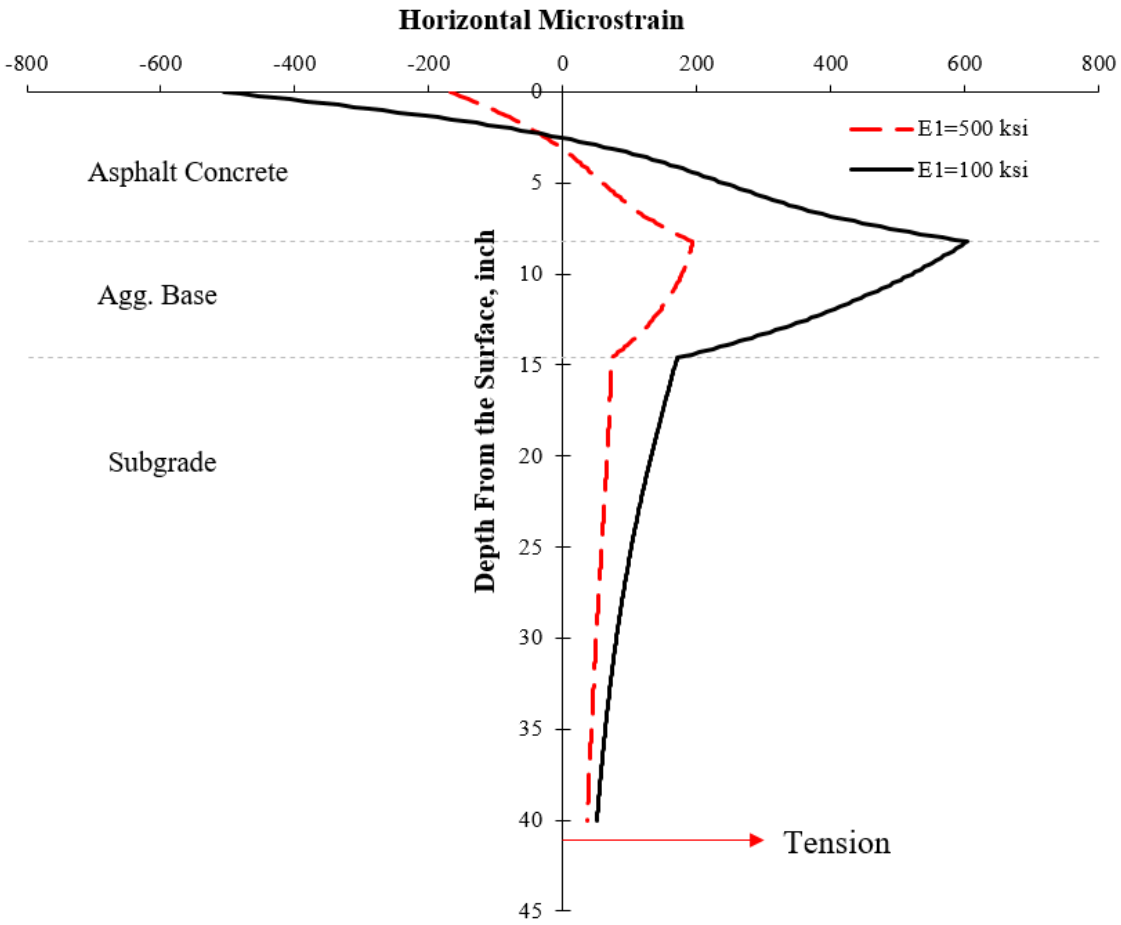

Figure 7.4 Strain Distribution of the Simulated CCPR Pavement Section (N4).

In Chapter 5, the field stress responses at the bottom of the AC layer were compared among the four sections. Likewise, all four sections were simulated for the stress response throughout the pavement depth for summer (Figure 7.5) and winter (Figure 7.6) conditions. The circle markers in each figure represents the location of layer interfaces for each pavement section. The analysis for summer response shows that having a stiff base layer actually increases the pressure in base and AC layer as evident in the cases of sections S12 and S2 which featured cement treated base material. However, they experience lower vertical pressure on top of the subgrade soil which helps reduce the structural rutting. Thus, in sections featuring stabilized layers, the vertical stress is higher in base and AC layers, but it is smaller in lower layers and in subgrade. The reduced pressure

on top of the subgrade highlights the benefits of the stabilized foundation layers as a support to subgrade. Also, similar to the measurements, the stress on top of the base layer was higher in the stabilized foundation section (S2) compared to other sections (refer to Chapter 5).

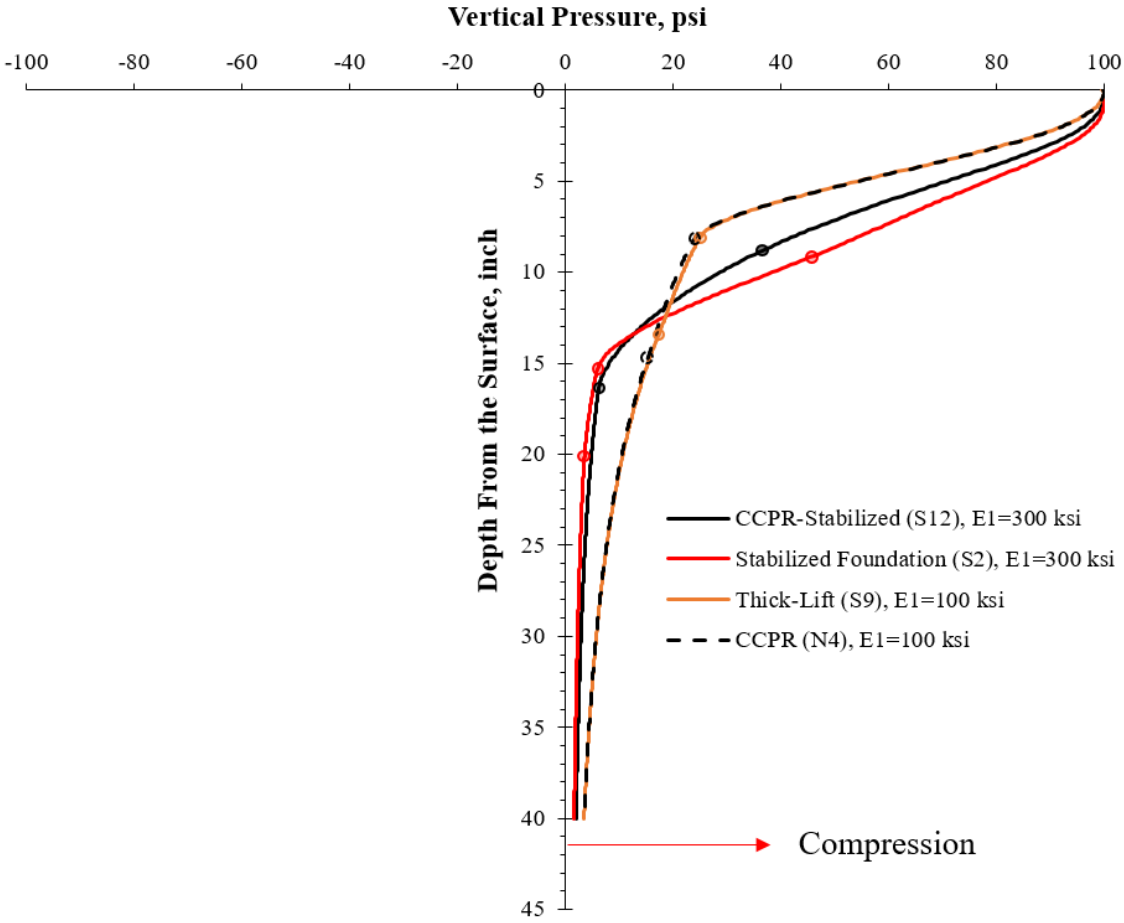

Figure 7.5 Pressure Distribution of the Simulated Pavement Sections for the Warm Weather Condition.

Figure 7.6 shows the same configuration but with higher elastic moduli for the AC layers to simulate the winter condition. Again, the stabilized foundation pavement (S2) had the highest simulated pressure within AC and base layers followed by the CCPR with stabilized foundation pavement (S12). The higher elastic moduli for the stabilized layers did result in higher pressure in upper layers. However, the stress response on top of the subgrade approached to similar values for

all sections in winter. The CCPR section (N4) experienced slightly higher pressure on top of the subgrade compared to other sections.

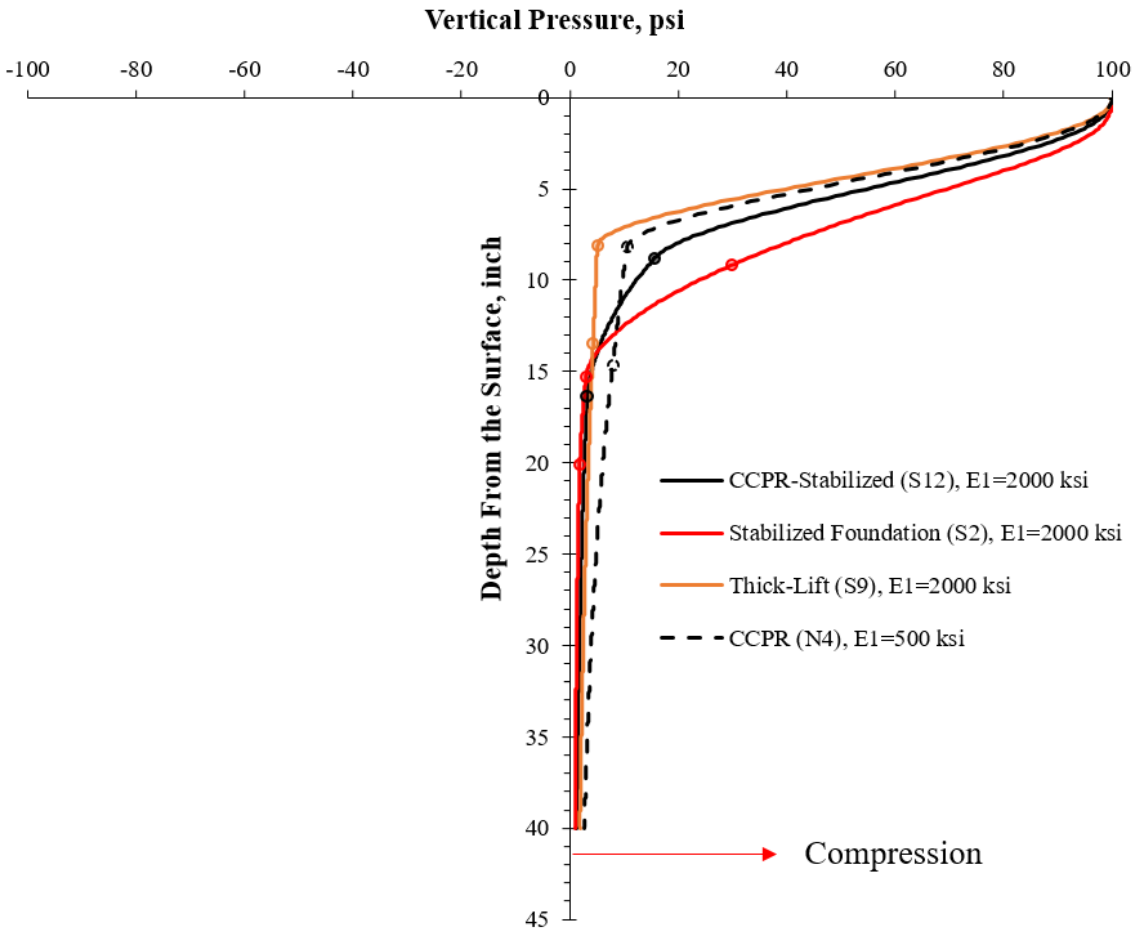

Figure 7.6 Pressure Distribution of the Simulated Pavement Sections for the Cold Weather Condition.

7.2. Sensitivity Analysis

To understand the stabilized foundation pavement (S2) behavior better, further analyses were conducted on the pavement sections, and in particular section S2, by alternating input values for multi-layer elastic solution.

7.2.1. The Effect of Bonding Condition

All analyses presented above were carried out assuming full bonding between pavement layers. This assumption may or may not be true. Further analyses were conducted to investigate the effect of bonding conditions on the location of the maximum tensile strain throughout the pavement thickness. Figure 7.7 illustrates the strain distribution of the stabilized foundation pavement (S2) in summer condition where the AC modulus is low (E1=300 ksi) with varying bonding conditions of the AC/CTB interface. The other two interfaces were assumed to be bonded for this simulation. Bonding condition was simulated by a horizontal spring. As was discussed in Chapter 6, setting the horizontal spring constant (K_1) to infinity results in fully bonded condition while setting it to zero results in full slip condition. The partial condition can be obtained by selecting any value between these two extremes. In the case of fully bonded, the maximum tensile strain occurs near the mid-depth, and the bottom of AC layer is in compression. When the K_1 value is set to zero, as shown in Figure 7.7, the bottom of the AC experiences a relatively large tensile strain while the top of the CTB experiences a compressive strain. In general, the higher bonding condition is a favorable condition since it results in smaller strain magnitudes. The partial friction conditions represent an intermediate state between fully bonded and slip conditions. The higher the friction value, the more favorable condition.

Based on this analysis, only by having strain response measurements at the bottom of the AC layer, one cannot determine whether the stabilized foundation pavement (S2) is fully or partially bonded. It is recommended that in future studies strain gauges be embedded at various depths to capture the strain distribution throughout the pavement thickness or at least throughout the AC layer. However, it is likely that the stabilized foundation section (S2) is strongly bonded if not fully bonded since prime coat was used to seal the CTB layer which can act as a bonding agent between the two layers. In addition, the measured strain response was negative at the bottom of the AC layer (as discussed in Chapter 5) which resembles the fully or strongly bonded condition.

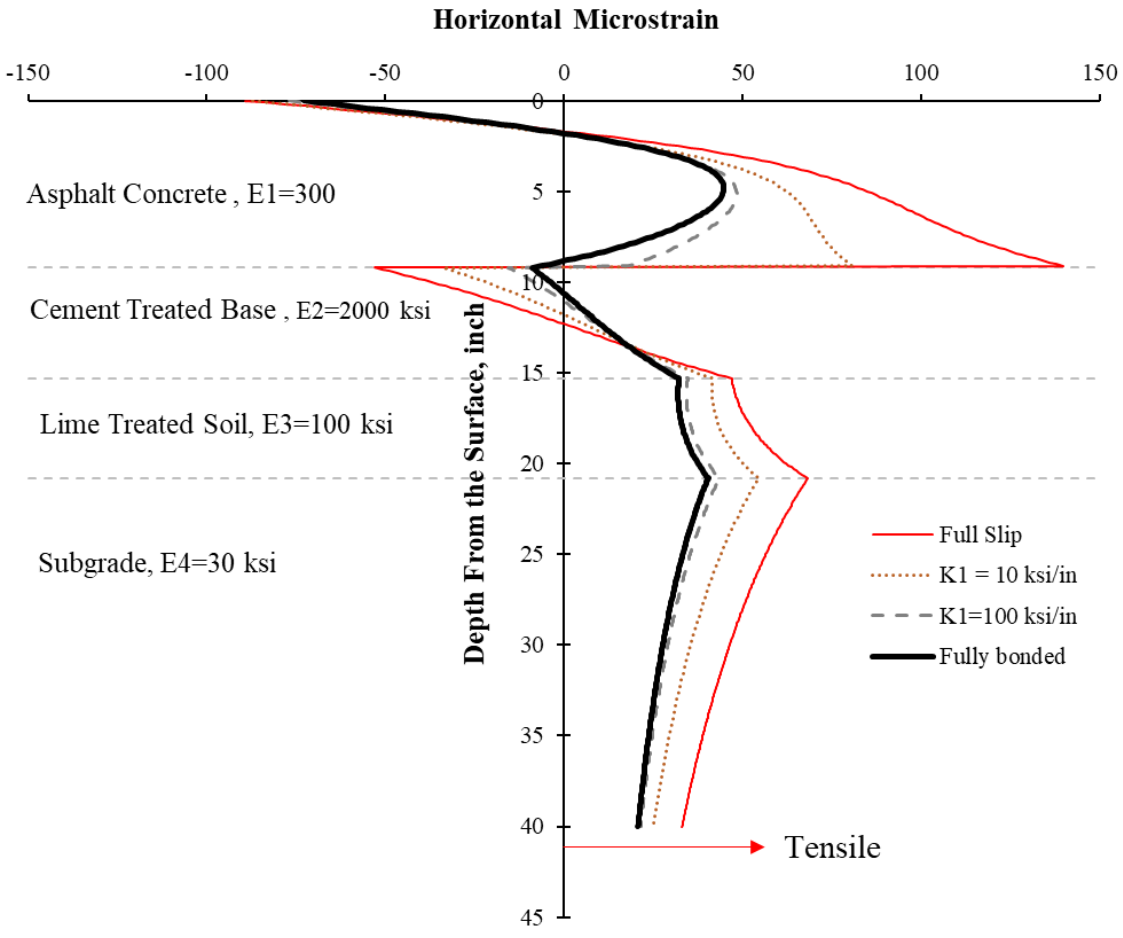

Figure 7.7 The Effect of Different Bonding Condition on the Simulated Strain Distribution for the Stabilized Foundation Pavement Section (S2) in Summer Condition (E1=300 ksi).

Figure 7.7 was based on the assumption that all interfaces are bonded except for AC/CTB interface which could vary from fully bonded to fully unbonded. To investigate the effect of bonding in all layers, Figure 7.8 has the same configuration but with varying interface bond conditions for the entire pavement section. This time the horizontal spring constant for all interfaces was set to 10 ksi/inch to simulate the partial friction. The slip condition was obtained by setting the K to zero while the fully bonded condition was calculated by setting this value to infinity. As shown, the strain at all interfaces in fully unbonded (slip) condition experiences both tensile and compressive mode. Also, the magnitude of horizontal strain is higher in the fully unbonded condition. It is also important to note that the maximum tensile strain in fully slip condition resides at the bottom of AC layer similar to regular flexible pavements with unbound base materials. The partial condition represented an intermediate state between the fully bonded and fully unbonded condition. Depending on the bonding stiffness, the distribution can be similar to fully bonded or fully unbonded condition. In summary, one can conclude that having a bonded pavement interface is crucial to obtain high quality pavement section especially for stabilized foundation sections. Also, to understand the true distribution of strain response, strain gauges should be embedded in multiple depths of AC layer. Since simulation of other pavement sections for varying bonding interfaces added no additional information, they were not included here for the sake of brevity.

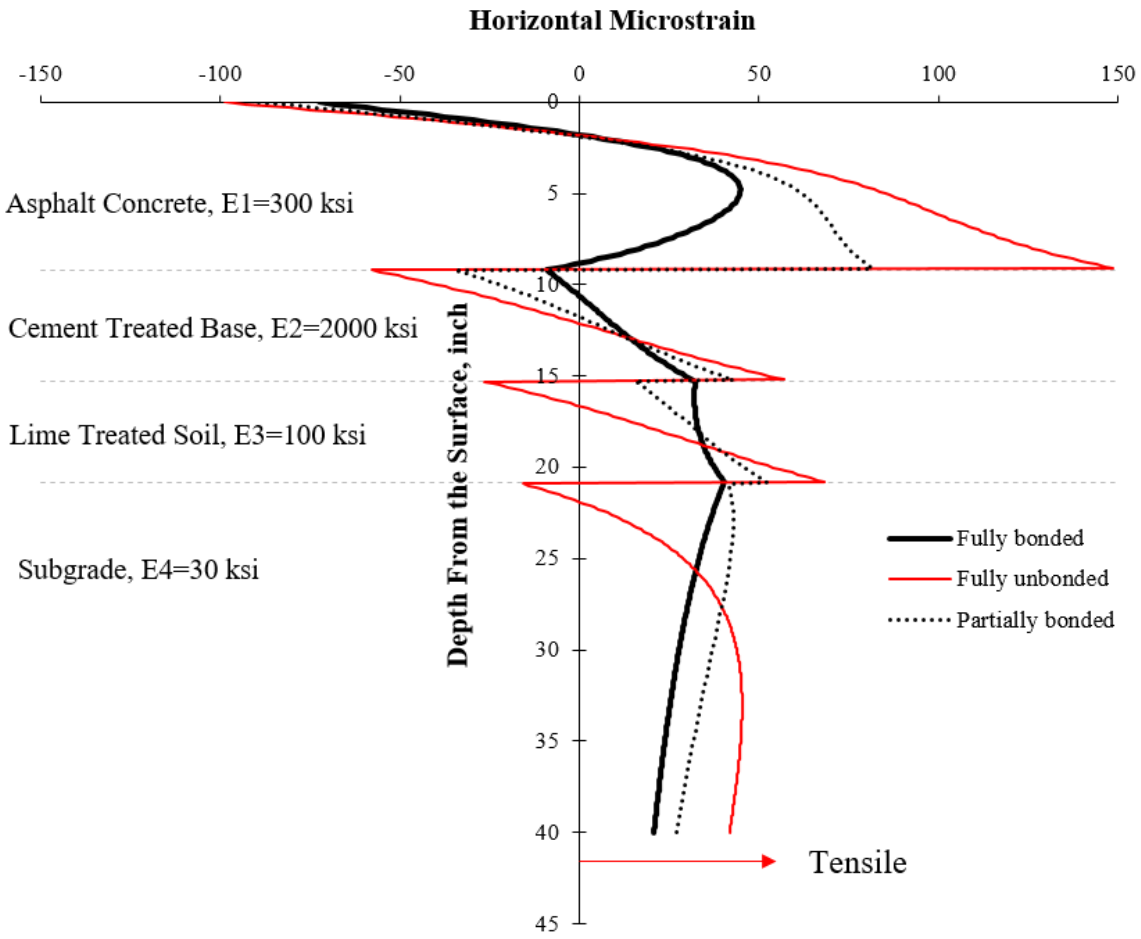

Figure 7.8 Fully Bonded, Partially Bonded, and Fully Unbonded Strain Distribution Simulation for the Stabilized Foundation Pavement Section (S2).

7.2.2. The Effect of Pavement Modulus

As shown in Chapter 5, the observed tensile strain response for the stabilized foundation pavement (S2) was almost insensitive to temperature and even reduced as temperature increased. The simulations conducted so far have shown that the underlying stabilized base layer, assuming it is stiffer than the overlying AC layers, can potentially constrain the AC layer from bending, and thus affecting the strain response near the bottom of the AC layer. Thus, the stabilized foundation pavement section (S2) was again simulated where the increase in temperature was represented by decreasing the AC modulus. In this simulation, the horizontal strain at the bottom of the AC layer

was plotted against the varying AC modulus. In addition, four base moduli were considered in this simulation to also investigate the effect base modulus.

Figure 7.9 and Figure 7.10 show tensile strain results in both the bonded and unbonded conditions, respectively. The top series (E2=10 ksi) in Figure 7.9a, where the AC modulus is always greater than or equal to the base modulus, is similar to a conventional flexible pavement where the tensile strain increases exponentially with decreases in AC modulus (or increases in temperature). Moving down to the next series in Figure 7.9a (E2=50 ksi) shows a lower magnitude tensile strain, as expected, since the stiffer supporting layer is limiting the overall AC bending. For E2=300 ksi, the general trend is upward until the AC modulus almost equals the base modulus (300 ksi). At that point, the tensile strain begins to decrease indicating the base layer is further restraining the bending action of the AC layer which becomes more pronounced as the AC modulus reduces relative to the base layer modulus. Similar behavior is noted in the E2=2000 ksi series, but the inflection point occurs at beginning of this series. Thus, it only shows a downward trend since the base modulus always exceeds the AC modulus. The bottom two series (E2=300 ksi and E2=2000 ksi) are replotted in Figure 7.9b with adjusted vertical scale to illustrate their behavior more clearly. A closer look on the stiffer base conditions highlights the effect of base layer. In Chapter 5, it was shown that the compressive strain response at the bottom of AC layer for stabilized foundation section (S2) follows a negative exponential trend which is very similar to simulated strain response for E2=2000 ksi series in Figure 7.9b.

For the unbonded condition (Figure 7.10) where the layers were free to slip along their interfaces, the decrease in AC modulus values accompanied exponentially increasing tensile strain for all base conditions. This analysis again emphasizes the importance of bonded layers in stabilized foundation pavements.

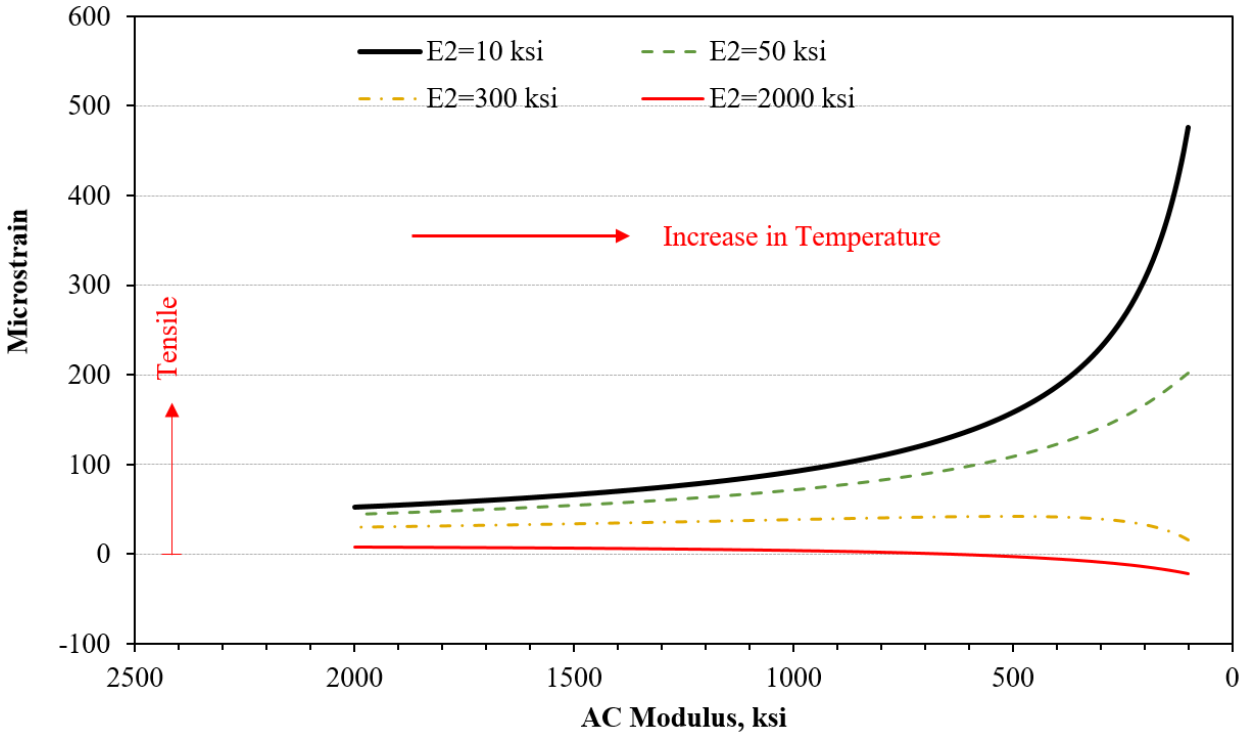

a) All Base Conditions

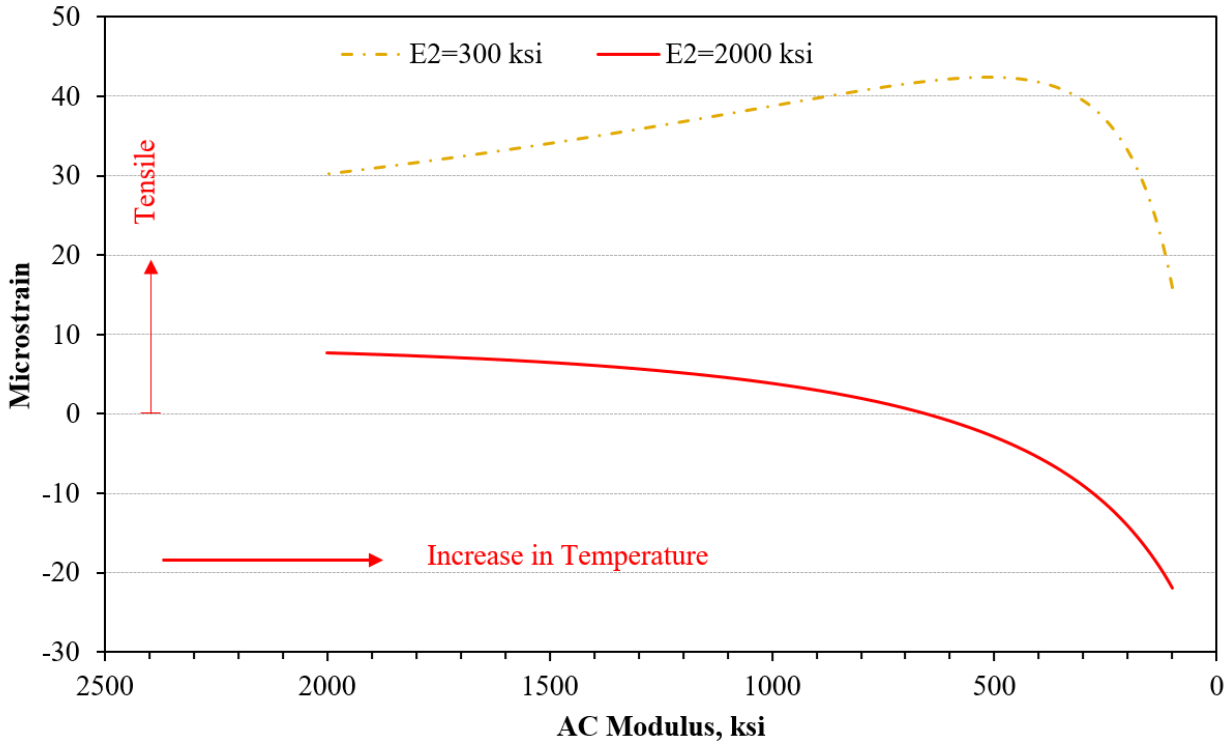

b) Stiffer base conditions

Figure 7.9 Simulated Horizontal Strain Responses using MASTIC for Fully Bonded Interfaces.

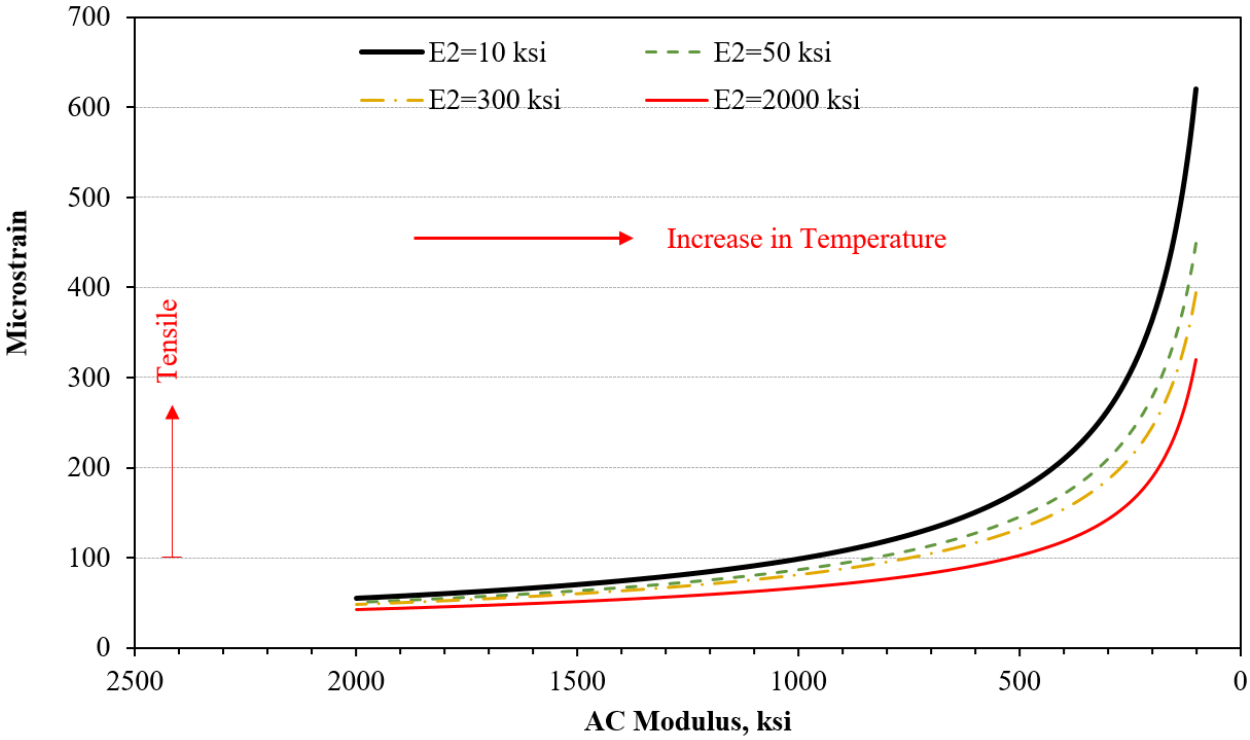

Figure 7.10 Simulated Horizontal Strain Responses using MASTIC for Fully unbonded Interfaces.

7.2.3. The Effect of Pavement Thickness

Although the maximum tensile strain in the middle of AC layer was found by simulating the stabilized foundation pavement section (S2) which was a 4-layer system, this can occur in any other pavement system with thick AC layer on top and stiff foundation underneath. Increases in either base modulus or AC thickness can increase the possibility of maximum tensile strain to occur at shallower depths. However, if the AC layer is thin enough, the maximum tensile strain could occur at the bottom of the CTB and the AC layer would be completely in compression. This is a critical finding for stabilized foundation pavements with thin layers of AC on top because the CTB layer is not generally designed to withstand tensile strain. In fact, excessive tensile strain at the bottom of the CTB could initiate the bottom-up fatigue cracking that could reflect through the

AC layer. These tensile cracks, if formed, may be confused by other type of cracks such as shrinkage cracking which is believed to be one of the main contributors of CTB pavement deterioration. Figure 7.11 shows a CTB pavement section simulation under the same configuration described earlier for stabilized foundation (S2) simulation but with a thinner pavement section (with AC thickness of 4.0 inches). As explained above, the AC layer in the thinner pavement section (Figure 7.11b) can experience full compressive mode throughout the AC layer whereas the maximum horizontal strain can occur at the bottom of CTB layer. This figure demonstrates that having a stiff layer at the bottom of the wearing course does not necessarily force the maximum tensile strain to reside at around the mid-depth. In fact, a combination of thick AC and high base modulus should exist to force the maximum tensile strain to occur at around the mid-depth.

Another interesting behavior that can be seen from Figure 7.11 and Figure 7.12 is the effect of AC thickness on critical pavement responses. While the choice of a thick AC layer has always been considered conservative in pavement engineering, it can produce higher tensile strain at shallower AC depths in stabilized foundation pavements (Figure 7.12b). As the AC thickness increases, the magnitude of the maximum tensile strain increases while its depth of occurrence remains almost unchanged. Thus, the choice of a very thick layer for increasing structural performance should be carefully considered since it may lead to middle-up fatigue cracking in pavements with high base modulus. On the other hand, the choice of a thin AC layer (Figure 7.11) for a stabilized foundation pavement section can produce excessive tensile strain at the bottom of CTB layer which is not generally designed to tolerate tensile strain. Having this choice may result in reflective cracking initiating from the bottom of CTB all the way up to the pavement surface which could be expensive to repair. Thus, one should balance the choice of AC thickness and base modulus to minimize tensile strain in both layers.

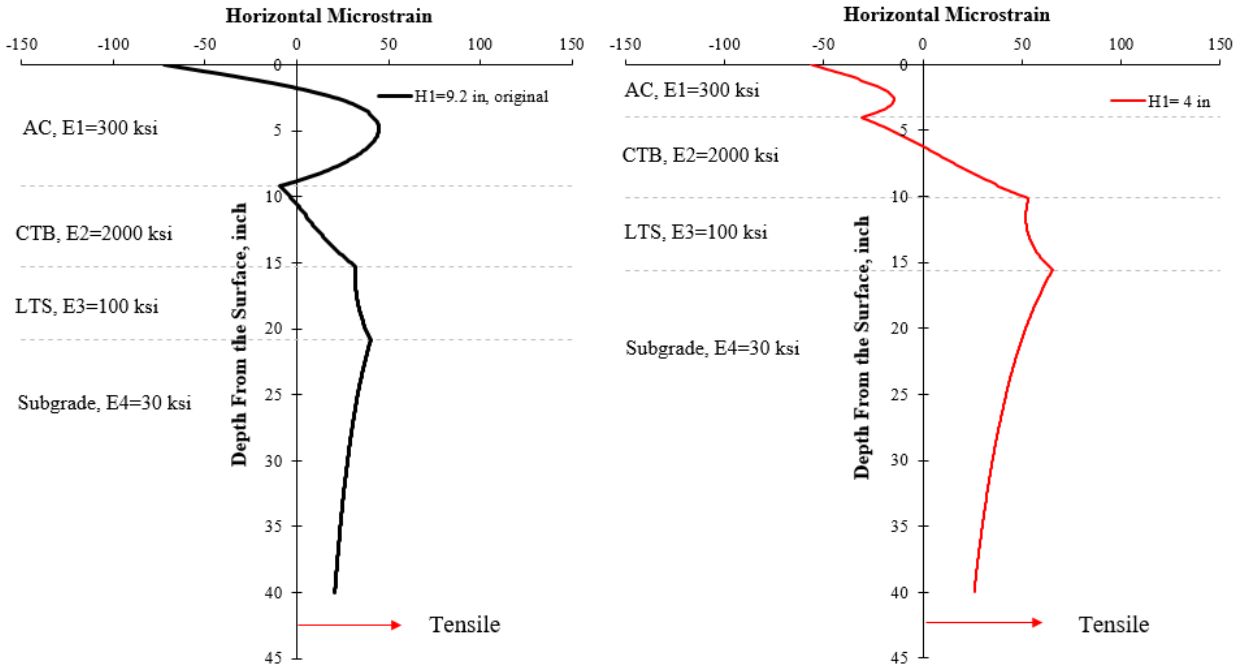

a) Original Cross Section b) Thinner Cross Section

Figure 7.11 Simulated Strain versus Depth for Thin and Original AC thicknesses.

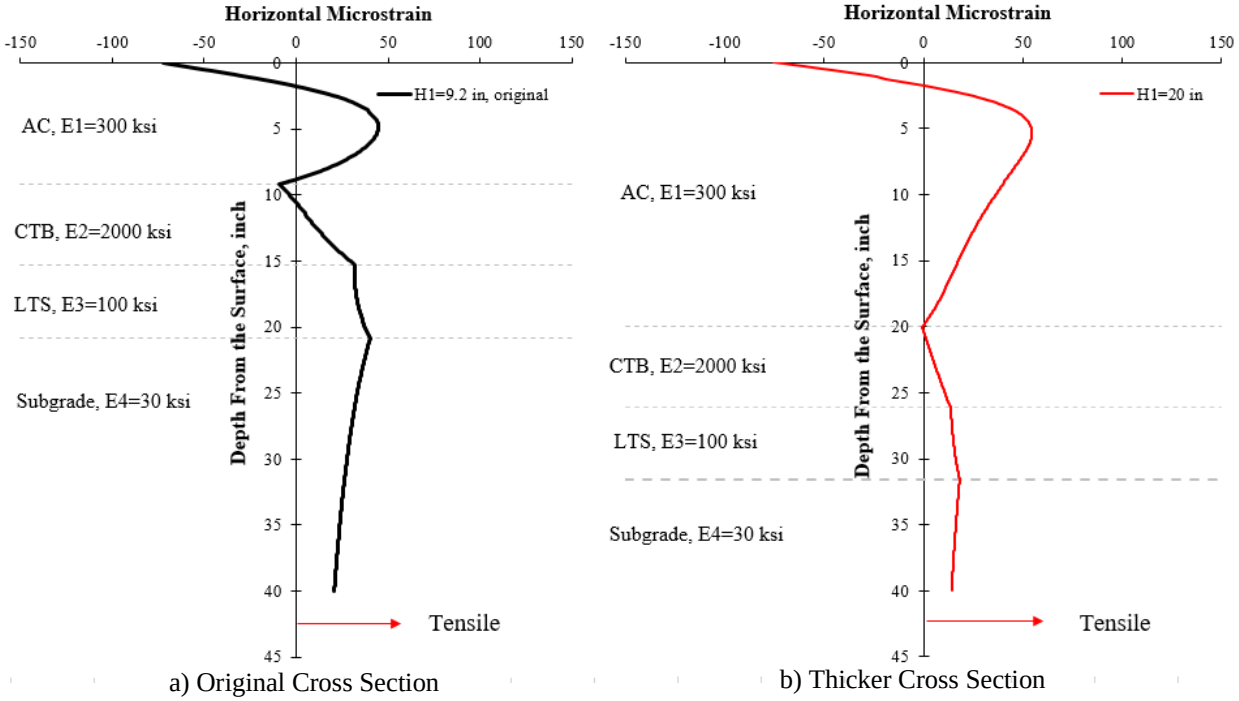

a) Original Cross Section b) Thicker Cross Section

Figure 7.12 Simulated Strain versus Depth for Thick and Original AC thicknesses.

If a stabilized foundation pavement section can experience maximum horizontal strain somewhere other than the bottom of AC, can a conventional flexible pavement experience it too? Based on literature review on this topic and many field measurements, the answer to this question is negative. Currently, all M-E designs assume the maximum tensile strain at the bottom of the AC layer regardless of the pavement settings. However, since the stabilized foundation pavement simulation had already shown that this premise cannot be held true for all circumstances, another set of simulation was conducted in which different combinations of pavement thickness and elastic modulus were considered for flexible pavements with crushed aggregate base. This time, the thick-lift pavement section (S9) was simulated with original and thicker AC thicknesses (8.1 in. and 15 in.) as well as different elastic modulus of the base layer of 10 ksi (original) and 50 ksi (stiffer base). The horizontal strain distribution throughout the depth of the simulated pavements were obtained for this scenario which is shown in Figure 7.13. This figure presents an interesting behavior about the effect of thickness and base modulus on horizontal strain response. Figure 7.13b suggests that in thick flexible pavement sections there could exist a secondary significant tensile strain at shallower AC depth. If the pavement section is thick enough, the secondary significant tensile strain could exceed the one at the bottom. This maximum tensile strain depends on two factors, the base to AC modulus ratio and the AC thickness. The increase in either one can force maximum tensile strain to reside at shallower depths. It is important to note that as the base modulus gets closer to the AC modulus (or possibly surpasses AC modulus in stabilized foundation pavements), the maximum tensile strain at the bottom of the AC migrates toward the surface. The effect of increasing base modulus is similar to the effect of AC modulus reduction in which both results in maximum tensile strain at shallower depths. The decrease in AC modulus over time due to pavement damage or due to hot weather conditions can shift the maximum tensile strain to

shallower depth in thick flexible pavements which could be more critical than the bottom of the AC since the maximum tensile strain could reflect through the surface easier.

This finding is important for several reasons. First, it suggests even flexible pavement sections can experience maximum tensile strain at shallower depths while M-E design analysis for fatigue criterion is purely based on the bottom-up or top-down criteria. Second, in designing perpetual pavements, which favors implementation of thick AC lifts with stronger foundation, more emphasis should be given to intermediate layers where maximum or secondary maximum tensile strain could potentially form. Third, in instrumentation of pavement sections with thick-lifts, mid AC layers should also be considered as critical layers especially if the base course has higher stiffness.

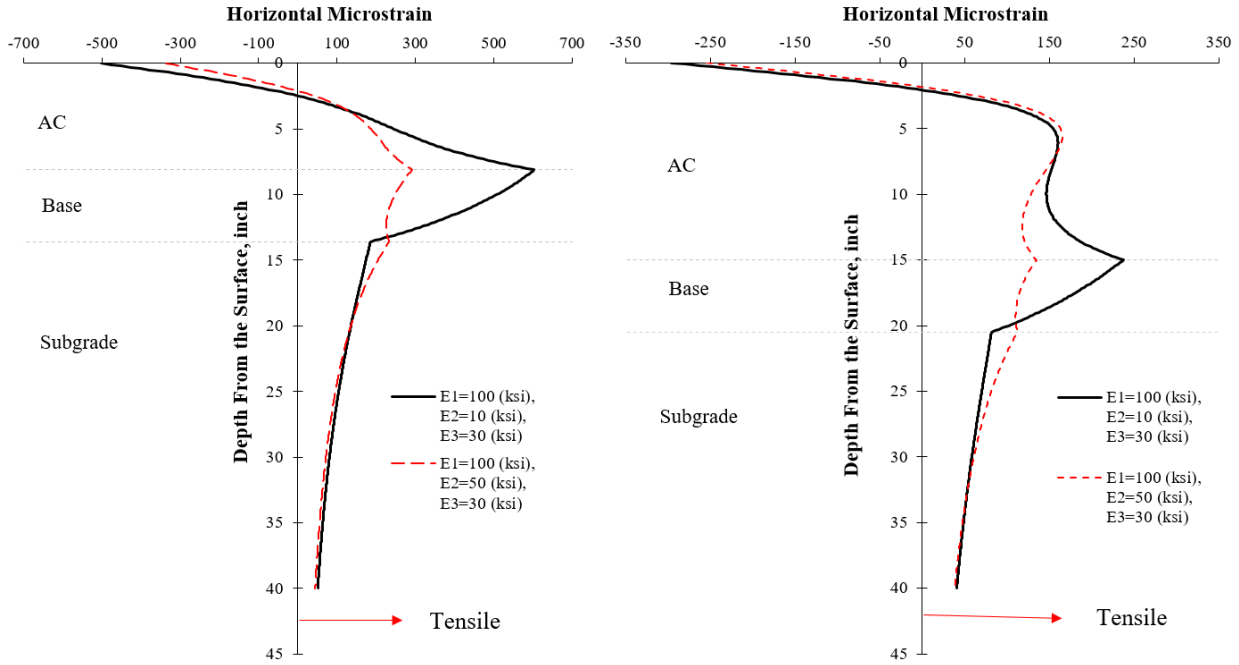

a) Original Cross Section b) Thicker Cross Section

Figure 7.13 Simulated Thick-Lift Pavement Section (S9) with Different Base Modulus and AC Thicknesses.

It was previously shown that the maximum horizontal strain in the CCPR with stabilized foundation section does not occur at the bottom but rather in shallower AC depth (Figure 7.3)

similar to stabilized foundation pavement section (S2). Since the CCPR with stabilized foundation section performed extremely well in the last three research cycles, is it possible to have a thinner CCPR with stabilized foundation section and still obtain a similar performance? Figure 7.14 shows the CCPR with stabilized foundation section (S12) again but with varying AC thicknesses. The small horizontal dashed lines show the pavement interfaces for each cross-section. This figure shows that increasing the AC thickness from 8.7 inches to 11.20 inches does not reduce the critical horizontal microstrain, but rather slightly increases the horizontal microstrain at around mid-depth. Thus, it is not cost-effective to increase the thickness of this pavement section since the traditional bottom-up fatigue cracking may not be a concern for this pavement type. This behavior was also seen for the stabilized foundation pavement section (S2). But what if one wants to reduce the AC thickness to obtain a more cost-effective pavement section? Figure 7.14 also depicts a 2.5-inch thinner cross-section. In this scenario, the bottom of AC layer experiences a slightly higher strain level, and the critical strain response transfers to the bottom of the AC layer. In addition, the cement treated base experiences larger horizontal strain response. It is not clear whether the slight increase in critical strain response could lead to pavement deterioration since the response increased only slightly while the depth of critical strain response moved down which can compensate the higher strain response.

In summary, the sensitivity analysis on pavement thicknesses showed that the critical horizontal strain response could be increased in thicker stabilized foundation pavement sections which can even accelerates the pavement damage. Also, it was shown that that even conventional flexible pavements can experience secondary maximum tensile strain throughout the AC depth depending on their thickness and base to AC modulus ratio. Thus, the location for maximum

horizontal strain cannot be assumed to be at the bottom of AC for all pavement types and should be first determined by strain analysis throughout the pavement depth.

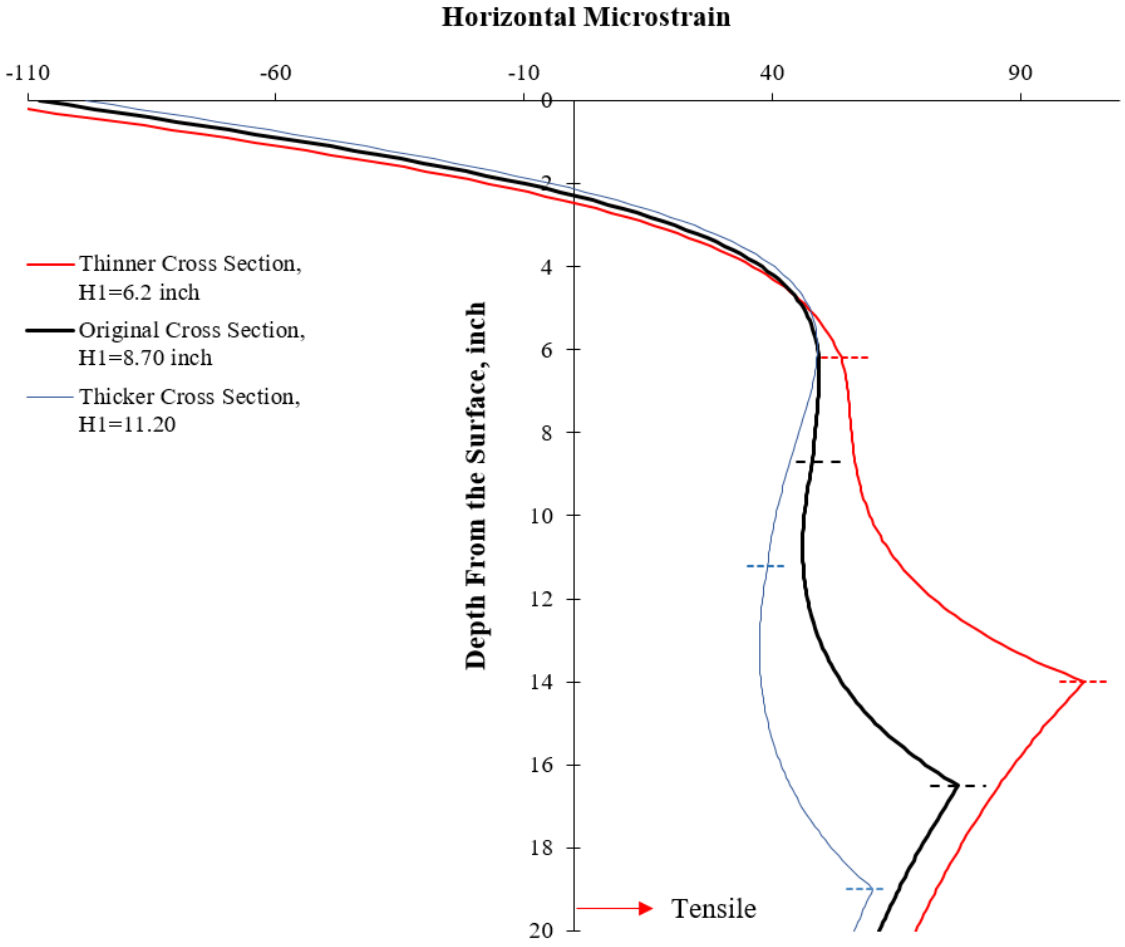

Figure 7.14 Simulated Strain Distribution for CCPR with stabilized foundation (S12) with different Cross Sections.

7.3. Dynamic Load Simulation

The results presented so far are all based on static load simulation but in reality, the loads are dynamic. To ensure that the findings are generalizable and can represent the dynamic load condition, a moving load was simulated with the MASTIC program. The same pavement configurations were considered for the simulations but only for summer condition with lower AC

modulus since it presents the critical condition. Figure 7.15 and Figure 7.16 represents two cases, the response at around mid-depth and at bottom of AC layer for the thick-lift pavement (S9) and the stabilized foundation pavement (S2), respectively. Similar to previous findings of this study, the simulated stabilized foundation pavement section (S2) experienced a dominantly compressive mode at the bottom of AC layer under a moving load (Figure 7.15). The AC mid-depth, on the other hand, experienced both modes at a very similar magnitude. The response converts to dominantly tensile when the center of the load exactly locates on top of the point of interest.

However, the strain at the bottom of AC for the thick-lift pavement section (S9) is in tension for mid-depth and bottom of the AC (Figure 7.16). It is also interesting that the shape of the simulated response in the thick-lift section (S9) under the moving load resembled the actual strain response in which it experienced a mode reversal. In fact, as the moving load approached, the flexible pavement squeezed into compression followed by a tensile peak when the axle was exactly on top of the point followed by compression again as the axle passed the point of interest. The same behavior can be seen in simulated stabilized foundation section (S2) but with a reversed sign. Again, this finding confirms the previous simulation and field observations suggesting bottom-up fatigue design criterion for stabilized foundation pavements should be revisited since cracks could initiate at shallower depths due to peak tensile response. Figure 7.15 also shows that the bottom of AC experiences a local spike right when the load is positioned on top of the point of interest orienting toward the tensile zone. This locally tensile spike in the compressive zone can grow bigger and bigger and eventually convert the response to predominantly tensile mode. The existence of the local tensile spike in the predominantly compressive zone is consistent with field measurements as explained in Chapter 5. The magnitude of this local spike depends on the ratio of elastic modulus of base to AC layer (E_2/E_1). Lower values of E_2/E_1 increase the magnitude of

the local spike. As the E_1 gets larger and larger with decreasing temperature, this local spike becomes larger and larger until it converts the dominantly compressive response to dominantly tensile mode (Figure 7.17). For conventional flexible sections, where the AC modulus is always larger than the base modulus, the E_2/E_1 remains small throughout the year and thus only the dominantly tensile mode can exist. However, for stabilized foundation pavements, depending on the E_2/E_1 ratio, the pavement can experience tensile or compression at the bottom of the AC. Figure 7.17 and Figure 7.18 illustrate the effect of AC modulus in simulated dynamic response of the stabilized foundation pavement section (S2) at bottom and mid-depth of the AC layer, respectively. As the elastic modulus increases for the AC layer (or temperature decreases), the local spike at the bottom of AC gets larger and larger until the whole response turns into predominantly tensile mode (Figure 7.17). However, the mid-depth simulated response shows that larger elastic modulus of the AC layer can decrease the maximum tensile strain at the mid-depth (Figure 7.18) and the strain response remains in the tensile zone regardless of the AC modulus (or E_2/E_1 ratio).

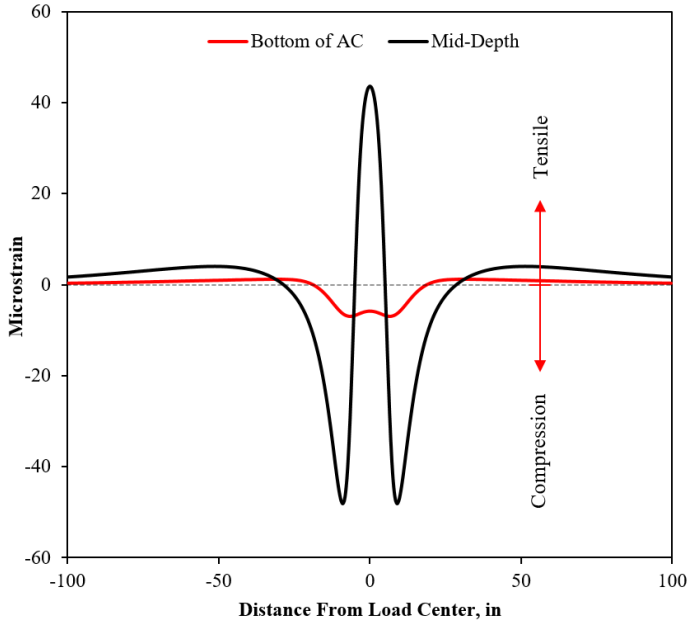

Figure 7.15 Simulated Pavement Response under Moving Load in Stabilized Foundation Pavement (S2) for Summer Condition.

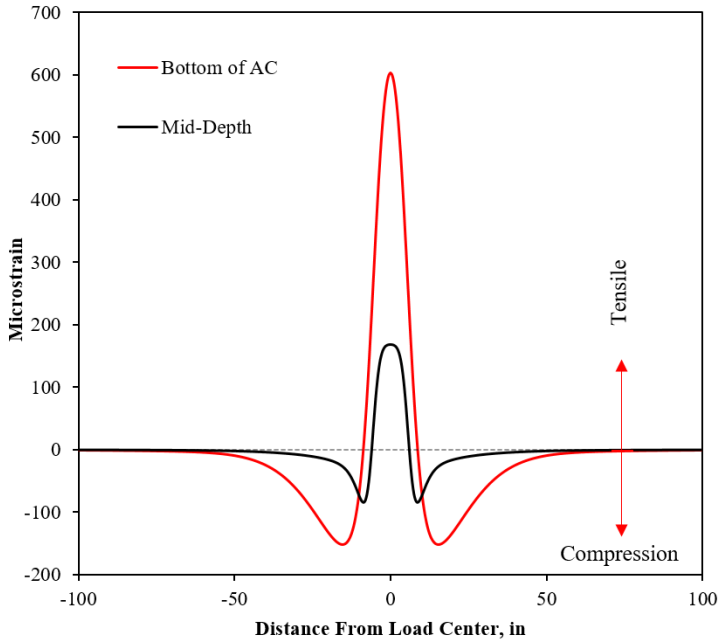

Figure 7.16 Simulated Pavement Response under Moving Load in Thick-Lift Pavement (S9) for Summer Condition.

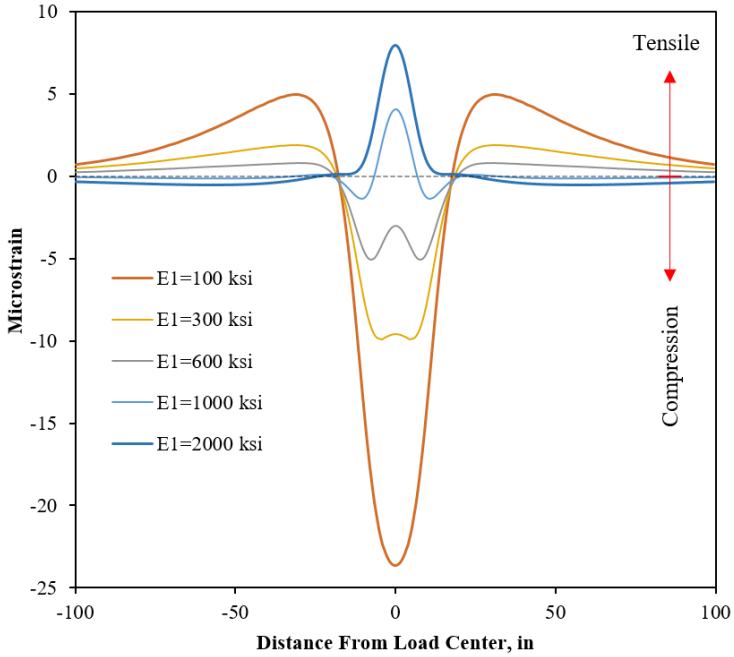

Figure 7.17 The Effect of AC Modulus on Dynamic Response of Stabilized Foundation Pavement (S2) at Bottom of AC.

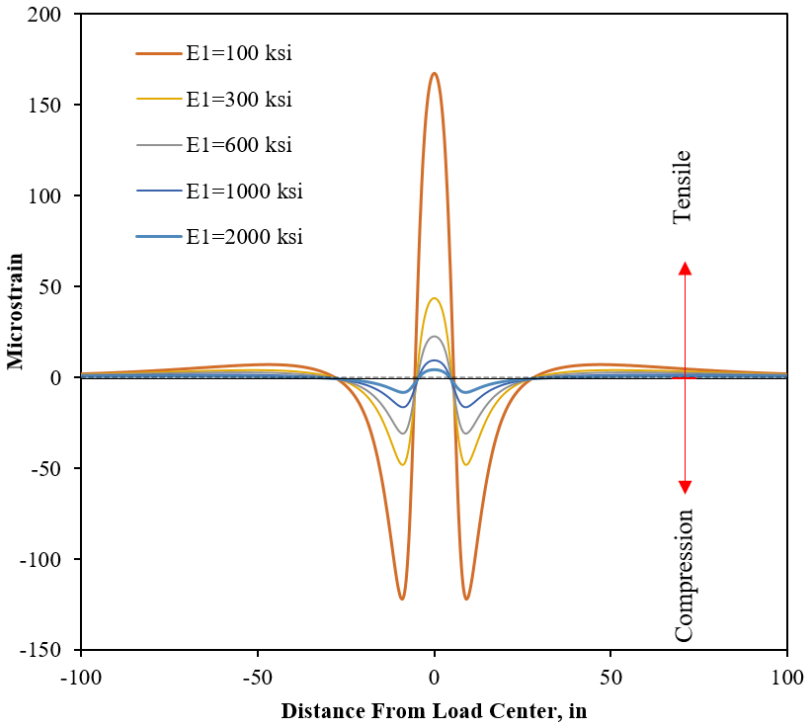

Figure 7.18 The Effect of AC Modulus on Dynamic Response of Stabilized Foundation Pavement (S2) at Mid-Depth of AC.

Figure 7.19 depicts the simulated dynamic response of the CCPR with stabilized foundation section (S12). The figure shows the dynamic response at the bottom of the AC layer and at a critical location at which the horizontal strain is maximum at the center of a static load event. The critical location occurs 6.7 inches below the surface for this section. While the magnitude of the two series in Figure 7.19 is very similar, the response at the depth of Z=6.7 inches is more likely to cause fatigue cracking since it occurs at shallower depth and is slightly larger. This analysis confirms that under dynamic or static loading, the stabilized foundation pavements can experience maximum horizontal strain somewhere other than the bottom of AC. The location of this maximum horizontal strain is not always around the mid-depth and can reside at any depth depending on E_2/E_1 ratio and pavement thicknesses.

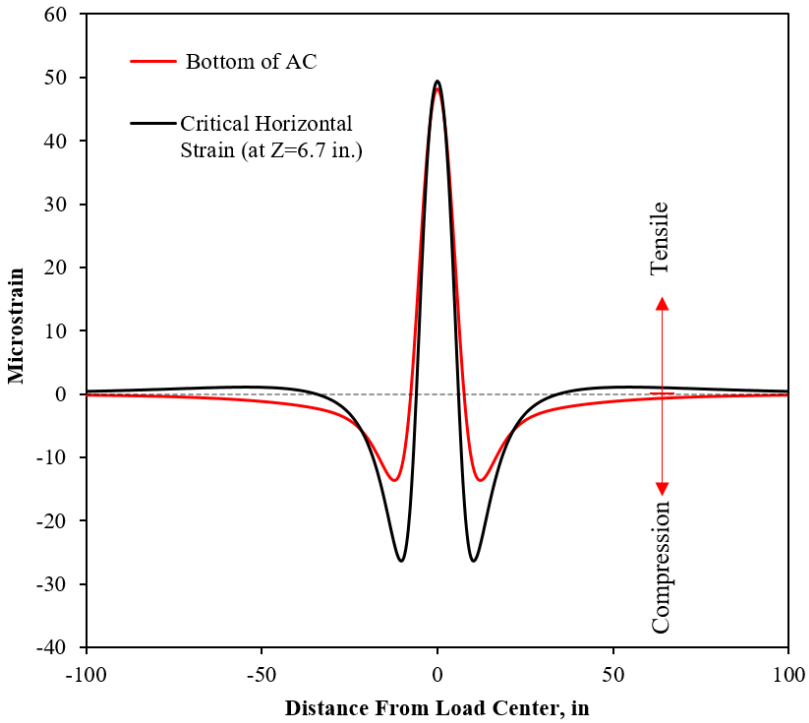

Figure 7.19 Simulated Pavement Response under Moving Load in CCPR with stabilized foundation (S9) for Summer Condition.

This Chapter showed that the behavior of the stabilized foundation section (S2) was different from conventional sections. However, having a higher horizontal strain at mid-depth is counter intuitive and could be difficult to visualize. Thus, Figure 7.20 was created to help better visualize the deformation of the stabilized foundation pavement (S2) under truck loading using MASTIC with pavement inputs as presented in Table 7.1. In this figure, the applied load caused a distinct elastic depression at the center of the pavement surface. The red lines show the interface of the pavement layers. For visualization, the elastic deformation was magnified to 1000 larger. To obtain this figure, each point on the grid was calculated for horizontal and vertical displacement and its new coordinates were deducted from its original coordinates resulting in the deformed grid.

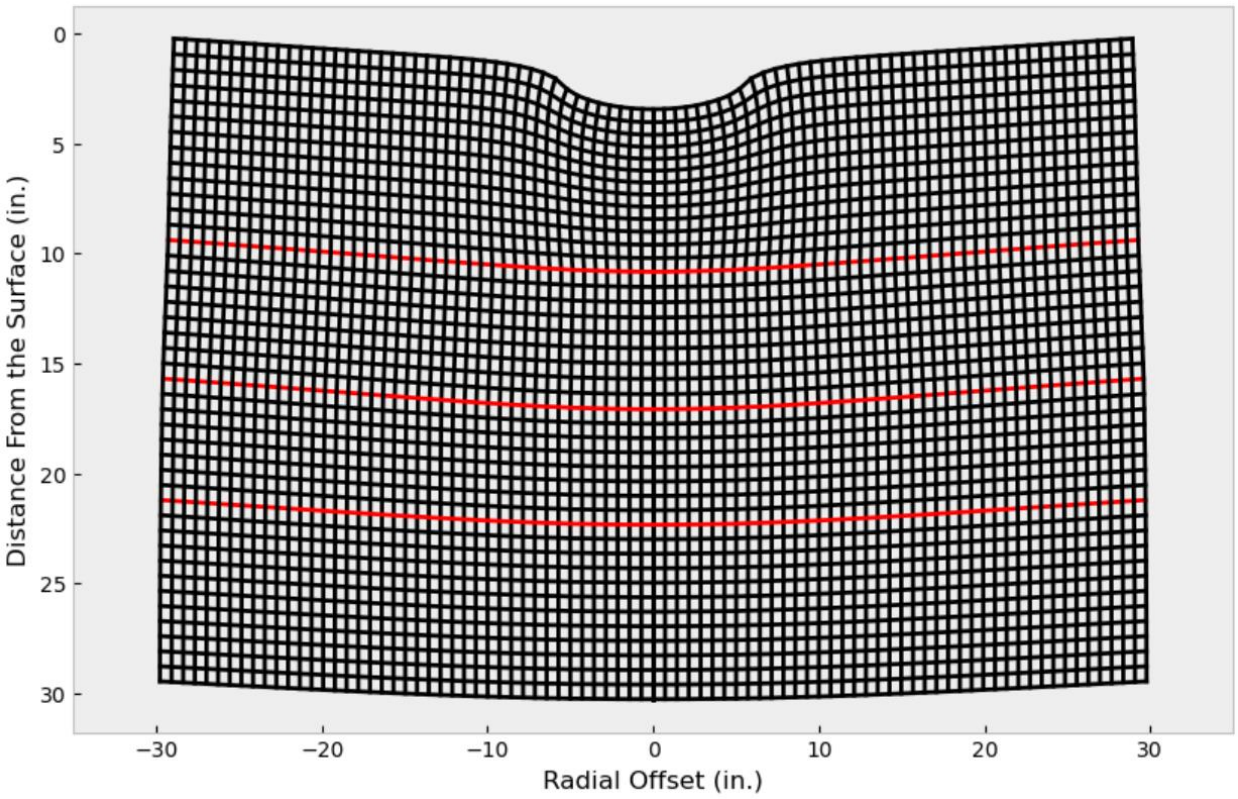

Figure 7.20 Magnified Elastic Deformation of the Stabilized Foundation Section (S2) (x1000).

In summary, the simulations showed strong evidence that the stabilized foundation sections can experience a different strain distribution throughout the pavement section. The bottom of the AC may not be the critical location for controlling the fatigue criteria for stabilized foundation sections and even thick conventional flexible pavements. The best method to determine the location of the maximum horizontal strain is to plot horizontal strain response throughout the pavement depth. The M-E design for these pavements should also be revisited since this chapter showed these sections are more prone to middle-up cracking than the bottom-up fatigue cracking. This chapter also illustrated that the friction stiffness at the layer interfaces plays a significant role on pavement section's behavior. This is particularly important for the backcalculation of the flexible pavement sections since in most commercial software programs full bonding condition is

often assumed. Chapter 8 discusses the backcalculation results of all the pavement sections. A new methodology will be introduced based on the partial bonding condition to enhance the backcalculation results of the stabilized foundation sections.

CHAPTER 8

STABILIZED FOUNDATION BACKCALCULTION

This chapter provides a detailed discussion on the backcalculation process of the stabilized foundation section (S2), the CCPR section (N4), the CCPR with stabilized foundation section (S12), and the thick-lift section (S9). However, the focus of this chapter is more on the stabilized foundation section (S2) since due to its complex structure, conventional backcalculation methods failed to provide reasonable backcalculated moduli. All backcalculation tasks were performed using EVERCALC except for the stabilized foundation section (S2) for which MASTIC was used to perform variety of backcalculation tasks. This study proposed a new methodology to backcalculate the elastic modulus of the stabilized foundation section (S2) which can potentially be used on other stabilized foundation sections to improve the backcalculation results.

8.1. Introduction

The falling weight deflectometer (FWD) is a nondestructive test device used to evaluate the in-situ structural characteristics of the pavements by determining the moduli of pavement layers or by directly evaluating the pavement deflections. A picture of an FWD owned by NCAT is shown in Figure 8.1. During FWD testing, a dynamic load is generated by dropping a weight onto a rubber plate placed on the pavement surface and measuring the subsequent deflections of the pavement at various distances away from the center of loading with a set of sensors placed on top of the pavement surface. By generating a short dynamic stress wave, the FWD equipment is able to

simulate the loading from a moving vehicle wheel in magnitude and duration *(Huang, 2004)*. In other words, the FWD is an impulse-type testing device that imparts a transient load on the pavement surface with the load duration and magnitude representative of the load induced by a truck moving at moderate speeds *(Gopalakrishnan, 2010)*.

The load level of an FWD drop is a result of the height at which the weight is dropped, and thus higher drops yields higher load levels. Figure 8.2 shows the induced deflections for an FWD drop with nine sensors. The subscripts in each deflection label (D_x) indicate the offset distance from the center of loading. These deflections along with the applied load levels are recorded, and used to obtain pavement section moduli through the process of backcalculation. The resulting deflection basin from an FWD drop is dependent on the load level, pavement structure, pavement temperature, and pavement condition. These factors must be carefully considered when analyzing deflection basins.

Given the thickness, and Poisson's ratio of each layer along with the number of layers in the pavement structure, a predicted deflection basin is generated using a mechanistic modelling and compared to the measured FWD deflection basin. The modulus value of each layer is adjusted during an iterative optimization process until the measured and modelled deflection basins match within tolerance limits. The process of finding a set of elastic moduli to achieve a deflection basin that matches the measured basin is called "backcalculation".

Figure 8.1 Dynatest Model 8000 FWD.

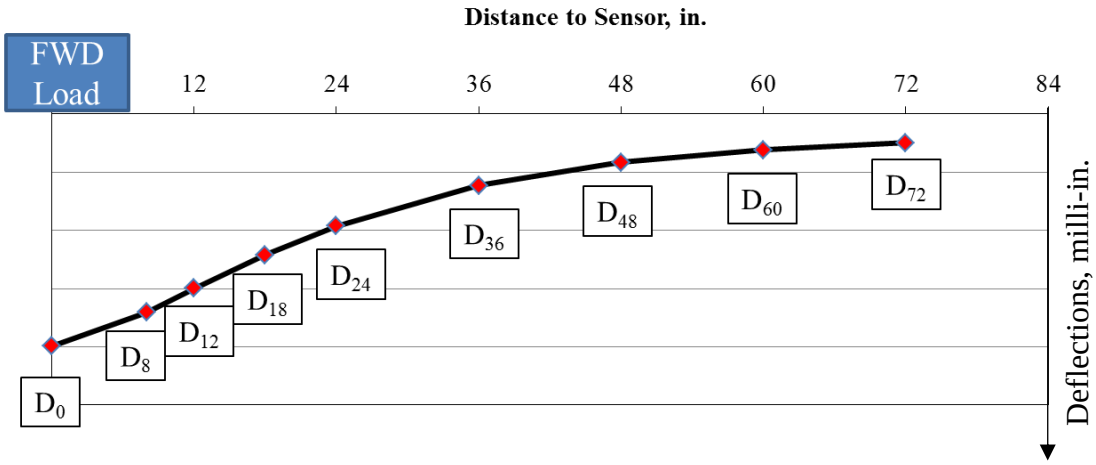

Figure 8.2 Typical FWD Deflection Basin.

In this study, EVERCALC was used for backcalculation of all pavement sections except for the stabilized foundation section (S2). EVERCALC is a backcalculation software package developed by the Washington State Department of Transportation. The EVERCALC program uses WESLEA as the layered elastic solution for forward calculation and deploys a modified augmented Gauss–Newton algorithm for optimization to obtain elastic moduli. EVERCALC can evaluate a flexible pavement structure with up to five layers. The inputs for backcalculation are the number of layers, layer thickness, Poisson's ratio of material in each layer, the presence of any rigid layer

underneath the subgrade, and seed moduli. The algorithm works by first calculating surface deflections at radial offset distances using the seed modulus and layer thickness. From an initial seed modulus, EVERCALC iteratively searches for the final modulus for each pavement layer. The deflections calculated using WESLEA (the forward elastic program) are compared with the measured ones that are obtained from FWD sensors. The process is repeated by changing the modulus each time recursively. When the root mean square error (RMSE) falls within the allowable tolerance, or the number of iterations reaches a limit, or the moduli do not change outside a specified a tolerance, the algorithm terminates *(Sharma and Das, 2008)*. EVERCALC was developed for production purposes and is intended to get to an "accurate" solution reliably. While EVERCALC, like other similar static backcalculation programs, usually converges to a solution reasonably quickly and reliably, the uniqueness of the set of layer moduli derived from the Gauss-Newton search method is not guaranteed *(Chatti et al., 2017)*. For this reason, this program uses various controls to guide the iterative search toward an "acceptable" set of layer moduli. These include making some assumptions about the type of pavement system and limiting the acceptable range of moduli for each individual layer type. For the stabilized foundation section (S2), EVERCALC yielded unrealistic results (which will be further discussed) and thus was not used for the backcalculation of this pavement section. MASTIC was deployed for backcalculation of this section which finds the elastic moduli through a process similar to that of EVERCALC but with additional flexibilities. Further discussion will be provided in the later sections of this chapter.

8.2. FWD Testing at the Test Track

FWD testing was conducted routinely at the Test Track using a Dynatest Model 8000 three times a month during the 2-year research cycle. The FWD had nine sensors installed at offsets of 0, 8,

12, 18, 24, 36, 48, 60, and 72 in. from the center of the load plate, and the plate radius was 5.90 in. The selected FWD load levels were 6,000, 9,000, 12,000 lb. Three replicate drops were generated for each load level. The FWD testing was conducted at 12 fixed stations within each test section including three transverse locations at four random longitudinal locations. Figure 8.3 shows the location of each numbered station within a test section. Similar to other chapters, the results of backcalculation for all test sections (e.g. sections S2, S9, S12, and N4) are discussed in this chapter.

To reduce the workload of FWD testing, Inside Wheel Path (IWP) and Outside Wheel Path (OWP) were tested three times a month for each test section while the Between Wheel Path (BWP) was tested only once a month starting from 2018. It is believed that the rate of structural decay for BWP is less than IWP and OWP which justified less testing of BWP. Thus, a total of 108 or 81 deflection basins (depending on whether BWP included) were generated for each test section on a given date.

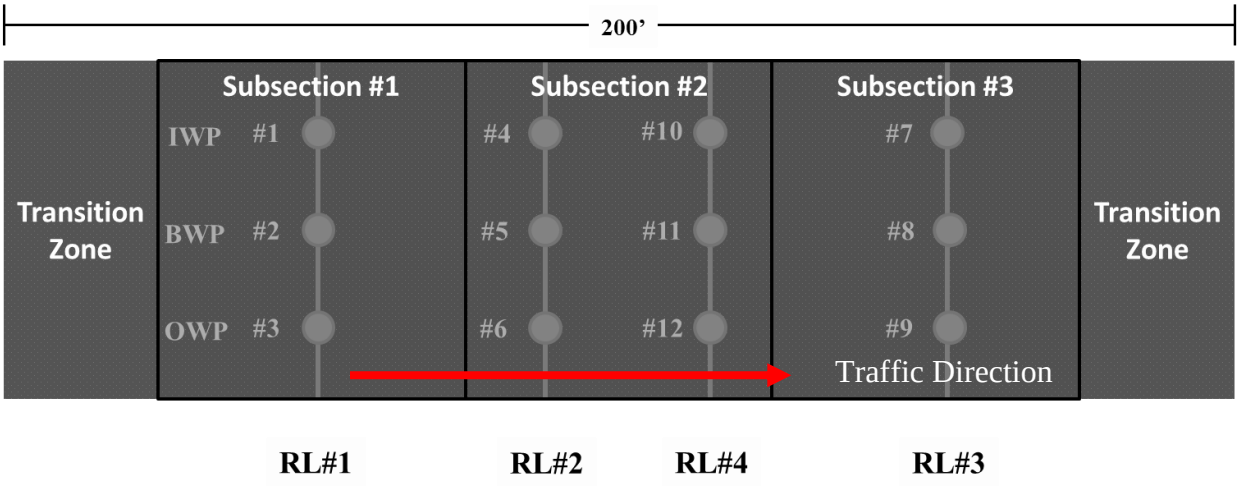

Figure 8.3 FWD Testing Locations within a Pavement Section.

In Figure 8.3, the first and the last 25 feet are transition zones between sections which were excluded from the analysis. The remaining 150 feet of the sections were divided into three 50-foot sub-sections. Within each sub-section, a randomly determined testing location was established (e.g. random location 1 (RL#1) through random location 3 (RL#3)). In addition, RL#4 was located in the middle of the instrumentation array. As shown in Figure 8.3, stations 1, 4, 7, and 10 were located in the inside wheel path. Stations 2, 5, 8, and 11 were located in between wheel paths while stations 3, 6, 9, and 12 were in the outside wheel path. Note that the RL#2 and RL#4 are the random locations positioned at the middle of the section.

8.3. Difficulties in Backcalculation

Backcalculation is an ill-posed inverse problem which involves searching for the optimal combination of pavement layer moduli solutions in a multimodal, unsmooth, and complex search space. Due to its complexity, many computer programs and backcalculation procedures have been developed during the past few decades. In most commercial backcalculation software packages, elastic layered analysis is deployed along with an iterative optimization method to arrive at an optimum solution for a particular deflection basin. Despite the effectiveness of this approach, it does not guarantee unique elastic moduli as there can be more than one combination of elastic moduli to achieve a good match between theoretical and measured surface deflections. Thus, unreasonable modulus values are often obtained *(Gopalakrishnan, 2010)* and thus the backcalculated output must be scrutinized for reasonableness.

To resolve the often-encountered difficulties in backcalculation, several static, dynamic, and adaptive techniques have been proposed such as least-squares methods (e.g. EVERCALC), database search (e.g. MODULUS), soft computing techniques such as neural networks, neuro-

fuzzy systems, and genetic algorithms *(Gopalakrishnan, 2010)*. However, there is no single method that can guarantee the best results and one should carefully select a backcalculation framework by screening the results to ensure reasonableness.

Regardless of the difficulties in backcalculation, most of the conventional pavements have been backcalculated successfully in the past using iterative optimization-based methods. These approaches are generally faster and yield reasonable results for most pavement structural settings. Thus, this study used EVERCALC 5.0 software package to backcalculate the moduli for all test sections but for the stabilized foundation pavement (S2). The backcalculation procedure for CCPR (N4) and the thick-lift (S9) sections followed the previous well-established method proposed by Timm and Tutu *(2017)* and is not discussed in this document for brevity.

MASTIC was used to backcalculate the stabilized foundation section (S2) due to unreasonable results obtained from EVERCALC. There could be variety of reasons that EVERCALC did not perform well on this section such as lack of the partial friction setting and lack of more advanced optimization methods. Since MASTIC provided more flexibility (such as ability to choose different optimization methods, consider more than 5 layers in backcalculation, take into account partial friction between the layers, etc.,), it was the primary tool for investigating a method that could produce reasonable elastic moduli for the stabilized foundation section (S2). However, as mentioned, the CCPR (N4), the CCPR with stabilized foundation (S12), and the thick-lift (S9) sections were all analyzed using EVERCALC to preserve consistency with historical data collected on these sections. In addition, the historical FWD data suggested that the CCPR (N4) and the CCPR with stabilized foundation (S12) sections can be successfully backcalculated using EVERCALC with some adjustments *(Timm and Tutu, 2017).*

8.4. Backcalculation Results for S12, S9, and N4

The backcalculation results for the CCPR (N4), the CCPR with stabilized foundation (S12), and the thick-lift (S9) sections are discussed in this section. The CCPR (N4) and the CCPR with stabilized foundation (S12) sections were considered as three-layer structures, where the top layer was the combination of the AC and CCPR. The logic behind combining AC layer with CCRP was supported by a previous research that demonstrated CCPR had a time-temperature dependent behavior *(Kim & Lee, 2002).* Subsequent laboratory testing performed by Virginia DOT confirmed that the CCPR layers in this study exhibited behavior similar to AC materials which supported the use of the combined AC/CCPR layer for backcalculation purposes *(Diefenderfer and Link, 2014)*. For the analysis of these sections, only backcalculated moduli corresponding to a RMSE of less than 3% had been considered. The thick-lift section (S9) was also considered to be a three-layer system with the AC on top of the aggregate base over the native Test Track soil. Following the study conducted by Timm and Tutu *(2017),* 16 inches was added to the base course thickness for the thick-lift (S9) and CCPR (N4) sections to compensate for the unreasonably low moduli obtained using conventional methods. No changes were deemed necessary to be made for the CCPR with stabilized foundation section (S12).

Figure 8.4 shows the backcalculated AC moduli over time for all three sections. The CCPR sections were constructed in 2012 and the data for the latest two research cycles (2015 and 2018) are presented in the figure. However, the thick-lift pavement section (S9) was constructed in 2018 and thus only the data for the most recent research cycle is provided.

The graph shows the cyclic behavior of the AC elastic moduli which is a function of the mid-depth pavement temperature. As shown, the elastic modulus for the CCPR with stabilized foundation section (S12) was on average higher than the two other sections with less sensitivity to

pavement temperature which can be attributed to the restraint provided by the stabilized foundation. Less sensitivity to temperature was also observed from direct strain and stress measurements for this section. Further discussion on the possible reason for having less sensitivity to temperature will be provided later in this chapter. In addition, the AC elastic moduli of the CCPR with stabilized foundation section (S12) did not appear to increase or decrease in the third research cycle indicating no ageing or damage accumulation. On the other hand, the AC modulus trend for the CCPR section (N4) in the third cycle does suggest the decrease in AC moduli and thus possibility for damage accumulation. The data indicated the precursor to pavement damage long before any crack was observed on this test section showing the robustness of the backcalculation method for structural evaluation of the pavement sections. The trend for the thick-lift section (S9) did not indicate any decrease or increase in AC modulus over the past two years of accelerated trafficking.

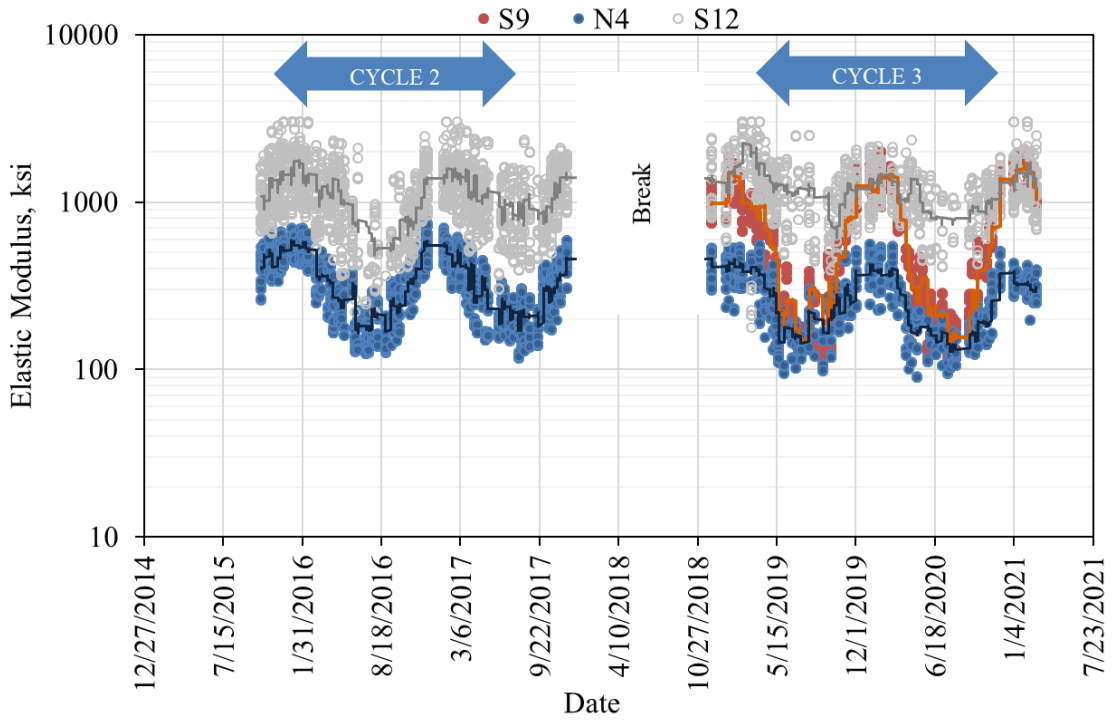

Figure 8.4 Backcalculated Moduli over Time for S9, S12, and N4.

Since the seasonal trend from the CCPR section (N4) suggested a decreasing trend, the same data was replotted against temperature and color coded for two different research cycles (shown in Figure 8.5). The data clearly shows a drop in the elastic modulus from the past research cycle to the most recent one which represented a precursor to damage for this section.

Note that

Figure 8.5 was plotted using the entire dataset from two test cycles and including all stations within section N4 combined. To see a better distinction with less variability, the same data were plotted (shown in Figure 8.6) for only one randomly selected station (station 1) and for data collected only in 2016 and 2020. Figure 8.6 confirmed the results that there existed a decreasing trend in elastic moduli. As mentioned in previous chapters, this section experienced cracking toward the end of the 2018 research cycle but the data suggested the precursor to damage long before the cracks were visible at the surface. The same conclusion was made using the measured stress and strain sensors (refer to Chapter 5).

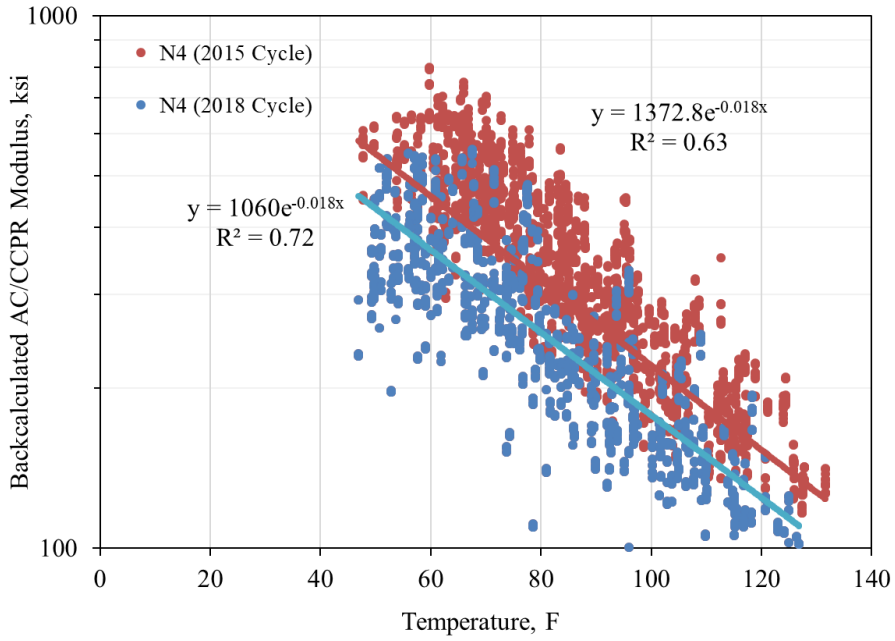

Figure 8.5 Backcalculated Moduli VS Temperature for the CCPR Section (N4).

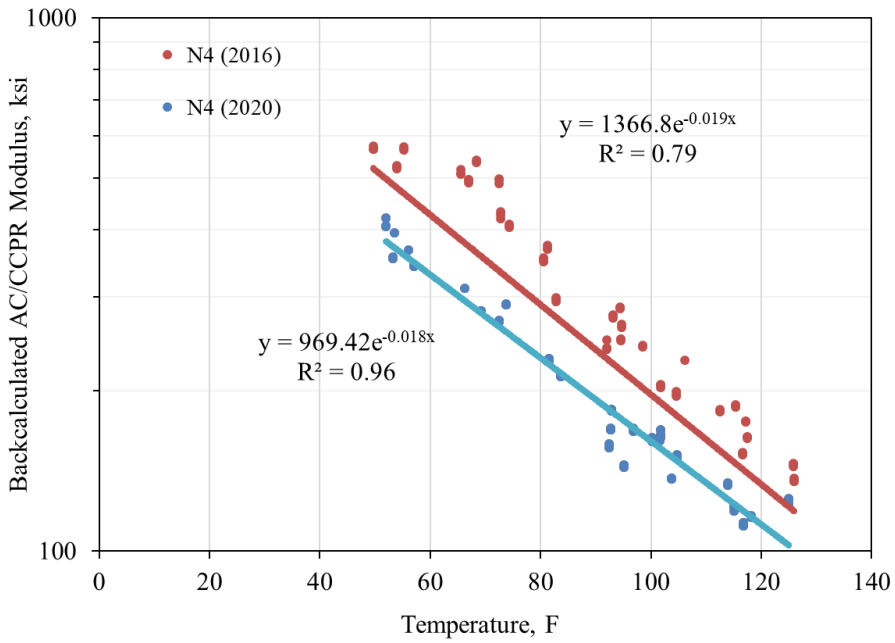

Figure 8.6 Backcalculated Moduli VS Temperature for the CCPR Section (N4).

The elastic moduli for all three layers of the thick-lift section (S9) are shown in Figure 8.7. As expected, the AC had a decreasing trend with the increase of temperature. The subgrade soil also shows a decreasing trend which can be attributed to the stress softening effect of the subgrade. The elastic modulus for the native Test Track soil was higher than the crushed aggregate base which confirmed the previous NCAT findings *(Timm and Tutu, 2017)*. The data did not suggest any structural decay for this section and this section continued to perform well at the end of the 2018 research cycle.

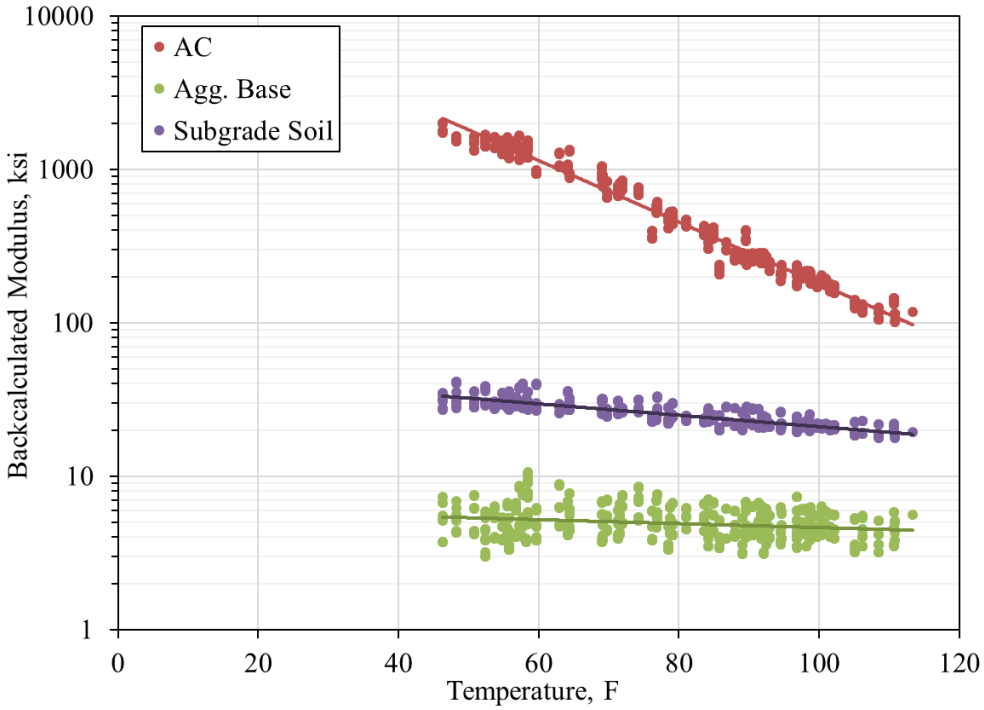

Figure 8.7 Elastic Moduli for All Three Layers of the Thick-lift Section (S9).

Although the backcalculation of the above sections (S12, S9, and N4) were successful using EVERCALC, the backcalculation process was found to be challenging for the stabilized foundation pavement (S2). The main reason was the high stiffness of this section. Therefore, this study proposed a new method to modify the current backcalculation procedure of the stabilized foundation pavement section (S2) which will be discussed later in this chapter. The proposed method can potentially be used for other stabilized foundation sections. The remaining sections of this chapter will discuss the methods attempted to backcalculate the stabilized foundation section (S2).

8.5. Backcalculation Using Conventional Settings for S2

As mentioned above, using conventional settings for backcalculating the stabilized foundation section (S2) had yielded unreasonable results. This section discusses the conventional settings

used for backcalculation along with the results and the reason behind obtaining unacceptable results from each setting. Table 8.1 shows the thicknesses used for backcalculation of each station within section S2. The relative position of each station was shown earlier in Figure 8.3. The load radius was considered to be 5.9 inches for all cases. The database contained 4752 deflection basins collected during the two years of research cycle over wide range of temperatures which included different stations within the stabilized foundation section (S2).

Table 8.1 The thicknesses for Backcalculation of the Stabilized Foundation Section (S2)

Station	AC thickness, inch	CTB thickness, inch	LTS thickness, inch
S2-1	9.49	5.95	5.5
S2-2	9.38	6.14	5.5
S2-3	9.23	6.62	5.5
S2-4	9.11	5.89	5.5
S2-5	9.20	5.87	5.5
S2-6	9.39	5.46	5.5
S2-7	9.51	5.54	5.5
S2-8	9.18	5.98	5.5
S2-9	9.18	6.27	5.5
S2-10	8.83	6.90	5.5
S2-11	9.08	6.46	5.5
S2-12	9.43	5.90	5.5

The following section discusses the backcalculation framework and results for a three-, four-, and five-layer systems, respectively. Although the results in the next section were obtained from MASTIC, the same results would have been obtained from EVERCALC since the settings used to backcalculate were similar to those of EVERCALC. However, MASTIC was selected since it provided more flexibility in the batch mode setting.

8.5.1. Three Layer System

For the three-layer system with conventional settings, the thickness of the CTB and LTS were combined together to form an equivalent base thickness for the analysis. The Poisson's ratio was assumed to be 0.35, 0.2, and 0.40 for the AC, CTB/LTS, and subgrade soil, respectively, with the boundaries for the search space shown in Table 8.2. All layers were considered fully bonded.

Table 8.2 Upper and Lower Bounds of the Search Space for Three-Layer System

	AC, ksi	CTB+LTS, ksi	Subgrade, ksi
Upper Limit	3500	5000	1000
Seed	500	1000	30
Lower Limit	80	1	1

Figure 8.8 through 8.10 plotted the elastic moduli for AC, base, and subgrade soil, respectively. Both seasonal variations (with moving average in red series) and trend with temperature are provided for each figure. The data is only provided for random locations 2 and 4 (e.g. stations 4, 5, 6 and 10, 11, 12) since they provided more reliable results (which will be discussed later in details). Figure 8.8 shows the seasonal effect for AC modulus as well as the decreasing trend with temperature. Although the AC trend seemed to meet the expectations, the magnitude of modulus was almost two times higher than the AC modulus of a conventional pavement section. For example, the backcalculated elastic modulus for the AC was 1707 ksi at 68 °F. Based on the NCAT database history, this value is expected to be around 600-1000 ksi for an unmodified AC layer of a conventional section with crushed aggregate base. The reason that this method reported a higher AC modulus is believed to be related to the compensation effect *(Timm and Tutu, 2017)*. In fact, a lower elastic modulus for the base course was compensated for a higher value of the AC layer. Mathematically speaking, there could exist multiple solutions for an optimization problem that satisfy the boundary conditions of a problem. This is referred to as non-

uniqueness problem in optimization which exits for non-convex problems. One way to possibly overcome this issue is to use global optimization methods such as Genetic Algorithms. Although there is no guarantee, these methods are believed to have more potential to avoid falling into local optimums. Further discussion of this topic will be provided later in the chapter.

The elastic modulus for the CTB layer appeared to be smaller than the expected values with an average of around 300 ksi. The lab data, as discussed in Chapter 4, indicated an average value of 1012.5 ksi for lab-fabricated lab-tested samples. Also, from field measurements and simulations it was shown that to achieve a reversed strain signal at the bottom of the AC layer (e.g., compression at the bottom of AC), the elastic modulus for the CTB layer must be higher than the AC modulus. With the base course value of about 300 ksi (on average), a reversed mode cannot be formed (refer to Chapters 5 and 7 for more details). Thus, it can be concluded that this method resulted in higher than expected AC modulus and lower CTB modulus. However, the subgrade modulus seemed reasonable and was obtained at around 30 ksi. It had a decreasing trend with temperature which could be due to stress softening of this layer (Figure 8.10). Note that in all the images (Figure 8.8, Figure 8.9, and Figure 8.10), the red line on the left graph represents a simple linear regression line, and the one on the right shows the 30 point moving average fitted to the data.

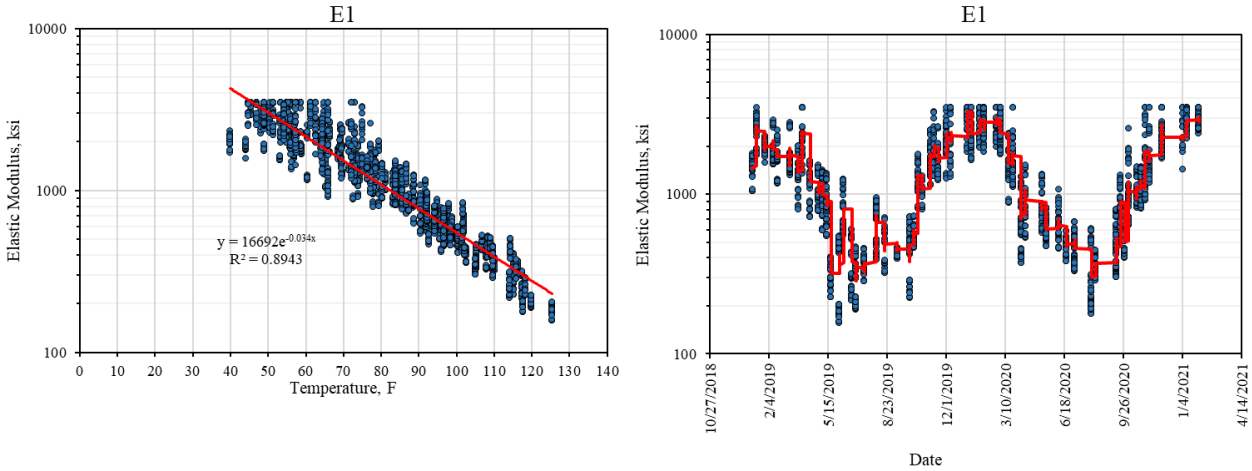

Figure 8.8 Elastic Moduli for AC against Temperature and Date (Three layer System).

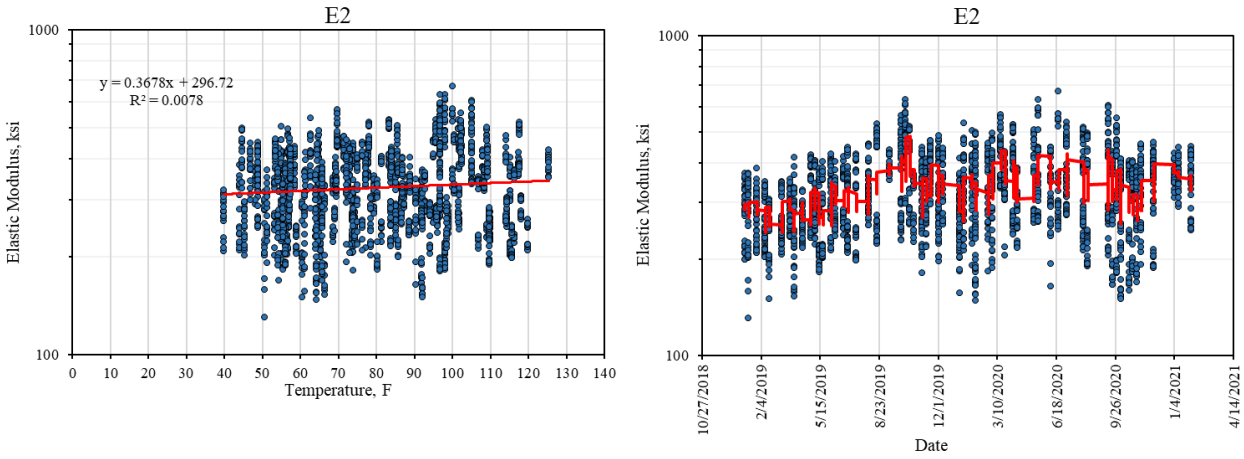

Figure 8.9 Elastic Moduli for CTB against Temperature and Date (Three layer System).

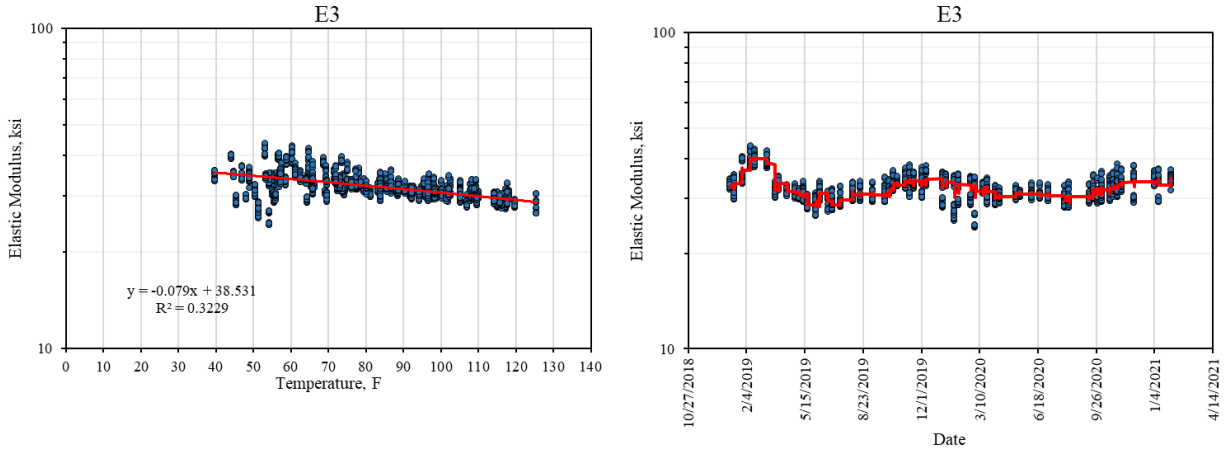

Figure 8.10 Elastic Moduli for Subgrade against Temperature and Date (Three-layer System).

The three-layer systems with other scenarios (such as combining AC/CTB, or LTS/Subgrade, etc) yielded unreasonable results as well and thus were excluded from the analysis and not presented here for brevity.

8.5.2. Four Layer System

For the four-layer system, the Poisson's ratio was assumed to be 0.35, 0.2, 0.3, and 0.40 for the AC, CTB, LTS, and subgrade soil, respectively. The boundaries for the search space are shown in Table 8.3. All layers were considered bonded. Again, the results are only shown for the random location 2 and 4.

Table 8.3 Upper and Lower Bounds of the Search Space for the Four-layer System

	AC, ksi	CTB, ksi	LTS, ksi	Subgrade, ksi
Upper Limit	3500	5000	2000	100
Seed	500	2000	100	30
Lower Limit	80	1	1	1

Figure 8.11 through Figure 8.14 illustrate the backcalculated data for all four layers of the stabilized foundation pavement (S2). While the AC in has a reasonable trend with temperature and conforms to seasonal variations, the moduli values are estimated higher than the expected values. At 68 °F, the AC modulus was 1585 ksi on average which was higher than the expected range of 600-1000 ksi. This could again be due to the compensation effect. Therefore, regardless of the choice of three-layer or four-layer system, the AC layer was backcalculated higher than expected.

While the AC modulus followed the expected behavior (but with higher magnitude), the variability in CTB and LTS moduli was so high that prevented any meaningful insight from the structural properties of these layers. In Figure 8.12, the elastic modulus for the CTB layer ranged from about 100 ksi to 3000 ksi, and 1 ksi to 1000 ksi for LTS.

Due to high variability in the two intermediate layers, the investigation was continued with the five-layer system. For the five-layer system, the original cross sections as shown in Chapter 3 was used with 51 inches of MS soil over native Test Track soil. Unfortunately, using the 5-layer system aggravated the backcalculation problem even more because the search space had more degrees of freedom and thus was easily trapped into local optima. Trapping into a local optimum can cause more variability in the backcalculation process. Hence, the five-layer system was excluded from further analysis. The results for five layers are not provided in this document for brevity. Regardless of the number of layers being used in the backcalculation process, the AC and subgrade soil appeared to converge to more or less similar values with less variability. Again, note that in Figures 8.11 through Figure 8.14, the red line on the left graph represents a simple linear regression line, and the one on the right shows the 30-point moving average fitted to the data.

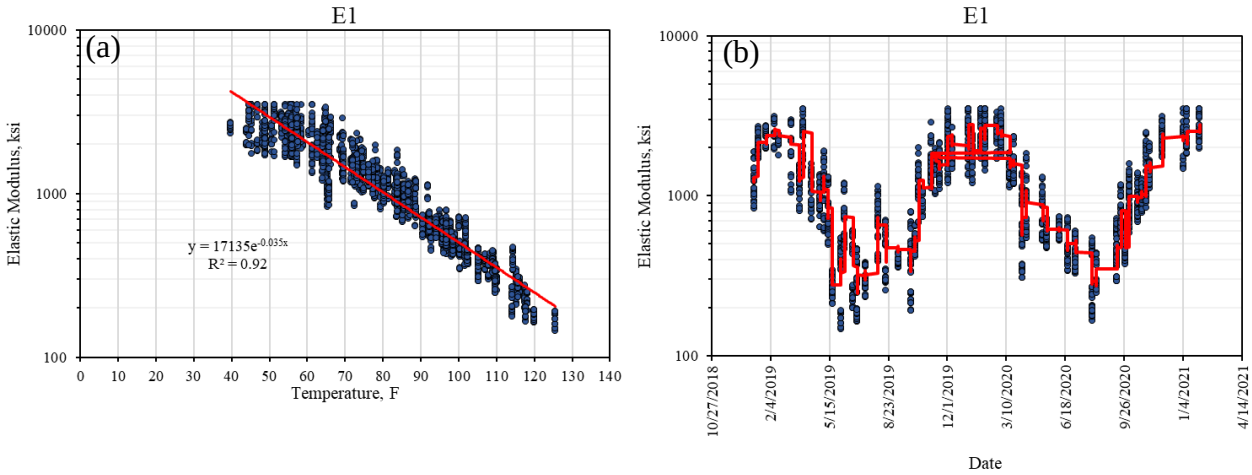

Figure 8.11 Elastic Moduli for AC against Temperature (a) and Date (b) (Four layer System).

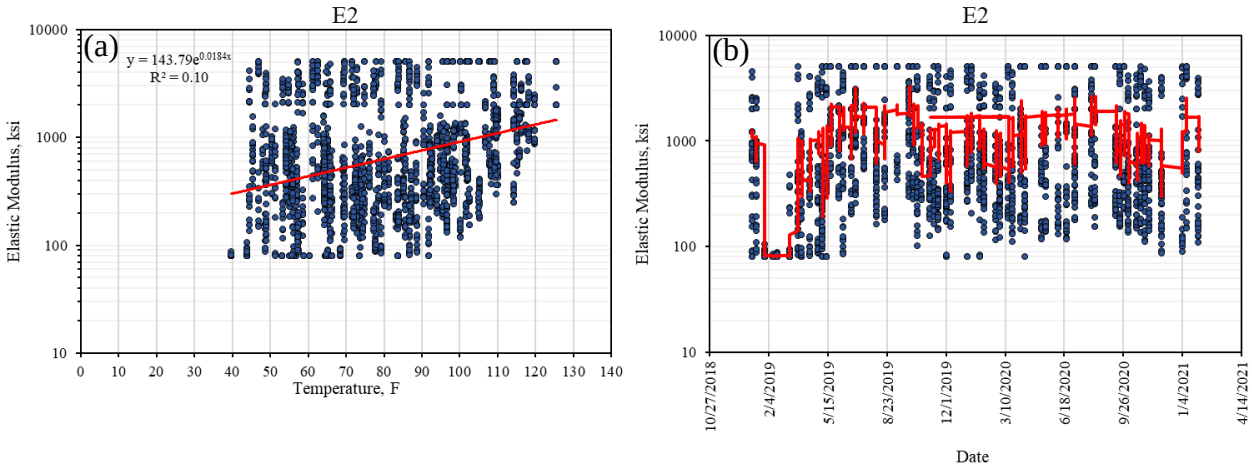

Figure 8.12 Elastic Moduli for CTB against Temperature (a) and Date (b) (Four-layer System).

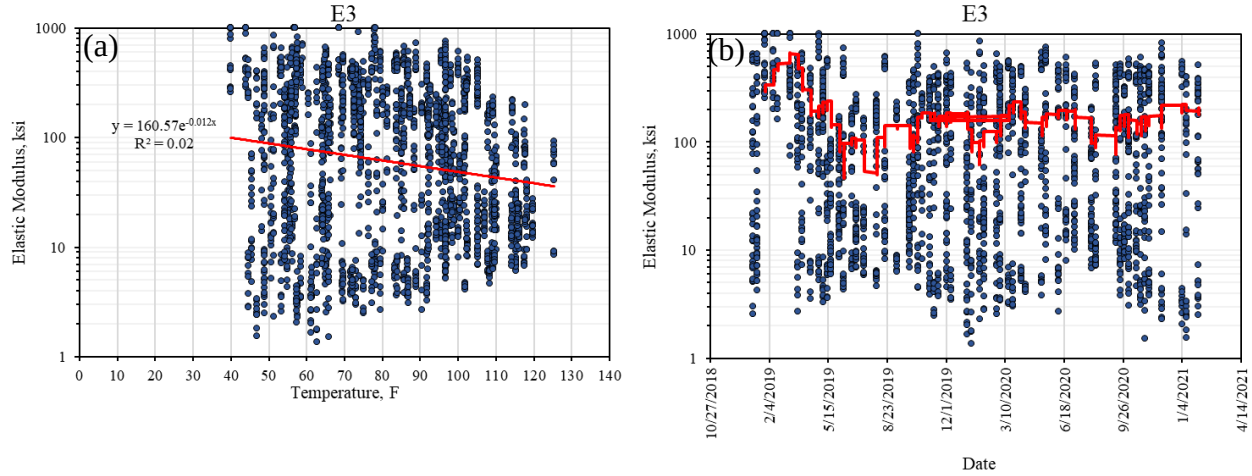

Figure 8.13 Elastic Moduli for LTS against Temperature (a) and Date (b) (Four-layer System).

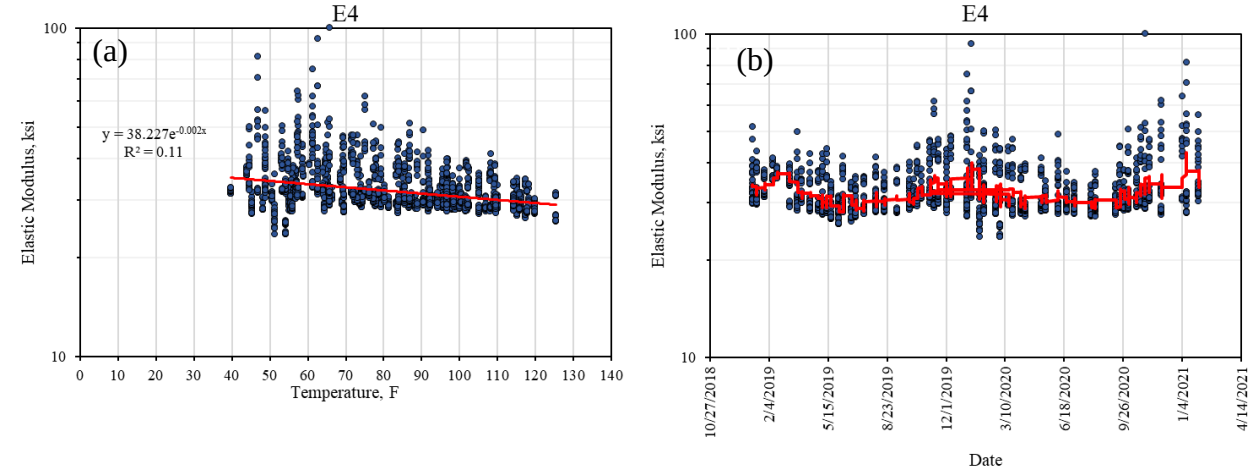

Figure 8.14 Elastic Moduli for Subgrade Soil against Temperature (a) and Date (b) (Four-layer System).

The backcalculation results from conventional methods with the three-, four-, and five-layer system had resulted in unreasonable results. A high variability was observed for the intermediate layers' moduli. To obtain more consistent results, several approaches were taken which are briefly discussed in the next section.

8.6. Candidate Models for S2

This section provides a brief discussion about other methods used in this study to find a set of elastic moduli that could best represent the stabilized pavement section's properties. The presented methods were all investigated in detail, but are only briefly presented in this document for the sake of brevity. The selected candidates will be discussed in more details in the next section.

8.6.1. Artificial Neural Network

Iterative optimization methods are not the only solution for backcalculating elastic modulus of the layered pavements. It is possible to optimize a problem numerically with high accuracy with Artificial Intelligence (AI) and Machine Learning methods. AI methods have been used extensively to address complicated problems in the field of pavement engineering (*Leiva et al., 2017*). This study tried to make use of AI to find an optimum solution for the stabilized foundation section. First, a deflection basin database composed of 100,000 records was generated with WESLEA (which provides a forward solution to a multilayer elastic system subjected to a circular load). All deflection basins were randomly generated. Three types of artificial intelligence methods including feed forward neural network, convolutional neural network, and random forest were used to train on the synthetic database. More emphasis was given to feed forward neural network architectures since they produced more promising results. Feed forward neural network with various architectures from the shallow networks to the deep ones (ranging from 1 layer to 20

layers) were trained and used to backcalculate Section S2's moduli using TensorFlow library of Python. The hyper parameters were tuned with auto-tuning methods. Although good accuracy was obtained, one issue with almost all networks was that they occasionally output negative values for elastic modulus. This problem was alleviated to some extent by introducing random noise (up to 10%) to inputs before training the models to prevent overfitting. However, in general, although the artificial intelligence models obtained good accuracy after training the models, the elastic modulus obtained using the best AI models were extremely close to the ones obtained from the conventional backcalculation methods. Since the AI models added no extra advantage over the traditional ones, and the process of training and testing was time consuming, no AI method was selected as the final approach. The details for the AI implementation and their comparison with conventional methods are outside the scope of this study and thus not presented in this document for brevity.

8.6.2. Modular Ratio

Another attempt on backcalculation was to use the laboratory knowledge to further constrain the optimization problem. In this method, the asphalt concrete to base course modulus ratio was divided into four categories based on asphalt pavement temperature. The optimization problem was solved with inequality constraints to enforce those ratios. As an example, for temperatures below 64 °F, the CTB/AC modulus was enforced to be greater than 3 when solving for optimum solution. Various constraints were considered to obtain the best solution by fine tuning the ratios; however, it was soon determined that further constraining the problem with arbitrary constraints would significantly affect the results and the solution might hit the boundaries of the arbitrary constraints to minimize the error. Consequently, this approach was withdrawn and thus not

selected as the top candidate. Additional methods were also investigated such as considering a fixed and known function for the AC layer (e.g. AC as a function of temperature based on historical data at the Test Track) and then trying to backcalculate other unknowns based on a known AC modulus at a particular temperature. However, this method yielded unacceptable results as well since the temperature dependency of the AC layer was not entirely captured by the proposed functions and thus some of the temperature dependencies were transferred artificially to other layers resulting in high RMSE values and unrealistic results.

8.6.3. Trial Cross Sections

The backcalculation was performed on the as-built cross-section as well as different trial cross sections following the methodology implemented by Timm and Tutu *(2017)*. Some of the trial cross-sections used in this study are presented in Table 8.4. The first column of Table 8.4 defines the pavement cross-section for simulation where each proposed layer in the backcalculation can be distinguished by a comma "," while the layers that were combined together as one layer are shown with a hyphen. For example, "AC, CTB-LSS, MS" represents a pavement cross section in which the original AC layer was considered as the surface layer. The CTB and LTS were combined together and considered to be the second layer (CTB-LTS), and the last layer was considered to be the Mississippi soil (MS). Although a wide range of cross-sections was tried (only some of the trial cross-sections are presented in Table 8.4), this approach could not find a cross-section that result in a reasonable moduli for all stations of the stabilized foundation section (S2). While some cross-sections resulted in slightly more reasonable results, the main source of the backcalculation issue was found to be high variability in backcalculation regardless of the cross-section used. The reason for high variability in the backcalculation is discussed in the next section. Again, the results

for trial cross sections are not presented in this document since they were not selected as the final approach to find elastic moduli of the pavement section.

Table 8.4 Trial Cross Sections for Backcalculation.

Cross Section	# Layers	Comment
AC, CTB, LSS-MS	3	The original cross section for three layer
AC, CTB-LSS, MS	3	-
AC-CTB, LTS, MS	3	-
AC, CTB, LSS-MS	3	AC+10”
AC, CTB, LSS-MS	3	CTB+15”
AC, CTB, LSS-MS	3	AC+5”
AC, CTB, LSS, MS	4	The original cross section for four layer
AC-CTB, LTS, MS, Track	4	-
AC, CTB, LSS-MS, Track	4	-
AC, CTB-LSS, MS, Track	4	-
AC, CTB, LSS, MS	4	AC+10”
AC, CTB, LSS, MS	4	CTB+10”
AC, CTB, LSS, MS	4	LSS+10”
AC, CTB, LSS, MS	4	LSS+15”
AC, CTB, LTS, MS, Track	5	The original cross section for five layer
AC, AC, CTB, LTS, MS	5	AC divided into two layers
AC, AC, AC, CTB, LSS-MS	5	AC divided into three layers

8.6.4. Evolutionary Optimizations

In addition to the traditional optimization methods, evolutionary optimization methods (genetic algorithm and particle swarm) were also tried for finding the elastic moduli of the stabilized foundation pavement section (S2). These methods can be used for solving both constrained and unconstrained optimization problems based on a natural selection process that mimics biological evolution. They were used as the alternative to traditional iterative optimization in MASTIC. The reason for using evolutionary optimization methods was the versatility in these methods to avoid falling into local optimum and their independence from seed moduli.

Since the possibility of falling into local optimum increases as the number of layers increases in complex pavement structures, the evolutionary optimization methods can be used to arrive at more optimum solutions. These methods have successfully been used in the past to obtain the elastic modulus of the pavement systems *(Gopalakrishnan 2010)*. Unfortunately, these methods are prohibitively time consuming to execute and finding an optimum solution for one deflection basin can take several hours. The fine tuning of the hyper parameters is another problem which prevents these methods to be used for practical purposes. This study compared modulus for some of the deflection basins using traditional and evolutionary optimization techniques (after fine tuning the hyper-parameters of evolutionary methods) and found no significant difference in the results compared to traditional optimization methods. Since the run-time for evolutionary methods was extremely high and no additional advantage was found, they were not selected as the final method to obtain the backcalculation results.

8.6.5. Backcalculation on Thickness

One possible reason for having high variability in the data can be an error in the thickness used during backcalculation. To investigate such a problem, the thickness was considered to be unknown in the optimization problem along with elastic modulus. In the optimization of the thicknesses, the upper and lower boundaries were considered to guide algorithm to reach a reasonable solution. However, this method was also omitted from further investigation since it resulted in unrealistic elastic moduli as well as high variability in thickness for each station. In reality, it is expected that the backcalculated thickness for each station be more or less constant which was not the case for this analysis.

Additional methods such as using different objective functions for optimization, using different weights for each sensor in the optimization process, changing the number of sensors, etc. were also investigated to find a method that could best represent the pavement section properties. However, the main problem for all backcalculation processes was high variability in the data which remained the same regardless of the methods used. It seemed none of the approaches could resolve the high variability issue in the backcalculation results. In fact, the high variability was persistent regardless of the method used. Thus, more investigation was conducted to evaluate the source of variability in the data by assessing the raw deflection basins.

8.7. Direct Modulus Measurement for S2

Since the backcalculation using conventional methods did not produce acceptable results, additional investigation was conducted on raw deflection data to obtain insight about the approximate values of each layer's elastic modulus. This section also introduces a new methodology for finding the elastic modulus of the stabilized pavement sections through simulation and direct stress and strain measurements. To do so, this section combines all the information from laboratory testing, field stress/strain data, and pavement simulation results discussed in previous chapters to approximate the pavement elastic modulus for each layer.

8.7.1. The Approximate Method

Recall that the simulated dynamic response of the stabilized foundation section (S2) at the bottom of the AC layer had the form of Figure 8.15. In this figure, the AC modulus is the only variable with values changing from 100 ksi to 2000 ksi, while the CTB modulus is constant with the value of 2000 ksi (refer to Chapter 7 for simulation details). As shown, when the AC modulus is much

lower than the CTB layer, the response at the bottom of AC is mainly in compression. For the case of E1=100 ksi, before the center of the tire is positioned on top of the point interest (or zero offset), there exist a positive tensile uptick which is followed by a predominantly compressive response with higher magnitude and opposite sign at the load center. When AC elastic modulus increases from E1=100 ksi to a rather large value, a secondary spike is formed right at the center of the load and grows larger and larger as AC increases until the strain wave converts to predominantly tensile (as in the case of E1=2000 ksi). This behavior was also observed from the field measurements as explained in Chapter 5 and Chapter 7. The existence of this secondary spike was interesting since it was the function of the AC to CTB modular ratio. The higher the AC/CTB modular ratio, the higher the magnitude of this secondary spike. The secondary spike was also observed in the field from the strain measurements as discussed in Chapter 5. Since the secondary spike is the function of modular ratio, is it possible to obtain an approximate elastic modulus for the stabilized layers based on the modular ratio?

Figure 8.16 illustrates how compressive strains at the bottom of the AC under dynamic load events change with decreasing AC modulus. To obtain this figure, the minimum value from the entire dynamic response corresponding to a particular AC modulus was obtained. The graph shows that the minimum values always remain in compressive zone (i.e., negative sign) with the magnitude of compression increases as AC modulus decreases. It was shown in Chapter 5 and Chapter 7 that smaller AC moduli lead to higher compressive strain and this graph is in good agreement with previous findings.

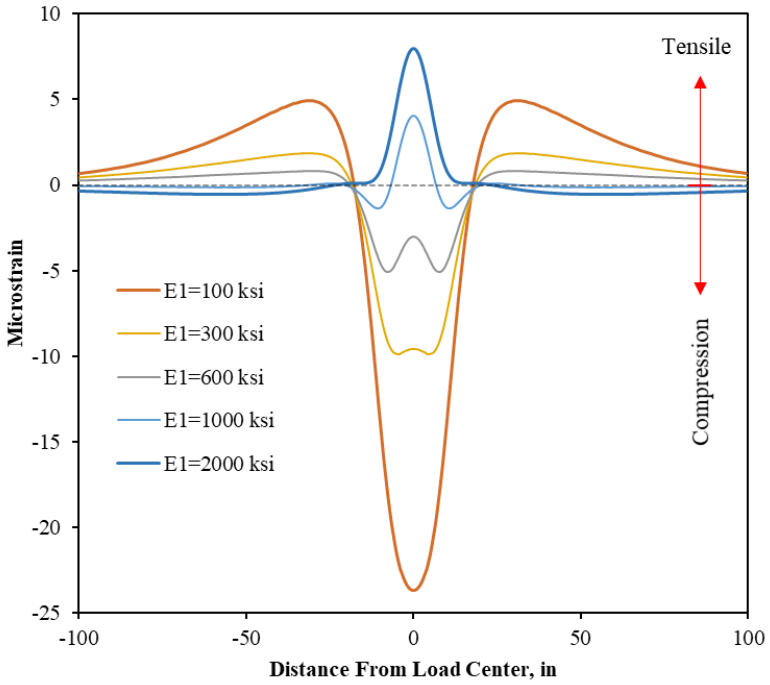

Figure 8.15 Simulated Dynamic Response of the Stabilized Foundation Section (S2) with Varying AC modulus.

A similar approach was taken to plot Figure 8.17 but this time the maximum value from each dynamic response was obtained. The maximum values are all positive and thus correspond to tensile microstrain at the bottom of the AC layer under dynamic load events. Interestingly, the response decreases with decreasing AC up to a point and then suddenly increases forming an inflection point with minimum value. For this particular simulation, there exist a clear inflection point at 670 ksi. Values less than 670 ksi have an increasing trend with AC modulus reduction, while values above 670 ksi have a decreasing trend. Thus, the pavement behaves completely different depending on the AC modulus.

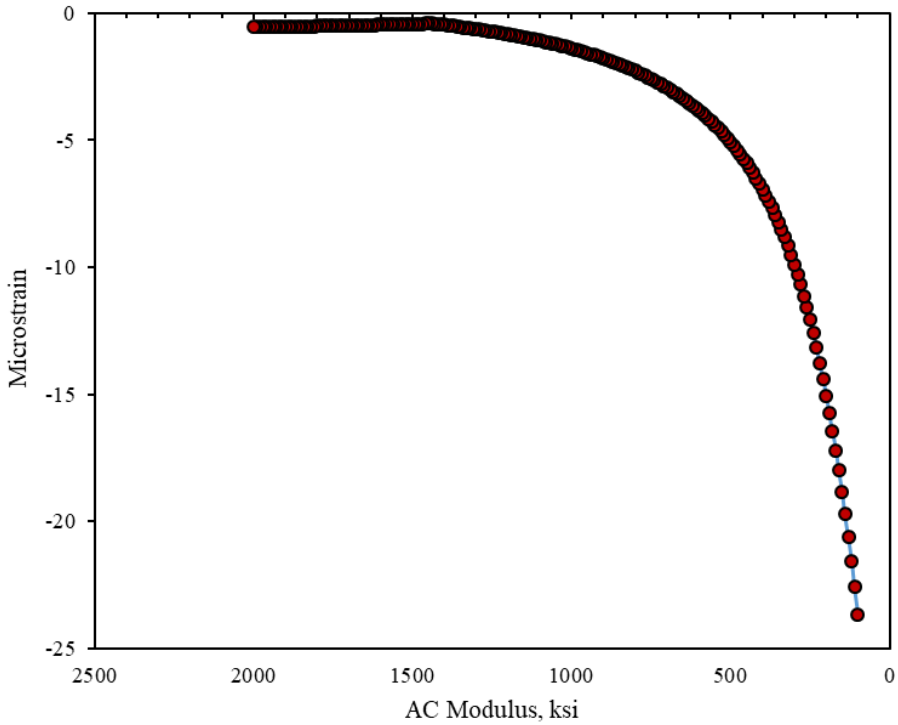

Figure 8.16 Simulated Compressive Strain for Dynamic Load with Varying AC modulus (CTB Modulus=2000 ksi).

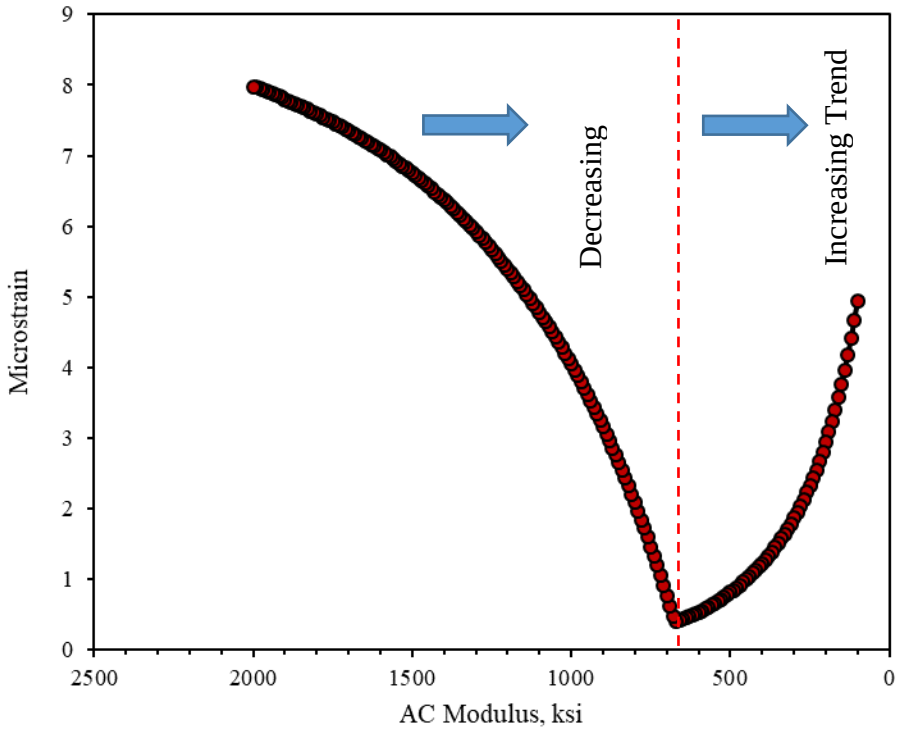

Figure 8.17 Simulated Tensile Strain for Dynamic Load with Varying AC modulus (CTB Modulus=2000 ksi).

The reason for such an interesting observation is the secondary spikes at the center of the load shown earlier in Figure 8.15. At the value of 670 ksi, the tip of the secondary spike just crosses the zero neutral axis and becomes positive (and hence in tensile mode), higher values than 670 ksi leads to larger positive strain responses since the secondary spikes keeps growing up as the AC modulus increases. However, at values less than 670 ksi, the dynamic strain response is predominantly in compression and the secondary spike is entirely in the compressive zone. Thus, the positive strain readings are coming from those little upticks before or after the load center. Thus, further reduction in AC modulus increases those positive upticks.

The inflection point occurred at the value of 670 ksi, or at CTB to AC modular ratio of 0.345 ($\frac{670}{2000} = 0.335$). Another set of analyses were conducted by changing the modular ratio to investigate at which ratio the inflection point occurs for different settings. All simulation configuration and settings followed those presented in Chapter 7. Figure 8.18 and Figure 8.19 illustrate two more cases with CTB modulus values of 1000 ksi and 5000 ksi, respectively. For Figure 8.18, the inflection point occurs at 320 ksi with modular ratio of $\frac{320}{1000} = 0.32$. Similarly, the modular ratio in Figure 8.19 is $\frac{1740}{5000} = 0.348$. This analysis demonstrates that changing elastic modulus drastically from 1000 ksi to 5000 ksi only slightly increases the modular ratio at which the inflection point occurs. In other words, the modular ratio at the inflection point is almost constant and is not influenced by pavement moduli. This finding could help approximating the elastic modulus for the CTB and since the CTB modulus is almost three times higher than the AC modulus at the inflection point. Thus, by finding the inflection point and having an approximate AC modulus at the inflection point temperature, one can obtain an estimate of CTB modulus in the field. But how to find an inflection point in the field from the strain measurements?

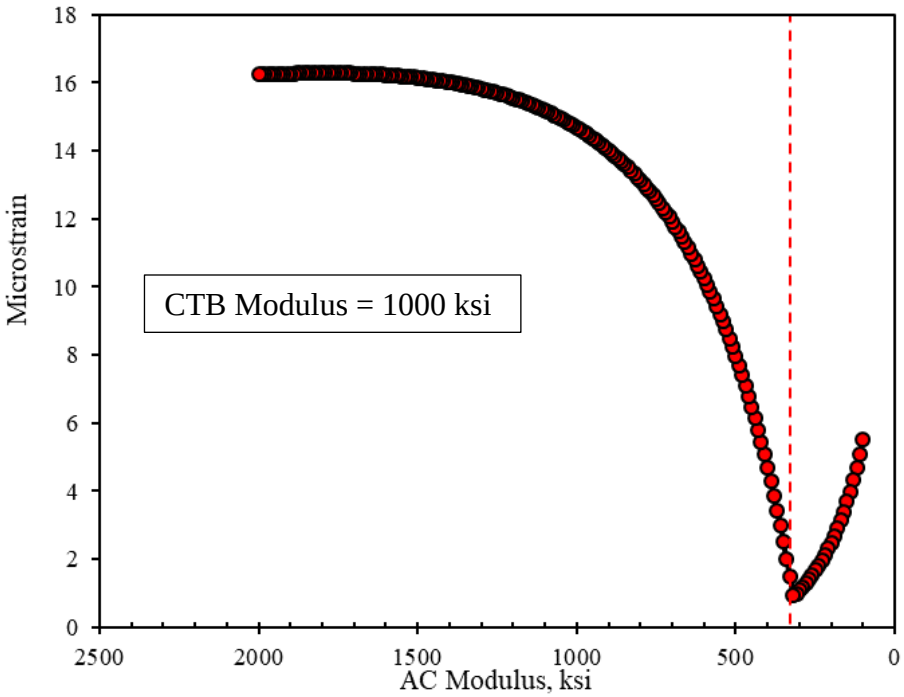

Figure 8.18 Simulated Tensile Strain for Dynamic Load with Varying AC modulus (CTB Modulus=1000 ksi).

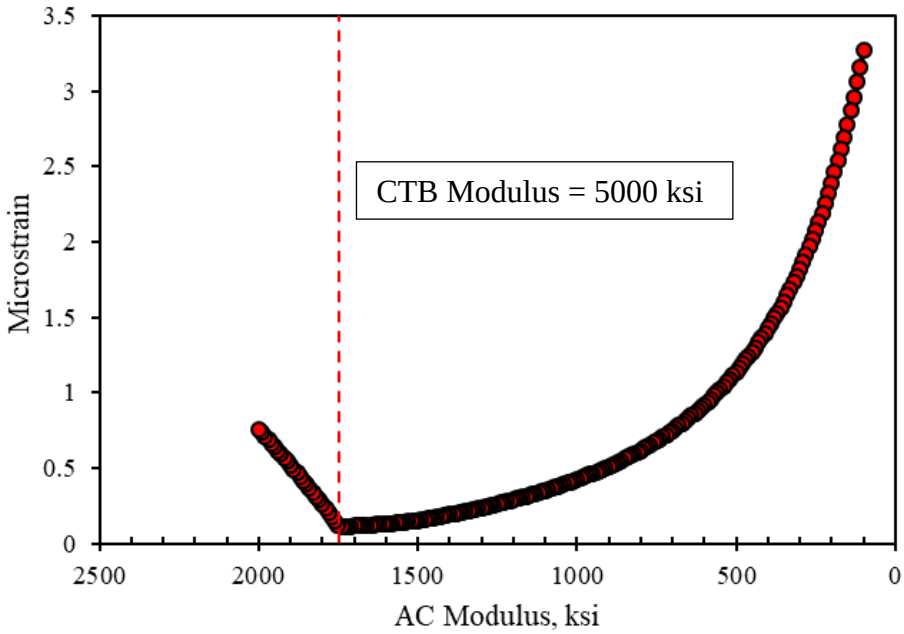

Figure 8.19 Simulated Tensile Strain for Dynamic Load with Varying AC modulus (CTB Modulus=1000 ksi).

The graphs above were plotted for the cases when the base course modulus was comparable or higher than the AC modulus. However, for conventional sections, the base modulus is significantly lower than the AC modulus. To capture the entire behavior of the tensile strain with respect to modular ratio at the bottom of the AC layer, the simulation results were plotted against modular ratio with a wider range of modular ratio, shown in Figure 8.20. In this figure, three zones can be perceived. When AC to base modular ratio is high, decreasing AC modulus increases the tensile strain response at the bottom of the AC layer (assuming a fixed base course modulus). This is a well-established phenomenon in pavement engineering where the decrease in AC modulus is generally accompanied with an increase in strain response and thus higher possibility for fatigue cracking. However, when the AC modulus is approximately two times higher than the base modulus to when it is around 0.3 of the base modulus, the graphs shows a reversed trend forming the second zone. In Zone 2, the tensile strain response is decreasing with the decrease in AC modulus assuming a fix base course modulus. This behavior was observed from the field measurements of the stabilized foundation section (S2) and discussed in previous chapters. In this zone, having smaller AC modulus helps prevent bottom-up fatigue cracking but the cracks may initiate from the middle of the AC layer (refer to Chapter 7). Zone 3 occurs when the AC/CTB modular ratio is less than about 0.3 where the decrease in AC modulus is accompanied with the increase in tensile microstrain (considering the base modulus to be constant).

These three proposed zones can potentially be used in the design of the stabilized foundation sections. For example, one can design a stabilized pavement such that its modular ratio falls into the Zone 2 and thus in the summer when the temperature is high and AC modulus is low, the decrease in AC modulus decreases the tensile microstrain. In addition, strain measurements for the stabilized sections are often observed to be less sensitive to temperature. This behavior can be

attributed to when the modular ratio is at around the boundary of the two adjacent zones. For example, the strain measurements at CCPR with stabilized foundation section (S12) were observed to be less sensitive to temperature (refer to Chapter 5). If the modular ratio is assumed to be at around the boundary of Zone 1 and Zone 2 (e.g. at AC/CTB modular ratio of around 2), then strain measurements can go up, down, or stay flat depending which side of the graph the ratio of AC/Base is, and thus would not necessarily follow a particular pattern with temperature.

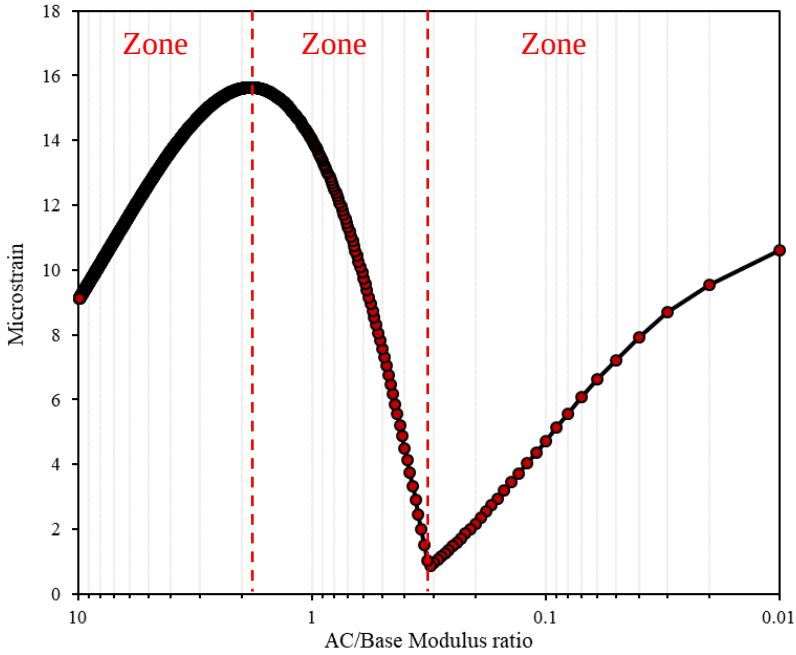

Figure 8.20 Microstrain Response VS Modular Ratio for the Four Layer System (Base Course Modulus= 1000 ksi).

Although the Figure 8.20 was shown for a four-layer system, the same conclusion can be obtained from a three-layer system as well. The zones are separated at around modular ratio of 2 and 0.3 similar to the four-layer system (and thus the graph for three-layer system is not shown here for brevity). Having the inflection point at almost constant modular ratios can help obtaining insight about the modulus of the pavement material using the observed strain measurements.

However, finding the inflection points in the field is challenging especially at Zone 2 and 3 since the strain levels approach zero which increases the noise to signal ratio. However, in Chapter 5, it was shown that 75 °F was the temperature at which the magnitude of strain at compression exceeded the magnitude of tension under the truck loading for the stabilized foundation section (S2). In other words, the actual measured response at this temperature changed from predominantly tensile to predominantly compression. Thus, this temperature can be considered as the inflection point temperature at which the behavior of the pavement changes. Below this temperature, the dynamic strain signal at the bottom of the AC is predominantly in tensile mode. Above 75 °F when the AC is relatively softer, the strain readings are predominantly in compression. Therefore, this temperature can be considered as the temperature at which the inflection point occurs.

In order to estimate the elastic modulus of the CTB layer, given the inflection point at 75 °F, the AC modulus should be first estimated. Estimating AC modulus for this section was more convenient than estimating the CTB modulus since NCAT had a database of historical elastic modulus for unmodified asphalt mixtures obtained from field backcalculation on regular sections. In addition, the comparison with the thick-lift pavement section (S9), which was constructed with unmodified binder in the same year and experienced the same level of traffic and climate, helped obtain an estimation of the AC modulus for the stabilized foundation section (S2). Based on Figure 8.7, the AC modulus of the thick-lift pavement (S9) is approximately 600 ksi at 75 °F. This value was in line with the values obtained from other structural sections at the Test Tack and was also in good agreement with the laboratory data for section S2 (refer to Chapter 4 for laboratory data). It can thus be assumed that the AC modulus for the stabilized foundation section (S2) is approximately 600 ksi at 75 °F. This value is just an estimate to obtain insight for this section and my not necessarily be exact. From the inflection point analysis, it was shown that the CTB modulus

is almost three times higher than the AC modulus at the inflection point (or at 75 °F). Thus, the CTB modulus can be assumed to be around 1800 ksi at the inflection point. Assuming CTB to be insensitive to temperature, this value can be considered for the CTB layer's modulus. Note that this value is just an approximation of the true value and slight changes in AC modulus can significantly change the CTB modulus estimation. As an example, considering an interval of 200 ksi for the AC value (600 ± 200 ksi), the CTB modulus changes from 1200 ksi to 2400 ksi. However, this analysis provides an insight about the range of values that can be expected from the field data.

So far, from the direct measurements and simulations, the value of CTB and AC have been approximated. In order to obtain LTS elastic modulus, the CTB to LTS modulus ratio from the laboratory data can be used. It can be assumed that despite the difference in field and laboratory measurements, the CTB to LTS modular ratio should be constant. It was shown in Chapter 4 that the CTB to LTS modular ratio is around 3.0, and thus CTB modulus is 3 times higher than the LTS. Assuming this ratio to hold true for the field as well, the elastic modulus for LTS can range from 400 ksi to 800 ksi with an average of 600 ksi. This estimate is not far away from the lab fabricated lab tested measurements where the average for LTS modulus was 366.6 ksi (refer to Chapter 4).

Using the inflection point analysis and laboratory data, the moduli for CTB and LTS were obtained based on the proposed approximate approach. However, subgrade modulus can be obtained independently following the approach presented in *(Irwin, 2002)*. The next section discusses the direct method used to calculate elastic modulus of the subgrade.

8.7.2. Direct Estimation of Subgrade Modulus

This section tries to calculate the modulus for the subgrade directly from the deflection basins using the method introduced in *(Irwin, 2002)*. From the Boussinesq equations, the relationship between the vertical deflection on the surface for a half-space system, δ_z, and the elastic modulus, E, can be described as the following equation for a point load on the surface:

$$\delta_z = \frac{P}{\pi E r}(1 - \mu^2) \tag{8.1}$$

where P is the surface load, r is the radial distance from the load, and μ is the Poisson's ratio. Irwin *(2002)* showed that this equation can be used to estimate the elastic modulus of the subgrade directly using outer sensors of the FWD. However, this equation cannot be used for sensors closer to the load center. By assuming $\mu = 0.45$, and plugging $P, r,$ and δ_z from FWD data, the subgrade modulus was obtained from the sensors at the offsets of 48 in., 60 in., and 72 in. for the entire deflection basin history collected with 4752 records. Table 8.5 presents the average and standard deviation for the elastic modulus of the subgrade calculated using the three outer sensors of the FWD at the Test Track. The results include all the 12 stations of the stabilized foundation section (S2). From the results, the subgrade modulus can reasonably be assumed to be at around 30 ksi.

Table 8.5 Average and Standard Deviation for Direct Subgrade Modulus Estimation

	Offset 48 in.	Offset 60 in.	Offset 72 in.
Average (ksi)	28.3	28.8	30.5
Standard Deviation (ksi)	4.5	5.3	7.2

**the number of records to calculate average and standard deviation: 4752.*

Although the approximate solution provided an insight about the range of values that should be expected from the backcalculation, having the exact solution was necessary to provide more accurate estimation of this section's properties. Unfortunately, high variability in the

backcalculated moduli was still the main issue and all tried models led to high variability. The next section discusses the efforts made to find the source of high variability by investigating the raw deflection data.

8.7.3. Bedrock Depth

Since it was important to establish that the source of backcalculation issue for the stabilized section was not coming from a shallow bedrock layer, the method introduced in *(Irwin, 2002)* was used to estimate the bedrock depth. Due to high stiffness of the CTB material, this layer could have potentially performed similar to a stiff bedrock. The presence of a very stiff layer (bedrock) at a shallow depth can be significant in backcalculation results.

In Equation 8.1, it can be seen that there is a relationship between the deflection, δ_z, and the reciprocal of the radius, r. According to this equation, the deflection can be expected to be zero when the radius is infinity. Thus, the plot of deflection versus 1/r which has a positive x-intercept is expected to possibly have a shallow stiff layer. Figure 8.21 shows an example of two deflection basins with and without a shallow bedrock. In this figure, the x-axis is normalized by multiplying it by the plate radius *a*. Note that the bottom graph with triangle markers crosses the positive side of x-axis and thus shows a possibility for a shallow bedrock whereas the upper graph crosses the negative side of the x-axis suggesting no bedrock at shallow depth. It is generally believed that the presence of a bedrock with depth greater than 10 feet would not affect the backcalculation results.

In order to investigate the possibility of a very stiff layer at shallow depth, this study conducted the regression analysis for the entire dataset (e.g. all 4752 deflection basins). Simple linear regression lines were fitted to the four outer most sensors of the deflection basins. The

summary of the data is presented in Table 8.6. In this table, the proportion of deflection basin with positive x-intercept to overall number of deflection basins is presented based on each station.

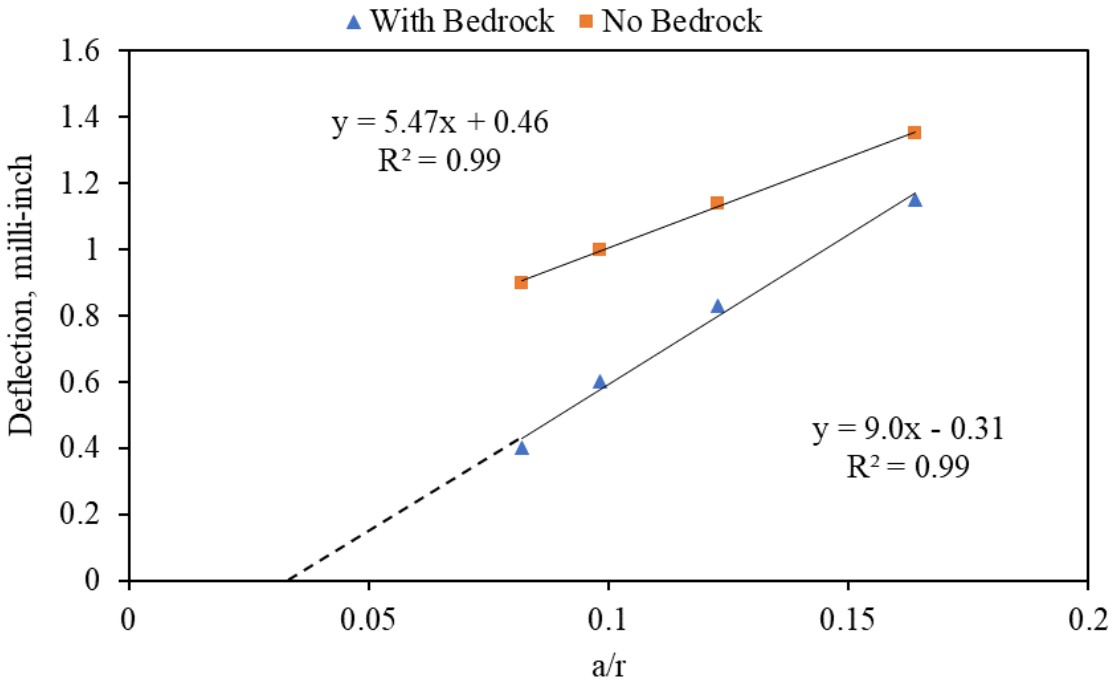

Figure 8.21 Depth of Bedrock Evaluation Graph.

Table 8.6 Shallow Bedrock Percentage for the Entire Dataset

Station	Positive x-Intercept	All	Percentage of Positive x-Intercept	Comment
S2-1	357	459	77.8%	Negative x-intercept occurred only for temps < 70 °F
S2-2	211	216	97.7%	Negative x-intercept occurred only for temps < 60 °F
S2-3	507	513	98.8%	Negative x-intercept occurred only for temps < 60 °F
S2-4	35	450	7.7%	Positive x-intercept occurred only for temp>115 °F
S2-5	14	216	6.5%	Positive x-intercept occurred only for temp>105 °F
S2-6	46	513	8.9%	Positive x-intercept occurred only for temps>105 °F
S2-7	358	468	76.5%	Negative x-intercept occurred only for temps < 73 °F
S2-8	94	216	43.5%	-
S2-9	197	513	38.4%	-
S2-10	5	504	1.0%	Positive x-intercept all at temp > 110 °F
S2-11	0	234	0.0%	-
S2-12	0	540	0.0%	-

Table 8.6 suggests there exists three types of stations within section S2. Stations S2-10, S2-11, S2-12, S2-4, S2-5, and S2-6 (which are RL#2 and RL#4) had at maximum less than 9% positive x-intercept. For these stations, the positive x-intercept was computed only when the mid-depth asphalt temperature was considerably high (more than 105 °F) resulting in low AC stiffness. On the other hand, sections S2-1, S2-2, S2-3, and S2-7 had at minimum 77% positive x-intercept. Exceptions were for cold days when the mid-depth temperature was less than 70 °F and AC modulus was high in general. Sections S2-8 and S2-9 represented an intermediate state between the two mentioned scenarios with a mixture of positive and negative x-intercept.

In Irwin's original research paper *(Irwin, 2002)*, the positive x-intercept was used to calculate the depth to the bedrock. Those with significantly shallow bedrock should be excluded from the backcalculation since the modulus is affected by the bedrock. It is generally assumed that the bedrock below 10 ft would not affect the backcalculation results. The negative depth also indicates no bedrock effect. The distribution of the bedrock is shown in Figure 8.22. The histogram shows an approximately normal distribution but with no value between 0- and 10-feet interval. According to the graph, none of the deflection basins should be affected adversely by the bedrock. However, this analysis suggested that there exist two distinct categories within the stabilized foundation section (S2). One category with large number of positive x-intercepts, and another with almost no positive x-intercept. The third category can be represented as a mix state between the two other categories.

To investigate more on the x-intercept, Figure 8.23 is plotted which illustrates the relationship between x-intercept and mid-depth pavement temperature for stations S2-3 and S2-12. These sections had highest and lowest positive x-intercept among the other stations, respectively. The data suggests two different behaviors. For station S2-3, the increase in

temperature increases the magnitude of intercept, while S2-12 shows a decrease in magnitude with a negative sign.

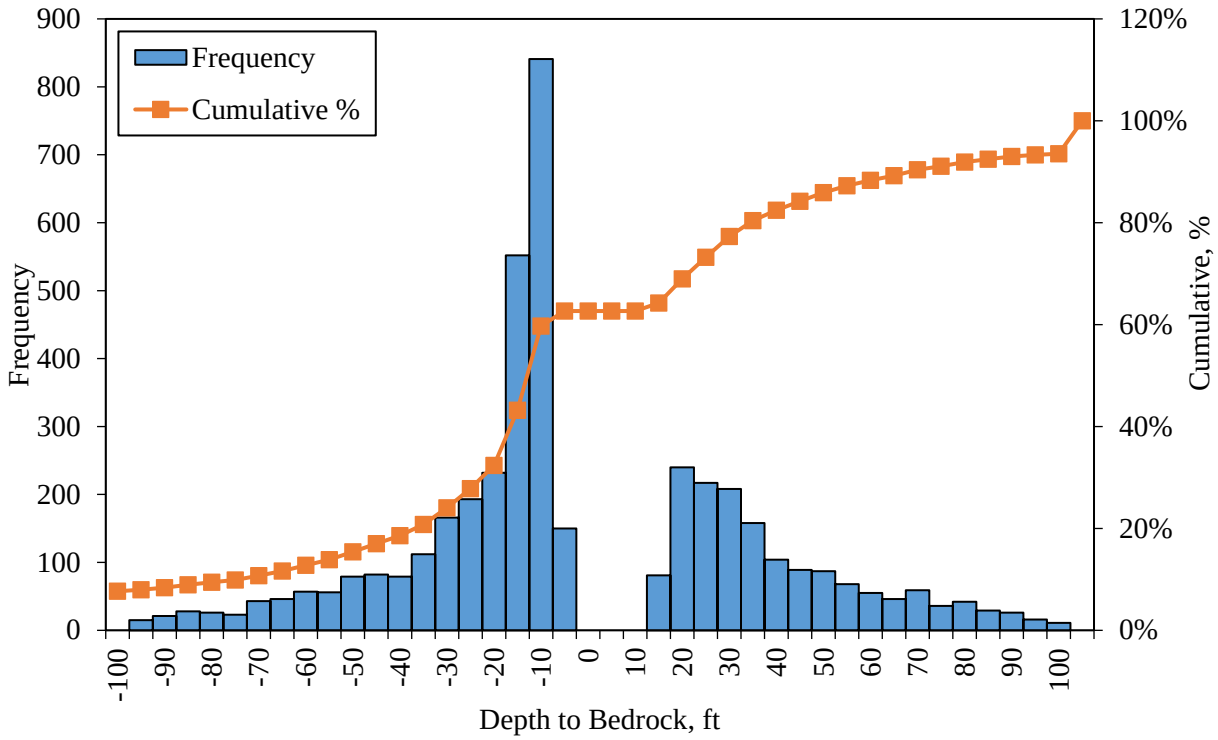

Figure 8.22 The Depth to the Bedrock for the Entire Dataset.

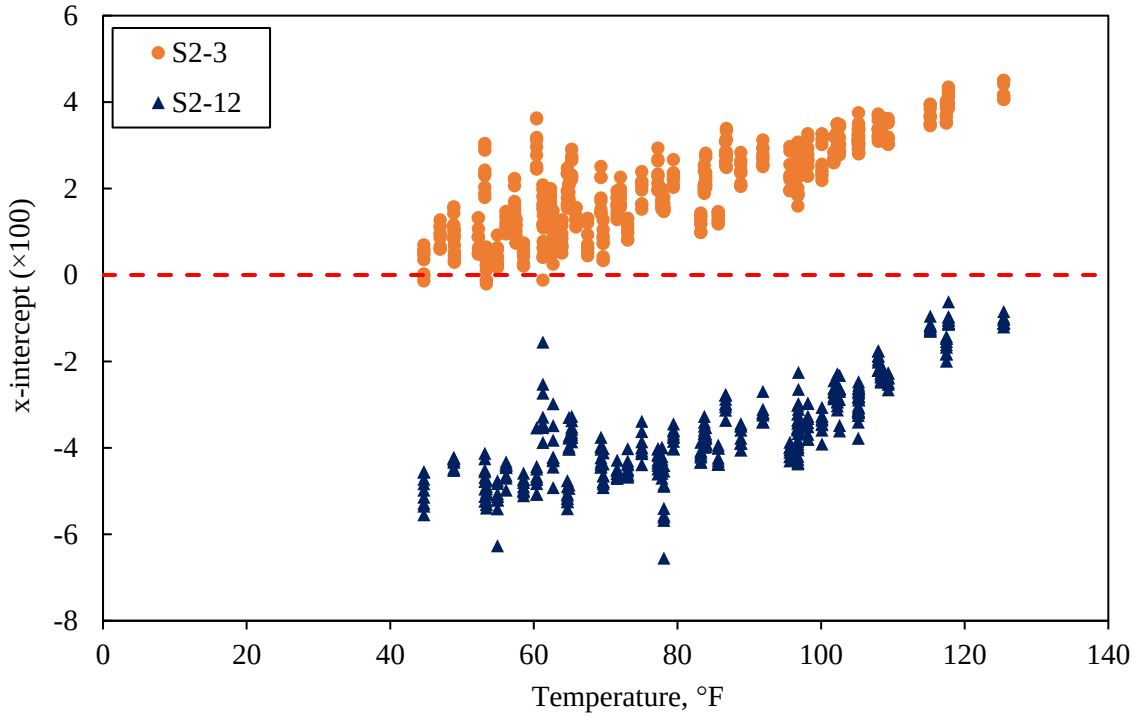

Figure 8.23 x-Intercept versus Temperature (for load level 8000-1000 lb.)

Figure 8.24 shows the same dataset but for the depth of the bedrock. Since the x-intercept is dependent on temperature, the depth to the bedrock is also affected by the temperature. Thus, finding the depth to the bedrock using the Irwin's approach should be carefully considered since the bedrock is a geological feature and should not be dependent on temperature. This analysis illustrates that Irwin's approach may lead to temperature sensitive results. However, this method can provide insight about the behavior of the pavement sections since it is directly conducted on the raw deflection data. This study made use of this analysis not for finding the bedrock depth but rather to distinguish different behaviors within the stabilized foundation section (S2). The difference in the behavior was the key to understand the high variability in the backcalculation for the stabilized foundation section (S2). The different structural behavior within S2 may be attributed to construction practices in the field.

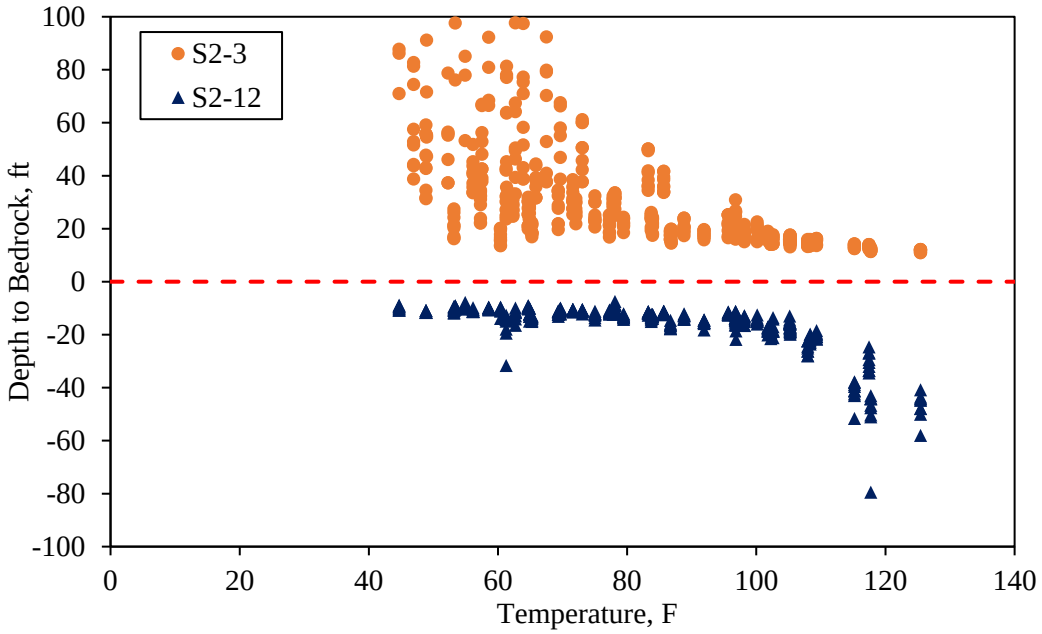

Figure 8.24 Depth to the Bedrock versus Temperature

Since different behaviors were observed within section S2, it was important to investigate the raw deflection basins for each station individually. For comparison purposes, the deflection basins had to first be normalized with respect to load level and temperature since they can vary depending on load level and pavement temperature. To normalize the data, a simple linear regression line was obtained for each station at each date and each radial offset by considering the load level as independent variable and the deflection as dependent variable. Then, using the calculated regression equations, the deflection at each radial offset was obtained for the standard load level of 9000 lb. Thus, the 9 deflection basins obtained from 9 FWD drops at each station and each date were replaced by a single deflection basin at 9000 lb. Using this approach, the calculated deflection basins were normalized for the load level. To normalize for the temperature, a similar approach was taken where a simple linear regression line was obtained from the load-normalized deflection basins at each station and each offset considering temperature as independent variable and load-normalized deflections as dependent variable. Using the regression lines for each station and each radial offset, the deflections at 68 °F were calculated. Thus, the final results were normalized based on temperature and load level.

Figure 8.25 compares the normalized deflection basins of the stations S2-3 and S2-12. The S2-3 had the highest percentage of positive x-intercept while S2-12 had the lowest. Both deflection basins were normalized based on temperature and load level. For all radial offsets, the station S2-12 had higher deflection values compared to S2-3. The reason for having smaller deflection at the S2-3 can be attributed to the construction factors (e.g. higher cement/lime content, higher compaction, thicker section, etc.). This analysis indicated the same results for other stations as well. The stations with higher positive x-intercept were stiffer and had smaller deflection basins. To illustrate this better, the normalized deflections are plotted again in Figure 8.26 but only for the

outer most FWD sensor, at the radial offset of 72 inches, for all stations. This figure distinctly demonstrates that the stations S2-2 and S2-3 had smaller normalized deflections for the outer most sensor. Interestingly, the stations with lowest number of positive x-intercepts (e.g. stations at RL#2 and RL#4) had the highest normalized deflections. It can thus be concluded that x-intercept can be regarded as a measure of station's stiffness. The larger the x-intercept, the stiffer the section. It is particularly evident in Figure 8.23 where the increase in temperature increased the x-intercept value for both S2-3 and S2-12. The different behaviors within section S2 was the key to understand the high variability in backcalculation which will be discussed in next section.

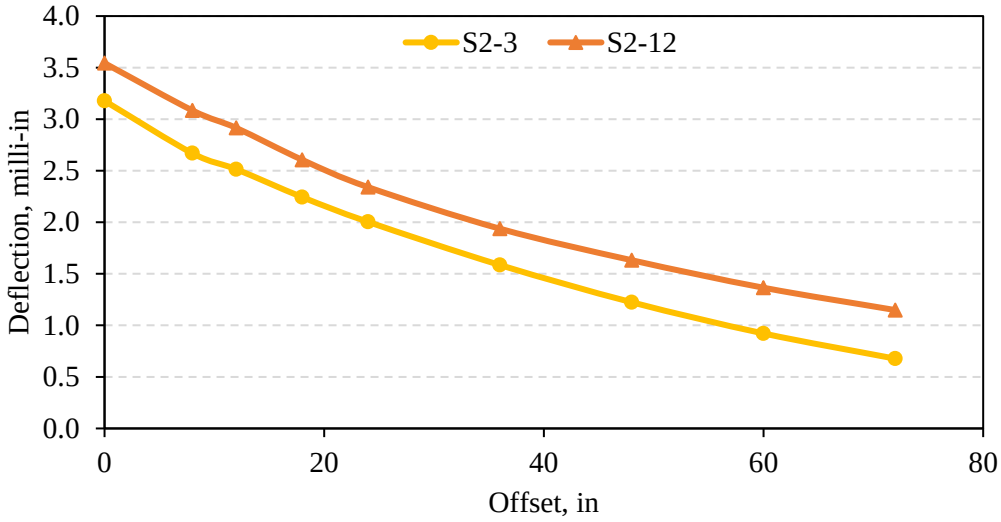

Figure 8.25 Temperature and Load Normalized Deflection Basin for S2-3 and S2-12.

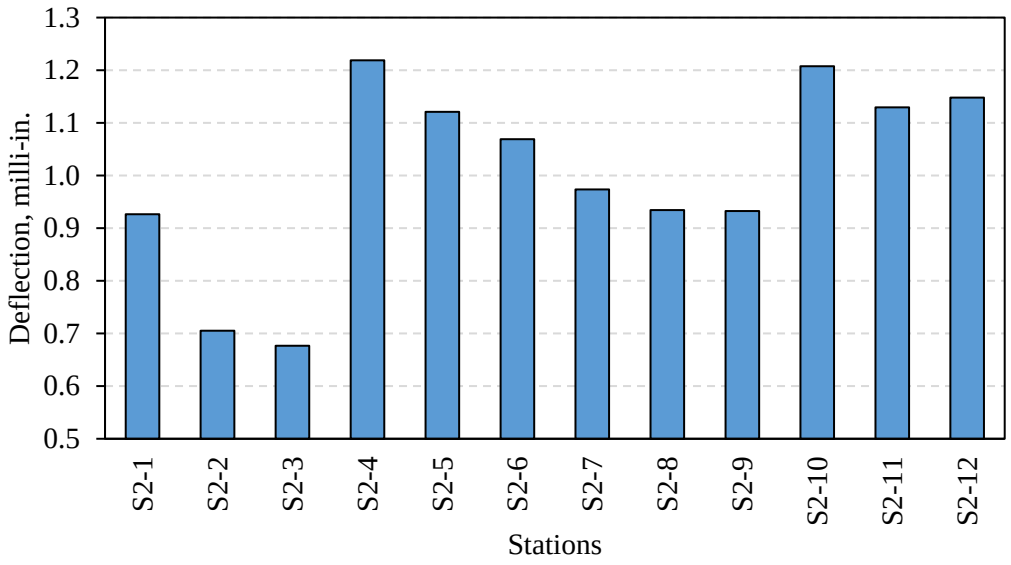

Figure 8.26 Normalized Deflection for Outer Most FWD Sensor

In summary, this subsection proposed a new approach for measuring the direct modulus from the strain measurements at the bottom of the AC layer for the stabilized foundation pavement (S2) using the inflection points. The estimated modulus values for AC, CTB, LTS, and subgrade were 600 ksi, 1800 ksi, 600 ksi, and 30 ksi, respectively. In addition, a new fundamental curve was proposed for all flexible pavements suggesting the pavements may exhibit different behaviors based on AC to base modulus ratio. These behaviors can be categorized into three zones. The proposed zones are a function of pavement modular ratio and thus can be used to characterize pavement sections. It was also found that some stations within the stabilized foundation had smaller deflection basins and possibility a different behavior that could explain the high variability in the data obtained from the backcalculation methods. The next section will discuss the final approaches used to backcalculate the elastic modulus for the stabilized foundation pavement section (S2) using the information presented so far.

8.8. Selected Models for S2

This section presents the final approaches that were taken to characterize elastic modulus values for the stabilized foundation section (S2). The proposed approaches are entirely based on the data obtained from FWD equipment and thus no changes is needed to the original equipment. The following section discusses the methods used to backcalculate the sections.

8.8.1. The Partial Friction Method

The backcalculation process is often implemented assuming all pavement layers to be bonded. This assumption affects the estimated elastic modulus for the pavement sections. However, it can be shown that this assumption may not result in a significant difference in the backcalculated elastic moduli of the conventional sections (see Appendix B for comparison). Thus, when MASTIC was initially developed, the fully bonded condition was the only setting considered in its development. However, since the backcalculation was found challenging, the slip and partial friction methods were added later to investigate the effect of bonding condition on the backcalculation results of the stabilized foundation section (S2). In addition, it was observed from the simulations that the stabilized foundation section was sensitive to bonding stiffness (see Chapter 7), hence it was hypothesized that the interface bonding could potentially affect the results.

To investigate which bonding stiffness would result in the lowest RMSE and variance, a grid search approach was taken to fine-tune the bonding interface values. All three, four, and five layer systems were considered again. For all systems, the bonding stiffness was ranged from slip to fully bonded (10^{-3}- 10^{13}) ksi/in. Different cross-sections were also considered. Since the number of scenarios to investigate all options was large (more than 130 different scenarios), only 70% of

the database was selected for evaluation of the results to speed up the process. Final, candidates were investigated further using the entire dataset.

After, reviewing all scenarios and cross sections, it was found through comparison that a four-layer system with the original cross-section and fully bonded condition for AC/CTB interface along with nearly full slip conditions for other layers (with horizontal stiffness of 10^{-3} ksi/in.) is the best-case scenario for having reasonable results and less variance. Figure 8.27 through Figure 8.30 illustrate the backcalculation results for the four-layer system obtained using partial friction method for the RL#2 and RL# 4 (see Figure 8.3 for the positions of the random locations). The reason for including only these random locations will be explained in the next section. In Figure 8.27 through Figure 8.30, the red line on the left graph represents a simple linear regression line, and the one on the right shows the 30-point moving average fitted to the data. The data for other scenarios are not provided in this document for brevity. The backcalculation results using partial approach were extremely sensitive to the bonding interface of AC/CTB and thus having a bonded condition for the top interface was necessary. It was shown in Chapter 7 that the behavior of the stabilized foundation section (S2) suggested a fully bonded condition for AC/CTB interface. The backcalculation process also suggested the same. However, having almost full slip conditions for other layers led to less variability and more reasonable results. The results were obtained considering the following bonding conditions (Table 8.7) and search space (Table 8.8):

Table 8.7 Bonding Interface Values for Final Backcalculation Model.

Interface	Horizontal Spring Stiffness (ksi/in.)	Comment
AC/CTB	10^{13}	Almost Bonded
CTB/LTS	10^{-3}	Almost Slip
LTS/Subgrade	10^{-3}	Almost Slip

Table 8.8 Upper and Lower Bounds of the Search Space for the Partial Friction Method

	AC, ksi	CTB	LTS, ksi	Subgrade, ksi
Upper Limit	3500	5000	2000	100
Seed	500	2000	300	30
Lower Limit	80	80	1	1

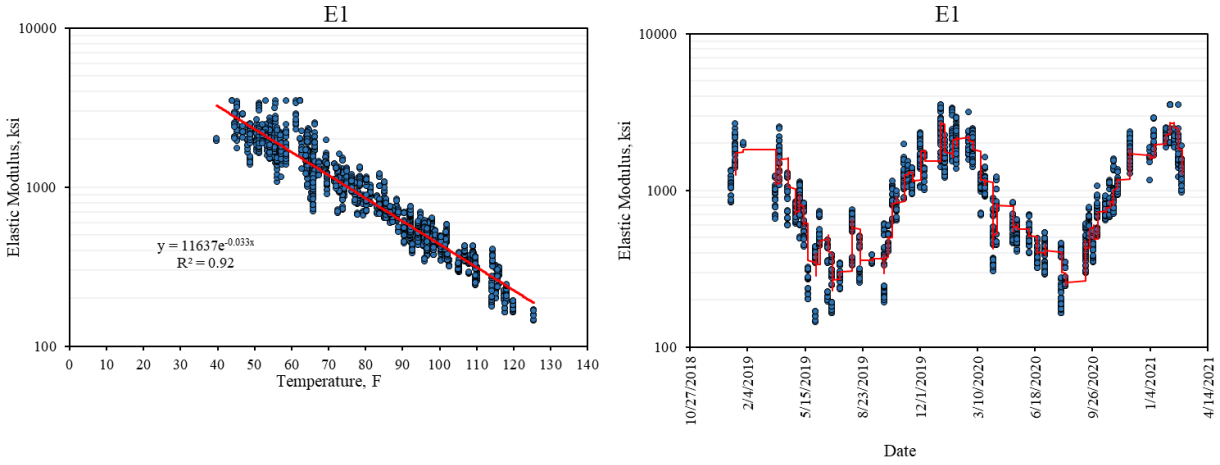

Figure 8.27 Backcalculated AC Moduli Using Partial Friction Method (RL 2 and 4).

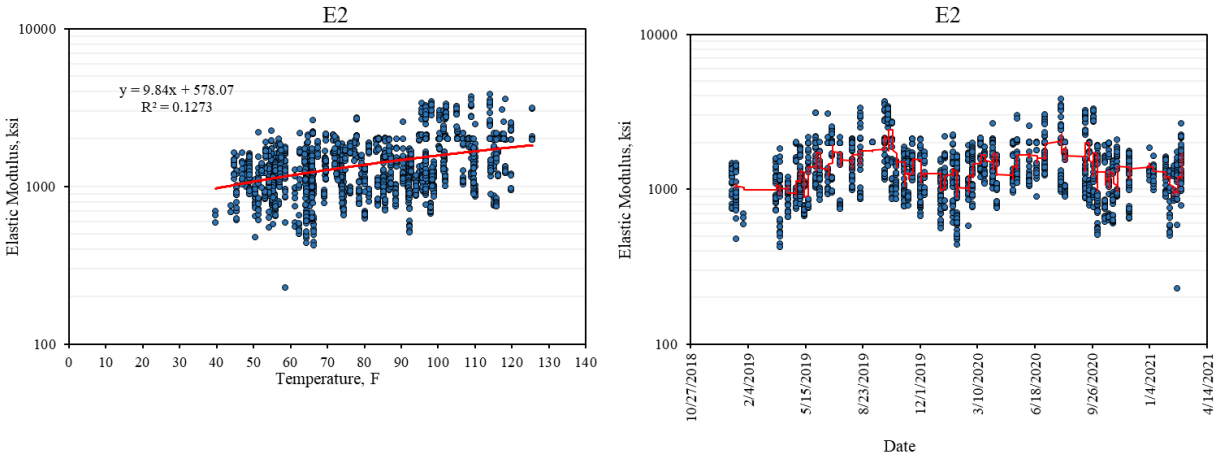

Figure 8.28 Backcalculated CTB Moduli Using Partial Friction Method (RL 2 and 4).

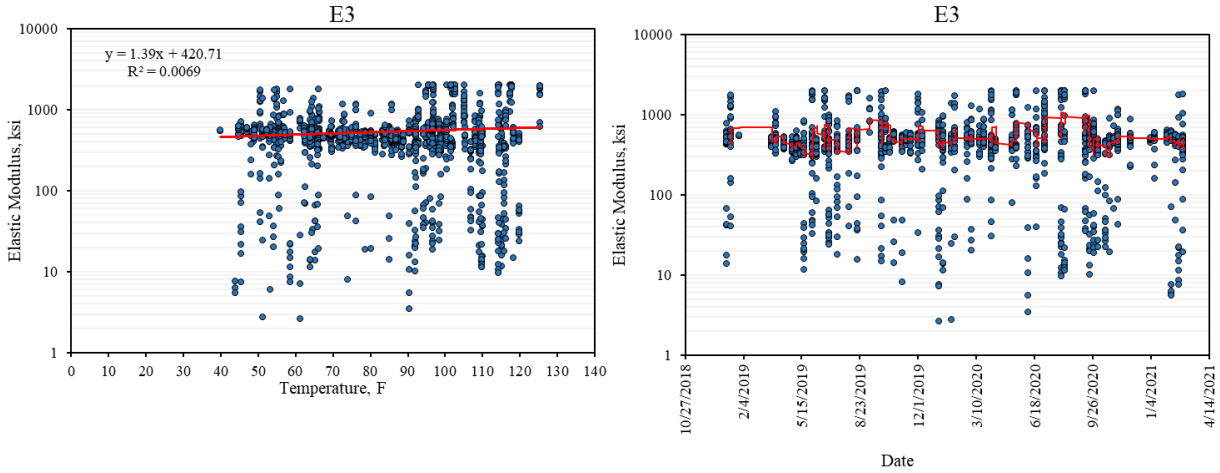

Figure 8.29 Backcalculated LTS Moduli Using Partial Friction Method (RL 2 and 4).

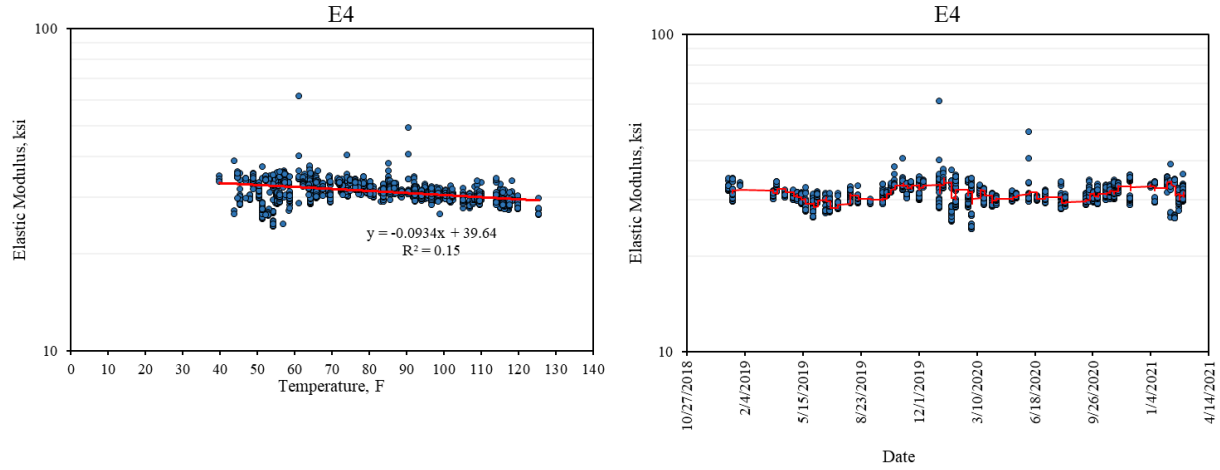

Figure 8.30 Backcalculated Subgrade Moduli Using Partial Friction Method (RL 2 and 4).

The thicknesses used for this analysis was shown earlier in Table 8.1 with Poisson's ratio of 0.35, 0.2, 0.4, and 0.45 for AC, CTB, LTS, and subgrade respectively. A quick comparison between bonded (Figure 8.11 through Figure 8.14) and the partial friction method (Figure 8.27 and Figure 8.30) suggests smaller variation in the data especially for CTB and LTS layers. The AC and subgrade moduli seemed to be less affected by the methods used. However, the CTB and LTS soil moduli were obtained with less variability for the partially friction method. In fact, the COV reduced from 100.8% to 41.8% for CTB, and from 100.5% to 66.4% for LTS.

Figure 8.28 suggests a small increasing trend for the CTB materials with temperature. This could be due to stress hardening effect of the CTB materials or due to error in backcalculation (e.g. possibly compensation error). A decreasing trend can be observed for subgrade soil modulus (Figure 8.30) which may indicate the stress softening of the subgrade materials.

In general, the partial friction method seemed to significantly reduce the variability in the data. But does the modulus obtained using this approach reflect the material properties? Table 8.9 compares the results obtained from the backcalculation using partial friction method, the approximate approach (presented in previous section), and the laboratory data for lab fabricated samples (see Chapter 4). As shown, the moduli obtained from each method had the same order of magnitude. The approximate approach seems to overestimate the elastic moduli of CTB and LTS on average, but obtained a very close value for the subgrade soil. This is because the approximate approach is dependent on the initial guess of the AC modulus and slightly different guess can over- or underestimate the CTB and LTS moduli.

The laboratory elastic modulus of CTB and LTS are close to those obtained from the backcalculation process. With 95% confidence level and assuming a t-distribution, the confidence interval of the CTB modulus for lab fabricated samples was 1012 ± 146.2 ksi. This interval for backcalculation CTB was 1384 ± 25.57 ksi. Although the difference on averages is statistically significant, the difference seems reasonable considering the two completely different testing approaches. The confidence interval of LTS modulus was 523.5 ± 16.7 ksi from the backcalculation process while was 366.6 ± 49.5 ksi for lab fabricated results. Again, although the difference was statistically significant, they were in the same order of magnitude from the engineering point-of-view.

Table 8.9 Elastic Moduli Comparison for Different Methods.

Method	Property	CTB	LTS	Soil
Backcalculation	Average, ksi	1384.5	523.5	31.3
	Standard Deviation, ksi	554.5	360.5	2.2
Approximate Approach	Average, ksi	1800	600	30.5
	Standard Deviation, ksi	NA[a]	NA[b]	7.2
Laboratory Data	Average, ksi	1012.5*	366.6**	NA
	Standard Deviation, ksi	294.6	69.2	NA

[a] CTB modulus ranged from 1200 ksi to 2400 ksi using approximate approach.
[b] LTS modulus ranged from 400 ksi to 800 ksi using approximate approach.
** Lab-fabricated, lab-tested samples for 180 and 360 days cured samples.*
*** Lab-fabricated, lab-tested samples for 180 days cured samples (no data for 360 days of curing).*

Using the partial friction method, the variability was reduced significantly, but there was still considerable variability in the data especially for CTB and LTS layers. These variabilities can be attributed to construction factors from one section to another or the model errors or a combination of both. To investigate the source of the variability further, Figure 8.31 and Figure 8.32 were plotted which show the distribution of elastic modulus for CTB and LTS layers. For the CTB layer, the majority of the data was around 1200 ksi, while for LTS the majority was centered at around 500 ksi.

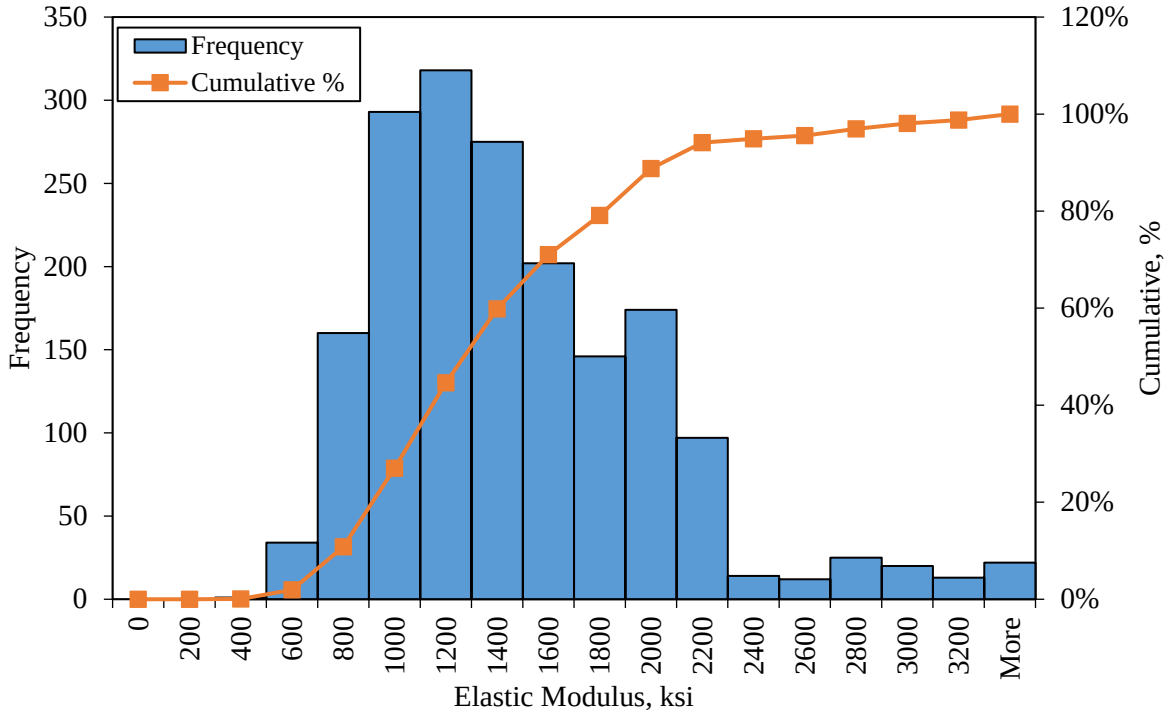

Figure 8.31 The Distribution of CTB Elastic Modulus for Random Location 2 and 4 Using Partial Friction Method (four layer system).

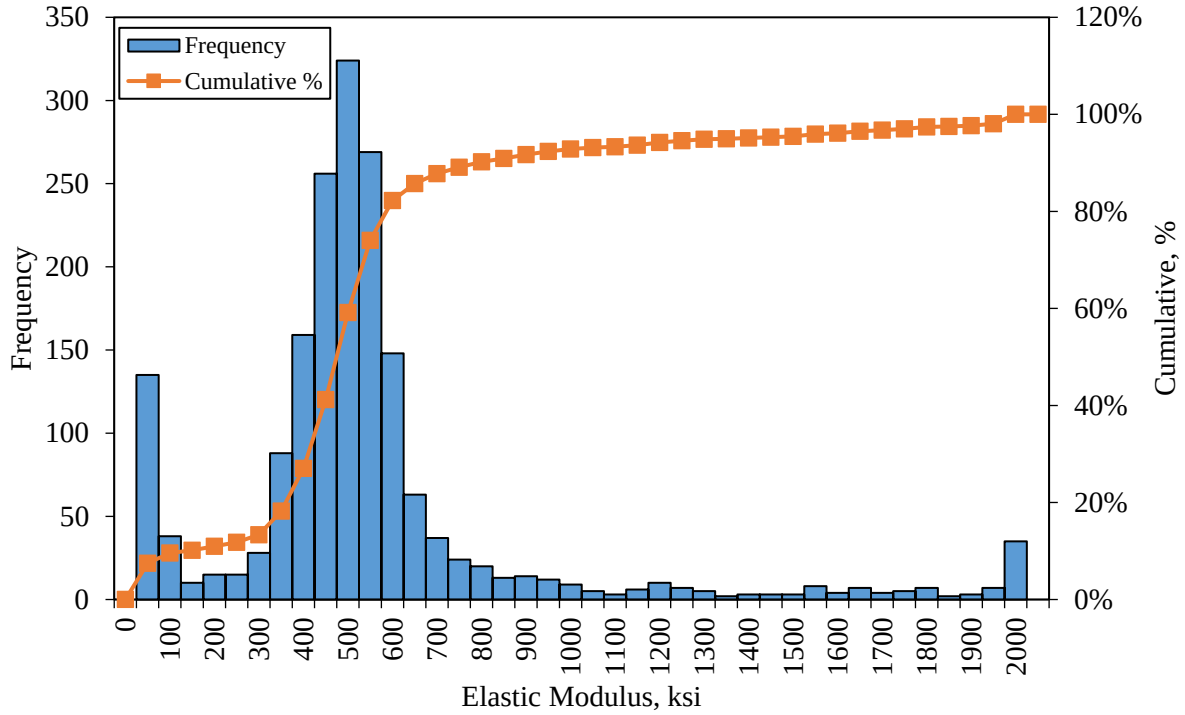

Figure 8.32 The Distribution of LTS Elastic Modulus for Random Location 2 and 4 Using Partial Friction Method (four-layer system).

In Figure 8.32, another group of data at the lower tail of the graph can be observed. For this group, the LTS elastic modulus was underestimated significantly. In fact, while the majority of data indicated much higher elastic modulus, a small portion did suggest otherwise. Due to ill-posed nature of the backcalculation process, especially for complex structures with more than three layers, it is possible that a solution falls into a local optimum and results in unexpected values. Another possibility is the existence of higher noise in the deflection measurements due to high stiffness for the CTB layer. For some deflection basins the noise to signal ratio could be higher than other drops resulting in erroneous backcalculation. It was particularly observed that the variation in LTS modulus came from lower weight FWD drops. The data that filtered for load levels of 8000 lb. to 10000 lb. provided smaller variation for LTS modulus. The data is presented in Appendix C.

Since small elastic modulus for LTS can indicate falling into local optimum, to investigate the elastic modulus for those that possibly converged to a global solution, the graphs were plotted again but by filtering the data for LTS that are between 300 ksi to 700 ksi (where the majority of the data exists). Figure 8.33 through Figure 8.36 illustrate the backcalculated modulus values for the stabilized foundation section (S2) using partial friction method obtained by limiting the LTS modulus to 300 ksi – 700 ksi. Similar to other graphs, in Figure 8.33 through Figure 8.36, the red line on the left graph represents a simple linear regression line, and the one on the right shows the 30-point moving average fitted to the data. By applying this filtering, the elastic modulus for AC and CTB layers did not change significantly and remained more or less constant. However, the elastic modulus for LTS was cleaned significantly. The COV further reduced from 66.4% to 17.5%.

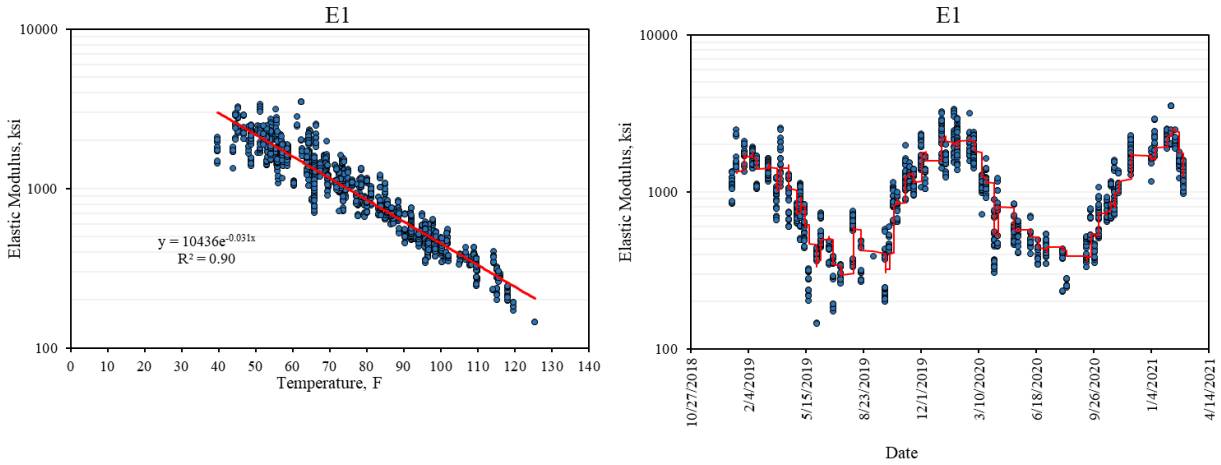

Figure 8.33 Backcalculated AC Moduli with Filtered Data (RL 2 and 4).

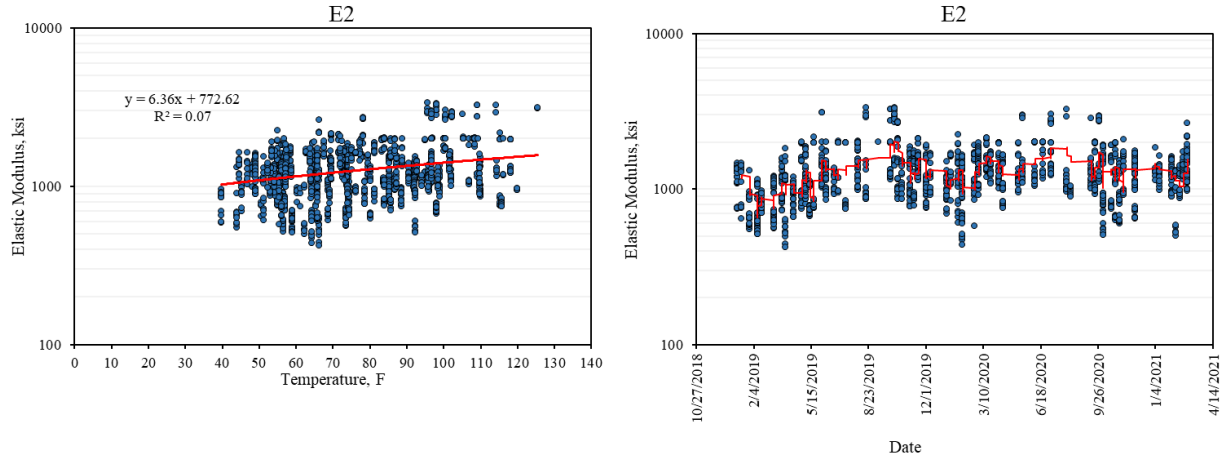

Figure 8.34 Backcalculated CTB Moduli with Filtered Data (RL 2 and 4).

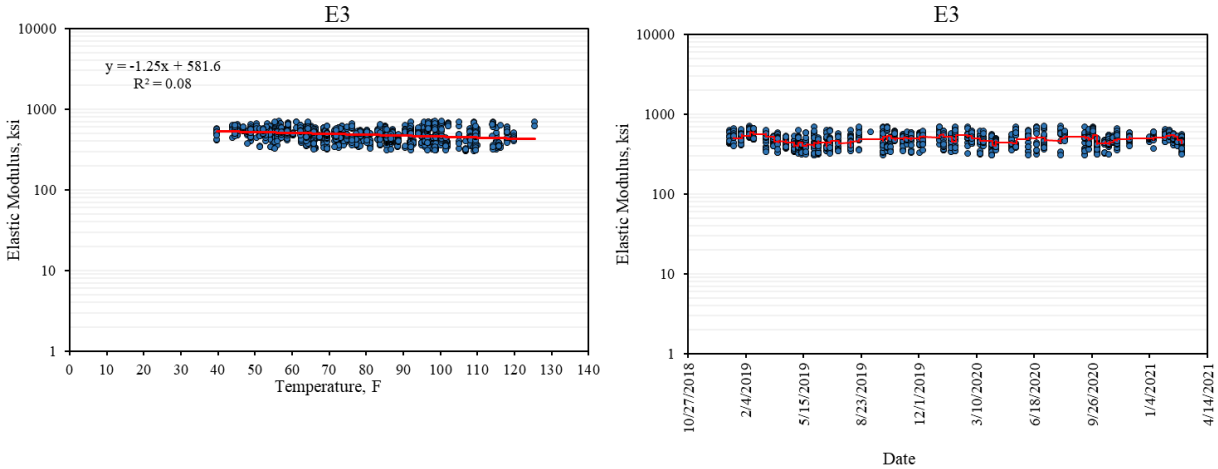

Figure 8.35 Backcalculated LTS Moduli with Filtered Data (RL 2 and 4).

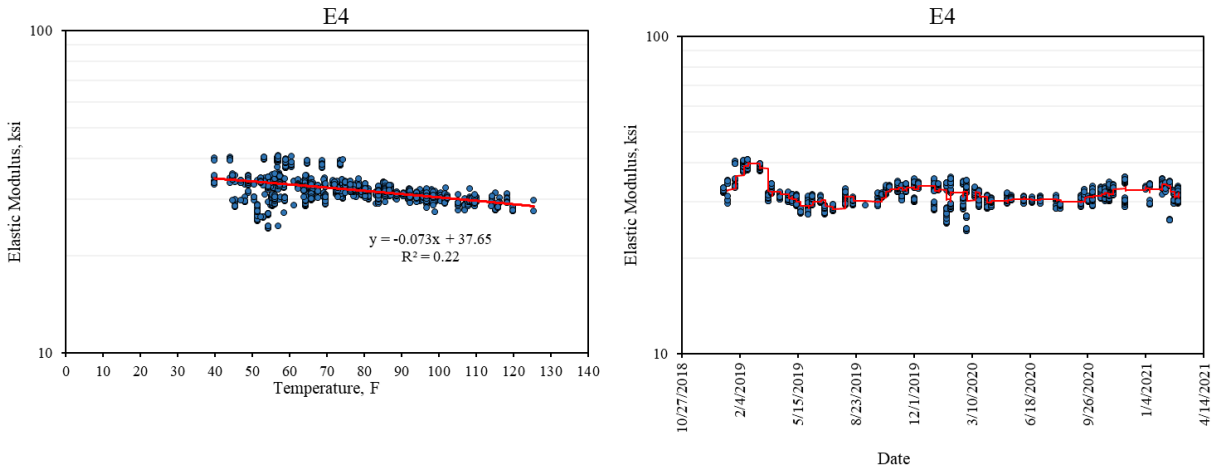

Figure 8.36 Backcalculated Subgrade Moduli with Filtered Data (RL 2 and 4).

In summary, with no filtering on the data, the majority of the elastic moduli calculated for CTB was at around 1000 ksi to 1400 ksi range, while for LTS was at around 400 ksi to 600 ksi. As expected, the elastic modulus for AC material was dependent on temperature with the average value of 979.4 ksi at 75 °F. The subgrade modulus calculated to be around 30 ksi in all methods. The obtained values seemed to confirm the results obtained from laboratory testing and the proposed approximate approach. Although, the filtering method reduced LTS variability significantly, the filtering range was arbitrary and local to the section. The next section discusses a proposed method that can be applied to all stabilized sections to remove erroneous deflection basins due to stiff layers.

8.8.2. The Proposed Approach for Backcalculation

The analysis provided so far for backcalculation only included RL#2 and RL#4 data. These random locations include Stations 4, 5, 6 and 10, 11, 12. As mentioned before, the behavior of the stabilized foundation section (S2) was variant within the section itself. The analysis of raw normalized deflection basins showed smaller deflections at random locations RL#1 and RL#3. These locations

also had higher number of positive x-intercepts compared to RL#2 and RL#4. This different behavior was the key to understand the high variability observed in this section. Figure 8.37 through Figure 8.40 illustrate the backcalculation results from the stations S2-12 (with no positive x-intercept) and S2-3 (with almost 100% positive x-intercept). The backcalculated elastic modulus for AC and CTB for both stations were very similar in magnitude and followed the same trend. However, the LTS modulus was significantly different between the two stations. The station S2-3 had unrealistically lower LTS elastic modulus (at around 3.4 ksi on average) compared to S2-12 station. The laboratory data and approximate approach indicated much higher elastic modulus for this section which contradicted the results for S2-3.

On the other hand, the subgrade moduli for S2-3 showed unrealistically high elastic moduli with the average of 144.6 ksi and some moduli as high as 2000 ksi. It appeared that there existed a compensation effect between the subgrade and LTS where the lower values of LTS was compensated for the higher values of the subgrade. Obtaining lower elastic moduli for LTS for RL#1 and RL#3 is counterintuitive since it was expected that these random locations yield a higher elastic moduli due to smaller deflection basins. Thus, considering the compensation effect between the subgrade and LTS, lower elastic moduli for LTS despite the lower deflection basins, and inconstancy with laboratory results, the elastic moduli for RL#1 and RL#3 were deemed unacceptable and removed from the analysis.

Further investigation revealed that the majority of the erroneous backcalculated data occurred when x-intercept was positive (or when the pavement was extremely stiff). Further analysis revealed that the backcalculation algorithm fails to estimate the elastic moduli (especially for deeper layers) where higher percentages of positive x-intercept exist. Although the x-intercept has been used to estimate the depth of bedrock in other studies, this study suggests using it to

eliminate the deflection basins that yield unreasonable elastic moduli. This is particularly important for stiff pavement sections were the FWD drops may result in small deflections. Also, since stabilized foundation sections are stiff pavement sections, it is suggested to use higher load levels for backcalculation (> 10,000 lb.) to have a better signal to noise ratio.

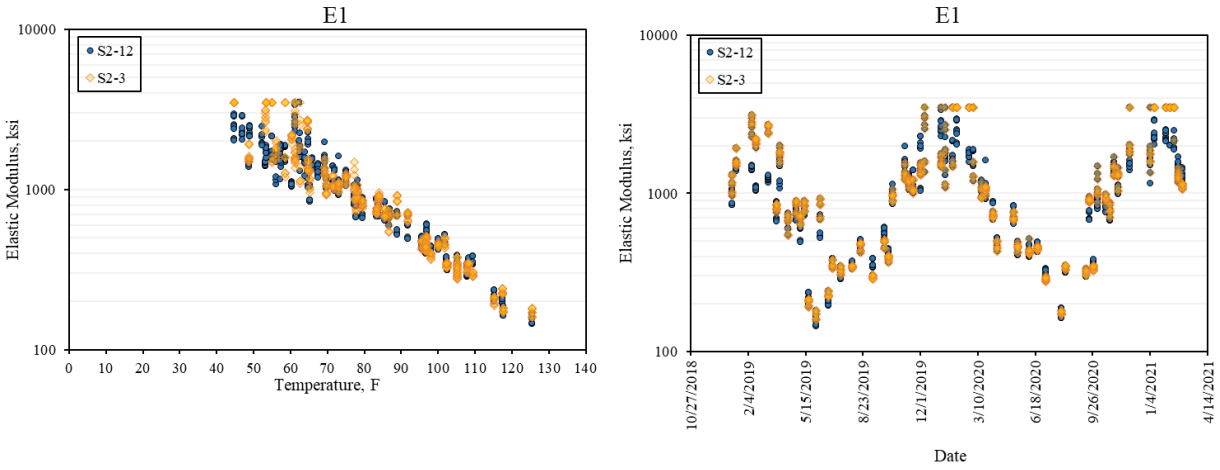

Figure 8.37 Backcalculated AC Modulus Comparison Using Partial Friction Approach.

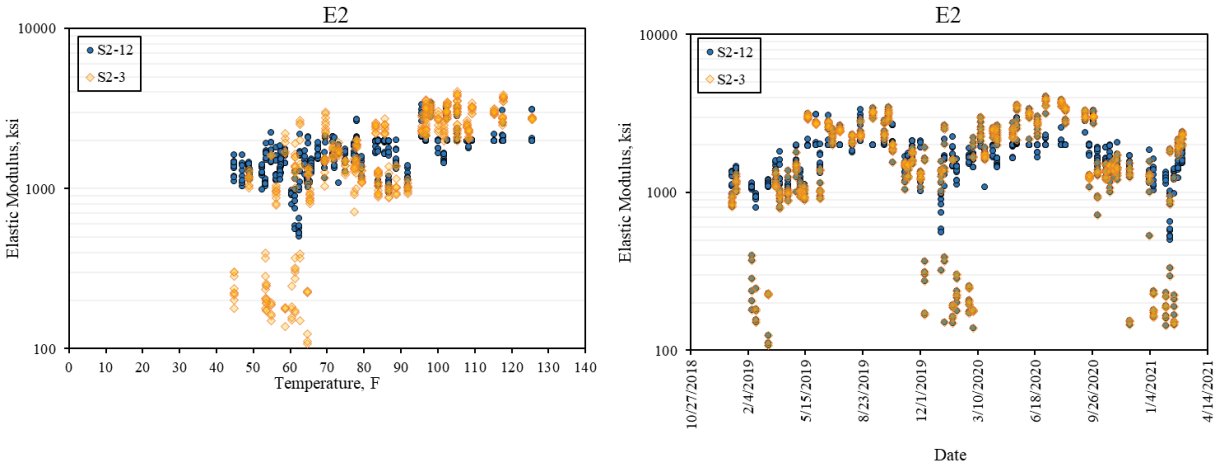

Figure 8.38 Backcalculated CTB Modulus Comparison Using Partial Friction Approach.

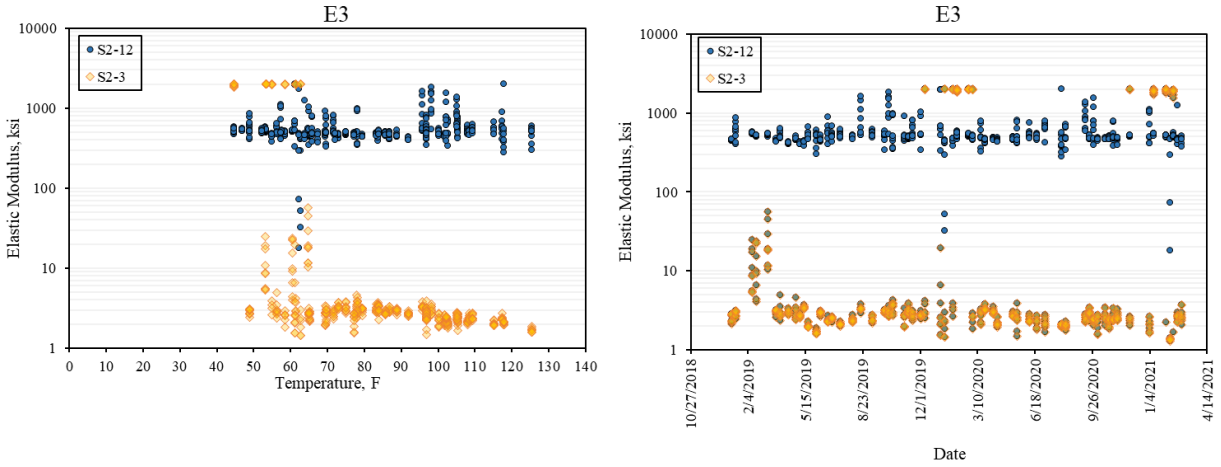

Figure 8.39 Backcalculated LTS Modulus Comparison Using Partial Friction Approach.

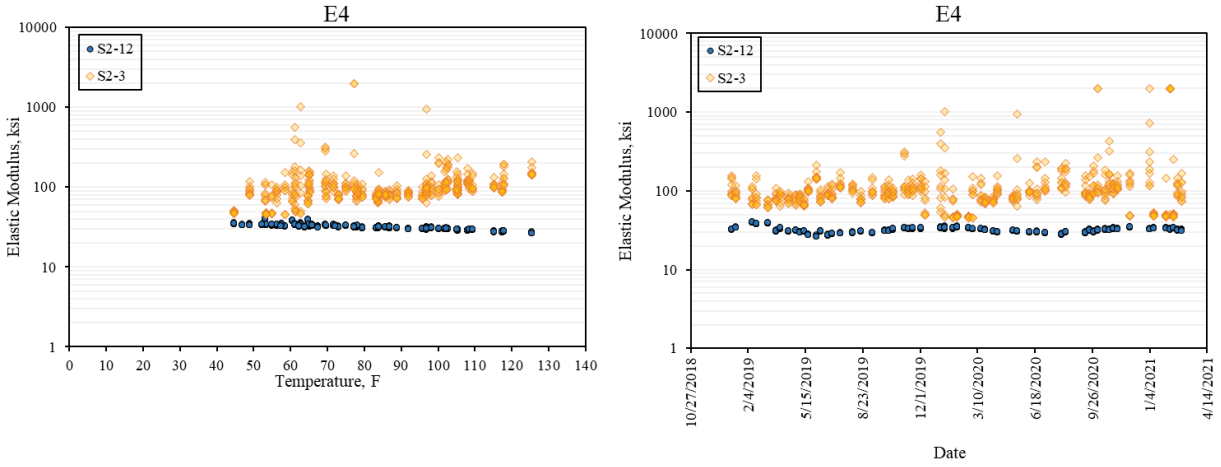

Figure 8.40 Backcalculated Subgrade Modulus Comparison Using Partial Friction Approach.

To illustrate the efficacy of this approach, the entire dataset including all stations (stations 1 through 12) processed using those only deflection basins that had negative x-intercept (or x-intercept < -0.02). The backcalculated moduli using this method are presented in Figure 8.41 through Figure 8.44. Similar to other graphs, the red line on the left graph represents a simple linear regression line, and the one on the right shows the 30-point moving average fitted to the data. The figures can be compared with the backcalculation results with no x-intercept analysis presented in Appendix D. By removing positive intercepts, the data showed significantly less

variability compared to when no filtering was considered (see Appendix D). For example, the COV for CTB decreased from 94.3% to 44.6% and from 194.1% to 59.6% for LTS. This significant reduction in variability shows the power of this method to remove erroneous data. In addition, this approach automatically removed the stations S2-1, S2-2, S2-3, S2-7, and S2-8 since all of their deflection basins had positive x-intercept. Since no additional equipment is needed, this method can potentially be used as a practical method to reduce variability in stiff layers. Note that although not shown here (See appendix E), using higher load levels, e.g. load > 10,000 lb., resulted in even less variability especially for LTS modulus (the COV for LTS was further decreased to 54.6%). Thus, to achieve better results, it is recommended that higher load levels be used in CTB backcalculation processes. Figure 8.43 suggests that some of the backcalculated moduli did result in low LTS modulus with values much lower than the average. This is particularly evident for cold temperatures which can be attributed to low deflection basins and high stiffness of the sections which prevented the search algorithm to find a reasonable solution. Choosing smaller negative x-intercepts would further remove those inconsistencies and one can fine-tune it to obtain the ideal results.

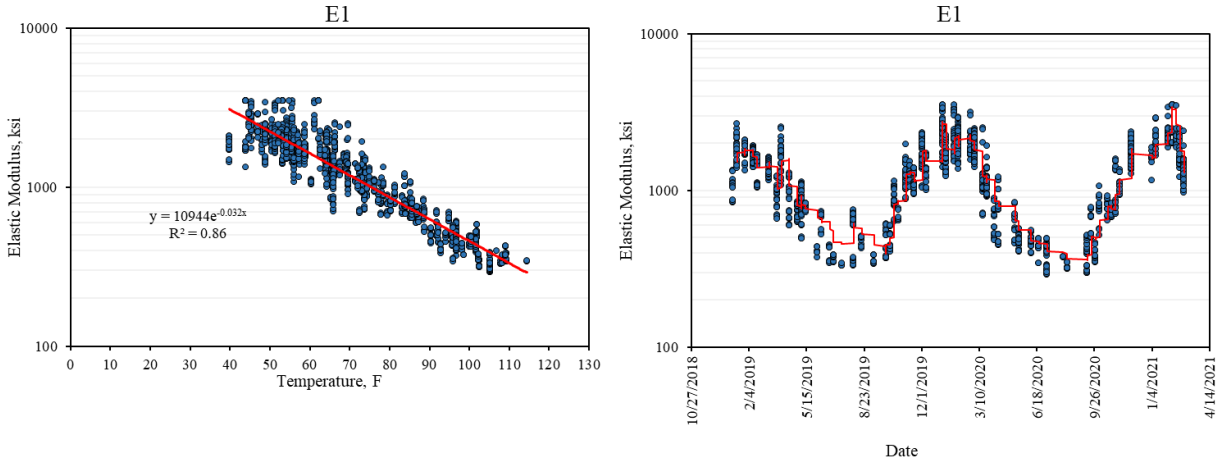

Figure 8.41 Backcalculated AC Modulus with no Positive X-Intercept (all stations).

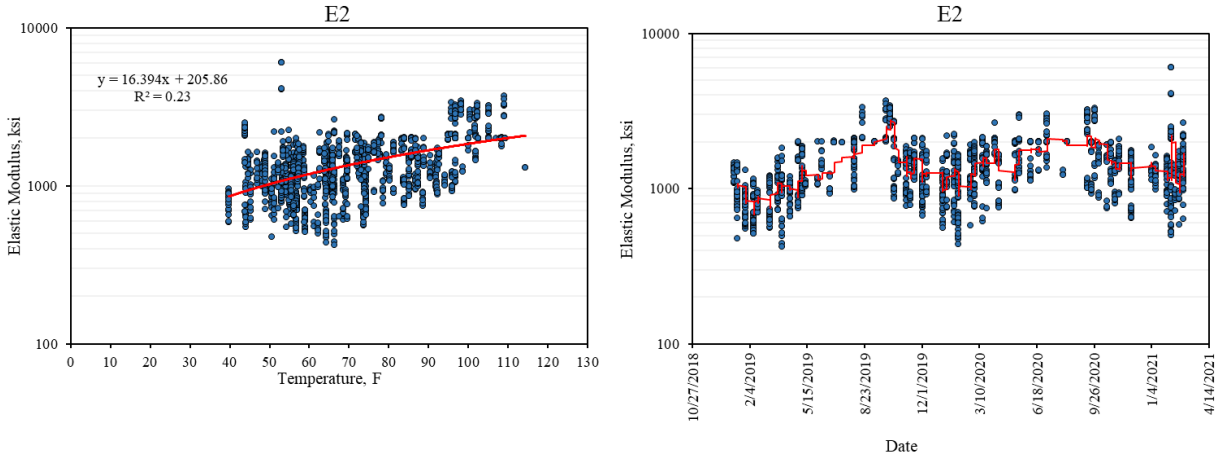

Figure 8.42 Backcalculated CTB Modulus with no Positive X-Intercept (all stations).

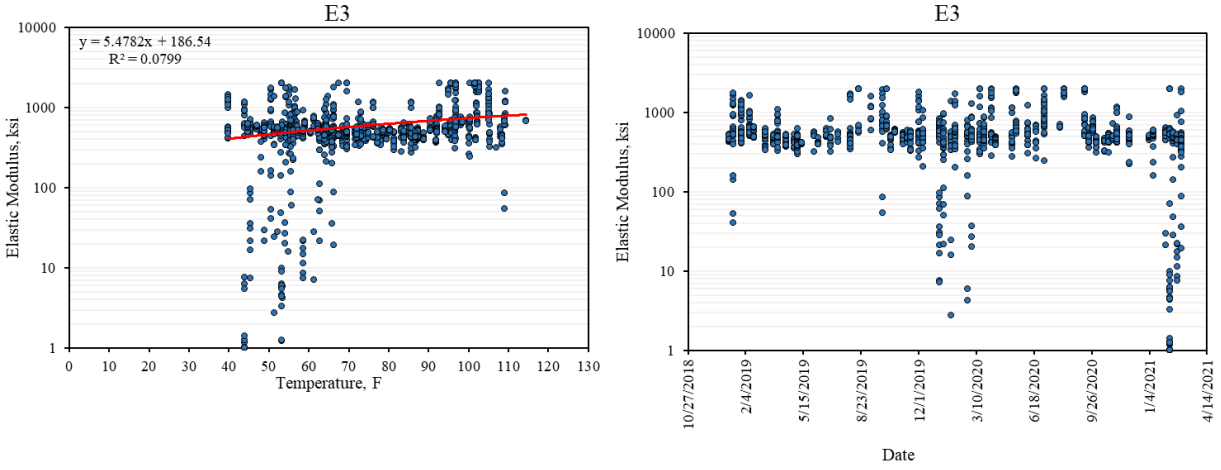

Figure 8.43 Backcalculated LTS Modulus with no Positive X-Intercept (all stations).

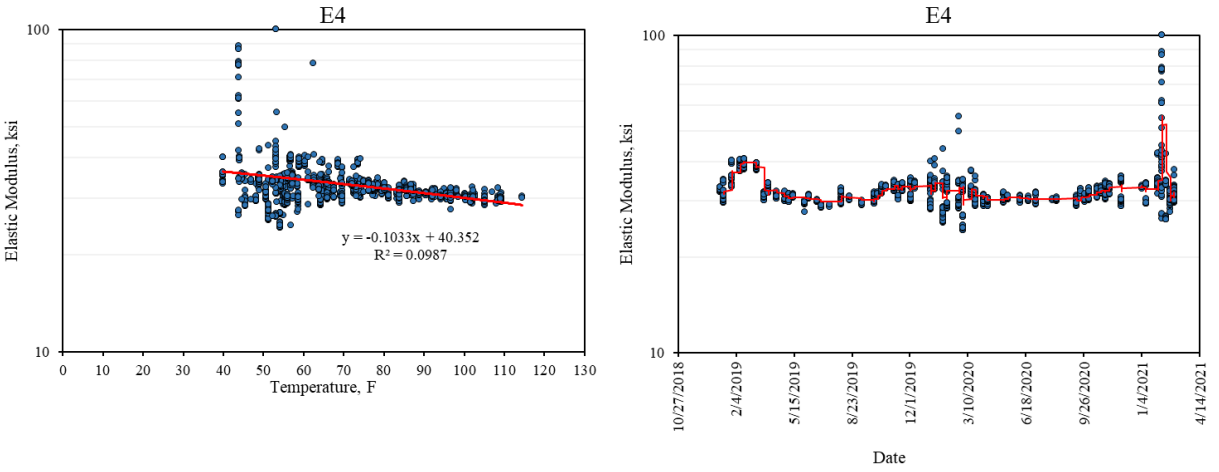

Figure 8.44 Backcalculated Subgrade Modulus with no Positive X-Intercept (all stations).

Since the data in the above graphs for the CTB and LTS layers suggested there exist small groups of data behaving different than others, Figure 8.45 and Figure 8.46 were plotted which show the distribution of elastic modulus for CTB and LTS layers, respectively. For the CTB layer, the majority of the data are around 1200 ksi, while for LTS the majority is centered at around 500 ksi. The value of 1200 ksi for CTB is similar to the values obtained from the laboratory samples which had the average of 1012.5 ksi. Figure 8.45 also suggests some outliers with values far away from the average. This could be attributed to when the algorithm did not converge to the global minimum but rather fell into the local optimum. This behavior is more significant for LTS where the two tails of the histogram showed considerable amounts of data. Since obtaining the data for LTS is adversely affected by the presence of the stiff layer on top, it is expected to see more outliers for LTS since less information can be obtained from deeper layers. This explains higher concentration of the data at the two tails of the histogram where the algorithm did not possibly converge to a correct solution. This is already shown to be the case for some of the stations in random location 1 and 3. However, the majority of the data suggest values that are close to laboratory measurements.

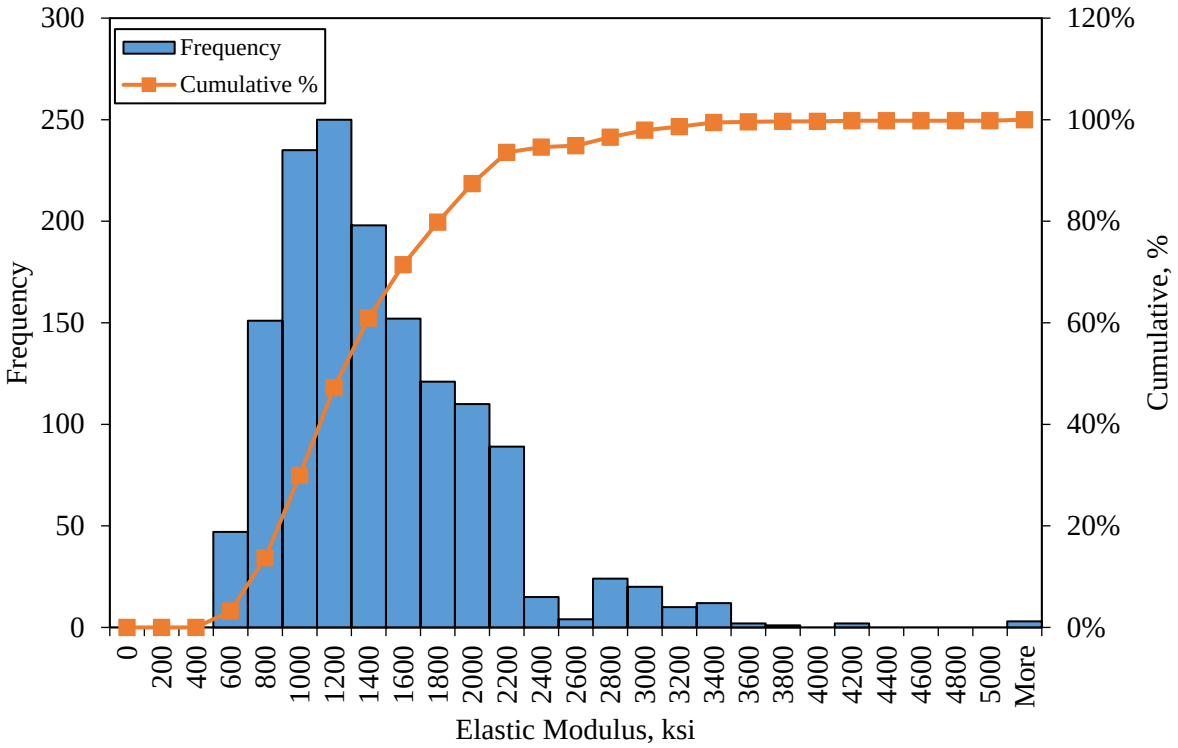

Figure 8.45 The CTB Modulus Distribution for the Proposed X-Intercept Approach.

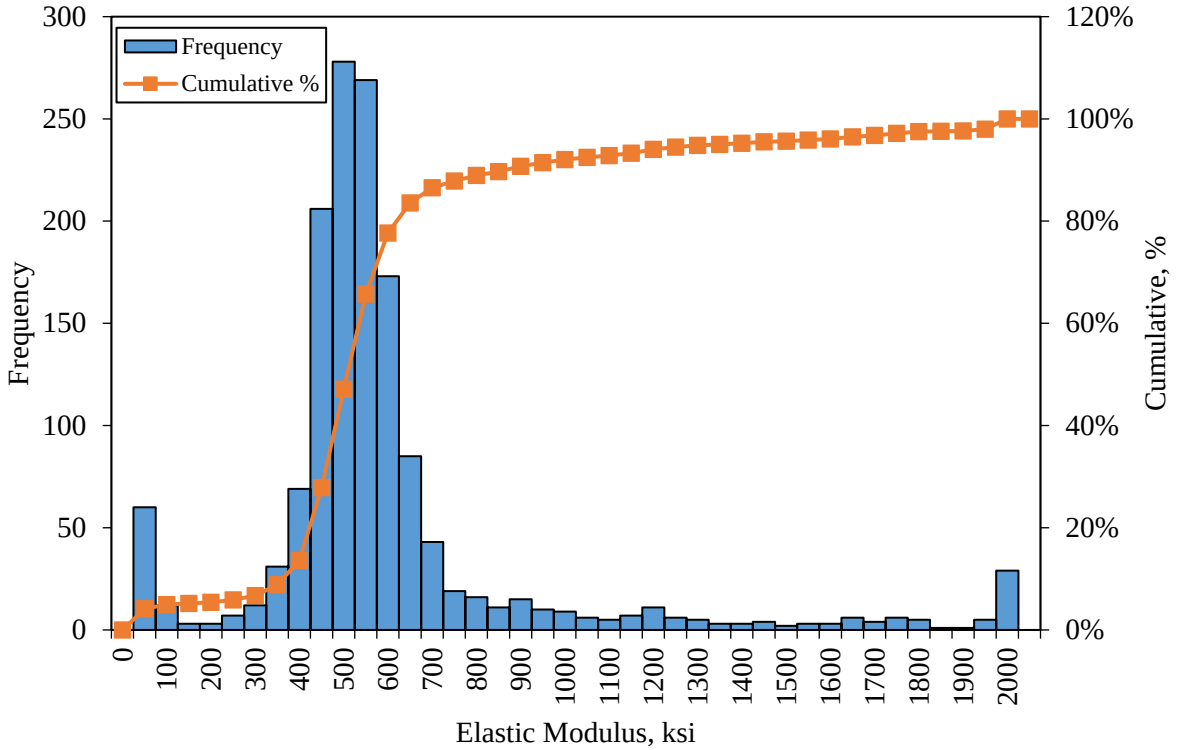

Figure 8.46 The LTS Modulus Distribution for the Proposed X-Intercept Approach.

To investigate the accuracy of the backcalculation, the backcalculation results were compared with laboratory data and the approximate method as presented in Table 8.10. As shown, the laboratory elastic modulus of the CTB and LTS are close to those obtained from the backcalculation process. With 95% confidence level and assuming a t-distribution, the confidence interval of the CTB modulus for lab fabricated samples was 1012 ± 146.2 ksi. This interval for backcalculation was 1353 ± 38.6 ksi. The difference on average is statistically significant, but seems reasonable from a practical perspective since the two methods of measurements were fundamentally different. The confidence interval of LTS modulus was 574.3 ± 17.653 ksi from the backcalculation process while was 366.6 ± 49.5 ksi for lab fabricated samples. Again, although the difference was statistically significant, they were in the same order of magnitude from the engineering point of view.

Table 8.10 Elastic Moduli Comparison for Different Methods.

Method	Property	CTB	LTS	Subgrade Soil
Backcalculation	Average, ksi	1371.2	574.3	33.0
	Standard Deviation, ksi	612.2	342.2	5.7
Approximate Approach	Estimate, ksi	1800[a]	600[b]	30.5
Laboratory Data	Average, ksi	1012.5*	366.6**	NA
	Standard Deviation, ksi	294.6	69.2	NA

[a] CTB modulus ranged from 1200 ksi to 2400 ksi using approximate approach.
[b] LTS modulus ranged from 400 ksi to 800 ksi using approximate approach.
** Lab-fabricated, lab-tested samples for 180 and 360 days cured samples.*
*** Lab-fabricated, lab-tested samples for 180 days cured samples (no data for 360 days of curing).*

The comparison between laboratory and backcalculated AC modulus requires consideration of frequency and temperature. Figure 8.47 compares the laboratory and backcalculated results over different ranges of temperature and frequency. The results show a good agreement between the laboratory and backcalculated values. At lower temperatures, it seems that the backcalculated moduli are slightly higher than the lab data on average. However, the

difference in moduli seems reasonable considering the fundamentally different methods of evaluation. In general, it can be concluded that the laboratory results were in good agreement with backcalculated moduli for all pavement layers which confirmed the proposed backcalculation framework for stabilized foundation sections.

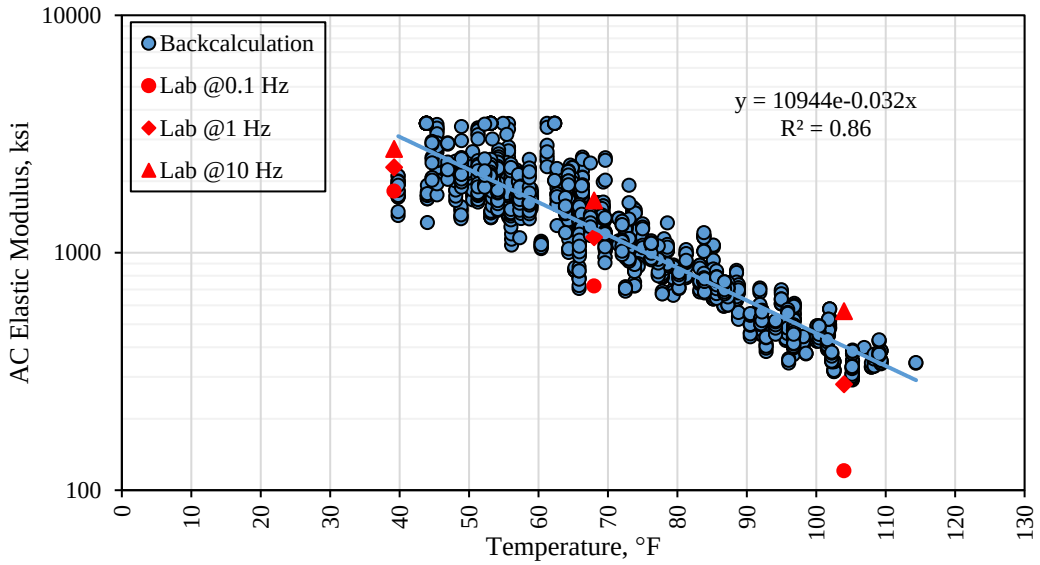

Figure 8.47 Laboratory Elastic Modulus VS Backcalculated Values.

The backcalculation process on the stabilized foundation section was shown to produce reasonable results using partial friction method and thus it is recommended to use this approach for the stabilized foundation pavement (S2). This section provided two additional approaches to further handle unrealistic elastic modulus and the high observed variability. First, to exclude those moduli that are extremely outside the expected range and thus obtaining a cleaner dataset. The second method suggested analyzing x-intercept from the raw deflection basins and excluding those that have a positive x-intercept (or x-intercept > -0.02). Using higher load levels during the testing process was also shown to provide cleaner data with less variability. Using fully bonded condition even with filtering approaches did produce data with high variance (See Appendix F for the bonded

condition with filters). However, it can provide a rough estimate of elastic moduli when the partial friction method cannot be implemented, provided that x-intercept method is applied on the raw dataset. In addition, it was found that regardless of the number of layers, the bonding stiffness, and any other settings, the backcalculation fails to accurately estimate pavement moduli at locations with a positive x-intercept. At these locations, the pavement is so stiff that obtaining knowledge from lower pavement layers is prohibited. Thus, it is suggested to exclude those deflection basins from the backcalculation process. However, it is possible to use the information of the top layers in those locations. The x-intercept analysis results in 100% negative x-intercept for the conventional pavement sections (such as sections S9 and N4), and thus would not affect the results. In general, it is recommended that the positive x-intercept analysis be included in all backcalculation tasks due its shown efficacy to remove erroneous deflection basins especially when a stiff pavement layer exists.

CHAPTER NINE

CONCLUSIONS AND RECOMMENDATIONS

9.1. Summary

This dissertation aimed to develop a fundamental understanding the behavior of a stabilized foundation flexible pavement. Understanding fundamental differences in the structural response of different pavement sections helps improve design processes and optimize sections that can lead to better pavement performance. In pursuit of this objective, a full-scale pavement section was constructed at the National Center for Asphalt Technology (NCAT) Test Track in 2018. The stabilized foundation section featured cement- and lime-treated layers under the asphalt layers. To monitor and investigate the structural integrity and overall health of the pavement section over time, and to measure the horizontal bending strain under traffic, twelve asphalt strain gauges were placed at the AC/base course interface. Earth pressure cells were installed on top of the cement treated base (CTB), lime treated soil (LTS), and Mississippi subgrade soil, respectively, to measure vertical compressive vertical stresses transferred through the layers. Temperature probes were installed outside the edge stripe at the top, middle and bottom of the asphalt concrete and three inches into the CTB layer. The structural behavior was observed over time under accelerated truck trafficking using the embedded instrumentation and surface measuring equipment such as falling weight deflectometer (FWD) and condition survey vans.

For comparison purposes and to obtain more insight regarding the differences and similarities of stabilized pavements with other pavement types, additional sections built at the

NCAT Test Track were included in this study. In particular, a thick-lift pavement section (S9) constructed in the same year (2018) and subjected to the same traffic level was used to compare their underlying structural differences. The thick-lift section (S9) was constructed with one lift of AC, with no lift interfaces, over crushed aggregate base course. Two additional sections included in this study consisted of two asphalt concrete layers placed on Cold Central Plant Recycling (CCPR) material. One section with a cement treated base, the CCPR with stabilized foundation section (S12), and the other with crushed aggregate base, the CCPR (N4) section. Both sections featured Stone-Matrix Asphalt (SMA) surface and Superpave dense-graded AC layers above the CCPR layer. These two sections were constructed in 2012 and have continued into the 2018 research cycle. The CCPR with stabilized foundation section (S12) provided historical data on stabilized foundation sections while its counterpart, the CCPR section (N4), provided a comparison with conventional flexible pavements. Both of the CCPR sections were embedded with pavement response instrumentation and were also evaluated with FWD and condition surveys throughout all research cycles.

In addition to full-scale evaluation of the pavement sections, laboratory characterization of the stabilized foundation section (S2) was conducted. The asphalt laboratory samples were all fabricated and tested at the NCAT laboratory while the CTB, LTS, and subgrade materials were tested at Mississippi State University testing facility. The Mississippi subgrade soil was classified as A6(20) according to AASHTO M145, and CL according to ASTM D2487. The top six inches of this soil was modified with 4% hydrated lime. The laboratory measurements of the lab-fabricated lab-tested samples showed the average of 366.6 ksi with standard deviation of 69.2 ksi and COV of 18.8%. The CTB soil was classified as SM according to ASTM D2487 and had the

modulus of 1012.56 ksi with the standard deviation of 294.56 ksi for samples cured at 180 or 360 days. This layer was modified with 5.1% Portland cement.

The asphalt laboratory data revealed that the AC material for the stabilized foundation section (S2) was stiffer than the AC material for the thick-lift section (S9) with less resistance to fatigue cracking based on bending beam fatigue test. The indirect tensile asphalt cracking test (IDEAL-CT) conducted on the asphalt samples showed poor CT_{index} with values less than the threshold of 30. Thus, the data suggested a possibly poor resistance to cracking for the stabilized foundation section. However, the Hamburg wheel tracking test (HWTT) showed good resistance to rutting and moisture damage with values well below the threshold of 12.5 mm.

In addition to laboratory characterization, the stress and strain levels were measured weekly under the standard eight-axle triple-trailer trucks for all pavement sections. The stress response for all pavement sections increased with increasing temperature, as expected and consistent with conventional multi-lift asphalt pavements. The strain measurement at the bottom of AC for the thick-lift section (S9) and the CCPR sections showed a familiar trend in which the tensile strain at the bottom of AC increased exponentially with temperature. However, the tensile strain response for the stabilized foundation section (S2) showed a fundamentally different behavior. In fact, the tensile horizontal strain response at the bottom of AC decreased with the increase in temperature. This was an interesting observation because it was initially expected that the horizontal strain response increases with the temperature.

Observing the strain response under individual truck loadings at higher temperatures revealed an interesting phenomenon. The strain response at the bottom of the AC layer for the stabilized foundation section (S2) switched to predominantly compression under individual truck loading. The compressive strain response at the bottom of AC contradicts the well-established

premise that the bottom of AC is in tension. This interesting behavior suggests that stabilized foundation pavement sections can behave fundamentally differently than other conventional flexible pavements. However, all other sections, as expected, had tensile strain readings in the summer. The results were confirmed by falling weight deflectometer (FWD) testing that was conducted directly above the embedded pavement sensors where the bottom of the AC layer was observed to be in compression in the summer for the stabilized foundation section.

Further investigation showed that the stabilized foundation section experiences two different strain modes depending on pavement temperature. At lower temperatures (less than 75°F), the pavement strain response at the bottom of AC is dominantly tensile. In fact, the absolute strain response for compressive mode is lower than the absolute value for tensile mode, making the strain wave under moving load dominantly tensile. However, the strain response converts to dominantly compressive mode at higher temperatures (above 75°F). In other words, 75°F is the critical temperature at which the strain readings change from dominantly tensile mode to dominantly compressive mode for this section.

The pavement sections were simulated to investigate their differences using the MASTIC simulation program. MASTIC was specifically developed for this research which implements the multilayer elastic theory. This program can perform various tasks such as calculating elastic response under static and dynamic loads on multi-layer pavement structure and backcalculating pavement moduli under FWD loading events. A comparison with EVERCALC, a commercial software program, showed MASTIC can outperform EVERCALC for backcalculation of pavement sections due to the advanced optimization techniques used in this program.

The multilayer elastic simulation of the stabilized foundation section (S2) illustrated the same trend that the bottom of AC should be in compression in summer. However, the analysis

revealed that the maximum tensile strain actually occurs at around the middle of the AC layer. This finding demonstrated that stabilized foundation pavements are effective in mitigating bottom-up fatigue cracking since they can limit tensile strain at the bottom of the AC layer. However, it also revealed that fatigue cracking could initiate at shallower depths since the maximum tensile strain occurs near the middle of the AC which has important implications in pavement design since focus is usually on the bottom of the AC. This also indicates that the stabilized foundation pavements could be prone to middle-up cracking and subsequent precautions should be taken to avoid middle-up fatigue cracking.

FWD testing was conducted routinely on all four pavement sections at the NCAT Test Track. The backcalculation results obtained from EVERCALC for the CCPR section (N4) suggested a precursor to damage. However, the CCPR with stabilized foundation (S12) and the Thick-lift section (S9) showed no sign of damage accumulation. The EVERCALC backcalculation results for the stabilized foundation section (S2) was unrealistic and led to extremely large variance in the moduli of each layer, regardless of the settings used. Thus, MASTIC was used to for the backcalculation of the stabilized foundation section (S2) since it provided more flexibility such as considering partial friction for interfaces. It was found through a comprehensive study that a four-layer system with the original cross-section and fully bonded condition for AC/CTB interface along with a nearly slip conditions for other interfaces is the best case scenario for having reasonable results and less variance.

Using the partial friction method for backcalculation, the variability was reduced significantly, but there was still considerable variability in the data especially for CTB and LTS layers. To investigate the source of the variability, the raw deflection basins were investigated based on Boussinesq equation on elastic half-space. Using the four outer most sensors of FWD,

the regression lines were fitted to the data considering deflections to be the dependent variable and reciprocate of the radial distance times plate radius to be the independent variable.

This study showed that x-intercept obtained from the simple regression equations are a measure of stiffness and they have direct correlation with temperature. A larger x-intercept indicates higher stiffness. Through a comparison, it was found that the backcalculation fails to arrive at a reasonable solution at locations where the x-intercept is positive. This is due to the pavement stiffness. When the pavement is extremely stiff and consequently has a large positive x-intercept, the FWD drop does not result in a significant deflection basin and thus the information for deeper layers cannot be obtained. By removing positive x-intercepts, the results showed significantly less variability compared to when no filtering was considered. The values obtained using this method were verified with laboratory data. Thus, this study suggested to use those deflection basins that have negative x-intercept (x-intercept <-0.02) along with partial friction method to reduce the observed variability in the field.

Table 9.1 summarized the findings of this study. One can safely assumes the CTB modulus range of 1000 to 2000 ksi and LTS range of 300-700 ksi for this pavement section or other sections with similar properties. It is also likely that these pavements experience compression in the summer due to stiff CTB layer. Unlike conventional pavement sections, maximum tensile strain is likely to occur somewhere other than the bottom of AC layer and thus middle-up fatigue cracking is more likely to occur than traditional bottom-up fatigue cracking. For backcalculation of these pavements, partial friction between layer interfaces along with x-intercept analysis should be conducted to achieve acceptable results with relatively smaller variability.

Table 9.1 Summary Findings of the Stabilized Foundation Section

Expected Modulus range are	**AC**: like other pavement sections **CTB**: 1000-2000 ksi **LTS**: 300-700 ksi
Strain @ Bottom of AC is	- In Compression in Summer - In Tension in Winter
Maximum Strain Occurs at	Around mid-depth
Best Backcalculated Method are	- Partial Friction - x-Intercept Analysis

9.2. Conclusion and Recommendation

This study conducted a fundamental investigation of the stabilized foundation sections by measuring the structural responses of four full scale pavement sections constructed at NCAT Test Track. The sections were simulated to further explore and understand their structural behavior. Based on the findings of this study, the following conclusions and recommendations are made:

- The stabilized foundation section exhibited good performance through the first 10 million ESALs with no cracking, no appreciable change in IRI (<80 in/mile) and limited rutting (≤2.5 mm). Continued monitoring will be needed to assess the longer term performance.
- Measured pavement responses in the stabilized foundation section (S2) showed typical stress responses (exponential increases with temperature) but dramatically different tensile strain responses. It was notable that tensile strain did not change, or even slightly decreased, with increasing temperature (and decreasing modulus).
- In the stabilized foundation section (S2), the response under dynamic loading converted to dominantly compressive at elevated temperatures which contradicted the existing premise that the bottom of the AC should experience maximum tensile strain. Thus, the bottom-up fatigue design criteria may not be applicable for such pavements and should be revisited.

- The series of FWD tests conducted directly on top of each pavement sensor confirmed the behavior that was observed under dynamic truck load events. The strain response at the bottom of AC converted to dominantly compressive at elevated temperatures.
- Simulations of section S2 showed that the presence of a high modulus foundation at the bottom of thick AC layer force the maximum tensile strain to migrate upward and reside on somewhere near the middle of AC layer. This finding may require M-E designs to consider depths other than the bottom of AC for critical strain consideration. It also suggests that fatigue cracking may occur at shallower depths in the form of middle-up cracking.
- Field investigation of cracked sections in Mississippi should be conducted to verify that middle-up cracking could occur on stabilized foundations.
- The backcalculation process on the stabilized foundation section (S2) was shown to produce reasonable results using partial friction method and thus it is recommended to use this approach for the stabilized foundation sections. In this approach, the top interface should be considered bonded and other interfaces to be unbonded.
- It was suggested conducting x-intercept analysis of the raw deflection basins using Boussinesq equation and excluding those that have a positive x-intercept to decrease the variability in the stabilized foundation sections (S2) backcalculation procedure.
- For future studies, it is recommended to embed strain sensors at various asphalt concrete depth to capture the whole strain response behavior of the stabilized foundation sections. Forensic studies need to be conducted on these sections for verifying the middle-up cracking concept.

REFERENCES

Adaska, W. S., & Luhr, D. R. (2004). Control of reflective cracking in cement stabilized pavements. In *Proceedings of 5th international RILEM conference on cracking in pavements* (pp. 309-316).

Andersen, E. D., & Andersen, K. D. (2000). The MOSEK interior point optimizer for linear programming: an implementation of the homogeneous algorithm. In *High performance optimization* (pp. 197-232). Springer, Boston, MA.

Bowers, B. F., Diefenderfer, B. K., & Diefenderfer, S. D. (2015). Evaluation of dynamic modulus in asphalt paving mixtures utilizing small-scale specimen geometries. *Journal of the Association of Asphalt Paving Technologists*, *84*, 497-526.

Burmister, D. M., Palmer, L. A., Barber, E. S., & Middlebrooks, T. A. (1944). The theory of stress and displacements in layered systems and applications to the design of airport runways. In *Highway Research Board Proceedings* (Vol. 23).

Burmister, D. M. (1945). The general theory of stresses and displacements in layered systems. I. *Journal of applied physics*, *16*(2), 89-94.

Burmister, D. M. (1945). The general theory of stresses and displacements in layered soil systems. II. *Journal of Applied Physics*, *16*(3), 126-127.

Burmister, D. M. (1945). The general theory of stresses and displacements in layered soil systems. III. *Journal of applied Physics*, *16*(5), 296-302.

Chatti, K., Kutay, M. E., Lajnef, N., Zaabar, I., Varma, S., & Lee, H. S. (2017). Enhanced analysis of falling weight deflectometer data for use with mechanistic-empirical flexible pavement design and analysis and recommendations for improvements to falling weight deflectometers. *Federal Highway Administration. (No. FHWA-HRT-15-063)*.

Diaz Sanchez, M. A. (2019). *Structural Characterization of Recycled Materials at the NCAT Test Track.* [Doctoral Dissertation, Auburn University]

Diefenderfer, B. K., & Link, S. D. (2014). Temperature and confinement effects on the stiffness of a cold central-plant recycled mixture. In *Proceedings of the 12th international society for asphalt pavements conference on Asphalt pavements*.

Ellison, A. L., & Timm, D. H. (2011). Speed and Temperature Effects on Full-Scale Pavement Responses in Non-Conventional Flexible Pavements. In *Transportation and Development Institute Congress 2011: Integrated Transportation and Development for a Better Tomorrow* (pp. 824-833).

George, K. P. (1990). Characterization and structural design of cement-treated base. *Transportation Research Record*, *1288*, 78-87.

Gopalakrishnan, K. (2010). Neural network–swarm intelligence hybrid nonlinear optimization algorithm for pavement moduli back-calculation. *Journal of Transportation Engineering*, *136*(6), 528-536.

Guthrie, W. S., Sebesta, S., & Scullion, T. (2002). *Selecting optimum cement contents for stabilizing aggregate base materials* (No. FHWA/TX-05/7-4920-2,). Texas Transportation Institute, Texas A & M University System.

Huang, Y. H. (2004). *Pavement analysis and design*. Pearson Prentice Hall.

Halsted, G. E., Luhr, D. R., & Adaska, W. S. (2006). *Guide to cement-treated base (CTB)*.

Isola, M., Betti, G., Marradi, A., & Tebaldi, G. (2013). Evaluation of cement treated mixtures with high percentage of reclaimed asphalt pavement. *Construction and Building Materials*, *48*, 238-247.

Irwin, L. H. (2002). Backcalculation: An overview and perspective. In *Pavement Evaluation Conference, 2002, Roanoke, Virginia, USA*.

Khazanovich, L., & Wang, Q. (2007). MnLayer: high-performance layered elastic analysis program. *Transportation Research Record*, *2037*(1), 63-75.

Leiva-Villacorta, F., Vargas-Nordcbeck, A., & Timm, D. H. (2017). Non-destructive evaluation of sustainable pavement technologies using artificial neural networks. *International Journal of Pavement Research and Technology*, *10*(2), 139-147.

Li, X., & Gibson, N. H. (2013). Using small scale specimens for AMPT dynamic modulus and fatigue tests. *Journal of the Association of Asphalt Paving Technologists*, (82).

Lim, S., & Zollinger, D. G. (2003). Estimation of the compressive strength and modulus of elasticity of cement-treated aggregate base materials. *Transportation Research Record*, *1837*(1), 30-38.

McCarty, C. (2019). *Early Characterization and Performance of a Flexible Thick Lift Pavement.* [Master Thesis, Auburn University]

Naderi, K., Nakhaei, M., Jalali, F., Nasrekani, A. A., & Timm, D. H. (2019). *Low PG Determination of Neat Binders: A Comparison Between AASHTO Procedure and Time Temperature Superposition Approach* (No. 19-00813).

Nakhaei, M., Naderi, K., Nasrekani, A. A., & Timm, D. H. (2018). Moisture resistance study on PE-wax and EBS-wax modified warm mix asphalt using chemical and mechanical procedures. *Construction and Building Materials*, *189*, 882-889.

Nakhaei, M., & Timm, D. H. (2021). Middle-Up Cracking Potential in Flexible Pavements with Stabilized Foundations. *Transportation Research Record*, 0361198121990691.

Nakhaei, M., Ziari, H., Korayem, A. H., & Hajiloo, M. (2020). Aging evaluation of amorphous carbon-modified asphalt binders using rheological and chemical approach. *Journal of Materials in Civil Engineering*, *32*(1), 04019321.

Hossain, M. S., Nair, H., & Ozyildirim, H. C. (2017). *Determination of mechanical properties for cement-treated aggregate base* (No. FHWA/VTRC 17-R21). Virginia Transportation Research Council.

Pratelli, C., Betti, G., Giuffrè, T., & Marradi, A. (2018). Preliminary in-situ evaluation of an innovative, semi-flexible pavement wearing course mixture using fast falling weight deflectometer. *Materials*, *11*(4), 611.

Sebesta, S. (2005). Use of microcracking to reduce shrinkage cracking in cement-treated bases. *Transportation research record*, *1936*(1), 2-11.

Sharma, S., & Das, A. (2008). Backcalculation of pavement layer moduli from falling weight deflectometer data using an artificial neural network. *Canadian Journal of Civil Engineering*, *35*(1), 57-66.

Sullivan, W. (2021). *Field application of the PM Device and assessment of early age behaviors of cement stabilized pavement layers.* [Doctoral Dissertation, Mississippi State University]

Timm, D. H. (2009). *Design, construction and instrumentation of the 2006 test track structural study.* National Center for Asphalt Technology *(NCAT Report*, 09-01.)

Timm, D. H., Diefenderfer, B. K., Bowers, B. F., & Flintsch, G. (2021). *Utilization of Cold Central Plant Recycled Asphalt in Long-Life Flexible Pavements* (No. TRBAM-21-01262).

Timm, D. H., Diefenderfer, B. K., & Bowers, B. F. (2018). Cold central plant recycled asphalt pavements in high traffic applications. *Transportation Research Record*, *2672*(40), 291-303.

Timm, D., & Tutu, K. (2017). Determination of an optimum backcalculation cross section for unconventional pavement profiles. *Transportation Research Record*, *2641*(1), 48-57.

Tran, N., Robbins, M. M., Timm, D. H., Willis, J. R., & Rodezno, C. (2015). *Refined limiting strain criteria and approximate ranges of maximum thicknesses for designing long-life asphalt pavements*. National Center for Asphalt Technology (NCAT Report 15-05R).

Wen, H., Muhunthan, B., Wang, J., Li, X., Edil, T., & Tinjum, J. M. (2014). *Characterization of cementitiously stabilized layers for use in pavement design and analysis* (No. Project 4-36).

Wen, H., Muhunthan, B., Wang, J., Li, X., Edil, T., Tinjum, J. M., ... & Casmer, J. D. (2014). NCHRP Report 789: Characterization of Cementitiously Stabilized Layers for Use in Pavement Design and Analysis. *Transportation Research Board of the National Academies, Washington, DC*.

West, R., Timm, D., Powell, B., Heitzman, M., Tran, N., Rodezno, C., ... & Vargas, A. (2019). *Phase VI (2015-2017) NCAT Test Track Findings.* (No. NCAT Report 18-04).

Willis, J. (2009). *Field-based strain thresholds for flexible perpetual pavement design.* [Doctoral dissertation, Auburn University].

Willis, J. R., & Timm, D. H. (2010). Development of stochastic perpetual pavement design criteria. *Journal of the Association of Asphalt Paving Technologists*, *79*.

Willis, J. R., Timm, D. H., Taylor, A. J., Tran, N. H., & Kvasnak, A. (2011). Correlating laboratory fatigue endurance limits to field-measured strains. *Journal of the Association of Asphalt Paving Technologists*, *80*.

Willis, R., Timm, D., West, R., Powell, B., Robbins, M., Taylor, A., ... & Bianchini, A. (2009). *Phase III NCAT test track findings.* (NCAT report, 09-08).

Xie, Z., Shen, J., Guo, Z., & Cong, L. (2015). Effect of distresses on deflection basins and backcalculation modulus of asphalt pavement with cement-treated base. *International Journal of Pavement Research and Technology*, *8*(4), 283.

Qiu, X., You, Q. I., & Yang, Q. (2013). Distribution characteristics of dynamic deflection basins of distressed asphalt pavements. *Journal of Highway and Transportation Research and Development (English Edition)*, *7*(4), 1-8.

Hunaiti, Y. M. (1996). Composite action of foamed and lightweight aggregate concrete. *Journal of Materials in Civil Engineering*, *8*(3), 111-113.

Ziari, H., Nakhaei, M., Akbari Nasrekani, A., & Moniri, A. (2016). Characterization of rutting resistance of EBS-modified asphalt mixtures. *Petroleum Science and Technology*, *34*(13), 1107-1112

Ziari, H., Moniri, A., Imaninasab, R., & Nakhaei, M. (2019). Effect of copper slag on performance of warm mix asphalt. *International Journal of Pavement Engineering*, *20*(7), 775-781.

Zhou, F., Im, S., Sun, L., & Scullion, T. (2017). Development of an IDEAL cracking test for asphalt mix design and QC/QA. *Road Materials and Pavement Design, 18*(sup4), 405-427.

APPENDIX A

2/3/2021

Quadrant: S
Section: 2
Sublot: 1

Laboratory Diary

General Descrription of Mix and Materials

Design Method:	Super
Compactive Effort:	85 gyrations
Binder Performance Grade:	67-22
Modifier Type:	NA
Aggregate Type:	Grv/Lms/RAP/Sand
Design Gradation Type:	DGA

Avg. Lab Properties of Plant Produced Mix

Sieve Size	Target	QC
25 mm (1"):	100	100
19 mm (3/4"):	100	100
12.5 mm (1/2"):	100	100
9.5 mm (3/8"):	96	96
4.75 mm (#4):	63	62
2.36 mm (#8):	42	40
1.18 mm (#16):	30	29
0.60 mm (#30):	20	21
0.30 mm (#50):	12	12
0.15 mm (#100):	8	8
0.075 mm (#200):	6.6	5.5
Binder Content (Pb):	5.5	5.1
Eff. Binder Content (Pbe):	4.9	4.5
Dust-to-Eff. Binder Ratio:	1.3	1.2
RAP Binder Replacement (%):	19	22
RAS Binder Replacement (%):	0	0
Total Binder Replacement (%):	19	22
Rice Gravity (Gmm):	2.390	2.414
Bulk Gravity (Gmb):	2.294	2.349
Air Voids (Va):	4.0	2.7
Aggregate Gravity (Gsb or Gse):	2.551	2.563
VMA:	15.1	13
VFA:	74	79

Construction Diary

Relevant Conditions for Construction

Completion Date:	October 8, 2018
24 Hour High Temperature (F):	86
24 Hour Low Temperature (F):	71
24 Hour Rainfall (in):	0.00
Planned Subot Lift Thickness (in):	1.5
Paving Machine:	Roadtec

Plant Configuration and Placement Details

Component	% Setting
Binder Content (Plant Setting)	5.0
MS Coarse Sand	6.0
MS G7/16 Crushed Gravel	52.0
MS #8 Vulcan Limestone	12.0
MS #10 Vulcan Limestone	9.0
MS Fine RAP	20.0
Hydrated Lime	1.0
As-Built Sublot Lift Thickness (in):	1.5
Total Thickness of All New Sublots (in):	9.5
Approx. Underlying HMA Thickness (in):	8.0
Type of Tack Coat Utilized:	NTSS-1HM
Undilluted Target Tack Rate (gal/sy):	0.70
Approx. Avg. Temperature at Plant (F):	325
Avg. Measured Mat Compaction:	92.3%

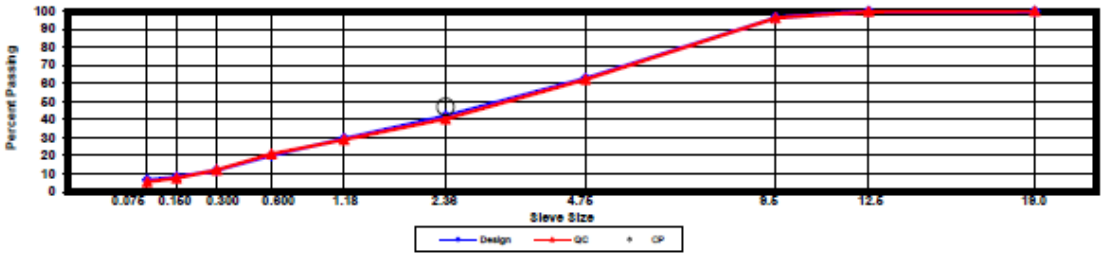

General Notes:
- References are by quadrant (E=East, N=North, W=West, S=South, L=Lee Rd 159, U=US-280), section #, and sublot (top=1).
- DGA, SMA, & OGFC refer to dense graded asphalt, stone matrix asphalt, & open-graded friction course, respectively.
- Production Gsb estimated using the actual production Gse and the difference between Gse and Gsb in the mix design.

Section and/or Sublot Specific Notes:
Pave run

Quadrant: S
Section: 2
Sublot: 2

Laboratory Diary

General Desccription of Mix and Materials

Design Method:	Super
Compactive Effort:	85 gyrations
Binder Performance Grade:	67-22
Modifier Type:	NA
Aggregate Type:	Grv/RAP/Lms/Sand
Design Gradation Type:	DGA

Avg. Lab Properties of Plant Produced Mix

Sieve Size	Target	QC
25 mm (1"):	100	100
19 mm (3/4"):	100	100
12.5 mm (1/2"):	95	97
9.5 mm (3/8"):	85	85
4.75 mm (#4):	56	55
2.36 mm (#8):	39	37
1.18 mm (#16):	28	28
0.60 mm (#30):	19	21
0.30 mm (#50):	11	12
0.15 mm (#100):	8	8
0.075 mm (#200):	5.9	5.7
Binder Content (Pb):	4.9	4.6
Eff. Binder Content (Pbe):	4.6	4.4
Dust-to-Eff. Binder Ratio:	1.3	1.3
RAP Binder Replacement (%):	29	33
RAS Binder Replacement (%):	0	0
Total Binder Replacement (%):	29	33
Rice Gravity (Gmm):	2.406	2.436
Bulk Gravity (Gmb):	2.310	2.377
Air Voids (Va):	4.0	2.4
Aggregate Gravity (Gsb or Gse):	2.563	2.588
VMA:	14.3	12
VFA:	72	81

Construction Diary

Relevant Conditions for Construction

Completion Date:	October 8, 2018
24 Hour High Temperature (F):	86
24 Hour Low Temperature (F):	71
24 Hour Rainfall (in):	0.00
Planned Subot Lift Thickness (in):	2.0
Paving Machine:	Roadtec

Plant Configuration and Placement Details

Component	% Setting
Binder Content (Plant Setting)	4.9
MS Coarse Sand	6.0
MS -5/8" Crushed Gravel	44.0
MS #8 Vulcan Limestone	12.0
MS #10 Vulcan Limestone	7.0
MS Coarse RAP	10.0
MS Fine RAP	20.0
Hydrated Lime	1.0
As-Built Sublot Lift Thickness (in):	2.0
Total Thickness of All New Sublots (in):	9.5
Approx. Underlying HMA Thickness (in):	6.0
Type of Tack Coat Utilized:	NTSS-1HM
Undilluted Target Tack Rate (gal/sy):	0.70
Approx. Avg. Temperature at Plant (F):	325
Avg. Measured Mat Compaction:	93.2%

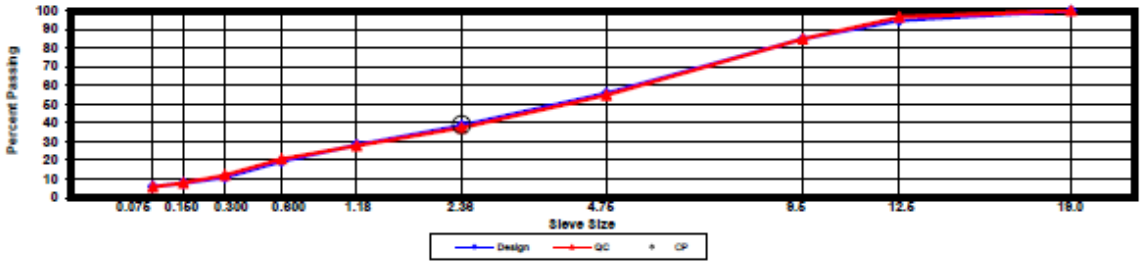

General Notes:
- References are by quadrant (E=East, N=North, W=West, S=South, L=Lee Rd 159, U=US-280), section #, and sublot (top=1).
- DGA, SMA, & OGFC refer to dense graded asphalt, stone matrix asphalt, & open-graded friction course, respectively.
- Production Gsb estimated using the actual production Gse and the difference between Gse and Gsb in the mix design.

Section and/or Sublot Specific Notes:
Pave run

2/3/2021

Quadrant: S
Section: 2
Sublot: 3

Laboratory Diary

General Desccription of Mix and Materials

Design Method:	Super
Compactive Effort:	85 gyrations
Binder Performance Grade:	67-22
Modifier Type:	NA
Aggregate Type:	Grv/RAP/Lms/Sand
Design Gradation Type:	DGA

Avg. Lab Properties of Plant Produced Mix

Sieve Size	Target	QC
25 mm (1"):	100	100
19 mm (3/4"):	99	100
12.5 mm (1/2"):	87	91
9.5 mm (3/8"):	74	78
4.75 mm (#4):	47	54
2.36 mm (#8):	32	36
1.18 mm (#16):	23	26
0.60 mm (#30):	16	20
0.30 mm (#50):	9	11
0.15 mm (#100):	7	6
0.075 mm (#200):	4.9	4.5
Binder Content (Pb):	4.7	4.5
Eff. Binder Content (Pbe):	4.2	4.0
Dust-to-Eff. Binder Ratio:	1.2	1.1
RAP Binder Replacement (%):	30	31
RAS Binder Replacement (%):	0	0
Total Binder Replacement (%):	30	31
Rice Gravity (Gmm):	2.419	2.438
Bulk Gravity (Gmb):	2.322	2.381
Air Voids (Va):	4.0	2.3
Aggregate Gravity (Gsb or Gse):	2.560	2.572
VMA:	13.6	12
VFA:	71	80

Construction Diary

Relevant Conditions for Construction

Completion Date:	October 4, 2018
24 Hour High Temperature (F):	90
24 Hour Low Temperature (F):	71
24 Hour Rainfall (in):	0.00
Planned Subot Lift Thickness (in):	3.0
Paving Machine:	Roadtec

Plant Configuration and Placement Details

Component	% Setting
Binder Content (Plant Setting)	4.5
MS Coarse Sand	7.0
MS -5/8" Crushed Gravel	40.0
MS #67 Fullen Dock Limestone	16.0
MS #10 Fullen Dock Limestone	6.0
MS Coarse RAP	20.0
MS Fine RAP	10.0
Hydrated Lime	1.0
As-Built Sublot Lift Thickness (in):	3.0
Total Thickness of All New Sublots (in):	9.5
Approx. Underlying HMA Thickness (in):	3.0
Type of Tack Coat Utilized:	NTSS-1HM
Undilluted Target Tack Rate (gal/sy):	0.70
Approx. Avg. Temperature at Plant (F):	325
Avg. Measured Mat Compaction:	95.6%

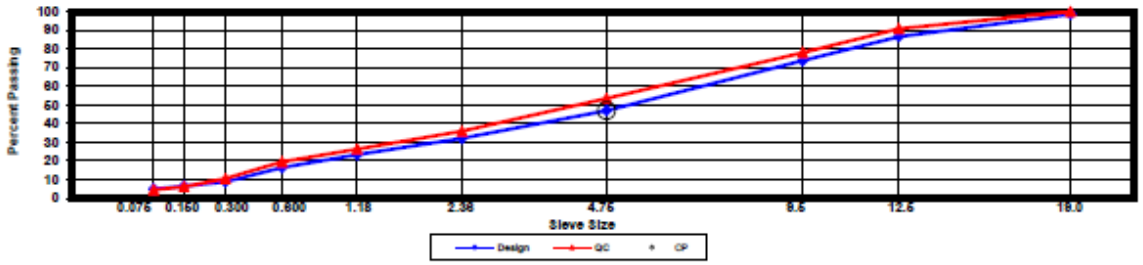

General Notes:
- References are by quadrant (E=East, N=North, W=West, S=South, L=Lee Rd 159, U=US-280), section #, and sublot (top=1).
- DGA, SMA, & OGFC refer to dense graded asphalt, stone matrix asphalt, & open-graded friction course, respectively.
- Production Gsb estimated using the actual production Gse and the difference between Gse and Gsb in the mix design.

Section and/or Sublot Specific Notes:
Pave run

2/3/2021

Quadrant: S
Section: 2
Sublot: 4

Laboratory Diary

General Descoription of Mix and Materials

Design Method:	Super
Compactive Effort:	50 gyrations
Binder Performance Grade:	67-22
Modifier Type:	NA
Aggregate Type:	RAP/Lms/Grv/Sand
Design Gradation Type:	DGA

Avg. Lab Properties of Plant Produced Mix

Sieve Size	Target	QC
25 mm (1"):	100	100
19 mm (3/4"):	96	100
12.5 mm (1/2"):	86	94
9.5 mm (3/8"):	74	83
4.75 mm (#4):	53	61
2.36 mm (#8):	35	40
1.18 mm (#16):	25	30
0.60 mm (#30):	19	23
0.30 mm (#50):	11	12
0.15 mm (#100):	8	7
0.075 mm (#200):	6.0	5.1
Binder Content (Pb):	4.7	4.7
Eff. Binder Content (Pbe):	4.0	4.1
Dust-to-Eff. Binder Ratio:	1.5	1.2
RAP Binder Replacement (%):	30	30
RAS Binder Replacement (%):	0	0
Total Binder Replacement (%):	30	30
Rice Gravity (Gmm):	2.440	2.453
Bulk Gravity (Gmb):	2.342	2.387
Air Voids (Va):	4.0	2.7
Aggregate Gravity (Gsb or Gse):	2.573	2.588
VMA:	13.3	12
VFA:	71	78

Construction Diary

Relevant Conditions for Construction

Completion Date:	October 4, 2018
24 Hour High Temperature (F):	90
24 Hour Low Temperature (F):	71
24 Hour Rainfall (in):	0.00
Planned Subot Lift Thickness (in):	3.0
Paving Machine:	Roadtec

Plant Configuration and Placement Details

Component	% Setting
Binder Content (Plant Setting)	4.5
MS Coarse Sand	10.0
MS -5/8" Crushed Gravel	25.0
MS #67 Fullen Dock Limestone	15.0
MS #10 Fullen Dock Limestone	19.0
MS Coarse RAP	20.0
MS Fine RAP	10.0
Hydrated Lime	1.0

As-Built Sublot Lift Thickness (in):	3.0
Total Thickness of All New Sublots (in):	9.5
Approx. Underlying HMA Thickness (in):	0.0
Type of Tack Coat Utilized:	UltraPrime
Undilluted Target Tack Rate (gal/sy):	0.10
Approx. Avg. Temperature at Plant (F):	325
Avg. Measured Mat Compaction:	93.7%

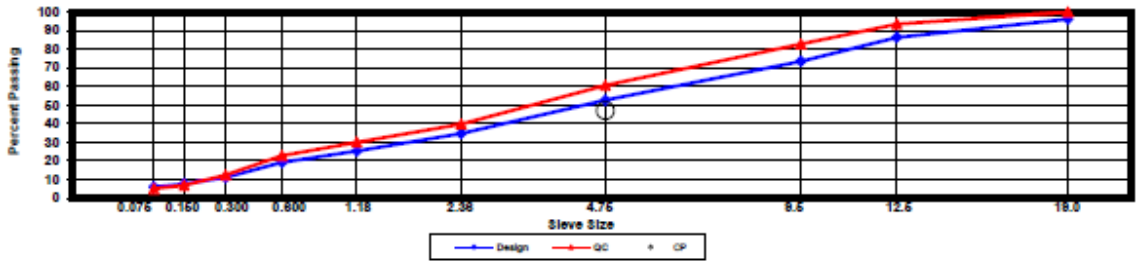

General Notes:
- References are by quadrant (E=East, N=North, W=West, S=South, L=Lee Rd 159, U=US-280), section #, and sublot (top=1).
- DGA, SMA, & OGFC refer to dense graded asphalt, stone matrix asphalt, & open-graded friction course, respectively.
- Production Gsb estimated using the actual production Gse and the difference between Gse and Gsb in the mix design.

Section and/or Sublot Specific Notes:
Pave run

APPENDIX B

In this Appendix, the elastic moduli obtained using the fully bonded and partial friction methods are compared for a conventional pavement section (the thick-lift pavement section (S9)). The results are presented in Table B.1. Partial friction method with 10^{13} and 10^{-3} ksi/in. horizontal spring constant for AC/Base and Base/Subgrade interfaces, respectively, resulted in higher base modulus and slightly lower AC modulus. Although the data is statistically different, they are in the same order of magnitude from the engineering point of view. For example, using partial friction method, the elastic modulus for base layer increased from 8.4 ksi to 13.4 ksi on average. Since the difference is not significant for conventional sections, the backcalculation analysis is usually conducted assuming fully bonded condition since most commercial software programs only are capable of fully bonded analysis. Also, the analysis using fully unbonded condition was extremely close to partial method, and thus not provided here. Although the difference was not notable for the conventional section, it resulted in significant difference in the stabilized foundation section (S2).

Table B.1 Comparison Between fully bonded and partially bonded approaches for the thick-lift section (S9).

Interface Condition	Property	AC	Base	Subgrade
Fully Bonded	Average, ksi	559.7	8.4	26.8
	Standard Deviation, ksi	319.8	4.2	5.3
Partial Friction	Average, ksi	488.0	13.4	28.0
	Standard Deviation, ksi	292.0	6.6	5.7

**the data was averaged for three randomly selected dates (01/07/2019, 01/28/2019, and 04/28/2019) collected at the Test Track with the total of 216 deflection basins.*

APPENDIX C

Backcalculated Moduli with Filtered Load Level (at 8000 lb. to 10000 lb.) for random locations 2 and 4 using partial method approach.

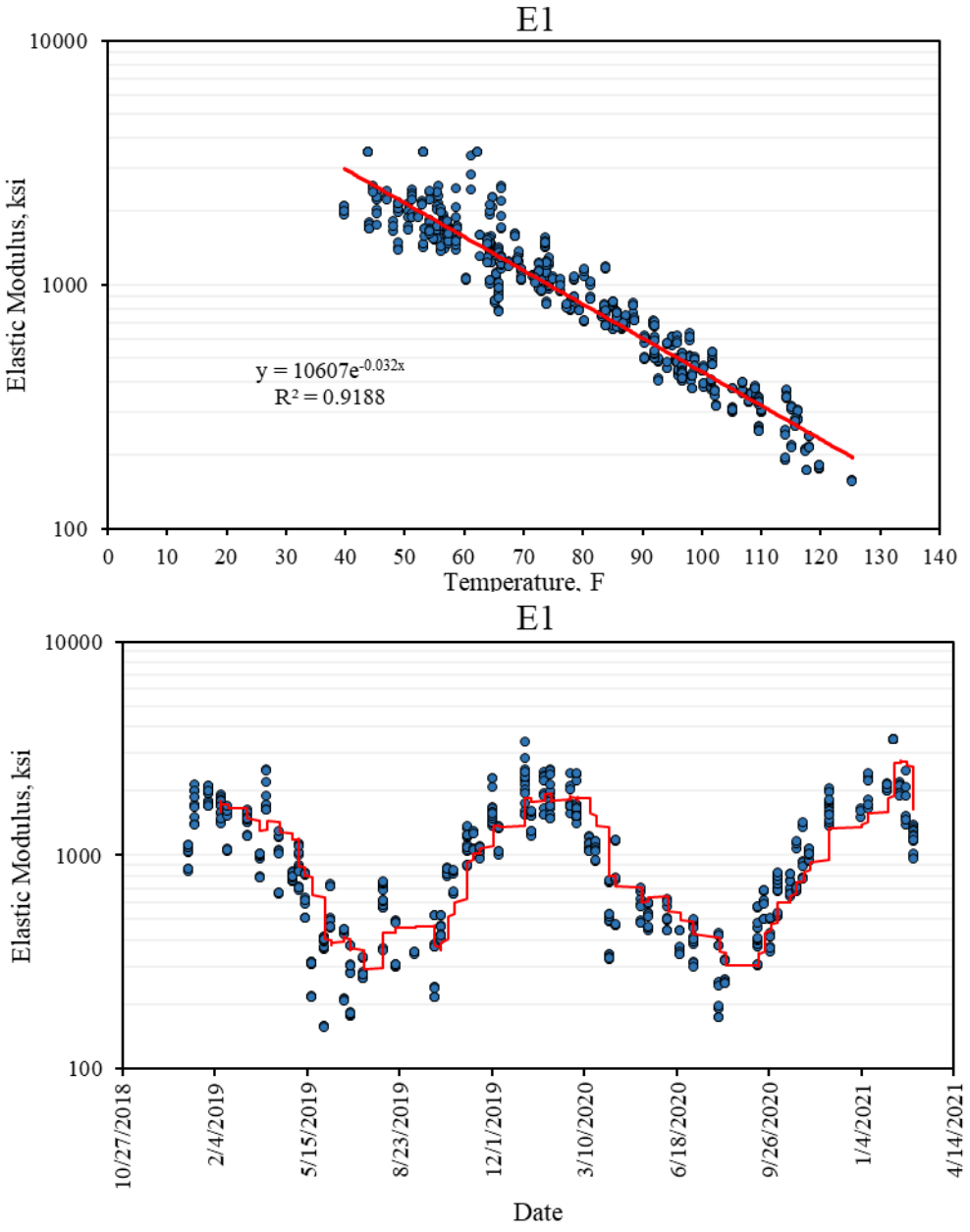

Figure C.1 Backcalculated AC Moduli with Filtered Load Level Data (8000 lb. to 10000 lb.) at RL 2 and 4 Using Partial Friction Method.

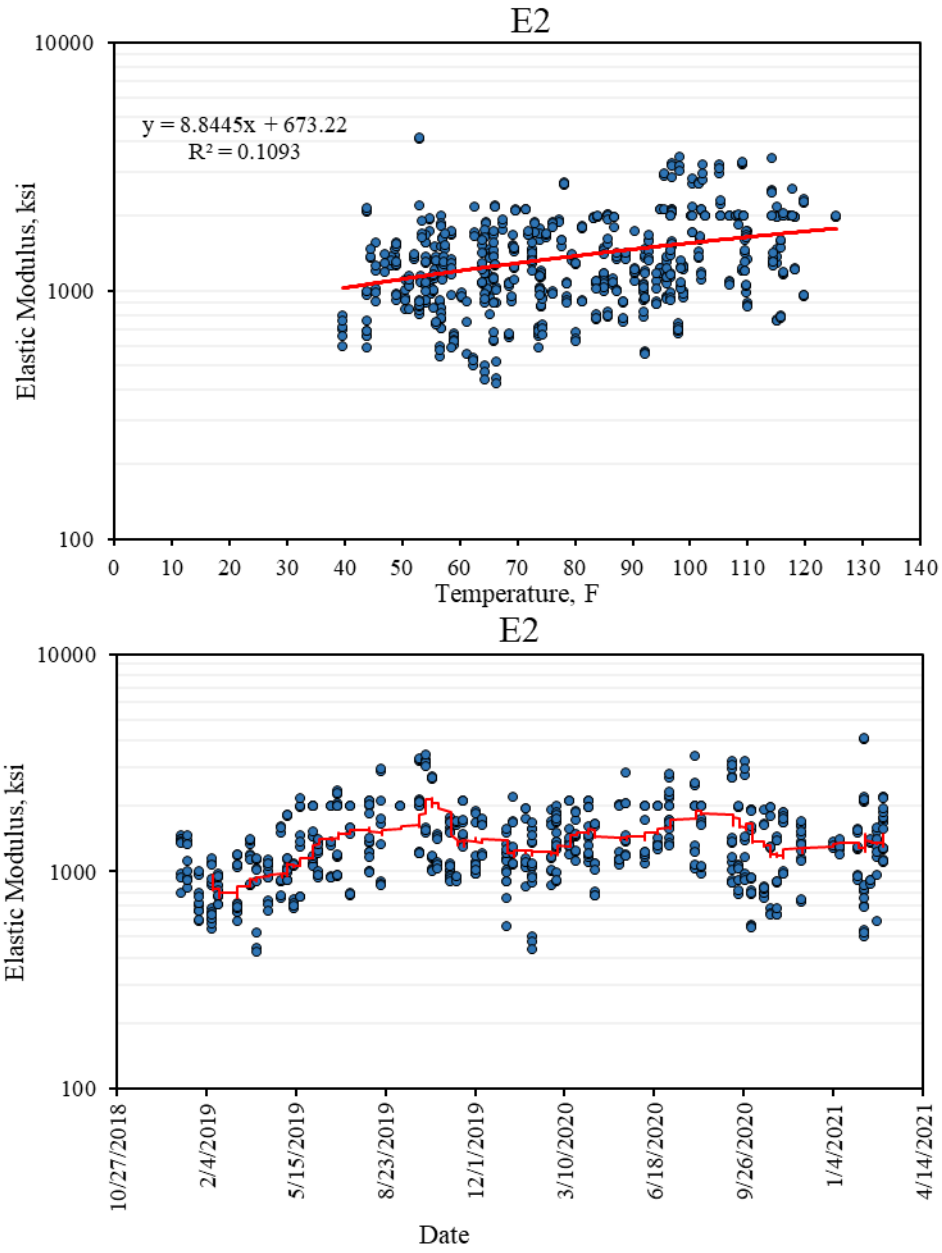

Figure C.2 Backcalculated CTB Moduli with Filtered Load Level Data (8000 lb. to 10000 lb.) at RL 2 and 4 Using Partial Friction Method.

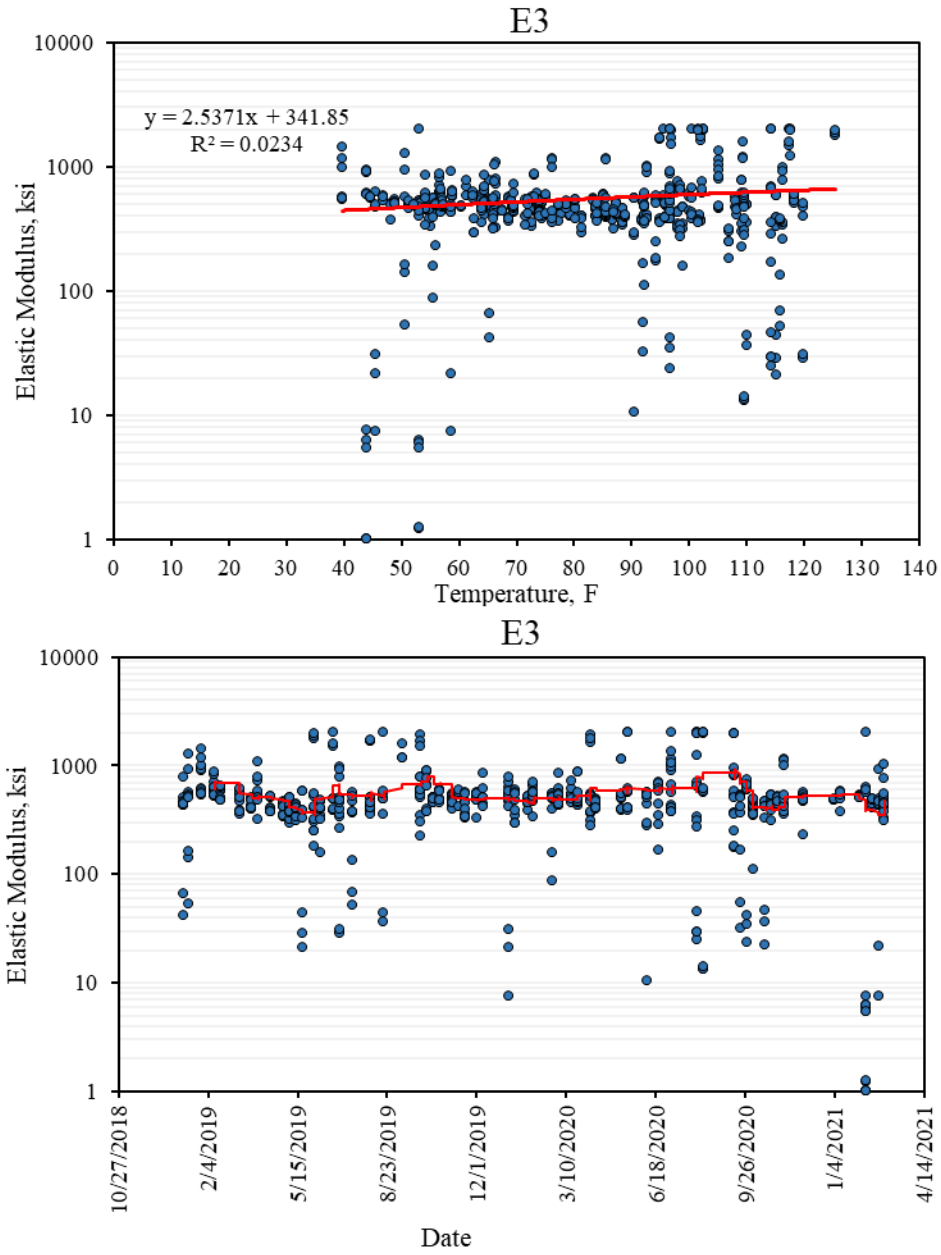

Figure C.3 Backcalculated LTS Moduli with Filtered Load Level Data (8000 lb. to 10000 lb.) at RL 2 and 4 Using Partial Friction Method.

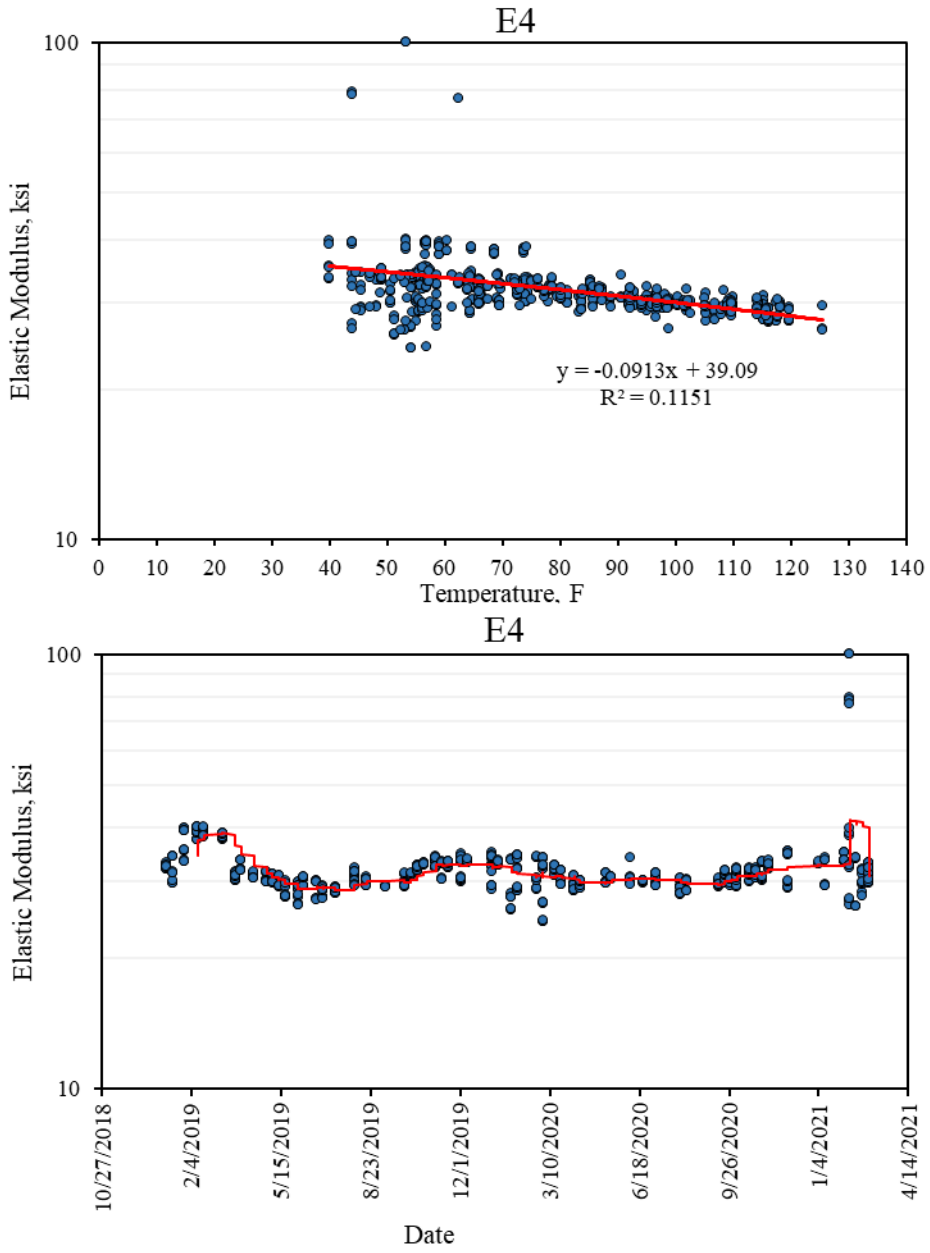

Figure C.4 Backcalculated Subgrade Moduli with Filtered Load Level Data (8000 lb. to 10000 lb.) at RL 2 and 4 Using Partial Friction Method.

APPENDIX D

The backcalculated results using the entire dataset including all stations with no filtering for a four layer system using partial friction method approach.

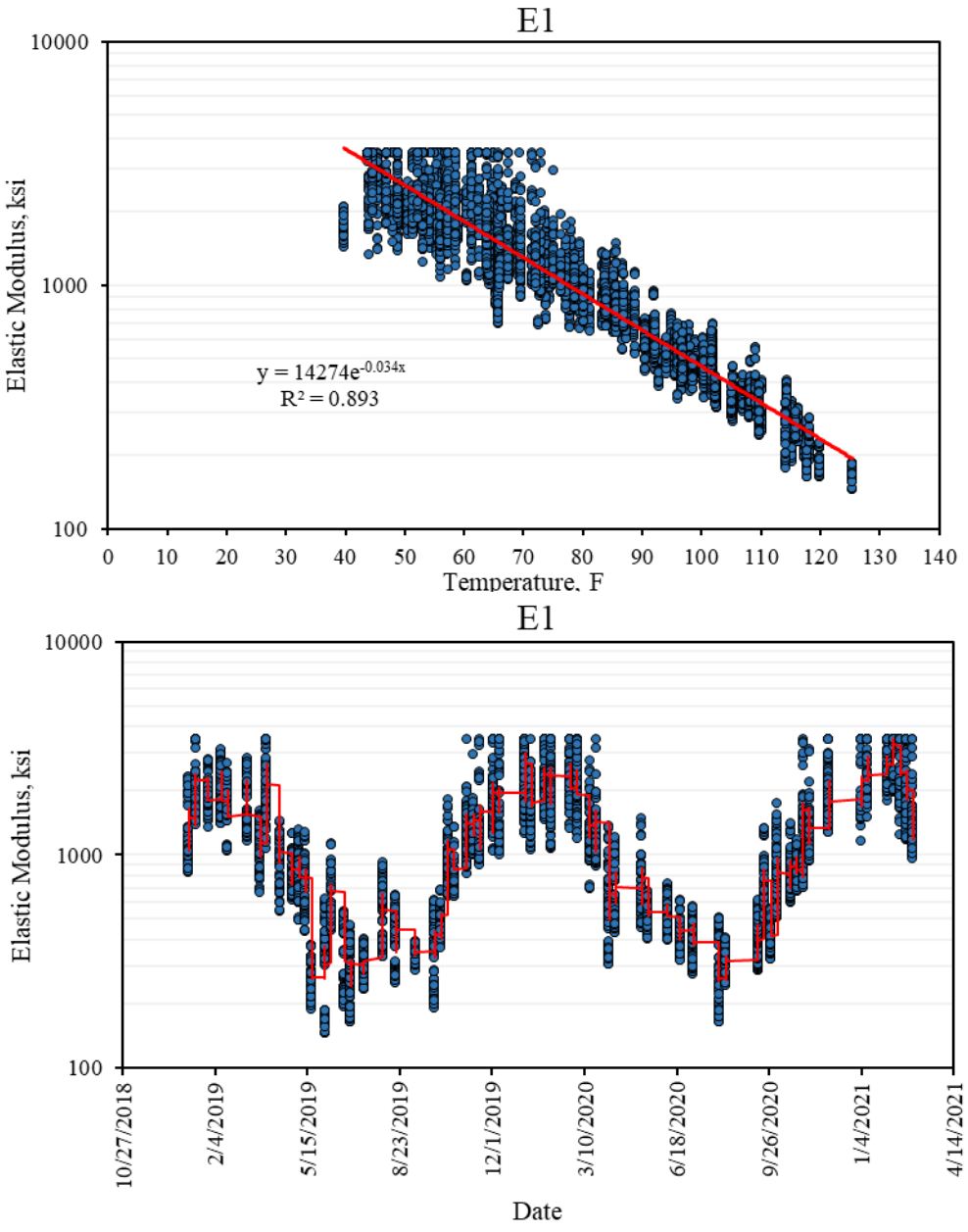

Figure D.1 Backcalculated AC Moduli with no Filtering for All Random Locations.

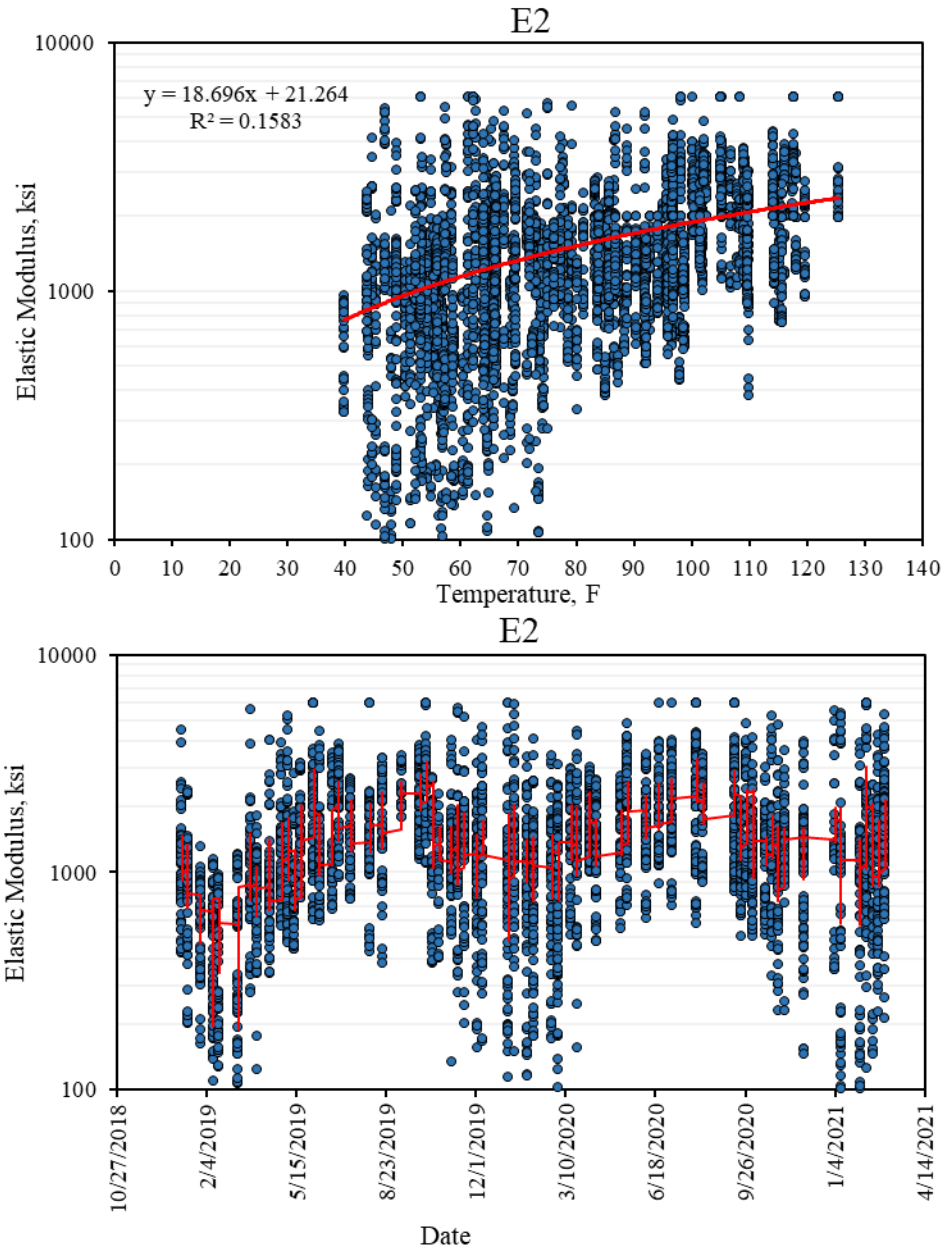

Figure D.2 Backcalculated CTB Moduli with no Filtering for All Random Locations.

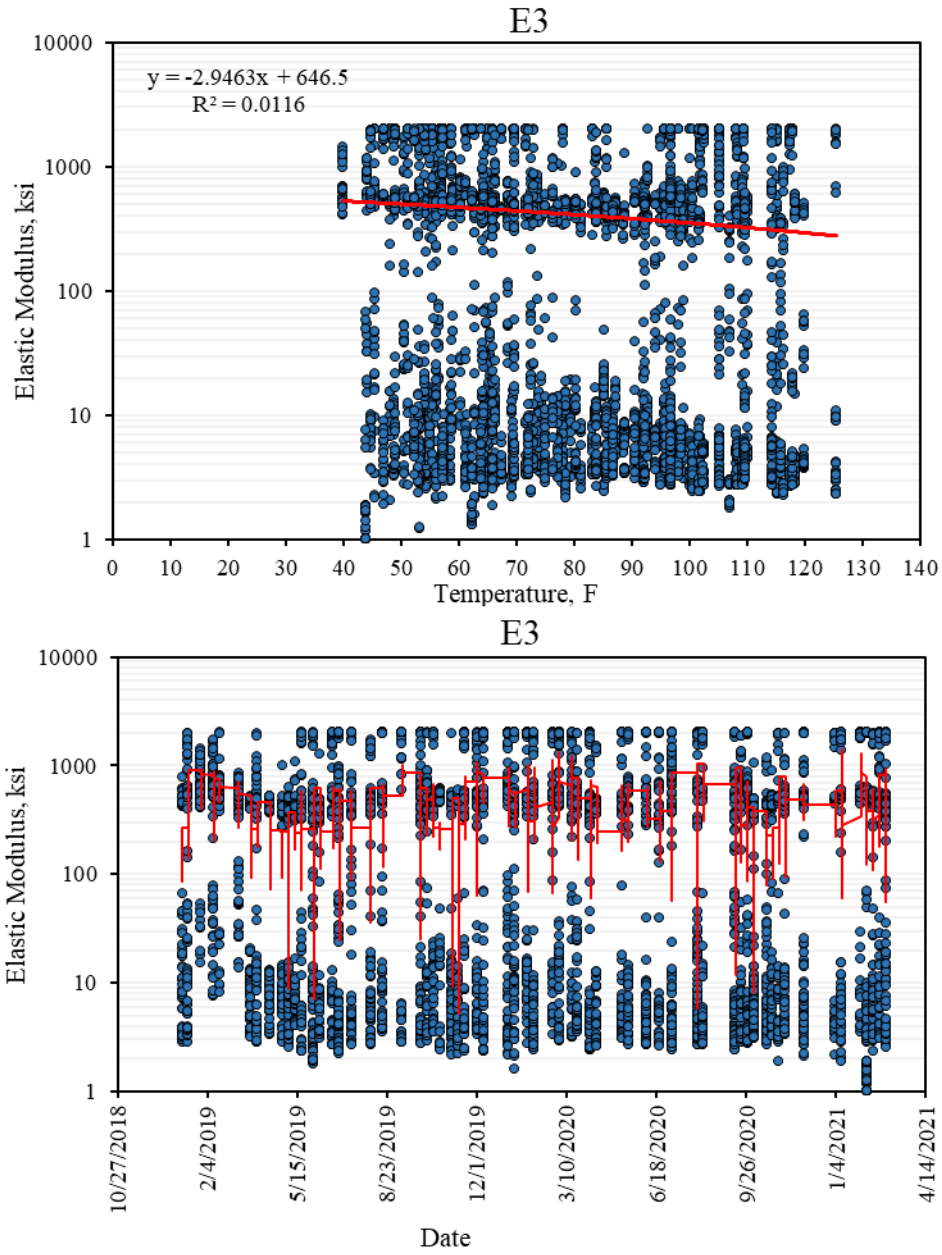

Figure D.3 Backcalculated LTS Moduli with no Filtering for All Random Locations (two separate category is evident).

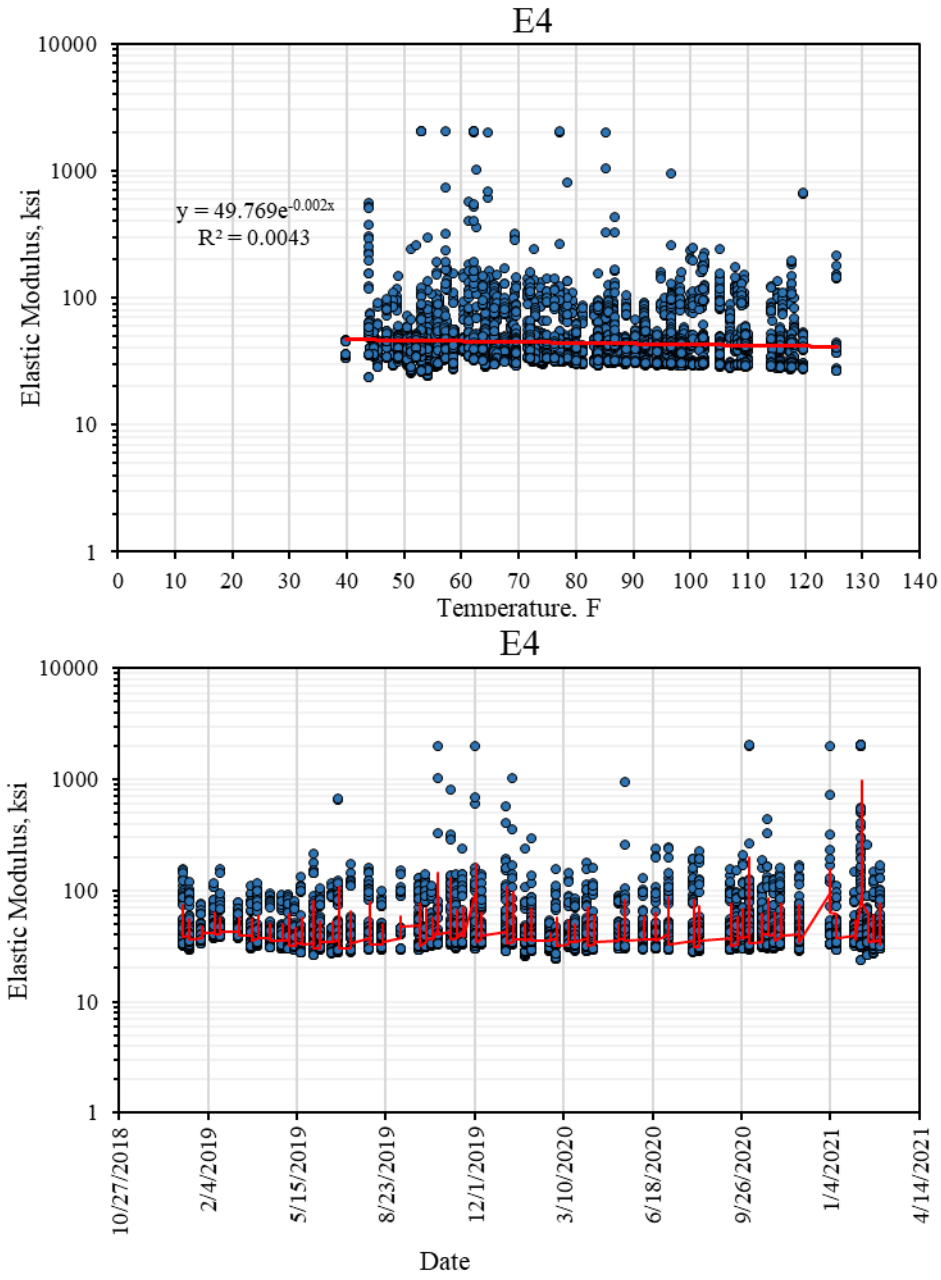

Figure D.4 Backcalculated CTB Moduli with no Filtering for All Random Locations.

APPENDIX E

Backcalculated results for x-intercept values of less than -0.02 and for load levels between 8000 lb. to 10000 lb.

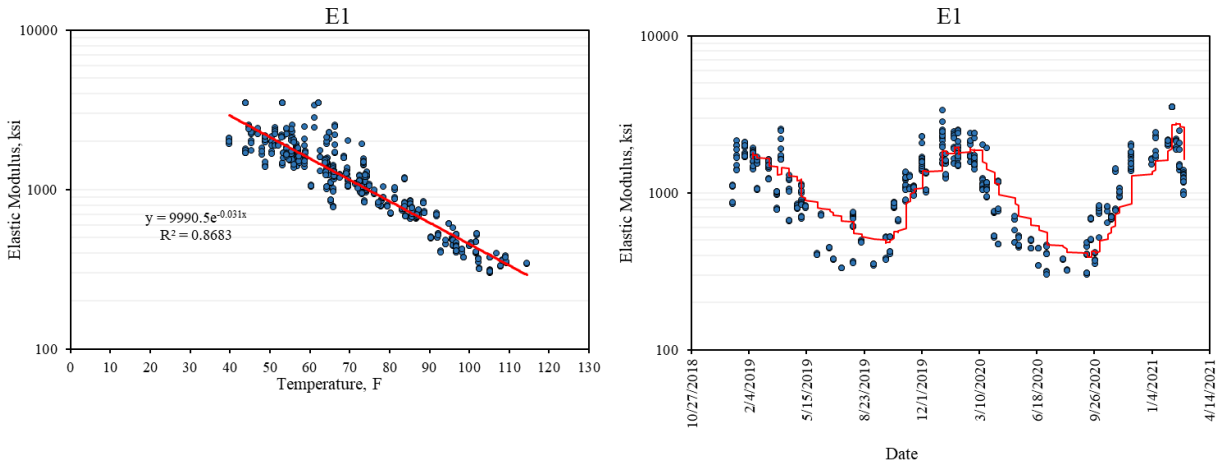

Figure E.1 Backcalculated AC Modulus with no Positive X-Intercept and Load Levels of 8000 lb. to 10000 lb.

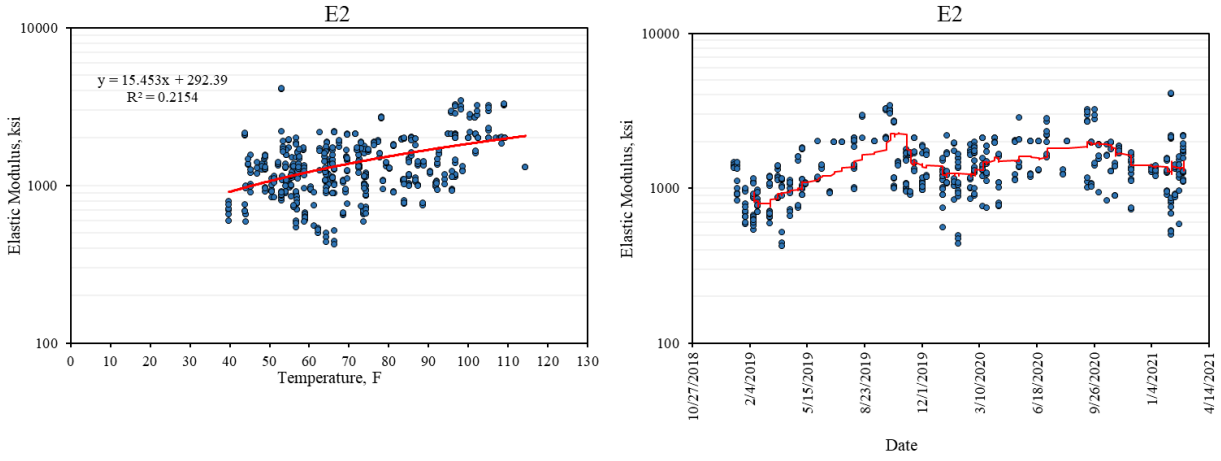

Figure E.2 Backcalculated CTB Modulus Excluding Positive X-Intercept and with Load Levels of 8000 lb. to 10000 lb.

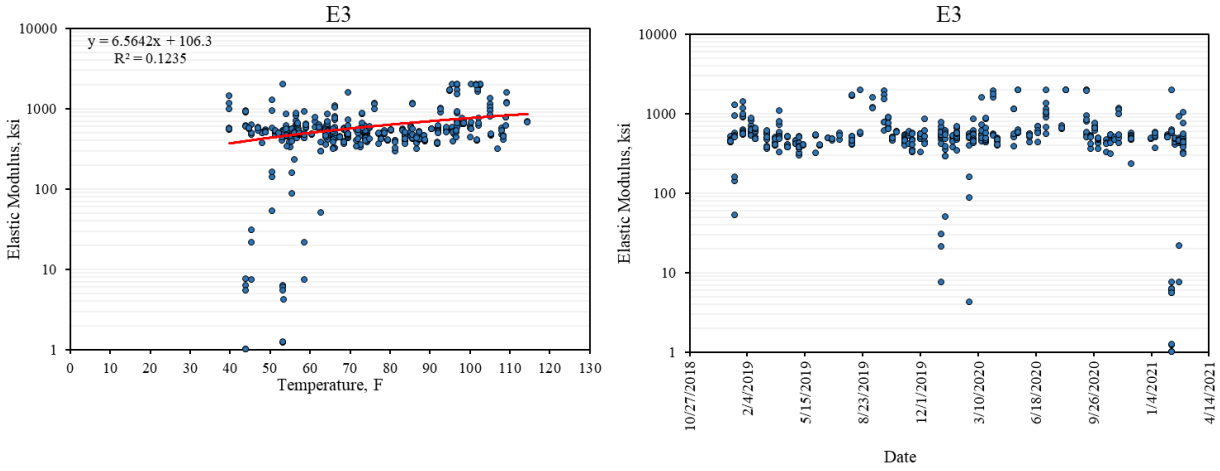

Figure E.3 Backcalculated LTS Modulus Excluding Positive X-Intercept and with Load Levels of 8000 lb. to 10000 lb.

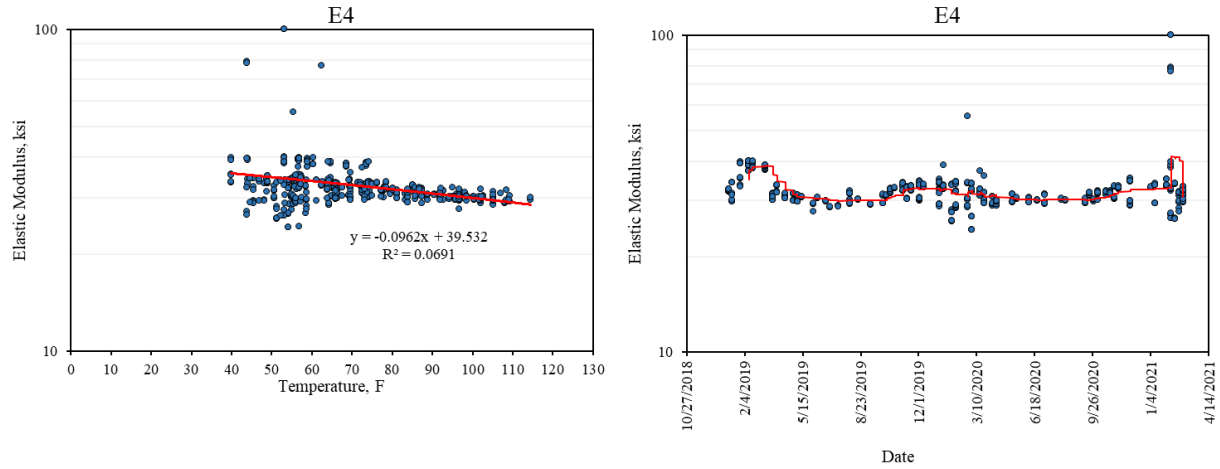

Figure E.4 Backcalculated Subgrade Modulus Excluding Positive X-Intercept and with Load Levels of 8000 lb. to 10000 lb.

APPENDIX F

The results for fully bonded condition and filtered for x-intercepts less than -0.02.

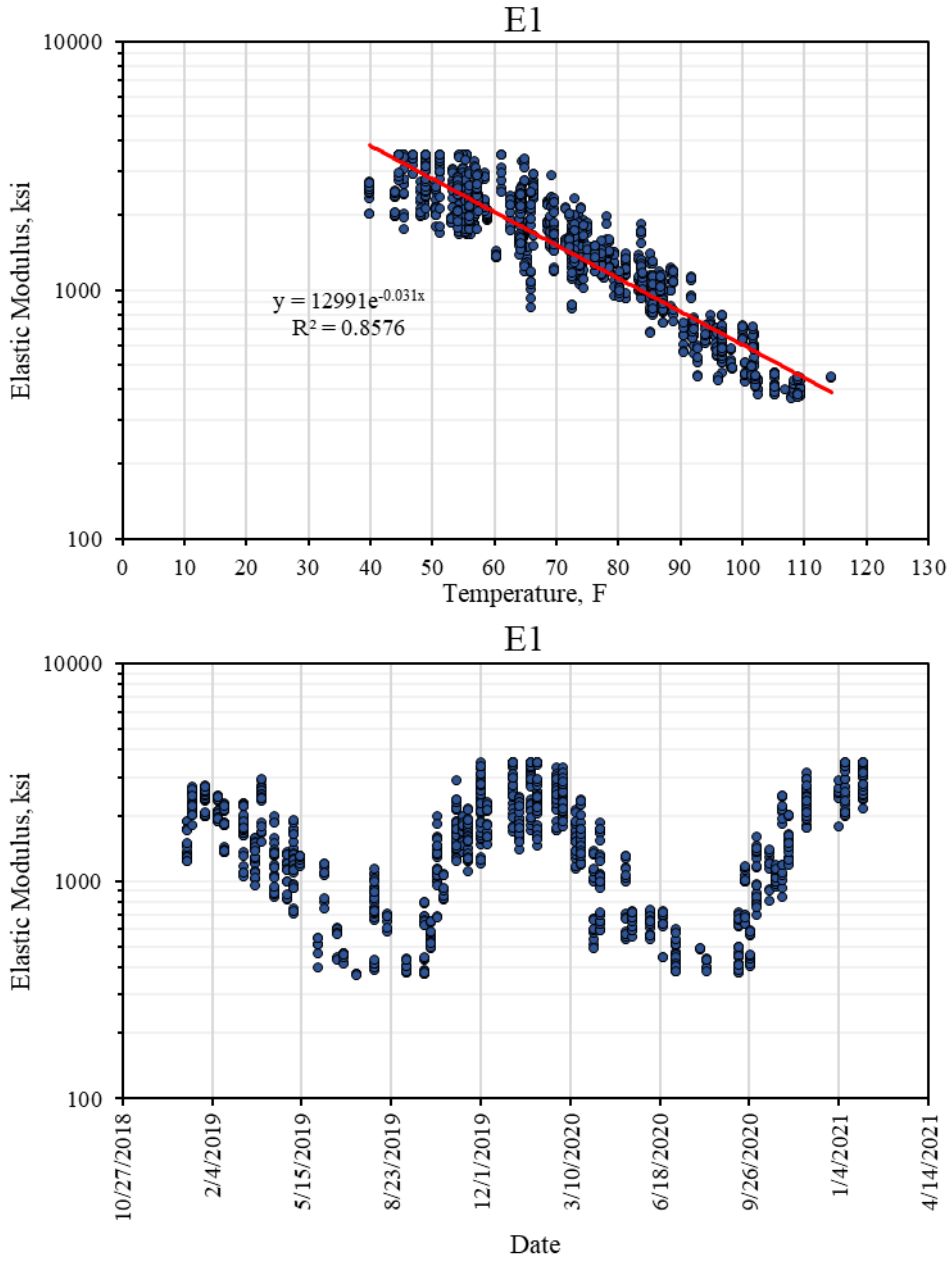

Figure F.1 Backcalculated AC Modulus Excluding Positive X-Intercept for Fully Bonded Condition.

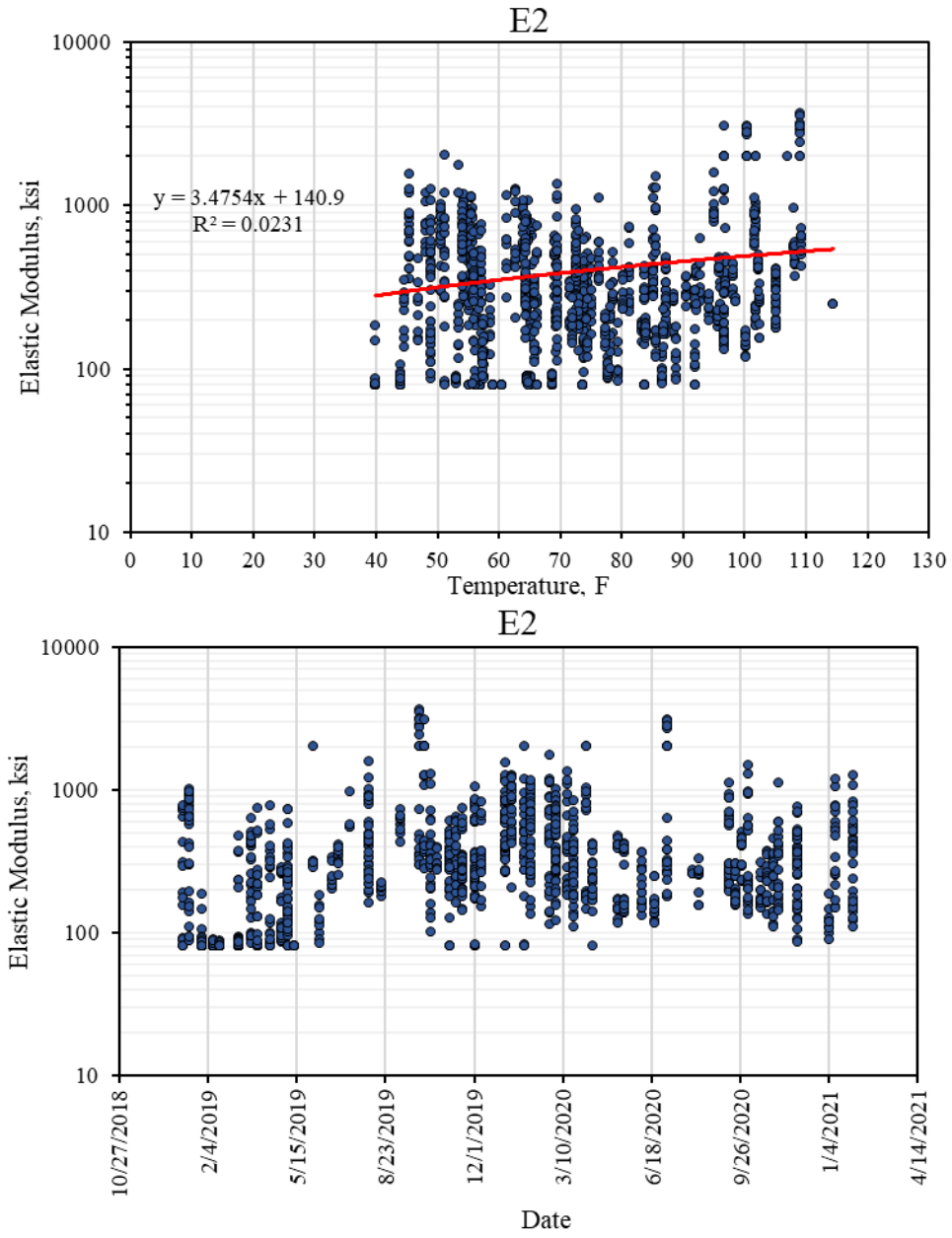

Figure F.2 Backcalculated CTB Modulus Excluding Positive X-Intercept for Fully Bonded Condition.

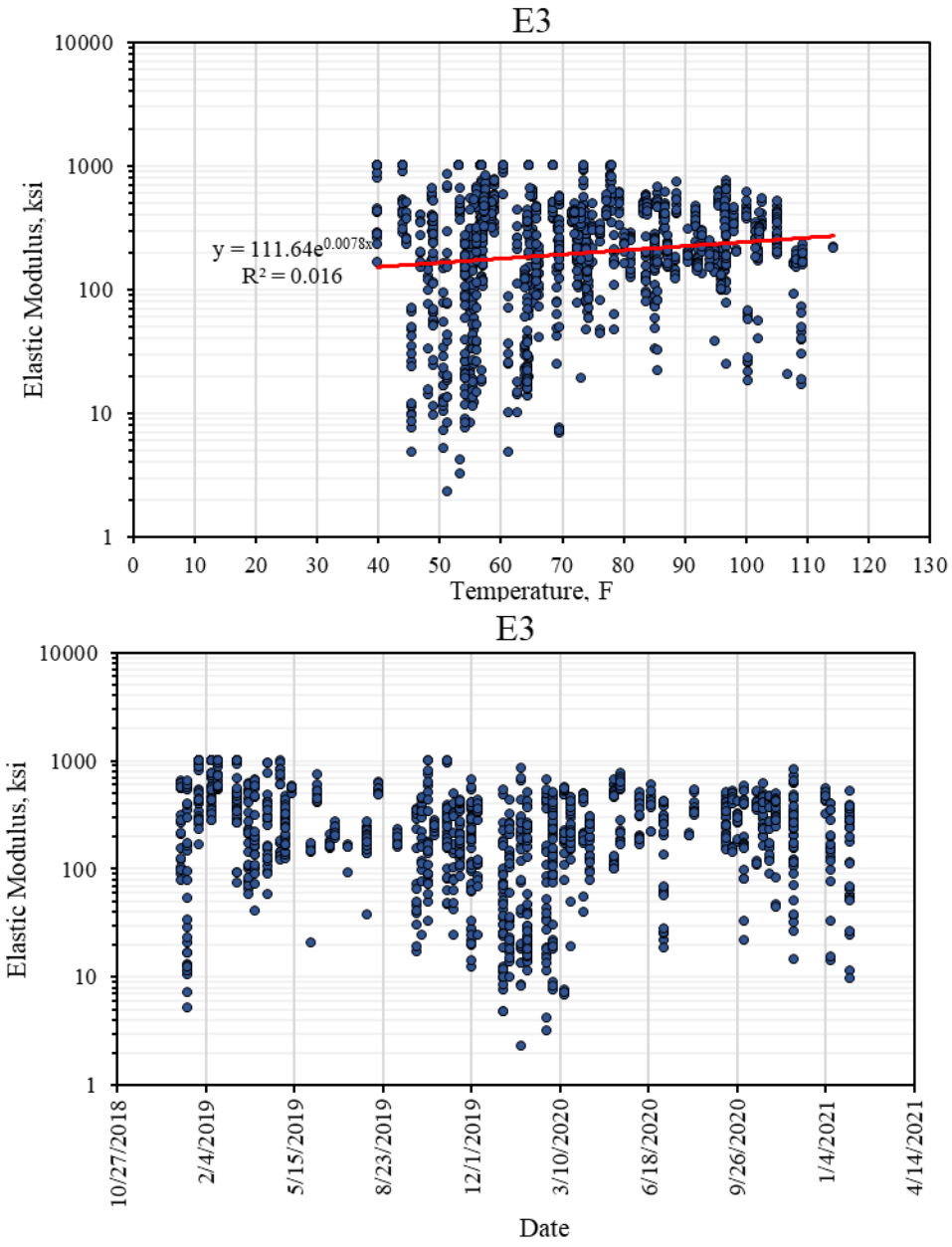

Figure F.3 Backcalculated LTS Modulus Excluding Positive X-Intercept for Fully Bonded Condition.

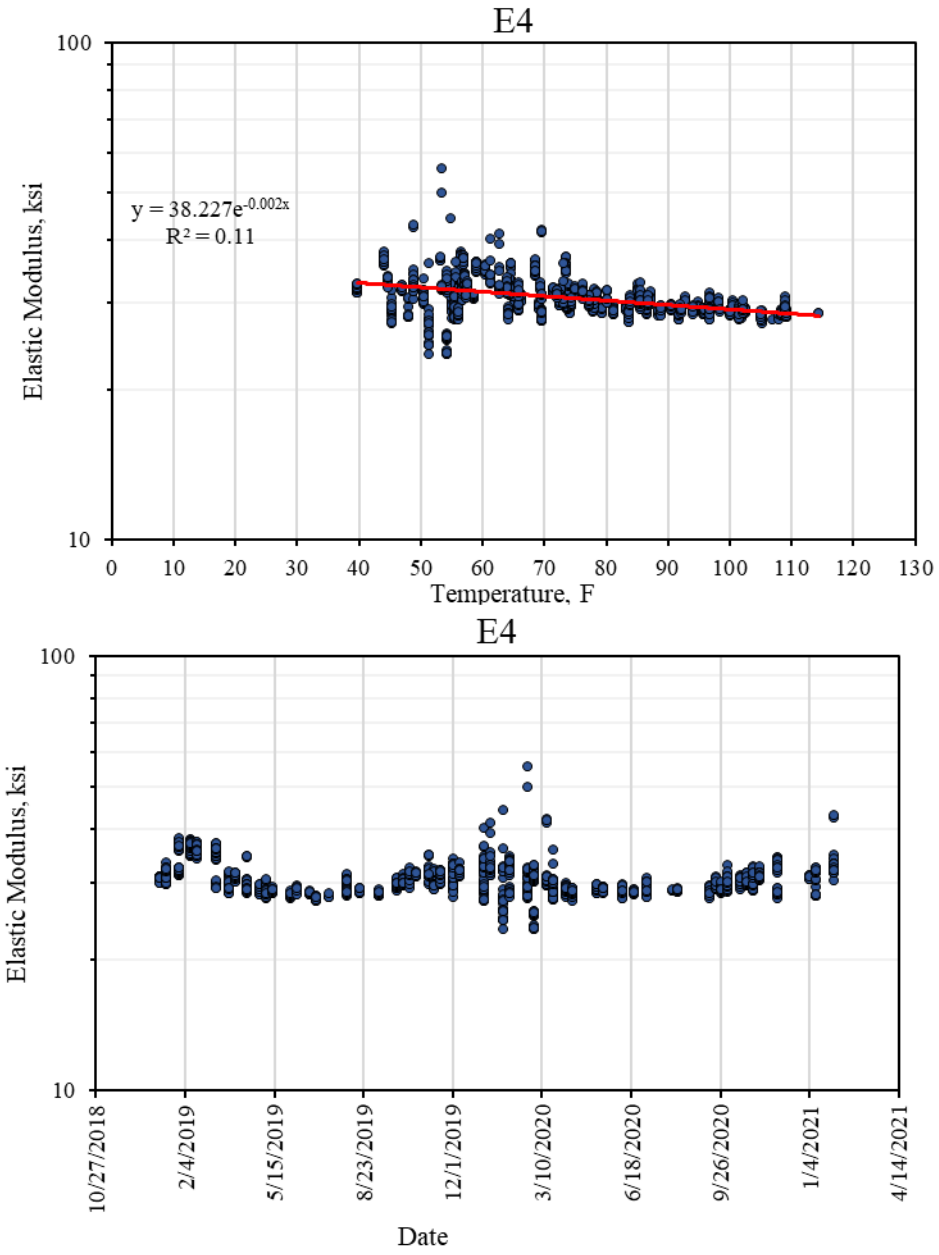

Figure F.4 Backcalculated Subgrade Modulus Excluding Positive X-Intercept for Fully Bonded Condition.